



Detection and motion parameters estimation techniques in Forward Scatter Radar

by

Nertjana Ustalli

A thesis submitted
in partial fulfillment of the requirements for the degree of
Doctor of Philosophy in Information and Communications Technologies
Curriculum in Radar and Remote sensing

at

Sapienza University of Rome

February 2018

Cycle XXX

Author

Nertjana Ustalli
Department of Information Engineering, Electronics
and Telecommunications

Thesis Supervisor

Prof. Debora Pastina
Department of Information Engineering, Electronics
and Telecommunications

This thesis was evaluated by the two following external referees:
Prof. Mikhail Cherniakov, University of Birmingham, Birmingham, UK
Dr. Carmine Clemente, University of Strathclyde, Glasgow, UK

The time and effort of the external referees in evaluating this thesis, as well as their valuable and constructive suggestions, are very much appreciated and greatly acknowledged.

*Thank you to my people,
to who surrounds me with happiness,
to who gives me love and I give love,
to who believes in me and in who I believe in.*

...this work is dedicated to them

*nertiana ustalli
Rome, February 2018*

Abstract

*F*orward scatter Radar systems designed to take advantage of the greater radar cross section, that is robust to Radar Absorbing Material and other stealth technology, and of the long integration times, due to the little phase and amplitude fluctuations, are attractive for a variety of applications. Many of which fit well with the needs of augmentation of the surveillance capabilities of low-observable targets that may have a small backscatter RCS when observed with the conventional radar systems. This thesis reports on research into this field of radar systems with additional contributions to *target detection* and *motion parameters estimation*.

Particularly, the *first part* of the thesis deals with the detection of moving targets that follow a linear trajectory in a single node FSR configuration. The detection scheme based on a square-law detector followed by an appropriate matched filter, here addressed as Crystal Video Detector (CVD) following the traditional terminology (Crystal Video Receiver), has already been put forward in the literature. Performance prediction and FSR system design were key motivator to analytically characterize the detection performance of CVD in terms of both, probability of false alarm and probability of detection. The derived closed-form expressions were validate from Monte Carlo simulations under different geometrical conditions and from experimental data acquired by a passive FSR based on FM signals. Furthermore, new detection schemes based on the CVD ensuring the constant false alarm rate (CFAR) condition were devised and analytically characterized. The performance analysis showed quite small losses of the CFAR-CVD detectors compared to the fixed threshold CVD.

The *second part* of the thesis still handles the problem of target detection through the derivation of innovative detection schemes based on the Generalized Likelihood Ratio Test (GLRT). A comparison with the detection performance of the CVD has proven the better performance of the GLRT-based detectors. In most cases the improvement has an upper bound of 3 dB. However, there are specific circumstances where the standard FSR detector shows significant losses while the GLRT schemes suffer a much smaller degradation. Moreover the possibility to have a set of secondary data assumed target free, drove to the devising of new GLRT schemes. The results demonstrated a non-negligible further improvement over the previous GLRT schemes when the operation conditions get close to the near field transition point. The detection performance of the derived detectors without and with secondary data

were analytically characterized. This analytical performance allowed to derive simplified equivalent SNR expressions that relate the GLRT detection performance to the main system and target parameters. These expressions showed to be useful for the design of effective FSR geometries that guarantee desired detection performance for specific targets.

In the *third part* of the thesis the focus is moved to the motion parameters estimation through both, a single baseline and a dual baseline FSR configuration. Accordingly, the Doppler signature extracted from the Crystal Video based scheme is exploited. Following motion parameters estimation approaches already introduced in the literature, a two dimensional filter bank technique was proposed. The main target parameters encoding Doppler rate, main lobe width and crossing time instant were estimated from such technique. The accuracy of the proposed technique was investigated from a theoretical point of view through the derivation of simplified closed-form expression of the Cramer Rao Lower Bound (CRLB). The analysis proved that unbiased estimates of the desired target parameters can be obtained that approach the derived CRLB in the high SNR region. After the dependence of the kinematic parameters on the parameters estimated from the bank was exploited. The cross baseline velocity in a single baseline configuration was estimated under the assumption that the baseline crossing point is known. Meanwhile the dual baseline configuration ensures the possibility to estimate also the baseline crossing point without a priori knowledge on the other target kinematic parameters. Once more, the CRLB of the target motion parameters for both reference scenarios was derived. The analysis proved that unbiased estimates of the target motion parameters can be obtained with high accuracy even for low SNR conditions. The effectiveness of the proposed approach was also shown from experimental data acquired by a passive FSR based on FM signals.

Acknowledgements

This work was carried out during the year 2014-2017 at the “Radar Remote Sensing and Navigation” (RRSN) group at the Department of Information Engineering and Telecommunications, Sapienza University of Rome.

First of all, I would like to express my sincere gratitude to my supervisor Prof. D. Pastina and to Prof. P. Lombardo for their support on my research during the PhD study. Thank you for providing me valuable feedback and advice, motivations and great knowledge sharing. I truly enjoyed working in this research environment that stimulates original thinking and initiative.

Sincere thanks goes to Dr. C. Bongioanni for his willingness to help and his valuable support throughout these years.

I would also like to thank my PhD colleagues for the moments shared together during the whole journey.

Contents

Abstract	v
Acknowledgements	viii
List of figures	xii
List of tables	xix
List of acronyms	xx
List of symbols	xxii
Symbols with Greek letters	xxii
Symbols with Latin letters	xxv
Chapter 1 Introduction	3
1.1 Background	3
1.2 Motivation	4
1.3 Objectives and novel contributions	5
1.4 Thesis structure	7
Chapter 2 Forward Scatter Radar overview	10
2.1 Introduction	10
2.2 Bistatic radar essentials	13
2.3 Forward Scatter Radar: phenomenology and applications	17
2.4 Forward Scatter Cross-Section	20
2.5 Signature of moving target	23
2.6 Target detection and motion parameters estimation	27
2.7 Passive Forward Scatter Radar	30
Summary	33
Chapter 3 Crystal Video Detector and performance analysis	34
3.1 Introduction	34
3.2 Forward scatter signal model	36
3.3 Crystal Video Detector	39
3.4 Performance analysis of CVD	43
3.4.1 Probability of false alarm	46

3.4.2	Probability of detection.....	54
3.5	CFAR CVD and performance analysis.....	59
3.5.1	CFAR CVD with secondary data.....	60
3.5.2	CFAR CVD without secondary data.....	65
3.5.1	CFAR CVD comparison	70
	Summary.....	73
Chapter 4	GLRT-based techniques and performance analysis	74
4.1	Introduction	74
4.2	GLRT-based detectors and performance analysis	75
4.2.1	GLRT-detectors	76
4.2.2	Performance analysis	80
4.3	Performance comparison with CVD and CFAR CVD	87
4.4	GLRT-based detectors with secondary data and performance analysis	89
4.4.1	GLRT-detectors with secondary data	89
4.4.2	Performance analysis	92
4.5	Signal to noise ratio analysis and design criteria for FSR system	95
4.5.1	Theoretical closed form expression of SNR	96
4.5.2	Design criteria for FSR system	98
	Summary.....	105
Chapter 5	Motion parameters estimation and performance analysis	106
5.1	Introduction	106
5.2	Signal parameter estimation technique.....	108
5.2.1	Two-dimensional filter bank approach	108
5.2.2	Performance evaluations.....	112
5.3	Accuracy performance analysis.....	118
5.3.1	Cramer Rao Lower Bound	119
5.3.2	Performance comparison	125
5.4	Target motion estimation and performance analysis	128
5.4.1	Single baseline configuration.....	128
5.4.2	Dual baseline configuration	130
	Summary.....	134
Chapter 6	Experimental data in Passive FSR configuration.....	136

6.1	Introduction	136
6.2	Acquisition campaign set-up	137
6.3	CVD detection performance	141
6.4	Motion parameters estimation	144
6.4.1	Single baseline configuration.....	144
6.4.2	Dual baseline configuration	148
	Summary.....	153
	Conclusions and Future work.....	154
	Appendix: Analytical derivation.....	160
	Appendix A Moments of the CVD.....	160
	Appendix B Evaluation of the P_{fa} of the CVD	161
	Appendix C Derivation of GLRT-based detectors	163
	Appendix D Derivation of GLRT-based detectors with secondary data	165
	Appendix E Evaluation of the SNR of GLRT-1 and GLRT-2 detector	167
	Appendix F Cramer Rao Lower Bound derivation of the 2D filter bank approach	168
	List of publications.....	172
	References	173

List of figures

Figure 2.1 Concept of radar operation	10
Figure 2.2 Monostatic radar geometry.	11
Figure 2.3 Bistatic radar geometry.....	11
Figure 2.4 Forward Scatter Radar geometry.....	12
Figure 2.5 Contour of constant SNR-ovals of Cassini, with $\mathcal{K} = 30L_4$ being $\mathcal{K} = R_{TRR} \max 2SNR_{min}$ the bistatic radar constant (from [1]).	15
Figure 2.6 Shadowing of the incident wave (the shadow field cancel the incident field behind the object). A is the cross-section of the shadow beam and C is the shadow contour, i.e. the boundary between the illuminated and the shadow sides of the object surface (reproduced from [29]).	18
Figure 2.7 Illustration of Babinet's principle to solve scattering problem (reproduced from [5]).	21
Figure 2.8 Radar cross section for spherical targets. Normalized values of monostatic radar cross- section and FSCS are shown as function of the normalized dimensionless parameter $p = \pi D / \lambda$ (from [39]).	22
Figure 2.9 Simulated 3D bistatic RCS for missile (a) with $\lambda = 3$ m and (b) with $\lambda = 0.3$ m and their corresponding cross-sections in (c) and (d). In (c) and (d) the red line shows the RCS in the azimuth plane; 0° is the backscatter direction and 180° is the Forward scatter (from [39]).	23
Figure 2.10 Comparison of measured forward scatter signatures of (a) a rectangular metallic plate, (b) absorbing rectangular plane and (c) simulated signature of absorbing plate (from [8]).	26
Figure 2.11 Recorded Doppler signature of the targets crossing the center of baseline: (a) small inflatable boat, (b) medium size yacht and (c) large motor boat, (from [8]).	26
Figure 2.12 Normalized velocity estimation output: real data vs simulated data (from [10]).	28
Figure 2.13 Comparison of the measured maritime target signature with matched waveforms from the correlation processing. Left images show the GPS location and trajectories, middle images show the measured target signatures and right images show the matching signature selected from the correlation processing (from [8]).	30
Figure 2.14 DVB-T and FM Doppler signatures and spectrograms of Cessna 172 ultralight aircraft at the height of 659 m (from [21]).	31
Figure 2.15 Measurements with 20 ms of integration time (from [31]).	32
Figure 2.16 Signatures comparison for the same target model on different tests: (a) Fiat Punto Evo; (b) Peugeot 107 (from [33]).	32
Figure 3.1 (a) FSR system geometry and (b) top view of the FSR configuration.	36

Figure 3.2 (a) Received signal and (b) Pattern signature and Doppler signature of a target crossing the baseline perpendicularly at midpoint.....	38
Figure 3.3 Crystal Video Detector block diagram.....	40
Figure 3.4 (a) Received signal and (b) Pattern signature and Doppler signature of a target crossing the baseline perpendicularly at midpoint for different observation times when $S=0.085$	43
Figure 3.5 (a) Received signal and (b) Pattern signature and Doppler signature of a target crossing the baseline perpendicularly at midpoint for different observation times when $S=0.76$	44
Figure 3.6 Simulated and theoretical P_{fa} as function of $T_{CVD} / (\sigma_n^2 \varepsilon)$ when $S=0.085$ and for (a) $DNSR=10$ dB and (b) $DNSR= 40$ dB.	50
Figure 3.7 Simulated and theoretical P_{fa} as function of $T_{CVD} / (\sigma_n^2 \varepsilon)$ when $S=0.76$ and for (a) $DNSR=10$ dB and (b) $DNSR= 40$ dB.	51
Figure 3.8 Theoretical and approximated P_{fa} as function of $T_{CVD} / (\sigma_n^2 \varepsilon)$ when $S=0.085$ and for (a) $DNSR=10$ dB and (b) $DNSR= 40$ dB.	52
Figure 3.9 Theoretical and approximated P_{fa} as function of $T_{CVD} / (\sigma_n^2 \varepsilon)$ when $S=0.76$ and for (a) $DNSR=10$ dB and (b) $DNSR= 40$ dB.	52
Figure 3.10 Histogram and PDF of the normalized test statistic, q_0 / σ_{q_0} when $S=0.085$ and (a) for a long observation time, $7L$ and (b) short observation time, $1/2ML$	56
Figure 3.11 Histogram and PDF of the normalized test statistic, q_0 / σ_{q_0} when $S=0.76$ and (a) for a long observation time, $7L$ and (b) short observation time, $1/2ML$	56
Figure 3.12 Simulated and theoretical P_d of the CVD detector for a $P_{fa}=10^{-5}$ when (a) $S=0.085$ and (b) $S=0.76$	57
Figure 3.13 The term at the denominator of the analytical expression in eq. (3.35) when (a) $S=0.085$ and (b) $S=0.76$	58
Figure 3.14 Theoretical and approximated P_d of the CVD detector for a $P_{fa}=10^{-5}$ when (a) $S=0.085$ and (b) $S=0.76$	58
Figure 3.15 CFAR CVD with secondary data block diagram.....	60
Figure 3.16 Histogram and PDF for different value of the $DNSR$ of the test statistic, ψ_0 for an observation time equal to the ML and (a) for $S=0.085$ and (b) for $S=0.76$	61
Figure 3.17 Simulated and theoretical P_{fa} of the CFAR CVD detector with secondary data for an observation time equal to ML and for (a) $S=0.085$ and (b) $S=0.76$	62
Figure 3.18 Histogram and PDF of the normalized test statistic ψ_0 when $S=0.085$ and (a) for a long observation time, $7L$ and (b) short observation time, $1/2ML$	64
Figure 3.19 Histogram and PDF of the normalized test statistic ψ_0 when $S=0.76$ and (a) for a long observation time, $7L$ and (b) short observation time, $1/2ML$	64

► List of figures

Figure 3.20 Simulated and theoretical P_d of CFAR CVD detector with $K=16$ for a $P_{fa}=10^{-5}$ when (a) $S=0.085$ and (b) $S=0.76$	65
Figure 3.21 CFAR CVD without secondary data block diagram.....	66
Figure 3.22 Histogram and PDF for different value of the DNSR of the test statistic, ψ_1 for an observation time equal to the ML and (a) for $S=0.085$ and (b) for $S=0.76$	67
Figure 3.23 Simulated and theoretical P_{fa} of the CFAR CVD detector without secondary data for an observation time equal to ML and for (a) $S=0.085$ and (b) $S=0.76$	67
Figure 3.24 Histogram and PDF of the normalized test statistic ψ_1 when $S=0.085$ and (a) for a long observation time, $7L$ and (b) short observation time, $1/2ML$	69
Figure 3.25 Histogram and PDF of the normalized test statistic ψ_1 when $S=0.76$ and (a) for a long observation time, $7L$ and (b) short observation time, $1/2ML$	69
Figure 3.26 Simulated and theoretical P_d of CVD CFAR detector without secondary data for a $P_{fa}=10^{-5}$ when (a) $S=0.085$ and (b) $S=0.76$	70
Figure 3.27 Theoretical P_d for a $P_{fa}=10^{-5}$ of the CVD detector compared to the CFAR CVD detector with $K=16$ and CFAR CVD without secondary data when $S=0.085$ and for (a) long observation time, $7L$, (b) main lobe, ML and (c) short observation time, $1/2ML$	71
Figure 3.28 Theoretical P_d for a $P_{fa}=10^{-5}$ of the CVD detector compared to the CFAR CVD detector with $K=16$ and CFAR CVD without secondary data when $S=0.76$ and for (a) long observation time, $7L$, (b) main lobe, ML and (c) short observation time, $1/2ML$	72
Figure 4.1 GLRT-1 detector block diagram.....	77
Figure 4.2 GLRT-2 detector block diagram.....	78
Figure 4.3 GLRT-3 detector block diagram.....	79
Figure 4.4 Simulated and theoretical P_{fa} of GLRT-1 and GLRT-2 detectors as function of T_{GLRTi} for $i=1,2$ when $S=0.085$ and for (a) long observation time, $7L$ and (b) for a short observation time, $1/2ML$	83
Figure 4.5 Simulated and theoretical P_{fa} of GLRT-1 and GLRT-2 detectors as function of T_{GLRTi} for $i=1,2$ when $S=0.76$ and for (a) long observation time, $7L$ and (b) for a short observation time, $1/2ML$	83
Figure 4.6 Simulated and theoretical P_{fa} of GLRT-3 detector as function of T_{GLRT3} (a) for $S=0.085$, $7L$ and (b) for $S=0.76$	84
Figure 4.7 Theoretical and simulated P_d for a $P_{fa}=10^{-5}$ when $S=0.085$ (a) for a long observation time, $7L$, (b) only main lobe, ML and (b) for a short observation, $1/2 ML$	85
Figure 4.8 Theoretical and simulated P_d for a $P_{fa}=10^{-5}$ when $S=0.76$ (a) for a long observation time, $7L$, (b) only main lobe, ML and (b) for a short observation, $1/2 ML$	86

Figure 4.9 Theoretical P_d of the GLRT-2 detector and CVD detector for different observation times and for a $P_{fa}=10^{-5}$ (a) when the target is in the deep far field area, $S=0.085$ and (b) when the target is getting close to the near field, $S=0.76$.	87
Figure 4.10 Theoretical P_d of the GLRT-3 detector and CFAR CVD without secondary data detector for different observation times and for a $P_{fa}=10^{-5}$ (a) when the target is in the deep far field area, $S=0.085$ and (b) when the target is getting close to the near field, $S=0.76$.	89
Figure 4.11 GLRT-2 with secondary data block diagram.	91
Figure 4.12 GLRT-3 with secondary data block diagram.	92
Figure 4.13 Simulated and theoretical P_{fa} of GLRT-2 detector with secondary data as function of $TGLRT2'$ for a target getting close to the near field, $S=0.76$ and small observation time, $1/2ML$ having set (a) $M=N$ and (b) $M=4N$.	94
Figure 4.14 Simulated and theoretical P_{fa} of GLRT-3 detector with secondary data for $M=N$ and $M=4N$ as function of $TGLRT3'$ for a target getting close to the near field, $S=0.76$ and small observation time, $1/2ML$.	94
Figure 4.15 Simulated and theoretical P_d when $S=0.76$ and for small observation time, $1/2ML$ (a) of GLRT-2 detector with secondary compared to GLRT-1 and GLRT-2 detector and (b) of GLRT-3 detector with secondary data compared to GLRT-1 and GLRT-3 detector.	95
Figure 4.16 DNSR necessary to ensure a $P_{fa}=10^{-5}$ and a $P_d=0.9$ as function of the baseline.	99
Figure 4.17 SNR achievable from GLRT-1 and GLRT-2 detectors as function of the observation time T for different values of DNSR.	100
Figure 4.18 DNSR necessary to ensure a $P_{fa}=10^{-5}$ and a $P_d=0.9$ as function of the baseline crossing point.	101
Figure 4.19 DNSR necessary to ensure a $P_{fa}=10^{-5}$ and a $P_d=0.9$ as function of the baseline crossing angle (a) for a long integration time, $T=15$ sec and (b) for short integration time, $T=1$ sec.	101
Figure 4.20 Pattern signature for baseline crossing angle $\varphi=0^\circ$ and $\varphi=60^\circ$ of a target size 2.5×1.5 m crossing the baseline at midpoint for different integration times.	102
Figure 4.21 DNSR necessary to ensure a $P_{fa}=10^{-5}$ and a $P_d=0.9$ (a) as function of the velocity for a perpendicular and midpoint crossing baseline and (b) as function of the target dimension.	103
Figure 4.22 $AmLkm$ as function of $vmsfGHz$ (a) for a target crossing the baseline in the middle for different value of shape parameter v and (b) for a target with a shape parameter $v = 1/2$ and different baseline crossing points, κ .	104
Figure 5.1 Two-dimensional filter bank block diagram.	109
Figure 5.2 Full construction of the impulse response.	111
Figure 5.3 Received signal after DC removal for different target trajectories as defined in Table 5.1.	113

► List of figures

Figure 5.4 Spectrogram normalized with respect to its maximum related to (a) case study (A) and (b) case study (B).	113
Figure 5.5 Radon transform of the spectrograms related to (a) case study (A) and (b) case study (B). ..	114
Figure 5.6 Spectrogram normalized with respect to its maximum related to (a) case study (C) and (b) case study (D).	114
Figure 5.7 Radon transform of the spectrograms related to (a) case study (C) and (b) case study (D). ..	114
Figure 5.8 (a) Received signal after DC removal filter when the target crosses the baseline with an angle of 45° and at $L/4$ from the RX for a long observation time and (b) its spectrogram normalized with respect to its maximum value.	115
Figure 5.9 Contour plot of $\Delta(\phi, \theta)$ as function of the normalized Doppler rate error and of the normalized main lobe width error (a) for a perpendicular and midpoint crossing baseline, (A) and (b) for a midpoint and non-perpendicular crossing baseline, (B).	116
Figure 5.10 Contour plot of $\Delta(\phi, \theta)$ as function of the normalized Doppler rate error and of the normalized main lobe width error (a) for a perpendicular and non-midpoint crossing baseline, (C) and (b) for a non-midpoint and non-perpendicular crossing baseline, (D).	117
Figure 5.11 (a) $\Delta(\phi, \theta)\theta = \theta$ cut along the Doppler rate axis and (b) $\Delta(\phi, \theta)\phi = \phi$ cut along the main lobe width axis.	117
Figure 5.12 Normalized elements of $J(\theta)$ as function of SNR (a) of the case study (A) and (b) of the case study (B).	121
Figure 5.13 Normalized elements of $J(\theta)$ as function of SNR (a) of the case study (C) and (b) of the case study (D).	122
Figure 5.14 Theoretical and approximated accuracy of the Doppler rate, crossing time and main lobe width against SNR (a) for the case study (A) and (b) for the case study (B).	124
Figure 5.15 Theoretical and approximated accuracy of the Doppler rate, crossing time and main lobe width against SNR for the case study (a) (C) and (b) (D).	124
Figure 5.16 Phase error approximation as function of the observation time, T for all the case studies.	125
Figure 5.17 Normalized error standard deviation of the Doppler rate, the crossing time and the main lobe width against integrated SNR (a) for the case study (A) and (b) for the case study (B).	126
Figure 5.18 Normalized error standard deviation of the Doppler rate, the crossing time and the main lobe width against integrated SNR (a) for the case study (C) and (b) for the case study (D).	127
Figure 5.19 Normalized error standard deviation of the Doppler rate, the crossing time and the main lobe width against integrated SNR for the case study (D) and for an observation time equal to the main lobe.	128
Figure 5.20 Normalized error standard deviation of the cross-baseline velocity against integrated SNR of the case study (A).	130

Figure 5.21 (a) Dual-baseline FSR system geometry and (b) top view of the dual-baseline FSR configuration.	131
Figure 5.22 Normalized error standard deviation (a) of the cross-baseline velocity and (b) of the baseline crossing point against integrated SNR of the case study (A).	134
Figure 6.1 16L-Instrumental approach chart.	138
Figure 6.2 Experimental topology of the FSR system used for data collection: the blue and the red markers indicate the TX and RXs position respectively, the yellow lines are the baseline and the red line indicates the trajectory of the aircraft during the landing.	139
Figure 6.3 (a) Multi channel receiver and (b) block diagram of the multi-channel receiver.	140
Figure 6.4 ICS-155 (GE Intelligence Platforms).	140
Figure 6.5 Received signal time signature after DC removal filter of an Airbus A320 (Test-1).	142
Figure 6.6 (a) Theoretical P_{fa} and P_{fa} in presence of real data as function of $T/(\sigma_n^2 \epsilon)$ for different value of DNSR and (b) theoretical P_d and P_d in presence of real data as function of $T/(\sigma_n^2 \epsilon)$ for three different value of DNSR.	143
Figure 6.7 Received signal after square law detector and decimation of an Airbus A319 (Test-2).	144
Figure 6.8 (a) Spectrogram of the signal received from RX1 and (b) its corresponding Radon transform (Test-2).	145
Figure 6.9 Contour plot of $\Delta(\phi, \theta)$ as function of the Doppler rate and of the main lobe width.	146
Figure 6.10 (a) $\Delta(\phi, \theta)$ cut along Doppler rate axis and (b) $\Delta(\phi, \theta)$ cut along the main lobe width axis.	147
Figure 6.11 Comparison of (a) the measured signal with (b) the impulse response of the matched filter, $h_{\phi, \theta}(t)$	147
Figure 6.12 Received signal after square law detector and decimation of a Boeing 737-800 (Test-3): (a) RX_1 and (b) RX_2	148
Figure 6.13 (a) Spectrogram of the signal received from RX_1 and (b) spectrogram of the signal received from RX_2	149
Figure 6.14 Radon transform of the spectrogram related to (a) the signal received from RX_1 and (b) to the signal received from RX_2	149
Figure 6.15 Contour plot of $\Delta(\phi, \theta)$ as function of the Doppler rate and of the main lobe width related to (a) RX_1 and (b) RX_2	150
Figure 6.16 (a) $\Delta(\phi, \theta)$ cut along Doppler rate axis and (b) $\Delta(\phi, \theta)$ cut along the main lobe width axis.	151
Figure 6.17 Comparison of (a) the received signal from RX_1 with the (b) impulse response of the matched filter, $h_{\phi, \theta}(t)$	151

► List of figures

Figure 6.18 Comparison of (a) the received signal from RX_2 with the (b) impulse response of the matched filter, $h_{\phi^*;\theta}(t)$	152
Figure 6.19 Part of the signal at the output of the matched filter with impulse $h_{\phi^*;\theta}(t)$ related to the first and second receivers.	153

List of tables

Table 3.1 <i>System parameters and target related parameters of the reference scenarios</i>	44
Table 3.2 <i>Moments of q_1 and q_2 for $S=0.085$ and $DNSR=10$ dB</i>	47
Table 3.3 <i>Moments of q_1 and q_2 for $S=0.085$ and $DNSR=40$ dB</i>	48
Table 3.4 <i>Moments of q_1 and q_2 for $S=0.76$ and $DNSR=10$ dB</i>	48
Table 3.5 <i>Moments of q_1 and q_2 for $S=0.76$ and $DNSR=40$ dB</i>	49
Table 3.6 <i>Moments of the CVD statistic q_0 under H_0 hypothesis for $S=0.085$.</i>	53
Table 3.7 <i>Moments of the CVD statistic q_0 under H_0 hypothesis for $S=0.76$.</i>	54
Table 5.1 <i>System parameters and target related parameters of the reference scenario.</i>	112
Table 5.2 <i>Case studies parameters.</i>	112
Table 6.1 <i>Main feature of ICS-155.</i>	141
Table 6.2 <i>Main characteristic of the target-Test 1</i>	142
Table 6.3 <i>Main characteristic of the target-Test 2</i>	145
Table 6.4 <i>Main characteristic of the target-Test 3.</i>	148

List of acronyms

The following acronyms are used throughout this thesis.

<i>Acronym</i>	<i>Definition</i>
AWGN	Additive W hite G aussian N oise
CFAR	Constant F alse A larm R ate
CVD	Crystal V ideo D etector
CW	Continuous W ave
DC	D irect C omponent (Continuous Component)
DNR	D irect signal to N oise P ower R atio
DNSR	D irect signal to N oise S pectral density R atio
dof	d egree of f reedom
FIM	F isher I nformation M atrix
FSCS	F orward S catter C ross S ection
FSR	F orward S catter R adar
GLRT	G eneralized L ikelihood R atio T est
GNSS	G lobal N avigation S atellite S ystems
MIMO	M ulti I nput M ulti O utput
ML	M ain L obe
MLE	M aximum L ikelihood E stimation
MTI	M oving T arget I ndicator
PCA	P rincipal C omponent A nalysis
PCL	P assive C oherent L ocation
PDF	P robability D ensity F unction

PTD	P hysical T heory of D iffraction
RCS	R adar C ross S ection
RF	R adio F requency
SD	S econdary D ata
SNR	S ignal to N oise power R atio
STFT	S hort T ime F ourier T ransform
UAVs	U nmanned A ir V ehicles

List of symbols

The following symbol definitions are used throughout this thesis.

Symbols with Greek letters

<i>Symbol</i>	<i>Definition</i>
α	Amplitude of the received direct signal
δ	Angle referenced to the bistatic sector
$\Delta\Omega$	Angular interval from which the target is viewed
φ	Baseline crossing angle with respect to the axis normal to the baseline
σ_{BS}	Bistatic radar cross section
σ_{FS}	Forward scatter radar cross section
ψ_0	CFAR CVD with secondary data test statistic
ψ_1	CFAR CVD without secondary data test statistic
β	Complex factor proportional to the target dimension and to the received direct signal
$\xi(t)$ or ξ	DC component signal after square law detector (continuous or discrete)
μ_{q_m}	Mean value of the quadratic form q_m
$\boldsymbol{\mu}_r$	Mean vector of the received signal
σ_n^2	Noise variance
τ_{CVD}	Non central parameter of the non-central T-student distribution of the CFAR CVD detectors
τ_{GLRT-3}	Non central parameter of the non-central F-distribution of GLRT-3 detector
τ'_{GLRT-3}	Non central parameter of the non-central F-distribution of GLRT-3 detector with secondary data
$\hat{\psi}_0$	Normalized CFAR CVD with secondary data test statistic
$\hat{\psi}_1$	Normalized CFAR CVD without secondary data test statistic

$\sigma_{fs}(t)$	FSCS pattern signature
μ'_{q_m}	Scale factor of the Gamma distribution of q_m
ν_{q_m}	Shape parameter of a Gamma distribution of q_m
$\mu_{q_m}(s)$	s-th moment of the quadratic form q_m
$\mu_{q_m}^N(s)$	s-th normalized moment of the quadratic form q_m
θ_R	Target aspect angle with respect to the receiver
θ_T	Target aspect angle with respect to the transmitter
$\phi(t)$	Target phase variation
$\sigma_{q_m}^2$	Variance of the quadratic form q_m
σ_r^2	Variance of the received signal
ξ_0	Vector with all elements set to unity
λ	Wavelength
Ω	Vector that collects the unknown parameters of the GLRT-based detectors
$\eta(t)$ or $\boldsymbol{\eta}$	Impulse response projected onto the subspace orthogonal to the DC component (continuous or discrete)
$\ddot{\phi}$	Doppler rate
θ	Main lobe width of the pattern signature
ν	Target shape parameter, i.e. the ratio between the horizontal and vertical target dimension
κ	Baseline crossing point parameter
$h_{\ddot{\phi},\theta}(t)$	Generic impulse response of the two-dimensional filter bank
$\tilde{\ddot{\phi}}$	Estimated Doppler rate from the Radon transform
$\ddot{\Phi}$	Doppler rate range vector
$\Delta\ddot{\phi}_{maxi}$	Maximum offset form the estimated Doppler rate from the Radon transform for i=1,2
$\tilde{\vartheta}$	Initial value of the main lobe width of the pattern signature
$\boldsymbol{\theta}$	Main lobe width range vector
$\Delta\theta_{maxi}$	Maximum offset form the initial value of the main lobe width for i=1,2
$\chi_{\ddot{\phi},\theta}(t)$	The signal at the output of each matched filter of the two-dimensional filter bank

► List of symbols

$\Delta(\ddot{\phi}, \theta)$	Cost function
$(\hat{\dot{\phi}}, \hat{t}_0, \hat{\theta})$	Estimated Doppler rate, baseline crossing instant and main lobe width from the 2D filter bank
$\delta\ddot{\phi}$	Doppler rate step
$\delta\theta$	Main lobe width step
μ_{u_i}	Mean value of the i-th sample of the signal $u(t)$
$\sigma_{u_i}^2$	Variance of the i-th sample of the signal $u(t)$
$\boldsymbol{\vartheta}$	Vector of the unknown parameters
$\boldsymbol{\vartheta}^A$	Vector of the unknown parameters of the primary interest
$\boldsymbol{\vartheta}^B$	Vector of the unknown parameters of the secondary interest
$J(\boldsymbol{\vartheta})$	Fisher Information Matrix
$CRLB_{\ddot{\phi}}$	Cramer Rao Lower Bound of the Doppler rate
$CRLB_{\theta}$	Cramer Rao Lower Bound of the main lobe width
$\ddot{\phi}^0$	Theoretical value of the Doppler rate
θ^0	Theoretical value of the main lobe width
$\mu_{\ddot{\phi}}$	Mean value of the estimated Doppler rate
μ_{t_0}	Mean value of the estimated baseline crossing instant
μ_{θ}	Mean value of the estimated main lobe width
$\sigma_{\ddot{\phi}}^2$	Variance of the estimated Doppler rate
$\sigma_{t_0}^2$	Variance of the estimated baseline crossing instant
σ_{θ}^2	Variance of the estimated main lobe width
$\sigma_{v_x}^2$	Variance of the estimated cross-baseline velocity
$\sigma_{y_{0i}}^2$	Variance of the estimated baseline crossing point

Symbols with Latin letters

<i>Symbol</i>	<i>Definition</i>
a	Amplitude of the transmitted signal
L	Baseline
t_0	Baseline crossing instant
y_0	Baseline crossing point
\mathcal{C}	Bistatic angle (or cut angle)
K	Boltzmann's constant
f_c	Carrier frequency
f_d	Doppler shift
S	Far field parameter
$s_{t0}(t)$ or \mathbf{s}_{t0}	Global target signature (continuous or discrete)
$h(t) \equiv h_{MF}(t)$	Impulse response of the Matched filter in the CVD scheme
$[x(t), y(t)]$	Instantaneous target position
n_{q_1}	Integer values of the shape parameter ν_{q_1}
f_{dMS}^{max}	Maximum Doppler shift in monostatic radar configuration
$n(t)$ or \mathbf{n}	Noise component signal (continuous or discrete)
F	Noise figure
N_0	Noise spectral density power
T	Observation (integration) time
F_R	Pattern propagation factor for target-to-receiver path,
F_T	Pattern propagation factor for transmitter-to-target-path
q_1 (q_2)	Positive definite quadratic forms of Gaussian random variable
\mathbf{P}^\perp	Projection matrix into the subspace orthogonal to the DC component
$\sigma_{fs}(t)$	RCS pattern signature
$s_d(t)$ or \mathbf{s}_d	Received direct signal (continuous or discrete)
$r(t)$ or \mathbf{r}	Received signal (continuous or discrete)
$s_t(t)$ or \mathbf{s}_t	Received target signal (continuous or discrete)

► List of symbols

B	Receiver bandwidth
L_R	Receiving system losses
$u(t)$ or \mathbf{u}	Signal at the output of the DC removal filter (continuous or discrete)
c	Speed of light
$z(t)$ or \mathbf{z}	Square law signal (continuous or discrete)
T_0	Standard temperature
l_h	Target horizontal dimension
v	Target velocity
l_v	Target vertical dimension
R_R	Target-receiver distance
R_T	Target-transmitter distance
q_0	Test statistic of the CVD detector
T'_{CVD}	Threshold of the CFAR CVD with secondary data detector
T''_{CVD}	Threshold of the CFAR CVD without secondary data detector
T_{CVD}	Threshold of the CVD detector
$s_{tot}(t)$	Total received signal in absence of disturbance
P_T	Transmitted power output
L_T	Transmitting system losses
\mathbf{s}_{d0}	Vector with all elements set to unity
v_x	Velocity component along x-axis (cross-baseline velocity)
v_y	Velocity component along y-axis
\mathcal{K}	Bistatic radar constant
H_0	Null-hypothesis
H_1	Alternative hypothesis
P_d	Probability of detection
P_{fa}	Probability of false alarm
x_i	Test statistic of the GLRT-i detector for $i=1,2,3$
T_{GLRT-i}	Threshold of GLRT-i detector for $i=1,2,3$
$I_0(\cdot)$	Modified Bessel function of the first kind with order zero
$P_{x_i}(x_i/H_0)$	Probability density function of the test statistic x_i for $i=1,2,3$ under

	hypothesis H_0
$P_{x_i}(x_i/H_1)$	Probability density function of the test statistic x_i for $i=1,2,3$ under hypothesis H_1
$\tilde{\mathbf{r}}$	Received signal projected onto the subspace orthogonal to the direct signal (discrete)
$\tilde{\mathbf{s}}_{t0}$	Global target signature projected onto the subspace orthogonal to the direct signal (discrete)
$\mathbf{P}_{s_d}^\perp$	Orthogonal projector onto the subspace of the direct signal
N	Dimension of the primary data
$\mathbf{P}_{\tilde{\mathbf{s}}_{t0}}$	Projector onto the subspace of $\tilde{\mathbf{s}}_{t0}$
$\mathbf{P}_{\tilde{\mathbf{s}}_{t0}}^\perp$	Orthogonal projector onto the subspace of $\tilde{\mathbf{s}}_{t0}$
$B(x, y)$	Beta function
$P_{fa} _{GLRT_i}$	Probability of false alarm of the GLRT-i detector for $i=1,2,3$
$P_d _{GLRT_i}$	Probability of detection of the GLRT-i detector for $i=1,2,3$
$Q_M(\cdot)$	Marcum function
SNR_{GLRT_i}	Signal to noise ratio of GLRT-i detector for $i=1,2$
$(\cdot)^T$	Transpose operator
$(\cdot)^H$	Hermitian operator
$E\{\cdot\}$	Expectation operator
$\Re\{\cdot\}$	Real part operator
$\Im\{\cdot\}$	Imaginary part operator
$B(x, a, b)$	Incomplete beta function
7L	Seven lobes
1/2ML	Time to move between the -3dB level points of the maximum FSCS pattern
\mathbf{r}'	Secondary data assumed to contain direct signal and noise component (discrete)
M	Dimension of the secondary data
$P_r(\mathbf{r}/H_0)$	Probability density function of the received signal under hypothesis H_0
$P_r(\mathbf{r}/H_1)$	Probability density function of the received signal under hypothesis H_1

► List of symbols

$P_{\mathbf{r}'}(\mathbf{r}'/H_0)$	Probability density function of the secondary data under hypothesis H_0
x'_i	Test statistic of the GLRT-i detector with secondary data for $i=2,3$
T'_{GLRTi}	Threshold of GLRT-i detector with secondary data for $i=2,3$
$P_{x'_i}\left(x'_i/H_0\right)$	Probability density function of the test statistic x'_i under hypothesis H_0
$P_{x'_i}\left(x'_i/H_1\right)$	Probability density function of the test statistic x'_i under hypothesis H_1
$P_{fa} _{GLRT-SD_i}$	Probability of false alarm of the GLRT-i detector with secondary data for $i=2,3$
$P_d _{GLRT-SD_i}$	Probability of detection of the GLRT-i detector with secondary data for $i=2,3$
SDR_{GLRTi}	Target signal-to-direct signal power ratio of the GLRT-i detector for $i=1,2$
SNR_{GLRTi}	Target signal to noise ratio of the GLRT-i detector for $i=1,2$
$C(\cdot)$	Fresnel Cosine
$S(\cdot)$	Fresnel Sine
SNR_{∞}^{opt}	The optimum SNR achievable from coherent detection techniques (GLRT-1 detector)
A	Target area
$s_u(t)$ or \mathbf{s}_u	New useful signal after the DC removal filter in the CVD scheme (continuous or discrete)
$s_n(t)$ or \mathbf{s}_n	New noise component after the DC removal filter in the CVD scheme (continuous or discrete)
$S_u(t, f)$	Short Time Fourier Transform of the signal $u(t)$
(v', l'_h, l'_v)	Expected ranges of the target velocity and target size
M_d	Amplitude of the received direct signal
M_t	The peak amplitude of the received target signal
\mathbf{J}^A	FIM of the primary parameters of interest
\mathbf{J}^B	FIM of the secondary parameters of interest
\mathbf{J}^{AB}	3x3 matrix collecting the off-diagonal elements of $\mathbf{J}(\boldsymbol{\vartheta})$
C_{CRLB}	The inverse of the FIM of the primary parameters of interest

$C_{CRLB}^{Approx-i}$	Approximated inverse of the FIM of the primary parameters of interest
$CRLB_{t_0}$	Cramer Rao Lower bound of the baseline crossing instant
t_0^0	Theoretical value of the baseline crossing instant
\hat{v}_x	Estimated cross-baseline velocity
v_x^0	Theoretical value of the cross-baseline velocity
\hat{y}_{0i}	Estimated baseline crossing point
y_{0i}^0	Theoretical value of the baseline crossing point
$CRLB_{v_x}$	Cramer Rao Lower Bound of the cross-baseline velocity
$CRLB_{y_0}$	Cramer Rao Lower Bound of the baseline crossing point
Δt	Time difference of arrivals
$\widehat{\Delta t}$	Estimated time difference of arrivals
TX	Transmitter
RX	Receiver

Chapter 1

Introduction

This chapter introduces the main topics of the work done for this thesis project. In particular, the research background is illustrated focusing on the Forward Scatter Radar systems, which is used as a baseline for highlighting the motivations, the objectives and the novel contributions of the thesis. The general overview of these aspects, which are deeply analyzed throughout the dissertation, is followed by a brief description of the chapters of this document.

1.1 Background

Radar has long been used in a variety of military and civilian applications. The main reason for this is an ability to survey rapidly wide areas in all weather conditions, during day and nights. The two main radars type as classified by their configurations are *monostatic* radar: with transmitter (TX) and receiver (RX) collocated and *bistatic* radar: with transmitter and receiver physically separated. This thesis concerns a particular configuration of bistatic radar: Forward Scatter Radar (FSR) which occurs when the bistatic angle approaches 180° , namely when the target is close to the segment (typically addressed as baseline) connecting TX and RX. However the physical operational principle of FSR is essentially different from that of bistatic radar, which is inherently a backscatter radar, [1]. The key peculiarity of the FSR is that it exploits the effect of electromagnetic wave shadowing the target, [2].

It has been demonstrated that the Forward Scatter (FS) configuration has two important properties: an enhanced radar cross-section in Mie and optical scattering regions which was shown robust to coating and to other stealth technology, [1]-[5] and a signature with extremely low phase and amplitude fluctuation, which allow long coherent integration times, [6]. While their history dates back to the early days of radar, the two mentioned properties pushed a recent interest on the FSR systems. Phenomenological and practical aspects of single baseline FSR systems have been largely studied in, [1],[6],[7],[8]. Among the multiple recent scientific contributions related to the exploitation of the FSR geometry properties, here are mentioned a

few recent papers, subdivided in four classes: target-detection, [7]-[11], localization, [12]-[13] motion parameters estimation, [7],[14]-[16] and classifications [6],[17]-[20].

In particular for the target detection the processing approach proposed in [8], has now become the reference processing scheme for FSR. Specially an envelope detector is applied to the received signal, this is followed by a DC removal filter and by a filter matched to the expected Doppler frequency response. This scheme employs the nice self-beating proprieties of the so called Crystal Video receiver to provide a coherent integration without requiring the I&Q demodulator. In addition it was recently shown to be very robust since it is able to operate effectively even against the modulated waveforms of passive forward scatter applications, [21].

The feasibility of target motion parameters estimation in a single baseline configuration by exploiting the Doppler signature extracted by the Crystal Video receiver was shown in [10] and [8]. Moreover in [14] the potentialities of a multi-node FSR configuration for the estimation of the motion parameters through a crossing time-based technique was shown.

Both detection scheme proposed in [8] and the motion parameters estimation approach proposed in [10], [8] are selected as references in this study.

The work done for this thesis project fits within the field of target detection and motion parameters estimation in a FSR configuration, and represents a contribution to the progress of the knowledge, having also interesting application potentialities.

1.2 Motivation

In recent years, the systems operating in Forward Scattering are receiving a renewed interest, mostly because of their special appeal in detecting and localizing low-observable targets. Detecting such objects has been a significant challenge for the present decade, due to the recent wide diffusion of light, remotely piloted air platforms and drones that call for increased surveillance capabilities. This target may have a small backscatter RCS when observed with a conventional monostatic radar system. Instead, in the FSR configuration, a pronounced Forward Scatter (FS) cross section in Mie and optical scattering regions, greatly enhances the detectability of this target. Moreover, their shadow response, because of a non-fluctuating nature of FS cross section which depends on the target silhouette and not on the shape or the

material will allow long integration times. These properties, as apparent, make the FSR particularly advantageous with respect to more usual monostatic or non-extreme bistatic radar sensors, when aiming at the detection of small objects or stealth target that certainly benefits of both non-reduced cross-section and long coherent integration time.

The possibility to operate without the need of a phase synchronization systems in a FSR configurations which include a large separation between the TX and RX is extremely attractive for reducing sensors cost. In [8] the target signature was extracted through a square envelope detector. The target signature extracted is useful to perform target detection, pattern recognition, motion parameter estimation by investigating the Doppler signature carrying the kinematic information as shown in [10]. Therefore, the characterization of the performance of this scheme could be relevant in many FSR applications other than the target detection.

The lack of a theoretical performance characterization of the detection scheme in [8] was a key motivator for research of Chapter 3. Also the possibility to exploits the I&Q baseband components to perform target detection drove to the devising of optimized detection scheme in Chapter 4 .

Another important key task in FSR is the accurate estimation of the target motion parameters as full knowledge of the target position and velocity components allows appropriate location and tracking of the target. Moreover this is a prerequisite of classification/recognition approaches which are based on target profile recognition by extracting the signature frequency spectrum or the time domain waveform. This motivates the derivation of explicit bounds on the performance of target motion parameters estimation through the formulation of the Cramer Rao Lower Bound (CRLB) in Chapter 5 .

1.3 Objectives and novel contributions

Following from the motivations, the main objective of this thesis is the development of innovative techniques for target detection and motion parameters extraction purposes, to be implemented in Forward Scatter radar systems. Analytical characterization of the detection performance and accuracy analysis of the estimated kinematic parameters will be a key feature, which will lead the definition of strategies for system design. Particularly for target detection a single node FSR is considered and a full analytical characterization of a widely used processing

approach for target detection, [8] is provided. Meanwhile, in relation to motion parameters estimation, the possibility to exploit both a single baseline and a dual baseline configuration is considered: thus a specific technique is derived and its performance analyzed. The advantages coming from the use of dual baseline configuration with respect to the single node configuration is highlighted.

Corresponding to the objectives previously discussed, the following novelties and main results have been reached and are presented which may be divided in two broad areas:

Target detection: Firstly motivated by the low cost implementation and by the easy deployment of the proposed technique in [8] that is addressed here as Crystal Video Detector (CVD) a full characterization of the performance for the detection of moving target against Additive White Gaussian Noise (AWGN) (or automatic detection) under the assumption that the target follows a linear trajectory was derived in Chapter 3 . Then two new adaptive detection scheme was devised based on the CVD detector to achieve a constant false alarm rate (CFAR) by removing the requirement to use a fixed detection threshold. An approximate analytical derivation was obtained for the performance of the new adaptive detection techniques, validated through Monte Carlo simulations. Their performance comparison shows limited losses of the CFAR CVD detectors with respect to fixed threshold CVD. The theoretical performance of the CVD was validated by processing real data acquired by a passive FSR system based on the FM signals in Chapter 6 , showing the practical effectiveness and the consistency.

Successively, advanced FSR detector schemes based on GLRT using both fixed threshold and CFAR threshold were derived in Chapter 4 , as previously under the assumption that the target embedded in AWGN follows a linear trajectory. The performance of the derived detectors is carefully investigated by providing a closed form characterization of the probability of false alarm and probability of detection. The performance analysis of the new detectors also in comparison with the standard scheme analytically characterized in the previous chapter shows that the new detectors always outperform the standard FSR detector (CVD). Finally, simplified equivalent SNR expressions that relates the SNR to the main system parameters and target size and motion parameters was provided which can be used for the design of effective FSR geometries.

Target motion parameters estimations: Taking advantage of the Doppler signature extraction from the Crystal Video based scheme and following the line in [10] and [8] a two dimensional filter bank approach was proposed for the estimation of the target parameters. Simplified closed-form expressions of Cramer Rao Lower Bound on the estimation of the target parameters of interest: Doppler rate, baseline crossing instant and main lobe width of the target pattern signature was derived. After exploiting the dependence of the kinematic parameters on the target parameters obtained from the bank, the cross-baseline velocity is estimated in a single node configuration. Meanwhile, in a dual baseline configuration also the baseline crossing point is estimated without a priori knowledge on the other target parameters. For both scenarios, the corresponding CRLB of the motion parameters that establish the minimum achievable variance of any unbiased estimator was derived. Finally, results obtained by applying the proposed processing to FM-based passive FSR experimental data in Chapter 6 had demonstrated the effectiveness of the considered approach.

1.4 Thesis structure

Once a preliminary analysis of the main topic of the thesis is done and its objectives established, the thesis is structured in this way:

Chapter 2 provides a short overview of the Forward scatter radar systems. Firstly general characteristic of the bistatic radar are discussed briefly in a qualitative manner and then the phenomenology of Forward scatter is introduced followed by relevant work published in the FSR area. Among the topics discussed are the proprieties of the FSR systems, the target cross section and the target signature in a FSR configuration. The study of the state of art about this topic let us find not only the main peculiarity but also some commonly used detectors and motion parameters estimation approach, which are taken as references in our study and are presented in the second part of this chapter. Finally, some aspects related to the exploitation of the transmitters of opportunity in a FSR configuration are discussed.

Chapter 3 deals with the problem of target detection by providing an accurate analytical expression for the detection performance in FSR configuration using the Crystal Video Detector. Firstly the signal model used through this study (also in the remaining chapters of the thesis) is introduced. Then the CVD scheme is described and the derived theoretical

performance expressions are validated by comparison to Monte Carlo simulations under two different geometrical scenarios. In the second part of the chapter two fully adaptive detectors are derived, based on the structure of the CVD scheme, which are shown to provide a constant false alarm rate (CFAR). The performance of these CFAR detectors in terms of P_{fa} and P_d are provided in closed-form and validated through Monte Carlo simulations.

Chapter 4 derives innovative detection schemes for FSR based on the GLRT for both cases, where a fixed threshold can be used and where a fully adaptive CFAR scheme is desired. The detection performance of the newly proposed detectors is characterized analytically and compared to the performance of the CVD scheme introduced in the previous chapter. This shows that the new detectors always outperform the standard FSR detector (CVD). In most cases the improvement has an upper bound of 3 dB, but there are specific cases where the standard FSR detector shows significant losses, while the new GLRT schemes suffer a much smaller degradation. Finally, simplified equivalent SNR expressions are introduced that relate the GLRT detection performance to the main parameters describing the FSR observation geometry and the target size and motion. These expressions are shown to be useful for the design of effective FSR geometries that guarantee desired detection performance for specific targets.

Chapter 5 deals with the motion parameters estimation of moving targets in a FSR configuration for both cases, where a single baseline and where a dual baseline with one transmitter and two separated receivers can be exploited. To this aim, based on the Crystal Video scheme introduced in Chapter 3 a two-dimensional filter bank approach is proposed to estimate the target signal parameters: Doppler rate, baseline crossing time and main lobe width of the target signature. Then taking advantage of the estimated target parameters, the cross-baseline velocity is estimated in a single baseline configuration. Meanwhile, the dual baseline configuration ensures the possibility to estimate two parameters without a priori knowledge: the cross-baseline velocity and the baseline crossing point. The performance of the proposed technique is investigated from a theoretical point of view in terms of accuracy. This lead us to the derivation of simplified closed-form expressions of Cramer Rao Lower Bound that establishes the minimum achievable variance of any unbiased estimator.

Chapter 6 presents results related to an experimental campaign exploiting FM transmission as signals of opportunity in a FSR configuration. The aim of the acquisition campaign is to

detect aircrafts landing at 16L runway of the “Leonardo Da Vinci” airport of Rome, Italy. The recorded signal data is used: (i) to assess the theoretical performance of the CVD derived in Chapter 3 in real environment and (ii) to assess the effectiveness of the two dimensional filter bank approach for the estimation of the target motion parameters through both single baseline and dual baseline configuration.

Conclusions summarize the main results of the study, which have led to this thesis; additionally, the conclusions are drawn and future activities are discussed.

Chapter 2

Forward Scatter Radar overview

This chapter provides a short overview of Forward Scatter phenomenology and of the principle characteristic of FSR systems. Firstly an abridged history of the development of radar is presented: FSR systems are historically thought of as the first type of bistatic radar. After we review the fundamental building blocks of bistatic radar in order to provide the concepts and definitions needed throughout the thesis and in order to emphasize the similarities and the differences with respect to monostatic radar. Lastly the study of the state of art about Forward Scatter Radar system let us find its peculiarities and some commonly used detectors and motion parameters estimation methods which are taken as references in our study.

2.1 Introduction

The two most basic functions of radar are inherent in the word, whose letters are an abbreviation of Radio Detection And Ranging (The acronym was by agreement adopted in 1943 by the Allied powers of World War II and thereafter received general international acceptance, [1]). The basic radar concept is that the Radio Frequency (RF) energy is radiated by the transmitting antenna and reflected from the reflecting object (target). A small portion of the reflected energy (radar returns or echoes) is collected by the receiving antenna and the target is detected in the radar receiver. This is illustrated in Figure 2.1.

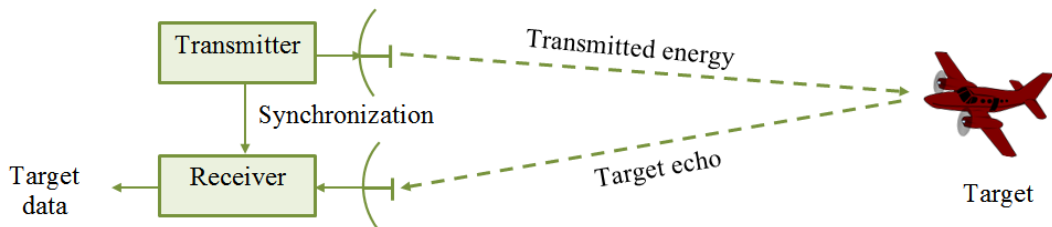


Figure 2.1 *Concept of radar operation*

Present-day radars are complex systems which by processing the radar returns can extract widely more information than its range. The principal radar function include: search or surveillance (examination of a volume of space for possible targets of interest), target detection, target position measurement and tracking, measurement of target characteristic. The radar has been used in a wide range of applications, both in military and civilian systems, [22]. This has led to many diverse radar classifications. The two main radars type as classified by their configurations are *monostatic* radar which comprise the majority of modern radar systems and *bistatic* radar which has received currently intensive interest. In monostatic radar system the transmitter (TX) and the receiver (RX) are located in close proximity to one another. A common antenna is often used for transmitting and receiving (see Figure 2.2). Conversely, in bistatic radar system the receiver is physically separated from the transmitter so that the echo signal does not travel over the same path as the transmitted signal (see Figure 2.3).

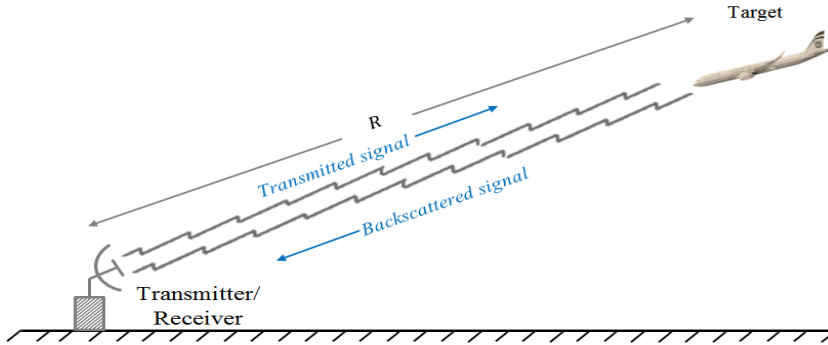


Figure 2.2 *Monostatic radar geometry.*

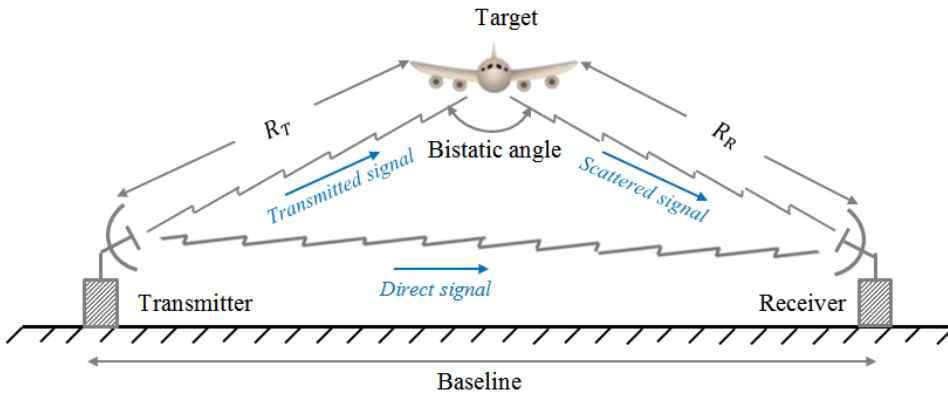


Figure 2.3 *Bistatic radar geometry*

The bistatic principle was known and demonstrated many years before the monostatic radar was demonstrated to be practical. Taylor and Young of the Naval Research Laboratory first demonstrated the bistatic radar for the detection of ships in 1922 that was disclosed in a patent issue in 1934,[23]. Most of the early developed radar were of the bistatic type configured as fixed, ground-based forward-scatter fences to detect the presence of aircraft, an emerging threat in the 1930s, [1]. Almost 200 of these fences were developed in Japan, France and Soviet Union before and during the World War II and one was deployed for a short time after the World War II in the U.S AN/FPD-23,[1]. In this geometry, when the target is near the segment joining the transmitter and the receiver (addressed as baseline) an enhanced radar cross section (RCS) was observed. The demonstration of the more versatile monostatic radar principle putted aside further development in bistatic radar that lay dormant for about 15 years, until in the early 1950's, [3].

Within the bistatic radar class there is a particular case, where the bistatic angle is large, near 180° (see Figure 2.4) which is known as Forward Scatter Radar and as mentioned previously their history dates back to the early days of radar. This particular configuration is the focus of this thesis.

FSR systems offers a number of interesting proprieties as an enhanced Radar Cross Section in Mie and optical scattering regions, which was shown robust to coating and to other stealth technologies, [3]-[5], and a signature with extremely low phase and amplitude fluctuation, which allows coherent integration times much longer than in conventional radar, [6].

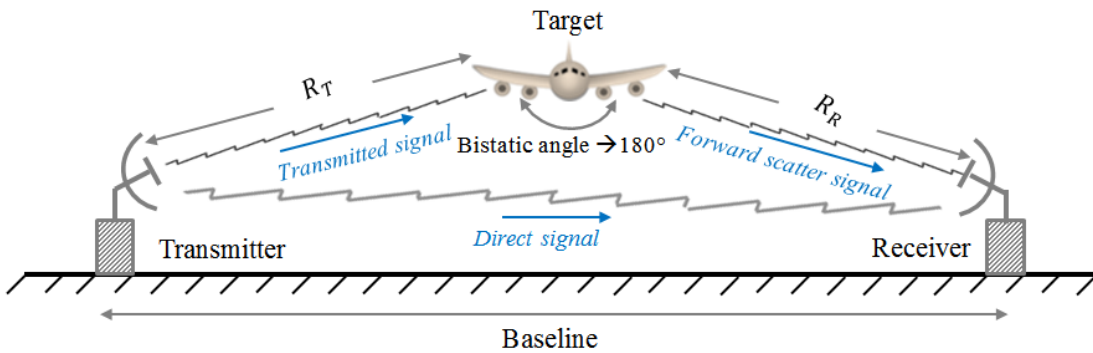


Figure 2.4 Forward Scatter Radar geometry.

In the following sections firstly general characteristic of the bistatic radar are discussed briefly in a qualitative manner and then the phenomenology of Forward scatter is introduced followed by a discussion of some of the characteristics, capabilities and limitations of the FSR systems compared to conventional radar configuration (monostatic and bistatic radar). Among the topics discussed are the proprieties of the FSR systems and its applications, the target cross section and the target signature, detection techniques and methods for extracting target motion information and finally some aspects related to the exploitation of the transmitters of opportunity in a FSR configuration.

2.2 Bistatic radar essentials

In this section is reported a review of the fundamental building block of bistatic radar emphasizing similarities and differences with the monostatic counterpart.

The IEEE standard 686-1997, [24] has defined bistatic radar as “a radar using antennas for transmission and reception at sufficiently different locations that the angles or ranges from those locations to the target are sufficiently different”. However, there is no stipulation as how far apart the two antennas should be.

Figure 2.3 illustrate this definition showing a transmitter and a receiver being situated at two locations with a baseline separation distance, L . The bistatic angle which is also known as cut angle, \mathcal{C} is the angle formed between the line joining the target and the transmitter and the line joining the target and the receiver. The bistatic angle is one of the important parameters which characterize the bistatic radar and affects system performance. The distance R_T is the range from the transmitter-to-target and the distance R_R is the range from the receiver-to-target.

The inherent geometry of the bistatic radar results in considerably different radar characteristics with respect to the monostatic radar. They have the advantages that the receivers may be passive and hence undetectable (covert operation of the receiver), [25]. The receiving systems are potentially simple and cheap. Moreover a possible enhanced radar cross section of the target due to geometrical effects is achieved. Countermeasures are difficult to deploy against bistatic radar. Now days the increasing use of systems based on Unmanned Air Vehicles (UAVs) makes bistatic systems very attractive and many of the synchronization

problem and geolocation that were previously very difficult now are readily soluble using Global Navigation Satellite Systems (GNSS). However there are some drawbacks in exploiting a system like this such as,[1],[25]: system complexity with respect to the monostatic systems, costs of providing communication between sites, lack of control over transmitter (if exploiting a transmitter of opportunity) and reduced low-level coverage due to the need for line-of-sight from several locations.

The bistatic radar is closer to that of a point-to-point communication systems than to the usual scanning monostatic radar. Moreover the bistatic geometry is more suited to a fixed fence-like coverage that is seen to be quite different from the hemispherical coverage of the monostatic radar.

The bistatic radar equation is derived in the same way as the monostatic radar but taking into account that R_T and R_R (see Figure 2.4) are different, and so the antenna gains of the transmitting (G_T) and receiving antennas (G_R) that must be evaluated in the direction of the target, [1]:

$$(R_T R_R)_{max} = \left[\frac{P_T G_T G_R \lambda^2 \sigma_{BS} F_T^2 F_R^2}{(4\pi)^3 K T_0 B SNR_{min} L_T L_R} \right]^{1/2} \quad (2.1)$$

Additional terms in eq. (2.1) are P_T the transmitter power output, λ the wavelength, σ_{BS} the bistatic radar target cross section, F_T the pattern propagation factor for transmitter-to-target-path, F_R the pattern propagation factor for target-to-receiver path, K the Boltzmann's constant, T_0 the receiving system noise temperature, B noise bandwidth of receiver's predetection filter, SNR_{min} the signal-to-noise ratio required for the detection and L_T (L_R) transmitting (receiving) system losses (> 1) not included in other parameters. Usually F_T and F_R can be significantly different, whereas they are usually identical for the monostatic case.

In agreement with eq. (2.1) the bistatic constant detection contours are defined by ovals of Cassini rather than by circles for the simplest monostatic case. In addition, the bistatic constant range sum contours (i.e. $R_T + R_R$) that are ellipses are not collinear with the ovals of Cassini differently from the monostatic case where they are collinear circles, [1].

Ovals of Cassini defines three distinct operating regions for a bistatic radar: receiver-centered region, the small oval around the receiver, transmitter-centered region, the small oval around the

transmitter and receiver-transmitter centered, or simply the cosite region, any of the ovals surrounding both transmitter and receiver. Figure 2.5 shows a contour plot of the ovals of Cassini in polar coordinate, [1]. In [1] useful bistatic radar applications based on the operating regions previously introduced are reported. The receiver-centered region can be used for air-to-ground attack (silent penetration), semiactive homing missile, short-range air defense, ground surveillance, passive situation awareness. The transmitter-centered region can be used for intelligence data gathering, missile launch alert. The cosite region can be used for medium-range air defense, satellite tracking, range instrumentation, intrusion detection, semiactive homing missile.

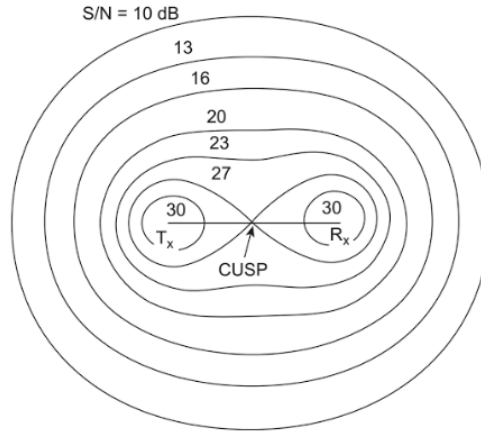


Figure 2.5 *Contour of constant SNR-ovals of Cassini, with $\mathcal{K} = 30L^4$ being*

$$\mathcal{K} = (R_T R_R)_{\max}^2 SNR_{\min} \text{ the bistatic radar constant (from [1]).}$$

The radiated signal from the transmitter arrives at the receiver via two separate paths: the direct path from transmitter to receiver and the scattered path that includes the target. The distance measured by the radar is the total scattered path, $R_T + R_R$ that locates the target somewhere on the surface of a prolate spheroid whose two foci are the transmitter and the receiver locations. To further localize the target position the two-dimensional angle of arrival of the scattered signal at the receiver is necessary. Techniques similar to that employed in monostatic radar may be employed for measuring the angle of arrival and the total scattered path length. For example for measuring the angle of arrival a transmitting antenna with a narrow fan beam in azimuth but wide in elevation may be used and a receiving antenna pattern with a number of independent, overlapping pencil beams arranged to cover a fan-shaped volume

similar to that covered by the transmitting antenna. For measuring the total scattered path, $R_T + R_R$ if for example pulse transmission are used and under the assumption that the baseline is known, the time difference of arrival between the scattered signals and the direct signals, Δt may be evaluated as $R_T + R_R = L + c\Delta t$ being c the speed of light, [1]. When the sum $R_T + R_R \rightarrow L$, the prolate spheroid degenerates into a line joining the two foci (i.e. the baseline) and the target position is indeterminate, other than it lies somewhere along the baseline, L . The location of the target in bistatic radar is not as in the monostatic case where the range measurements locates the target on the surface of a sphere.

In the bistatic radar the Doppler shift of the target scattered signal with respect to the direct signal is proportional to the time rate of change of the total path of the scattered signal:

$$f_d = \frac{1}{\lambda} \frac{\partial}{\partial t} [R_T + R_R] \quad (2.2)$$

Doppler shift depends on the motion of target, transmitter and receiver, and in general case the equation are quite complicated, [26]. In the case where only the target is moving is given by:

$$f_d = \frac{2v}{\lambda} \cos \delta \cos (\mathcal{C}/2) \quad (2.3)$$

where v is the magnitude of the target velocity vector and δ is the angle referenced to the bistatic sector and when the bistatic angle, $\mathcal{C} = 180^\circ$ the $f_d = 0$ for any δ . The maximal Doppler shift occurs for target trajectory normal to the baseline, $\delta = 0^\circ$ that even in this case is smaller than the corresponding Doppler shift of a monostatic radar, $f_{dMS}^{max} = \frac{2v}{\lambda}$.

The Doppler frequency shift may be determined by conventional frequency measurements as: filter banks, spectrum analyzers, zero crossing counters, discriminators, etc.

The bistatic radar cross section is a measure of the energy scattered from the target in the direction of the receiver as in the monostatic radar but this does not mean that a monostatic radar and a bistatic radar viewing the same target will necessary see the same cross section, [1]. On the average the two cross section will be comparable besides when the bistatic angle is close to 180° in the forward scatter region that will be investigated in detail in Section 2.4.

There are also some important differences in the technology between the bistatic and monostatic radars. For example in monostatic radar the synchronization between transmission and reception is done usually through a local oscillator meanwhile in the bistatic radar due to the separation of the transmitter and receiver as mentioned previously is done via synchronized automatic clock by exploiting GNSS signals or by reception of reference signal received directly from the transmitter (typically used in Passive Coherent Location, PCL systems). Furthermore, a directional receive antenna must scan at a non-uniform rate in order to follow the position of the transmitted signal through space hence the use of one or more electronically agile beams as in phased array radar is required because the design based upon mechanical scanning is very challenging.

2.3 Forward Scatter Radar: phenomenology and applications

The Forward Scatter Radar as extreme configuration of bistatic radar with the transmitter and the receiver facing each other and the target in a spatial region very close to the baseline (see Figure 2.4) exploits the enhanced RCS in the forward direction. The FSR system is able to provide a Forward Cross Section (FSCS) several dB higher than the conventional backscatter RCS. This enhancement is produced by forward scattering, a phenomenon first discussed in a publish work in 1908 by Mie who observed that the forward scattering produced by a sphere was in many cases larger than the backscattering, [5].

The forward scattered lobe is produced when an electromagnetic wave illuminates an object and casts a shadow. This fact puts an essential restriction on the FSR configuration as the target shadow exists within a narrow corridor around ($< 20^\circ$) the baseline. For a bistatic angle, $\mathcal{C} \cong 170^\circ$ that may be considered as a boundary of the FS corridor, in agreement with the above consideration of the Doppler shift in bistatic radar we have, $f_d \sim 0.01 f_{dMS}^{max}$, [6].

Moreover as is well known, close to the FSR configuration the range resolution is dramatically reduced, [1]. This is obvious also from the equation of the range resolution in a bistatic radar configuration, [1] where for a bistatic angle, $\mathcal{C} \rightarrow 180^\circ$ the range resolution goes

to ∞ (i.e. a continuous wave (CW) can be effectively used in FSR configuration). Only very wide bandwidth systems introduce some range resolution, [27] that are not considered here.

Other disadvantages of the FSR systems are due to the geometry as the synchronization of the receiver and the transmitter and the saturation of the receiver due to a strong direct signal (the signal from the transmitter to receiver).

However, as mentioned previously, the target scattering nature in this particular configuration shows quite useful proprieties that may be explained through the phenomenon of the electromagnetic shadowing described by the Physical Theory of Diffraction (PTD) developed by Ufimtsev, [2]. When an electromagnetic wave, illuminate an opaque object a shadow is produced on the opposite side of the object from the transmitter (see Figure 2.6) and describes a region in which the electromagnetic fields are very small (approximately zero field intensity) called as ombra region.

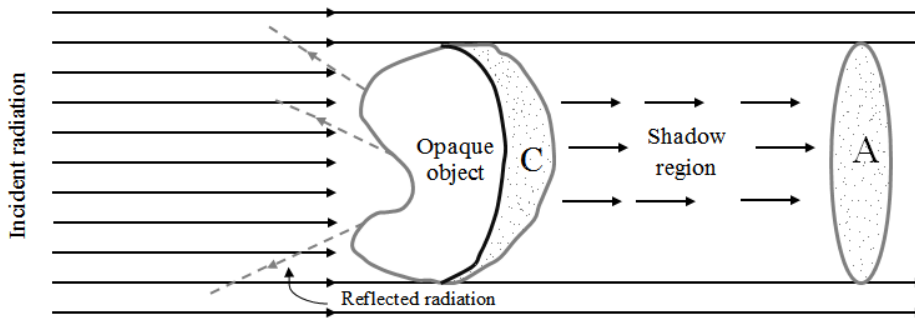


Figure 2.6 *Shadowing of the incident wave (the shadow field cancel the incident field behind the object). A is the cross-section of the shadow beam and C is the shadow contour, i.e. the boundary between the illuminated and the shadow sides of the object surface (reproduced from [29]).*

The scattered field in the shadow region near the black body surface differs only in sign from the incident radar beam. For this reason it is called the shadow radiation. It is worth mentioning that the smaller the electrical size of the object and the bigger the distance receiver-object, the less will be the shadowing effect. Two fundamental proprieties are inherent to shadow radiation from the analysis in [2]:

(i) Forward Cross Section is rather robust with respect to the target material, so that non-metallic objects have a good chance to provide a high response, [3]-[5]. In fact, following the

Shadow Contour Theorem in [2], the FSCS only depends on the contour of the illuminated target area. Specifically, even a non-reflecting target made of purely absorbing material shows the same cross section of a metallic target with the same shape and size.

(ii) FSCS it only depends on the contour and not on the amplitude and phase combination of the individual responses by a number of scattering centers inside the target body, as is usually the case outside the forward scatter configuration. Therefore the FSCS has a long temporal stability and consequently a long integration time equal to the target time visibility can be considered and an enhanced Doppler frequency resolution is obtained, [6].

The two mentioned properties pushed a recent resurgence of the interest for the FSR systems, especially with reference to the detection of low-observable targets and to the design of e.m. fences for both air and sea targets, [30]. Among the multiple recent scientific contributions related to the exploitation of the properties of the FSR geometry, we devote in Section 2.6 a special attention to the target detection, [7]-[11] and motion parameters estimation techniques, [7], [14]-[16].

Also, a set of publications in FSR are dedicated to the target classification where the Fourier transform and Principle Component Analysis (PCA) are exploited, [6], [17], [18]. In [19] the low-frequency FSR network for the classification of ground target is shown supported by experimental results for different operational frequencies. The concept of micro-sensors wireless network for ground target recognition supported by experimental results has been presented in [9]. Meanwhile a neural network-based methodology with various type of training algorithm for automatic target classification has been proposed in [20].

Moreover target localization in FSR system has been discussed in [12] where the feasibility of radiolocation of real air object was proved and in [13] where a multi-static FSR with several transmitter with omni-directional antennas and one multi-channel receiver has been exploited for measuring the target angular coordinates by the amplitude mono-pulse technique, [22]. The multiple frequencies are exploited for the first time as orthogonal waveforms of a MIMO (Multiple Input Multiple Output) FS radar, increasing robustness of FSR signal from a low-observable target in presence of clutter, multipath and interferences in [11].

In addition, the FSR principle of operation has recently been demonstrated largely compatible with the exploitation of transmitters of opportunity, [21]. This also confirms

previous specific investigations of passive FSR with specific sources of opportunity: GPS, [31], GSM, [32], Wi-Fi, [33], FM and DVB-T, [21], [34], so that we can state that the passive FSR is now an emerging research area (see Section 2.7).

In this work we refer to airborne target detection application that are least affected by clutter. However, statistical and spectral characteristic related to the FSR clutter for ground-based applications mainly related to the vegetation may be found in [35],[36] and for seaborne target detection applications due to the dynamic sea surface may be found in [37].

2.4 Forward Scatter Cross-Section

The RCS of a target illuminated by the radar is a measure of the energy scattered in the direction of the receiver. The scattering mechanisms depends on the ratio of the characteristic dimension of an object, denoted by D to the wavelength of the transmitted signal, λ this for both monostatic or bistatic configuration. In [22],[38] three different regions are defined:

- the Rayleigh region, when the ratio λ/D is much larger than unity. In the Rayleigh region, the phase distribution of the scatterers of the target varies little, and the target signal is determined mainly by its volume, rather than by its shape.
- the Mie region or the resonance region when the ratio λ/D is close to unity. In this region both the volume and the shape of the target influence its RCS since the phase distribution starts to vary over the surface.
- the Optical region when the ratio λ/D is much smaller than the unity. In this region the RCS of the target is determinate by a distribution of discrete scatterers determined by the shape of the target rather than its volume.

For the FSR configuration it was shown that in the upper Mie region ($\lambda/D \approx 1$) there is some increase of the forward scatter cross section with respect to the backscattered radar cross section and in the optical region ($\lambda/D \ll 1$) a significant enhanced is observed.

This increase can be explained through the well-known Babinet principle which consist in constructing a problem equivalent to the original problem but easier to solve it as shown in Figure 2.7, [5]. Babinet's principle applied to the forward scatter case can be summarized as follows: the target (object) is replaced with an appropriate shape plane defined by the shadow

contour (i.e. Shadow contour theorem, [2]) and then is replaced by a complementary aperture antenna. Therefore, the scattered radiation of a target in the forward direction is identical to the radiation produced by a planar aperture whose shape is the same of target's silhouette.

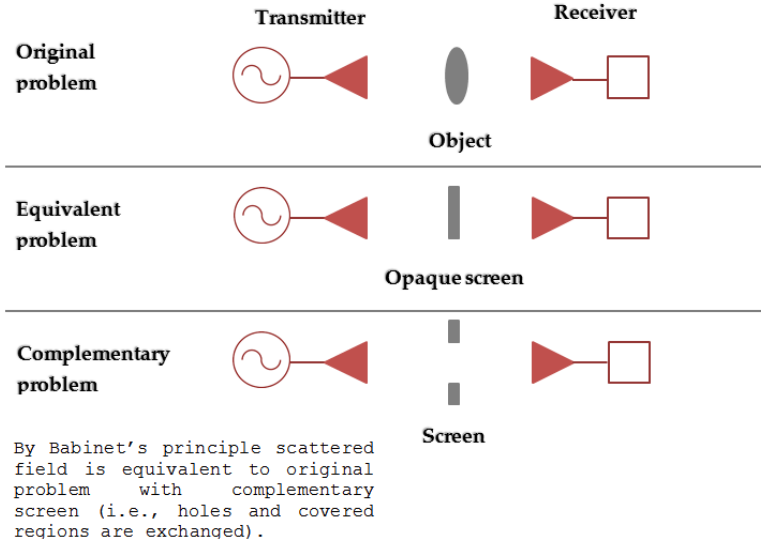


Figure 2.7 Illustration of Babinet's principle to solve scattering problem (reproduced from [5]).

The bistatic RCS of a target in the far field area (i.e. the target dimensions are much smaller than the distance target-receiver) can be written as, [5]:

$$\sigma_{BS} = \frac{4\pi}{\lambda^2} \left| \iint \exp(j\mathbf{k}\boldsymbol{\rho}) ds \right|^2 \quad (2.4)$$

where \mathbf{k} is the wavenumber vector and $\boldsymbol{\rho}$ is the coordinate vector in the screen plane and ds is the differential surface area. From the eq. (2.4) when the target lies on the baseline the peak of the RCS in the forward scatter lobe is obtained, [1] :

$$\sigma_{FS} = \frac{4\pi A^2}{\lambda^2} \quad (2.5)$$

where A is the target shadow area and the wavelength is assumed small compared to the target dimension. From this equation can be calculated that the FSCS can be many orders of magnitude greater than the backscatter cross section. For example, for a small car with a physical area, $A \sim 4 \text{ m}^2$ at a frequency of 900 MHz, a FSCS of $\sigma_{FS} \sim 2000 \text{ m}^2$ is expected while in monostatic case the same target is expected to have a RCS about 50 m^2 , [6].

In [39] the monostatic RCS and the FSCS of a conductive sphere of diameter D has been compared as shown in Figure 2.8. We note that starting from the Mie region the normalized monostatic RCS does not depend on the wavelength meanwhile the FSCS presents a monotonic rise.

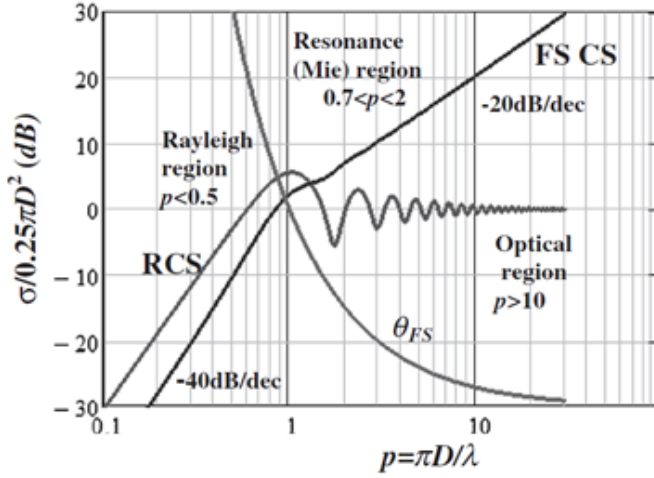


Figure 2.8 Radar cross section for spherical targets. Normalized values of monostatic radar cross-section and FSCS are shown as function of the normalized dimensionless parameter $p = \pi D / \lambda$ (from [39]).

In the same paper, [39] for a side illuminated missile with horizontal dimension 3.6 m and vertical dimension equal to 1.1 m that moves with a velocity of 200 m/s the 3D RCS were simulated for two different wavelength, $\lambda = 3$ m (FM signal) and $\lambda = 0.3$ m (satellite TV signal) (see Figure 2.9).

Therefore in accordance with the scattering regions previously defined, when the missile is illuminated by a FM signal ($\lambda = 3$ m) is in the upper-Rayleigh region (Figure 2.9 (a) and Figure 2.9 (c)) and when the missile is illuminated by a satellite TV signal ($\lambda = 0.3$ m) is in the optical scattering region (Figure 2.9 (b) and Figure 2.9 (d)). Figure 2.9 (c), shows that the back scattering (0°) and forward scattering (180°) are approximately with the same intensity. Meanwhile when the missile is in the optical region, Figure 2.9 (d), the maximum intensities of both back and forward scattering are greater with respect to the case of $\lambda = 3$ m and the forward scatter peak is 10 dB stronger than that of back scattering. Also it is noted that in the bistatic (or side) scattering the RCS is 30-35 dB smaller than the RCS in the forward direction.

Also in [39] for different shaped targets the bistatic radar cross section has been calculated in CST microwave studio for different carrier frequency. In accordance with the target dimension and the wavelength all the three scattering region (Rayleigh, Mie and Optical region) were investigated. The results once more has shown a significant large FSCS with respect to the bistaic RCS in the Mie and Optical region.

The enhanced radar cross section in terms of both magnitude and stability is an important benefit of FSR configuration.

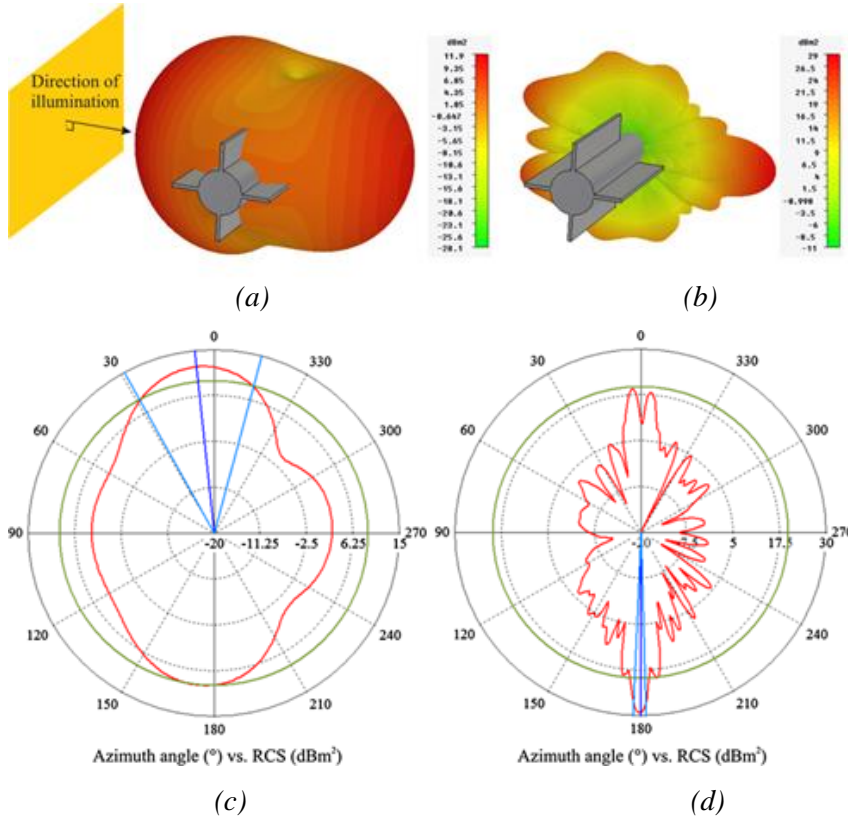


Figure 2.9 Simulated 3D bistatic RCS for missile (a) with $\lambda=3$ m and (b) with $\lambda=0.3$ m and their corresponding cross-sections in (c) and (d). In (c) and (d) the red line shows the RCS in the azimuth plane; 0° is the backscatter direction and 180° is the Forward scatter (from [39]).

2.5 Signature of moving target

In this particular configuration a target crossing the baseline provides a variation (i) in the received signal's phase due to the target movement producing a time-varying Doppler shift and

(ii) in the received signal's amplitude, specified by the FSR pattern approximately coinciding with the pattern of a uniform illuminated antenna with the shape of the target shadow as shown in [8].

Considering the same geometry of the Figure 2.4 the transmitted signal from the TX arrives at the receiver via two separated paths, the direct path from the transmitter to the receiver (direct signal, $s_d(t)$) and the scattered path due to the presence of the target (target signal, $s_t(t)$), [8]:

$$s_{tot}(t) = s_d(t) + s_t(t) \quad (2.6)$$

where

$$s_d(t) = \frac{a}{L} \cos(2\pi f_c t) \quad (2.7)$$

$$s_t(t) = \beta \sigma_{fs}(t) \sin\left(2\pi f_c(t + t_{tg})\right) \quad (2.8)$$

A continuous wave is transmitted with a carrier frequency f_c and amplitude a . A point-like target is considered in [8] where $\sigma_{fs}(t)$ is the pattern FSCS of the target, t_{tg} the delay time of the signal from moving target and β is proportional to the target dimension and takes into account the propagation losses. Let firstly analyze the target phase signature omitting for the moment the amplitude modulation due to the pattern FSCS, $\sigma_{fs}(t)$:

$$s_{tot}(t) = \frac{a}{L} \cos(2\pi f_c t) + \beta \sin\left(2\pi f_c(t + t_{tg})\right) \quad (2.9)$$

The target is assumed in the far field area of both transmitter and receiver, that means the far field parameter $S = 2d_{max}^2/\lambda R_T$ ($S = 2d_{max}^2/\lambda R_R$) is smaller than 1 where d_{max} is the maximum dimension of the target.

As mention previously in Section 2.3 the target shadow exists within a narrow corridor around the baseline, therefore the assumption of a linear target trajectory can be regarded as reasonable. Moreover being shadow the target scattered signal is $\pi/2$ shifted with respect to the direct signal (in literature the direct signal is also indicated as leakage signal, [8]).

The Doppler signature in a FSR configuration that occupies a very low frequency band may be extracted from an envelope detector with quadratic characteristic. After passing the signal in the square law detector and in the low pass filter the signal, $s_{tot}(t)$ becomes, [8]:

$$s_{RO}(t) = DC - a_{sc} \sin\left(\frac{2\pi}{\lambda}(R_T(t) + R_R(t) - L)\right) \quad (2.10)$$

where DC is the continuous component and $a_{sc} = a\beta$ is the amplitude of the phase signature and $R_T(t)$ ($R_R(t)$) are the distance target-TX (target -RX) and L is the baseline as shown in Figure 2.4. For a target crossing the baseline the phase signature is a two sided chirped signal.

Meanwhile the signature envelope of the target signal is specified by the pattern signature, $\sigma_{fs}(t)$ that is unknown a priori even if the target and its motion parameters are known as analytical solution of FSCS are available only for few convex shapes based on the PTD. In [8] the FSCS pattern of a rectangular target was derived and verified experimentally by considering a rectangular metallic plate and a similar plate covered by absorbing material as shown in Figure 2.10.

Considering both, the FSCS pattern signature and the phase signature the received target signal after passing through the DC removal filter is, [8] :

$$s_u(t) = \sigma_{fs}(t) \sin\left(\frac{2\pi}{\lambda}(R_T(t) + R_R(t) - L)\right) \quad (2.11)$$

Also in [8] measured signatures of maritime target for a baseline $L=300$ m and carrier frequency of 7.5 GHz (see Figure 2.11) has been reported. In particular, Figure 2.11 (a) shows the signature of a inflatable boat of size $2.9 \text{ m} \times 1 \text{ m}$ that is in the far field area, Figure 2.11 (b) shows the signature of a medium size sailing yacht of size $5 \text{ m} \times 3 \text{ m}$ that is in the border between the near and the far field and Figure 2.11 (c) shows the signature from a large motor boat $15 \text{ m} \times 4 \text{ m}$ that is in the near field. From Figure 2.11 we observe in all cases the noticeable amplitude modulation due to the target crossing.

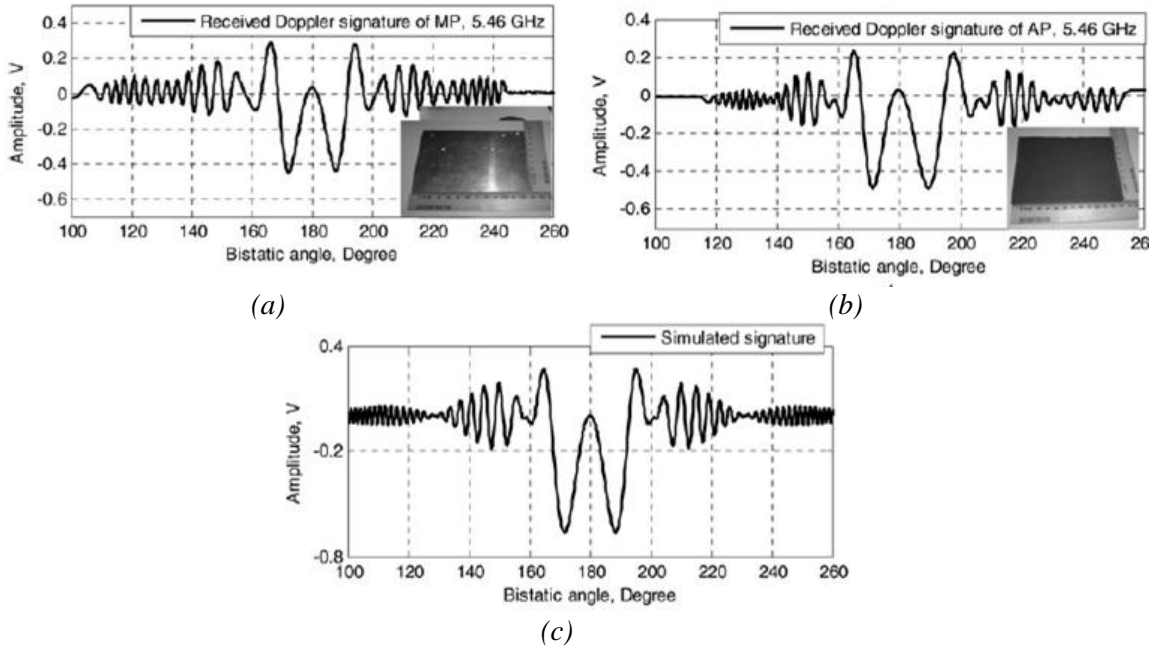


Figure 2.10 Comparison of measured forward scatter signatures of (a) a rectangular metallic plate, (b) absorbing rectangular plane and (c) simulated signature of absorbing plate (from [8]).

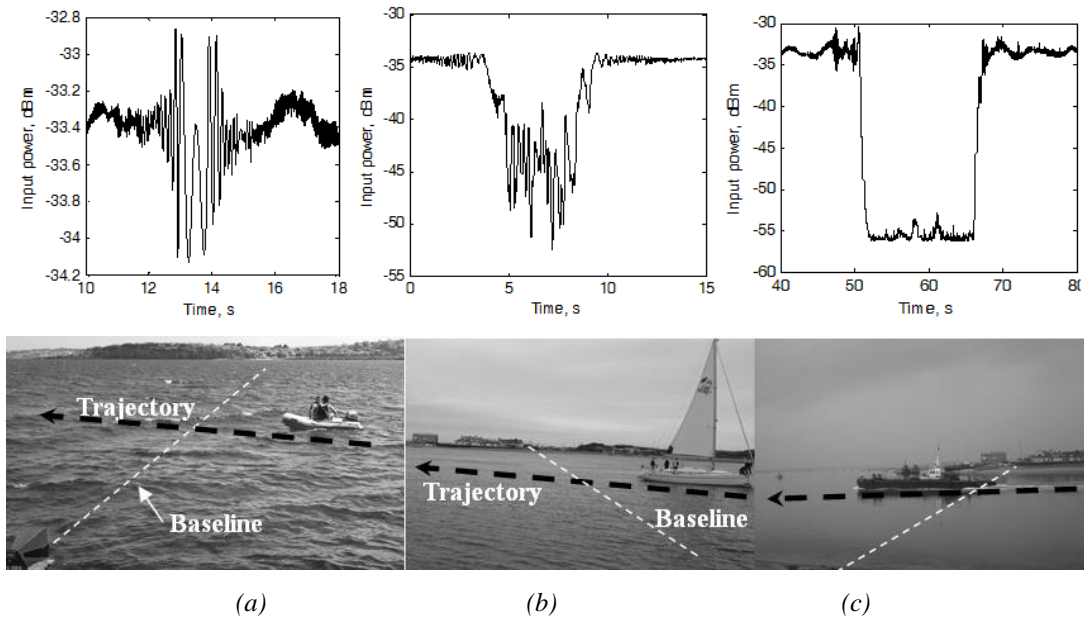


Figure 2.11 Recorded Doppler signature of the targets crossing the center of baseline: (a) small inflatable boat, (b) medium size yacht and (c) large motor boat, (from [8]).

Based on [14] and [8] the forward scatter signal used through this work that refers to a rectangular target in the far field area following a linear trajectory is detailed in the Section 3.2.

2.6 Target detection and motion parameters estimation

The processing approach in [10] and [8] has become the reference processing scheme for the FSR.

Assuming the target in background of Additive White Gaussian Noise (AWGN) the received signal in accordance with eq. (2.6) is $r(t) = s_{tot}(t) + n(t)$ being $n(t)$ the noise component. In agreement with the signal model introduced in Section 2.5 (i.e. the target is in the far field area of TX and RX and follows a linear trajectory) to test for target detection an envelope with quadrature characteristic is applied to the received signal this is followed by a DC removal filter and by a filter matched to the expected target Doppler frequency response. Here with $z(t)$ and $u(t)$ are indicated the signal at the output of the square law detector and at the output of the DC removal filter respectively.

The surviving signal, $u(t)$ after the DC removal filter may be approximated as the sum of two components: $s_u(t)$ defined in eq.(2.11) representative of the new useful signal containing the target signature and $s_n(t)$ the new noise component. The signal at the output of the matched filter is given by the correlation of the signal at the output of the DC removal, $u(t)$ and the impulse response, $h(t)$, [10]:

$$s_{out}(\tau) = \int_{-T/2}^{T/2} u(t)h(t - \tau) dt \quad (2.12)$$

The impulse response of the matched filter is equal to the possibly scaled, conjugate, time-reversed, target signature defined in eq. (2.11).

This scheme employs the nice self-beating proprieties of the so-called crystal video receiver, [40]-[41], to provide a coherent integration without requiring the I&Q demodulator. In addition, it was recently shown to be very robust since it is able to operate effectively even against the modulated waveforms of passive forward scatter applications, [21]. Motivated by its

low implementation cost and by its qualities we have fully characterized the performance of this Crystal Video Detector (CVD) in Chapter 3 ([42]-[43]).

It is clear that the impulse response, $h(t)$ depends on both FS pattern signature and the Doppler signature which in turn depend on the target electrical size and trajectory that are a priori unknown. In [10] an appropriate set of reference functions is defined to estimate the target velocity and target signal duration, $h_{T_n, v_m}(t)$ defined by considering different target speed, v_m for $m=1,2,3,\dots$ and time durations, T_n for $n=1,2,3,\dots$ under the assumptions that the unknown pattern signature is approximated with a rectangular signature and the distances target-TX and target-RX when the target is on the baseline are assumed known. The correlation of the signal at the output of the DC removal filter with each reference function is performed:

$$s_{T_n, v_m}(\tau) = \int_{-T_n/2}^{T_n/2} s_u(t) h_{T_n, v_m}(t - \tau) dt \quad (2.13)$$

and the maximum is obtained for a specific value of (T_n, v_m) that indicates the estimated target speed and time duration.

Figure 2.12 compares the velocity estimation of simulated and experimental data related to human target that moves with the velocity of 1.2 m/s crossing the baseline of $L=50\text{m}$ perpendicularly in middle and it is noted that the velocity is correctly estimated.

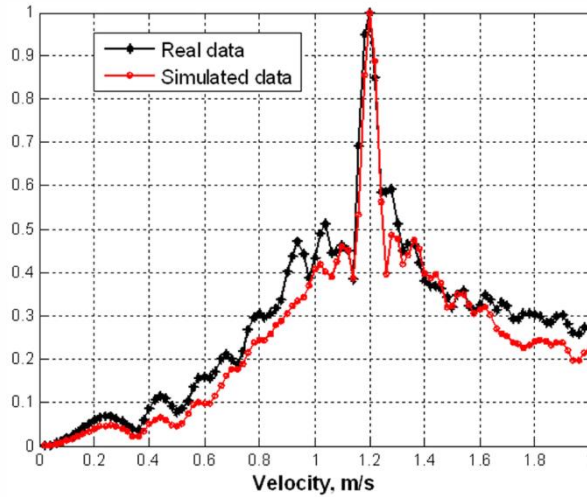


Figure 2.12 Normalized velocity estimation output: real data vs simulated data (from [10]).

In [8] a similar approach as in [10] for the velocity and baseline crossing point estimation is derived. As previously, in [8] was shown that a complete knowledge of the pattern signature representative of the signal envelope is not necessary for relatively short integration time as the correlation between the signal at the output of the DC removal filter and the impulse response (see eq. (2.12)) depends more on the target phase signature (the chirp like signal is a sign altering function) presenting fast variation than on the envelope signature that varies slowly. Therefore the FSCS pattern signature for short integration time is approximated with the envelope of a rectangular target.

Therefore a set of reference waveforms, $h_{v_x, v_y, y_0}(t)$ covering the desired range of velocities and baseline crossing points is considered. v_x and v_y represent the velocity component in the (x,y) coordinate system representative of the ground plane where the target is moving and the baseline crossing point, y_0 is the distance target-RX when the target is on the baseline. The total number of the reference functions is defined by the increments chosen in order to have an accuracy within 1-10% and by the expected ranges of the parameters under consideration. After the correlation of the signal at the output of the DC removal filter with each reference function is performed and the global maximum of all the correlations is searched. From the latter the trajectory and the velocity are estimated.

Figure 2.13 show measurement of maritime target signatures relative to small inflatable boat of length 2.9 m that crosses the baseline with different trajectories. In particular in Figure 2.13 (a) the target crosses the baseline perpendicularly in the middle, in Figure 2.13 (b) the target crosses the baseline near to the receiver and Figure 2.13 (c) the target crosses the baseline with an angle of 60° . The results of parameter extraction compared to the data truth provided by a GPS tracking device confirm the feasibility of the proposed approach in [8].

Recently in [54] by exploiting the same proposed approach in [8] the possibility to estimate the target motion parameters in a moving FSR systems was shown under the assumption that the transmitter and receiver position during the time are known. This system presents the advantage to increase the flexibility of the surveillance area and allow the detection of stationary targets.

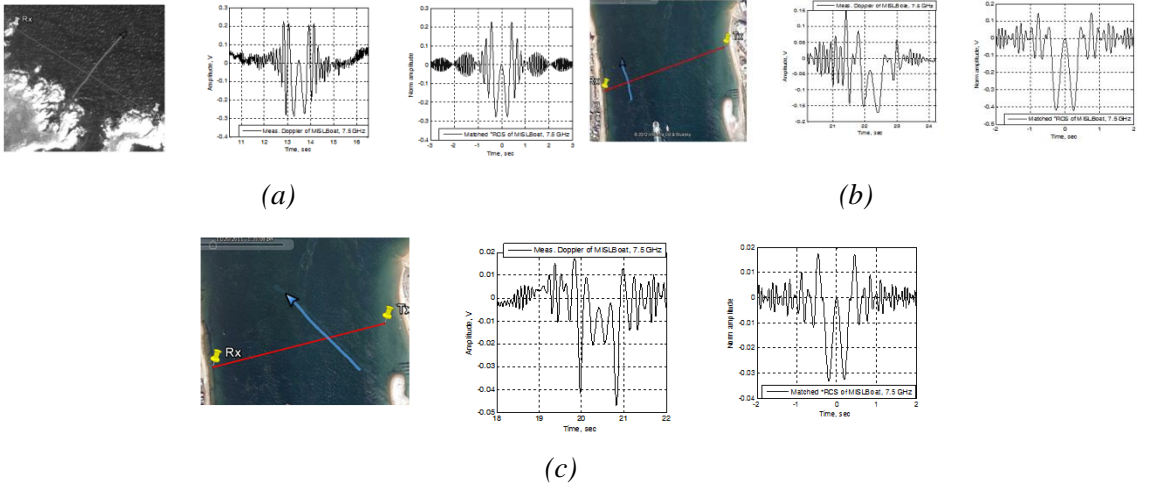


Figure 2.13 Comparison of the measured maritime target signature with matched waveforms from the correlation processing. Left images show the GPS location and trajectories, middle images show the measured target signatures and right images show the matching signature selected from the correlation processing (from [8]).

In [14] was shown the potentialities to use a multiple FSR nodes for a reliable and accurate estimation of all target motion parameters. A crossing time-based estimation technique was devised that exploits the information concerning the time instants at which the target crosses each baseline in order to retrieve the motion parameters of the target. The performance, validated also through recorded Multi-input Multi-output (MIMO) FSR data, proved that unbiased estimate of the initial positions and velocity component can be achieved with high accuracy.

The detection scheme proposed in [8] and the motion parameters estimation approach proposed in [10] and [8] are selected as references in this study.

2.7 Passive Forward Scatter Radar

As a particular configuration of bistatic radar, FSR can operate with dedicated transmitters of transmitters of opportunity dedicated to other purpose but find suitable for FSR operation.

In particular in [21] the feasibility of a passive FSR for airborne target detection has been demonstrated using FM, DAB, and DVB-T waveforms. It has been shown that simultaneous multifrequency/multiband operation increases robustness of detection. Also, the velocity of the

detected targets has been estimated using the approach proposed in [10] (see Section 2.6) and good correspondent to ground truth data has been demonstrated. Figure 2.14 (a) and Figure 2.14 (b) shows the time domain signature of Cessna 172 light aircraft with dimension 7.3 m length and 2.3 m height that crosses the baseline of 25 km at the altitude of 650 m where the DVB-T and the FM are exploited as waveforms of opportunity respectively. Figure 2.14 (c) and Figure 2.14 (d) shows their respective spectrograms. Increasing the flight altitude results in smaller signal powers, and, therefore, in a more noisy picture (see Figure 2.14 (c) and Figure 2.14 (d)) , but the typical V-shape Doppler chirp which indicates the presence of a target can still be seen in the spectrograms.

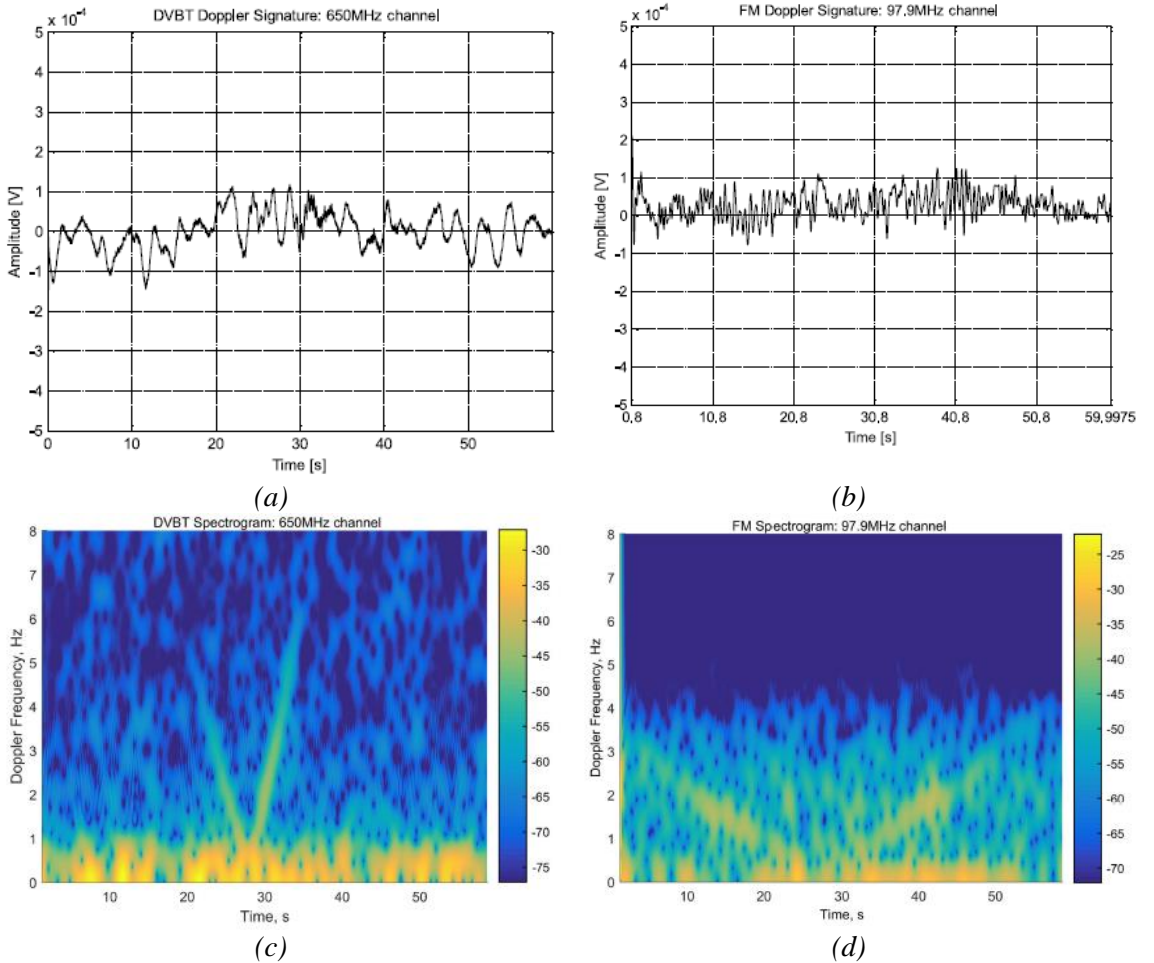


Figure 2.14 DVB-T and FM Doppler signatures and spectrograms of Cessna 172 ultralight aircraft at the height of 659 m (from [21]).

In [31] the feasibility of GPS-FSR system was demonstrated. The amplitude modulation due to the aircrafts crossing the receiver-satellites baselines was shown through experimental results as in Figure 2.15.

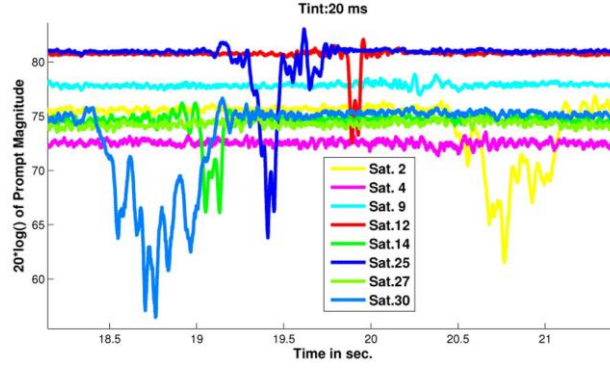


Figure 2.15 Measurements with 20 ms of integration time (from [31]).

In [32] results related to the detection of target located in the line of sight between the receiver and the non-cooperative transmitter where GSM signals were exploited as waveform of opportunity was shown.

In [33] some preliminary results related to WiFi-based Passive FSR system obtained through an experimental setup developed at Sapienza University of Rome are shown. The results shown that that different targets yield quite different vehicular signatures. Figure 2.16 (a) shows all the signatures of the Fiat Punto Evo obtained in the performed tests.

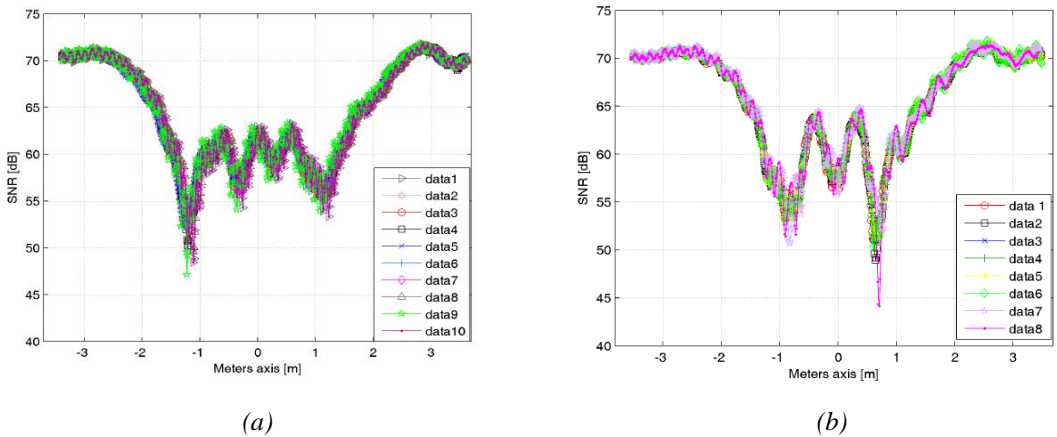


Figure 2.16 Signatures comparison for the same target model on different tests: (a) Fiat Punto Evo; (b) Peugeot 107 (from [33]).

A similar shape is clearly visible for all the cases. Figure 2.16 (b) shows the signature of the Peugeot 107 on 8 tests and again a very stable signature is noted. In addition is observed that different car models presents different signature shapes.

The extracted signatures are exploited in a classification stage where a minimum Euclidean distance criteria has been adopted to evaluate the similarity among different car models. The results had shown a good capability of the proposed system to correctly associate a vehicle signature to its car model.

The reported results allows the conclusion that Passive FSR systems are a practical solution not only for target detection but also for motion parameter estimation, target classification.

Summary

This chapter introduced the fundamentals characteristics of FSR systems that are of relevance to this research. Initial attention is given to the difference between the bistatic and monostatic radar before moving on to the FSR configuration. Then the phenomenology of forward scattering was briefly introduced. After this the various applications that exploits the Forward scatter principle were summarized. Considerations is given to the Forward scatter cross-section and to the target time domain signature. The literature survey outlined the current publications of interest to the presented work. In particular the publications relating the target detection and motion parameters estimations were discussed.

Acknowledgments

I want to thank Prof. Mikhail Cherniakov of the University of Birmingham, for providing the high resolution figures used in Section 2.5 and 2.6.

Chapter 3

Crystal Video Detector and performance analysis

This chapter focus is on providing an accurate analytical expression for the detection performance of the FSR target detection using the Crystal Video Detector, both in terms of probability of false alarm and of probability of detection in order to support performance prediction and FSR system design. The derived expressions are validated by comparison to Monte Carlo simulations under two different geometrical scenarios. Finally, to remove the need to operate the CVD with a fixed detection threshold, two fully adaptive detectors are derived, based on the structure of the CVD scheme, which are shown to provide a constant false alarm rate (CFAR). The performance of these CFAR detectors in terms of P_{fa} and P_d are provided in closed-form and validated through Monte Carlo simulations, showing quite small losses with respect to the fixed threshold CVD.

3.1 Introduction

The possibility to operate without the need of a phase synchronization system is extremely attractive when aiming at reducing the sensor cost and providing its easy deployment. This is even more appreciable when passive FSR is considered, which usually does not even include the access to the TX device.

In most of the mentioned papers,[10],[8], the target time domain signature is extracted from an envelope detector with quadrature characteristic followed by a low pass filter. This type of receiver is well known from the early days of radar as the simplest form of signal demodulation and is typically addressed as Crystal Video Receiver, [40], [41]. Despite the absence of an external phase reference, it is well known that this type of receiver under specific circumstances is able to maintain the temporal coherence from sample to sample, so that a Doppler processing is still feasible in the receiver chain after its use. This is certainly the case in the presence of a received signal including a strong and stable signal component that is

essentially a copy of the transmitted waveform, together with its attenuated and Doppler frequency-shifted reflection from the target. The stable signal component provides the coherent reference for the target-reflected signal, [40], [41]. This principle was largely used in the past for two types of radar systems: (i) to provide Moving Target Indication (MTI) capability to noncoherent radar, and (ii) to allow simple operation of Continuous Wave (CW) radar. In the first case, the strong echo from a stationary clutter yields a significant stable signal copy that is used as a reference for the target scattered signal, [22], [44]. In the second case, the feed-through of the continuous transmitted waveform that couples into the receiver provides the strong and stable copy of the transmitted waveform, so that CW Doppler operation is obtained without the need of I&Q receiver, [45].

In the FSR case, the stable copy of the transmitted waveform present in the received signal is provided by the direct signal, that acts as the stable reference for the echo scattered by the target. Its presence provides the FSR system with the required coherence to cancel the direct signal and apply the required Doppler processing before comparing the result to an appropriate threshold selected to detect the target. Consistently with the previous notation, we address this detection scheme as Crystal Video Detector (CVD). As mentioned previously, when exploiting the long integration times allowed by the nonfluctuating echoes of the FSR configuration to detect low-observable targets, the target echo does not maintain a constant Doppler frequency. Therefore, the processing scheme required by the CVD after the square-law envelope detector is different from the standard Doppler processing required by noncoherent MTI and standard CW schemes. It requires direct signal removal and appropriate matched filtering to collect all the available signal energy, [10]. Therefore, its detection performance cannot be directly obtained from previous contributions.

In this chapter the issue of moving target detection against Additive White Gaussian Noise (AWGN) under the assumption that the target follows a linear trajectory is addressed through: (i) an analytical characterization of the CVD, when using a fixed threshold and (ii) by developing new adaptive detection schemes to achieve a constant false alarm rate (CFAR) by removing the requirement to use a fixed detection threshold, also analytically characterized.

3.2 Forward scatter signal model

In this extreme configuration of the bistatic radar the main characteristic feature with respect to the conventional bistatic configuration lies in the target scattered signal. In this section the FSR system geometry and the signal model used throughout this work are introduced following the forward scatter signal in [14] and [8].

Figure 3.1 shows the considered FSR configuration where the x and y axes specify the ground plane : the receiver (RX) is placed at the origin of the coordinate system meanwhile the transmitter (TX) is placed along the y -axis at distance L (baseline) from the RX.

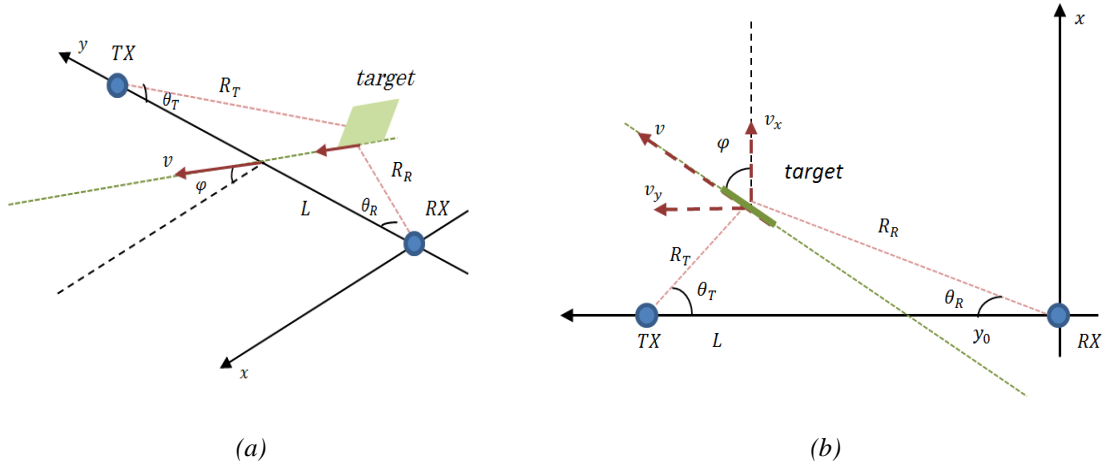


Figure 3.1 (a) FSR system geometry and (b) top view of the FSR configuration.

We assume the transmitter emitting a continuous wave at a carrier frequency f_c ($\lambda = c/f_c$) with amplitude a . Let $s_d(t) = \frac{a}{L} e^{j\frac{2\pi}{\lambda}L} = \alpha$ be the received direct signal from TX to RX taking into account only the free space propagation losses where λ is the wavelength and with $M_d = |\alpha| = a/L$ is defined the amplitude of the received direct signal. In the presence of a target crossing the baseline, the signal scattered from the target, $s_t(t)$ adds to the direct signal, $s_d(t)$ to provide a total signal $s_{tot}(t)$.

We consider a rectangular shaped target with horizontal and vertical dimensions l_h and l_v respectively, large with respect to the probing wavelength that moves in the area between TX and RX with constant velocity component v_x and v_y , respectively along the x and y axes and

crosses the baseline at a distance y_0 from RX indicated as baseline crossing point at time $t_0 = 0$. This yields a global speed $\left(v = \sqrt{v_x^2 + v_y^2} \right)$, with an angle $\varphi = \tan^{-1} \left(v_y / v_x \right)$ with respect to the normal to the baseline. The assumption of a linear trajectory can be regarded as reasonable for many practical scenarios as FSR systems typically operate within narrow angles around the baseline. Due to the target motion, the distance target-TX (target-RX) $R_T(t) = \sqrt{x(t)^2 + [L - y(t)]^2}$ ($R_R(t) = \sqrt{x(t)^2 + y(t)^2}$) and the target aspect angle with respect to the TX (RX) $\theta_T(t) = \tan^{-1} [x(t) / (L - y(t))]$ ($\theta_R(t) = \tan^{-1} [x(t) / y(t)]$) vary with time being $[x(t), y(t)]$ the instantaneous target position (see Figure 3.1 (b)). The target is assumed in the far field of both TX and RX: this requires the far field parameter, $S = 2d_{max}^2 / \lambda R$ to be smaller than 1, being $R = \min\{y_0, L - y_0\}$ and $d_{max} = \max\{l_h, l_v\}$, [46].

To be noted that the angular interval from which the target is viewed is $\Delta\Omega = 2\tan^{-1}(v_x T / L)$ being T the observation time.

As previously discussed in Chapter 2 the signal scattered from the target in the forward direction, $s_t(t)$ is due to the shadow of the emitted electromagnetic energy which occurs in the opposite side of the TX and introduces a variation in the received signal's phase, $\phi(t)$ and in the received signal's amplitude, $\sigma_{fs}(t)$. The RCS pattern, $\sigma_{fs}(t)$, modulates the amplitude of the signal scattered by target: it depends on the shape of the shadow contour, [2], and on the motion parameters, [29],[9], [8] and can be explained by considering the target as a secondary antenna having an area outlined by the target shadow profile. For the above rectangular shadow aperture the pattern can be written as, [15]:

$$\sigma_{fs}(t) = \frac{L^2}{R_T(t)R_R(t)} \frac{\cos(\theta_T(t) - \varphi) + \cos(\theta_R(t) + \varphi)}{2} \operatorname{sinc} \left\{ \frac{l_h}{\lambda} [\sin(\theta_T(t) - \varphi) + \sin(\theta_R(t) + \varphi)] \right\} \quad (3.1)$$

The Doppler shift is induced by the target motion. The phase variation of the target signal with respect to the direct signal is here defined only by the path difference, [8][29],[14] and it is written as follows:

$$\phi(t) = \frac{2\pi}{\lambda} [R_T(t) + R_R(t) - L] \quad (3.2)$$

Finally, the received target signal can be represented as:

$$s_t(t) = \beta s_{t0}(t) \quad (3.3)$$

where $s_{t0}(t) = \sigma_{fs}(t)e^{j\phi(t)}$ is the global target signature (pattern and Doppler signature) and $\beta = j \frac{l_v l_h a}{\lambda L} e^{j \frac{2\pi}{\lambda} L}$ is a complex factor proportional to the target dimensions and to the transmitted signal (i.e. proportional to α). We define with $M_t = |\beta| \max_t |\sigma_{fs}(t)|$ the maximum peak of the received target signal. We note that the target scattered signal in the forward direction is $\pi/2$ phase shifted with respect to the direct signal, $s_d(t)$ ($\angle\beta = \angle\alpha + \pi/2$) since as previously mentioned, the object's size is large with respect to λ , [3]. Disregarding for the moment possible disturbances, the received signal can be written as

$$s_{tot}(t) = s_d(t) + s_t(t) \quad (3.4)$$

An example of a typical received signal for a target crossing the baseline perpendicularly in the middle is shown below.

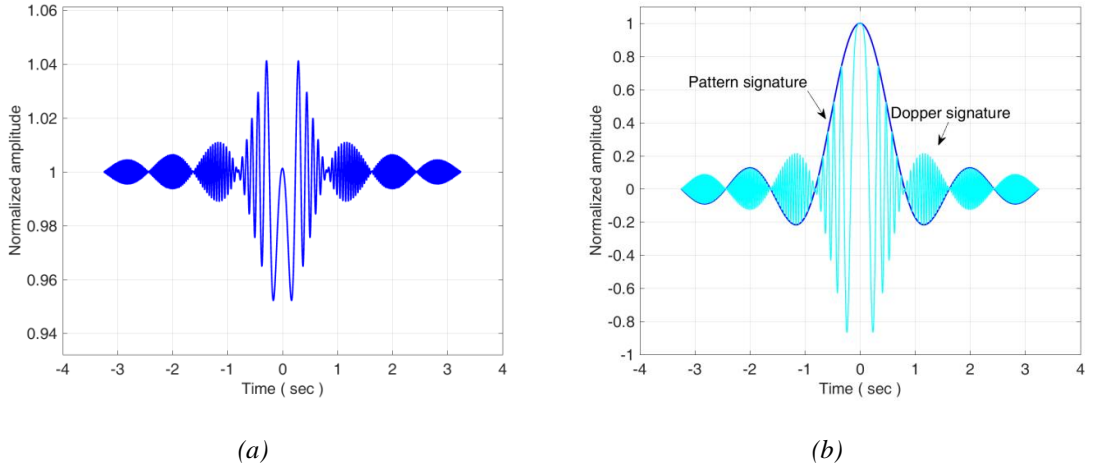


Figure 3.2 (a) Received signal and (b) Pattern signature and Doppler signature of a target crossing the baseline perpendicularly at midpoint

Figure 3.2 shows the amplitude of the received signal $s_{tot}(t)$ normalized to the amplitude of the direct signal (sub-figure (a)) and the target RCS pattern $\sigma_{fs}(t)$ and Doppler signature

$\Re\{s_{t_0}(t)\}$ both normalized to the RCS patterns peak value (sub-figure(b)). It is noted the chirped phase term characterized by a zero Doppler frequency at the crossing time, t_0 and a linearly increasing Doppler frequency when departing from this time instant. It is also evident the similar amplitude modulation provided by the RCS pattern ($\sigma_{fs}(t)$ term).

Finally, white Gaussian thermal noise is added to the combination of the direct and forward scattered signal thus providing the received signal $r(t) = s_{tot}(t) + n(t) = s_d(t) + s_t(t) + n(t)$ being $n(t)$ the noise component with power $\sigma_n^2 = KT_0BF$ where K is the Boltzmann's constant, T_0 the standard temperature, B the receiver bandwidth and F the noise figure. This gives rise to a Direct signal to Noise Spectral Density Power Ratio (DNSR) defined as:

$$DNSR = \frac{|\alpha|^2}{N_0} = \frac{|a|^2}{L^2 N_0} \quad (3.5)$$

being $N_0 = kT_0F$, while the Direct signal to Noise power Ratio (DNR) is:

$$DNR = \frac{|\alpha|^2}{N_0 B} = \frac{|a|^2}{L^2 \sigma_n^2} \quad (3.6)$$

3.3 Crystal Video Detector

We deal with the issue of the detection of moving targets in the considered FSR configuration introduced in Section 3.2 against AWGN. In agreement with the model previously introduced for the received signal, the detection problem can be described in terms of a binary hypothesis test as follows:

$$H_0: \mathbf{r} = \alpha \mathbf{s}_{d0} + \mathbf{n} \quad (3.7)$$

$$H_1: \mathbf{r} = \alpha \mathbf{s}_{d0} + \beta \mathbf{s}_{t0} + \mathbf{n}$$

where \mathbf{r} , \mathbf{s}_{t0} and \mathbf{n} are $N \times 1$ column vectors collecting the samples respectively of the baseband-equivalent received signal r_i , of the global target signature s_{t0_i} and of the noise contribution n_i at sampling times $t_i = i/B$ for $i = 0, \dots, N-1$. Since the transmitted signal is a pure tone, the baseband-equivalent $\mathbf{s}_{d0} = \boldsymbol{\zeta}_0$ is a $N \times 1$ column vector with all elements set to unity (i.e. constant direct signal). Under this condition the PDF of the received signal is a circular complex Gaussian distribution:

$$\begin{cases} p_r(\mathbf{r}/H_0) = \frac{1}{\pi^N \sigma_n^{2N}} e^{-\frac{1}{\sigma_n^2} \|\mathbf{r} - \alpha \mathbf{s}_{d0}\|^2} \\ p_r(\mathbf{r}/H_1) = \frac{1}{\pi^N \sigma_n^{2N}} e^{-\frac{1}{\sigma_n^2} \|\mathbf{r} - \alpha \mathbf{s}_{d0} - \beta \mathbf{s}_{t0}\|^2} \end{cases} \quad (3.8)$$

with mean vector respectively equal to $\mu_r = \alpha \mathbf{s}_{d0}$ under hypothesis H_0 and $\mu_r = \alpha \mathbf{s}_{d0} + \beta \mathbf{s}_{t0}$ under hypothesis H_1 and the same variance under both hypothesis $\sigma_r^2 = \sigma_n^2$. In eq. (3.8) $\|\cdot\|^2$ denotes the Euclidean norm.

For such detection problem the Crystal Video Detector has been proposed in previous literature, [9], [15], as a sub-optimal detection strategy under the assumption that the global target signature, $s_{t0}(t)$ is known: the CVD is composed by the cascade of a square-law detector followed by a DC removal filter and finally by a filter matched to the target signature. The output from this processing chain is compared to a decision threshold to assess the presence of the target (see Figure 3.3).

The main steps related to the CVD are summarized in the following.

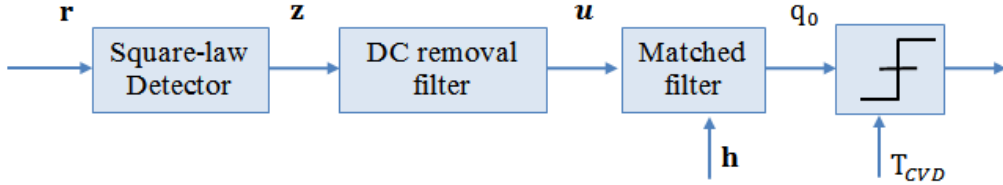


Figure 3.3 *Crystal Video Detector block diagram*

Based on Section 3.2, the i -th element of the received signal vector \mathbf{z} , at the output of the square law detector under hypothesis H_0 and H_1 can be written as:

$$z_i|_{H_0} = |\alpha|^2 + |n_i|^2 + 2\Re\{n_i \alpha^*\} \quad (3.9)$$

$$\begin{aligned} z_i|_{H_1} = & |\alpha|^2 + |\beta|^2 |s_{t0i}|^2 + |n_i|^2 + 2\Re\{\alpha^* \beta s_{t0i}\} + 2\Re\{n_i \alpha^*\} \\ & + 2\Re\{n_i (\beta s_{t0i})^*\} \end{aligned} \quad (3.10)$$

where $\Re\{\cdot\}$ is the real part operator and $(\cdot)^*$ denotes the complex conjugate. Even under the null-hypothesis (see eq. (3.9)) the expected value of \mathbf{z} gives a non-zero direct component (DC), $\zeta = (|\alpha|^2 + \sigma_n^2) \zeta_0$, due to the direct signal equal to its square value and to the noise component which contribution is equal to the noise power. To remove this DC component, a

narrow highpass filter is applied. By operating on the sampled vector \mathbf{z} , this is encoded by the projection of \mathbf{z} into the subspace orthogonal to the DC component vector $\boldsymbol{\zeta}_0$. We observe that the DC removal filter, perfectly removes the direct signal component, so that the only non-DC noise terms are left under hypothesis H_0 . In contrast, under the alternate hypothesis H_1 , various additional terms remain, that depend on the target-scattered signal: (i) the mixed product between target-scattered signal and direct signal, (ii) the mixed term between target-scattered signal and noise, and (iii) the squared envelope of the target-scattered signal (see eq.(3.11)). In practical application, both noise and target-scattered signal are much smaller than the direct signal component, so that is reasonable to assume that the squared envelope of these two terms are not the dominant contributions. Moreover, they are also partially removed by the highpass filter. Therefore, in addition to the residual non-DC noise term of the H_0 case, only components (i) and (ii) represent the important contributions. After DC removal, we have the signal vector $\mathbf{u} = \mathbf{P}^\perp \mathbf{z}$, where $\mathbf{P}^\perp = \mathbf{I} - \frac{\boldsymbol{\zeta}_0 \boldsymbol{\zeta}_0^H}{\|\boldsymbol{\zeta}_0\|^2}$ is the $N \times N$ symmetric and idempotent projection matrix, [47]. By neglecting all smaller terms, the expected value of \mathbf{u} can be approximated by the projection of component (i) as:

$$E\{\mathbf{u}\} = E\{\mathbf{P}^\perp \mathbf{z}\} \approx 2\Re\{\alpha^* \beta \mathbf{P}^\perp \mathbf{s}_{t0}\} \quad (3.11)$$

which can be interpreted as the new useful signal term, $\mathbf{s}_u = E\{\mathbf{u}\}$ of the signal vector \mathbf{u} being $E\{\cdot\}$ the expectation operator, As mentioned previously, we notice that this mixed term between target-scattered signal and direct signal maintains a coherence from sample to sample, due to the presence of the stable direct signal component that keeps the phase reference.

The random component of \mathbf{z} under H_0 , is given by a vector with elements $2\Re\{n_i \alpha^*\}$ and under the H_1 hypothesis, is given by a vector with elements $2\Re\{n_i(\alpha + \beta s_{t0i})^*\}$ for $i = 0, \dots, N-1$. Its projection through \mathbf{P}^\perp can be seen as the noise component of vector \mathbf{u} indicated as \mathbf{s}_n . This last component is still zero mean white Gaussian noise, but with a different variance under the two hypotheses. Under hypothesis H_0 only the direct signal is present, thereby the variance of the random component of \mathbf{z} is equal to $2\sigma_n^2 |\alpha|^2$ in each of the $N-1$ remaining dimensions. Under the alternative hypothesis H_1 , also the target contribution must be considered so that the variance of the random component of \mathbf{z} is equal to $2\sigma_n^2 |\alpha + \beta s_{t0i}|^2$, and the variance of \mathbf{u} is directly obtained through the projection through \mathbf{P}^\perp . Based on the approximation above that only retains terms (i) and (ii), after applying to the received signal the

squared modulus operation and the DC removal filter, the target detection problem can be reformulated as a standard binary decision problem. The detector must decide between Hypothesis H_0 (the considered sample vector only contains zero mean Gaussian noise samples) and the alternate Hypothesis H_1 (the considered sample vector contains zero mean Gaussian noise samples, plus a target vector with known shape).

Under this approximation, we can resort to the matched filter theory to detect the target-scattered signal present inside y . To this purpose, we define the filter vector $\mathbf{h}_{MF} = \kappa E\{\mathbf{u}\}$, being κ any desired scalar value. Under the assumption that the global target signature, s_{t0} is known and as the useful signal after squared modulus and Dc removal is given by term (i), we can set $\mathbf{h}_{MF} = \frac{2\Re\{\alpha^* \beta s_{t0}\}}{|\alpha \beta|} = -2\Im\{s_{t0}\} \equiv \mathbf{h}$, so that the global filter vector applied to z is given by $\mathbf{P}^\perp \mathbf{h}$. Under hypothesis H_1 , the maximum output of the matched filter is known to be given by $q_0 = \mathbf{h}^T \mathbf{u}$

Finally, the output of the matched filter is compared to a specific decision threshold T_{CVD} chosen in order to ensure the desired false alarm rate at the decision device:

$$q_0 = \mathbf{h}^T \mathbf{u} = \mathbf{h}^T \mathbf{P}^\perp \mathbf{P}^\perp \mathbf{z} = \mathbf{h}^T \mathbf{P}^\perp \mathbf{z} \underset{H_0}{\overset{H_1}{\geq}} T_{CVD} \quad (3.12)$$

where $(\cdot)^T$ denotes the transpose. Therefore, the CVD statistic consists in applying to the output of the square-law detector, \mathbf{z} , first the projector operator \mathbf{P}^\perp which is followed by a coherent integration operated by the filter \mathbf{h} , with impulse response defined by:

$$h(t) = -\sigma_{fs}(t) \sin \phi(t) \quad (3.13)$$

This implies that $h(t)$ depends on both the FS pattern signature and the Doppler signature which in turn depend on the target electrical size and target trajectory. We explicitly notice that, the filter \mathbf{h} compensates for the time-varying Doppler frequency (chirped) component, by performing a proper coherent target signal integration. In the typical case, where a target with unknown size and velocity is searched for, an appropriate bank of filters \mathbf{h} is used, after the DC removal filter,[10] (see Chapter 5).

3.4 Performance analysis of CVD

This section focuses on the analytical characterization of the performance of the CVD detector. Firstly an accurate closed-form expression of the probability of false alarm is derived and its correctness is shown and then the theoretical expression of the probability of detection is derived and also approximated closed-forms are provided useful to support performance prediction and system design. It is worth mentioning that two scenarios are taken as references in the following analysis : the first one corresponds to a target in the deep far field area ($S=0.085$) and the second one to a target approaching the transition to the near field ($S=0.76$), but still satisfying the far field condition ($S<1$). In both cases the target trajectory is orthogonal to the baseline intersecting it in the middle ($y_0 = L/2$).

Figure 3.4 and Figure 3.5 show the amplitude of the received signal $s_{tot}(t)$ normalized to the amplitude of the direct signal (sub-figures (a)) and the target RCS pattern $\sigma_{fs}(t)$ and Doppler signature $\Re\{s_{t0}(t)\}$ both normalized to the RCS patterns peak value (sub-figures (b)); all plots refer to noise free conditions while Table 3.1 shows the main system and target related parameters.

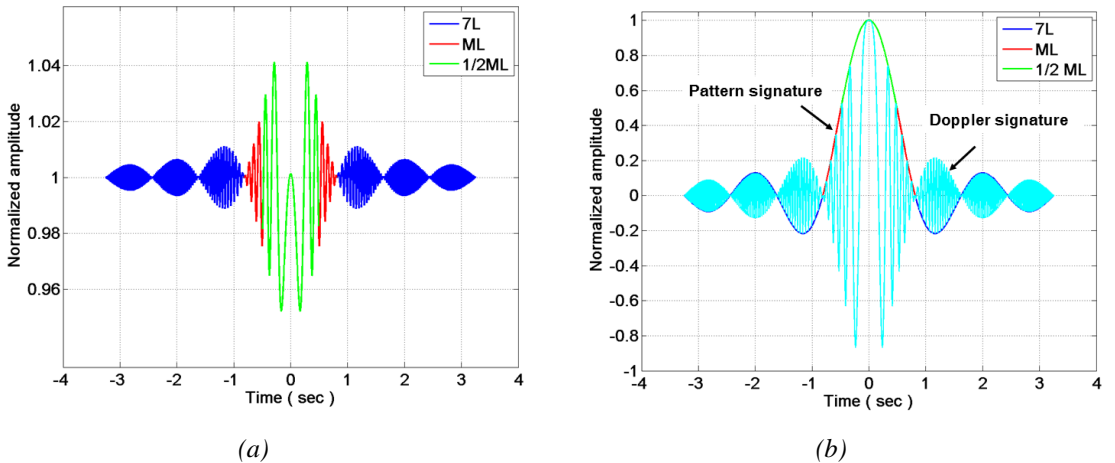


Figure 3.4 (a) Received signal and (b) Pattern signature and Doppler signature of a target crossing the baseline perpendicularly at midpoint for different observation times when $S=0.085$.

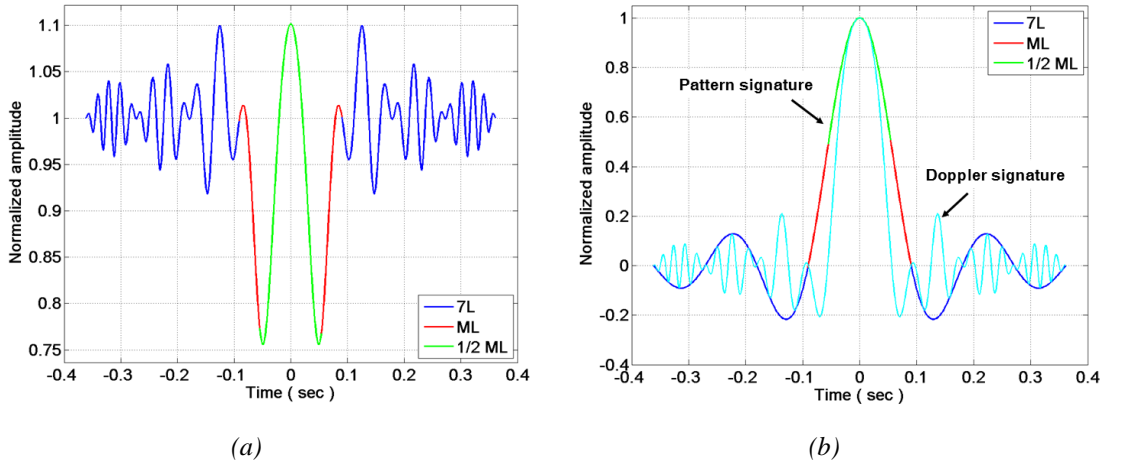


Figure 3.5 (a) Received signal and (b) Pattern signature and Doppler signature of a target crossing the baseline perpendicularly at midpoint for different observation times when $S=0.76$.

Table 3.1 System parameters and target related parameters of the reference scenarios

	$S=0.085$	$S=0.76$
<i>System parameters</i>		
Carrier frequency	$f_c = 4.612\text{GHz}$ ($\lambda = 6.5\text{ cm}$)	$f_c = 4.612\text{GHz}$ ($\lambda = 6.5\text{ cm}$)
Baseline	$L=4500\text{ m}$	$L=500\text{ m}$
Observation time	$T=6.5\text{ sec (7L)}$ $T=1.63\text{ sec (ML)}$ $T=0.98\text{ sec (1/2ML)}$	$T=0.72\text{ sec (7L)}$ $T=0.18\text{ sec (ML)}$ $T=0.1\text{ sec (1/2ML)}$
<i>Target related parameters</i>		
Target size	$l_h = 2.5\text{ m (}l_h/\lambda \approx 38\text{)}$ $l_v = 1.5\text{ m (}l_v/\lambda \approx 23\text{)}$	$l_h = 2.5\text{ m (}l_h/\lambda \approx 38\text{)}$ $l_v = 1.5\text{ m (}l_v/\lambda \approx 23\text{)}$
Motion parameters	$v = 36\text{ m/s}$ $\varphi = 0^\circ$ $y_0 = L/2$	$v = 36\text{ m/s}$ $\varphi = 0^\circ$ $y_0 = L/2$

Three different observation time intervals are investigated, corresponding to the same observation angle, $\Delta\Omega$ for both scenarios and representative of a long observation time (time to span the main lobe and 6 side lobes of the pattern signature, 7L, $\Delta\Omega = 5.96^\circ$), a medium observation time (only main lobe, ML, $\Delta\Omega = 1.49^\circ$) and a small observation time (i.e. the time to move between the -3dB level points of the maximum Forward Scatter pattern, 1/2ML, $\Delta\Omega = 0.89^\circ$). Both cases show the chirped phase term characterized by a zero Doppler frequency at the crossing time and a linearly increasing Doppler frequency when departing from this time instant. Comparing the two cases it is possible to observe that a large number of phase cycles

related to the Doppler component occur in the main-lobe of the RCS pattern when $S=0.085$, while in contrast the Doppler signature is only appreciable in the side lobes region when $S=0.76$ namely when approaching a near field condition.

To characterize the detection performance of the CVD, we rewrite the test statistic q_0 as follows:

$$q_0 = \mathbf{h}^T \mathbf{P}^\perp \mathbf{z} = \boldsymbol{\eta}^T \mathbf{z} = \sum_{n=1}^N \eta_n z_n \quad (3.14)$$

where:

$$\eta_n = h_n - \frac{1}{N} \sum_{k=1}^N h_k \quad (3.15)$$

is the n -th sample of the impulse response projected onto the subspace orthogonal to the DC component (coincident with the n -th sample of the matched filter vector previously defined).

This formulation allows us to easily verify that q_0 is an indefinite quadratic form in normal random variables that is not necessarily symmetric. In accordance with [48], we notice that q_0 can be written as the difference between two positive variables q_1 and q_2 , namely $q_0 = q_1 - q_2$, where q_1 is related to the N_1 positive values of η_i (η_i^+) while q_2 is related to the N_2 negative values of η_i (η_i^-):

$$q_1 = \sum_{i=1}^{N_1} \eta_i^+ z_i \quad , \quad q_2 = \sum_{i=1}^{N_2} \eta_i^- z_i \quad (3.16)$$

Indeed, it can be easily verified that both q_1 and q_2 are positive definite quadratic forms of Gaussian random variables. For the sake of compactness, a general formulation for the three quadratic forms q_m , $m=0, 1, 2$ is introduced, as:

$$q_m = \sum_{n=1}^N \theta_n(q_m) z_n \quad (3.17)$$

where

$$\theta_n(q_0) = \eta_n$$

$$\theta_n(q_1) = (|\eta_n| + \eta_n)/2 \quad (3.18)$$

$$\theta_n(q_2) = (|\eta_n| - \eta_n)/2$$

To obtain an approximate statistical characterization of these quadratic forms, we start from the evaluation of their s -th moment, which is derived in Appendix A:

$$\begin{aligned} \mu_{q_m}(s) = \sum_{i=0}^{s-1} \frac{(s-1)!}{i!} \sigma_n^{2(s-i-1)} \mu_{q_m}(i) \cdot \\ \left\{ (\sigma_n^2 + (s-i)|\alpha|^2) \sum_{k=1}^N \theta_k^{(s-i)}(q_m) \right. \\ \left. + (s-i)|\beta|^2 \sum_{k=1}^N \theta_k^{(s-i)}(q_m) |s_{t0k}|^2 \right. \\ \left. + 2(s-i)|\alpha||\beta| \sum_{k=1}^N \theta_k^{(s-i)}(q_m) h_k \right\} \end{aligned} \quad (3.19)$$

To provide the performance in terms of P_{fa} and P_d we analyze separately the case of the null-hypothesis, H_0 and the case of the hypothesis H_1 .

3.4.1 Probability of false alarm

An accurate characterization of the PDF under hypothesis H_0 , particularly on the PDF tails by means of a moment-based approximation is firstly provided and the behavior of the high order moments is here investigated. After the correctness of the closed-form expression of the P_{fa} is established through Monte Carlo simulations.

Under hypothesis H_0 , q_0 is by definition a zero mean value random variable, while the generic moment of q_m is given by the simplified recursive expression:

$$\mu_{q_m}(s) = \sum_{i=0}^{s-1} \frac{(s-1)!}{i!} \sigma_n^{2(s-i-1)} \mu_{q_m}(i) (\sigma_n^2 + (s-i)|\alpha|^2) \sum_{k=1}^N \theta_k^{(s-i)}(q_m) \quad (3.20)$$

Table 3.2 reports the first ten normalized moments $\mu_{q_m}^N(s) = \mu_{q_m}(s)/\mu_{q_m}^s(1)$ for $s=1, \dots, 10$ of both q_1 and q_2 for the reference scenario characterized by $S=0.085$ and the three different integration times (see Table 3.1) and DNSR=10 dB (see eq. (3.5)). For comparison the table

also reports the same normalized moments of a Gamma distributed random variable with PDF written as, [49]:

$$p_{q_m}(q_m) = \frac{1}{\Gamma(v_{q_m})} \frac{q_m^{v_{q_m}-1}}{\mu_{q_m}'^{v_{q_m}}} e^{-\frac{q_m}{\mu_{q_m}'}} , \quad q_m > 0 \quad (3.21)$$

with shape parameter v_{q_m} and scale factor μ_{q_m}' respectively, being $\Gamma(\cdot)$ the Gamma function, [50].

$$v_{q_m} = \frac{\mu_{q_m}^2(1)}{\mu_{q_m}(2) - \mu_{q_m}^2(1)} , \quad \mu_{q_m}' = \mu_{q_m}(1)/v_{q_m} \quad (3.22)$$

Table 3.2 Moments of q_1 and q_2 for $S=0.085$ and $DNSR=10$ dB

s	q_1						q_2					
	7ML			ML			7ML			ML		
	Gamma $v_{q_1}=137.67$	q_1	Gamma $v_{q_1}=52.65$	q_1	Gamma $v_{q_1}=32.28$	q_1	Gamma $v_{q_2}=86.70$	q_2	Gamma $v_{q_2}=49.60$	q_2	Gamma $v_{q_2}=38.16$	q_2
1	1	1	1	1	1	1	1	1	1	1	1	1
2	1.00	1.00	1.02	1.02	1.03	1.03	1.01	1.01	1.02	1.02	1.03	1.03
3	1.02	1.02	1.06	1.06	1.10	1.10	1.03	1.04	1.06	1.06	1.08	1.08
4	1.04	1.04	1.12	1.12	1.20	1.20	1.07	1.07	1.13	1.13	1.16	1.17
5	1.07	1.08	1.20	1.20	1.34	1.35	1.12	1.12	1.22	1.22	1.29	1.29
6	1.11	1.12	1.32	1.32	1.55	1.56	1.18	1.19	1.34	1.34	1.46	1.46
7	1.16	1.17	1.47	1.48	1.84	1.86	1.27	1.27	1.50	1.51	1.68	1.69
8	1.22	1.23	1.66	1.68	2.24	2.27	1.37	1.38	1.71	1.72	1.99	2.00
9	1.29	1.30	1.91	1.94	2.80	2.84	1.50	1.51	1.99	2.01	2.41	2.44
10	1.38	1.38	2.24	2.28	3.58	3.66	1.65	1.67	2.35	2.38	2.98	3.02

Table 3.3 shows the same moments for $DNSR=40$ dB. Table 3.4 and Table 3.5 contain similar results for a shorter baseline, which provided a valued of $S=0.76$, namely when approaching the near field.

Table 3.3 Moments of q_1 and q_2 for $S=0.085$ and $DNSR=40$ dB

s	q_1						q_2					
	7ML		ML		1/2ML		7ML		ML		1/2ML	
	Gamma $\nu_{q_1}=6928.76$ q_1		Gamma $\nu_{q_1}=2649.94$ q_1		Gamma $\nu_{q_1}=1624.54$ q_1		Gamma $\nu_{q_2}=4363.95$ q_2		Gamma $\nu_{q_2}=2496.25$ q_2		Gamma $\nu_{q_2}=1920.84$ q_2	
1	1	1	1	1	1	1	1	1	1	1	1	1
2	1.00	1.00	1.00	1.00	1.00	1.00	1.00	1.00	1.00	1.00	1.00	1.00
3	1.00	1.00	1.00	1.00	1.00	1.00	1.00	1.00	1.00	1.00	1.00	1.00
4	1.00	1.00	1.00	1.00	1.00	1.00	1.00	1.00	1.00	1.00	1.00	1.00
5	1.00	1.00	1.00	1.00	1.01	1.01	1.00	1.00	1.00	1.00	1.01	1.01
6	1.00	1.00	1.01	1.01	1.01	1.01	1.00	1.00	1.00	1.00	1.01	1.01
7	1.00	1.00	1.01	1.01	1.01	1.01	1.01	1.01	1.01	1.01	1.01	1.01
8	1.00	1.00	1.01	1.01	1.02	1.02	1.01	1.01	1.01	1.01	1.01	1.01
9	1.01	1.01	1.01	1.01	1.02	1.02	1.01	1.01	1.01	1.01	1.02	1.02
10	1.01	1.01	1.02	1.02	1.03	1.03	1.01	1.01	1.02	1.02	1.02	1.02

Table 3.4 Moments of q_1 and q_2 for $S=0.76$ and $DNSR=10$ dB

s	q_1						q_2					
	7ML		ML		1/2ML		7ML		ML		1/2ML	
	Gamma $\nu_{q_1}=1863.40$ q_1		Gamma $\nu_{q_1}=453.33$ q_1		Gamma $\nu_{q_1}=248.28$ q_1		Gamma $\nu_{q_2}=697.59$ q_2		Gamma $\nu_{q_2}=453.33$ q_2		Gamma $\nu_{q_2}=280.20$ q_2	
1	1	1	1	1	1	1	1	1	1	1	1	1
2	1.00	1.00	1.00	1.00	1.00	1.00	1.00	1.00	1.00	1.00	1.00	1.00
3	1.00	1.00	1.01	1.01	1.01	1.01	1.00	1.00	1.01	1.01	1.01	1.01
4	1.00	1.00	1.01	1.01	1.02	1.02	1.01	1.01	1.01	1.01	1.02	1.02
5	1.01	1.01	1.02	1.02	1.04	1.04	1.01	1.01	1.02	1.02	1.04	1.04
6	1.01	1.01	1.03	1.03	1.06	1.06	1.02	1.02	1.04	1.04	1.05	1.05
7	1.01	1.01	1.05	1.05	1.09	1.09	1.03	1.03	1.05	1.05	1.08	1.08
8	1.02	1.02	1.06	1.06	1.12	1.12	1.04	1.04	1.07	1.07	1.10	1.10
9	1.02	1.02	1.08	1.08	1.15	1.15	1.05	1.05	1.09	1.09	1.14	1.14
10	1.02	1.02	1.10	1.10	1.20	1.20	1.07	1.07	1.12	1.12	1.17	1.17

Table 3.5 Moments of q_1 and q_2 for $S=0.76$ and $DNSR=40$ dB

s	q_1						q_2					
	7ML		ML		1/2ML		7ML		ML		1/2ML	
	Gamma $\nu_{q_1}=323.43$	q_1	Gamma $\nu_{q_1}=78.69$	q_1	Gamma $\nu_{q_1}=43.09$	q_1	Gamma $\nu_{q_2}=121.08$	q_2	Gamma $\nu_{q_2}=70.26$	q_2	Gamma $\nu_{q_2}=48.63$	q_2
1	1	1	1	1	1	1	1	1	1	1	1	1
2	1.00	1.00	1.01	1.01	1.02	1.02	1.01	1.01	1.01	1.01	1.02	1.02
3	1.01	1.01	1.04	1.04	1.07	1.07	1.02	1.03	1.04	1.04	1.06	1.06
4	1.02	1.02	1.08	1.08	1.15	1.15	1.05	1.05	1.09	1.09	1.13	1.13
5	1.03	1.03	1.13	1.13	1.25	1.25	1.09	1.09	1.15	1.15	1.22	1.22
6	1.05	1.05	1.20	1.21	1.40	1.40	1.13	1.13	1.23	1.23	1.35	1.35
7	1.07	1.07	1.30	1.30	1.59	1.60	1.19	1.19	1.34	1.34	1.51	1.51
8	1.09	1.09	1.41	1.41	1.85	1.86	1.25	1.26	1.47	1.47	1.73	1.73
9	1.12	1.12	1.56	1.56	2.19	2.21	1.34	1.34	1.64	1.64	2.01	2.02
10	1.15	1.15	1.73	1.74	2.65	2.67	1.44	1.44	1.85	1.85	2.39	2.40

As apparent, there is a close match between the normalized moments of both q_1 and q_2 and the corresponding moments of the Gamma PDF with the same normalized second moment. This justifies the use of the Gamma PDF as the approximate PDF for both q_1 and q_2 . By inverting the first and second order moments defined in eq. (3.20) and in accordance with eq. (3.22) these are characterized by the following shape factors and scale parameters:

$$\begin{cases} \nu_{q_1} = \frac{1(1 + DNR)}{2} \frac{\omega^2}{\rho(DNR)(1 + \delta)} \\ \nu_{q_1} = \frac{1(1 + DNR)}{2} \frac{\omega^2}{\rho(DNR)(1 - \delta)} \end{cases} \quad (3.23)$$

$$\begin{cases} \mu'_{q_1} = \sigma_n^2 \varepsilon \rho(DNR) / \omega (1 + \delta) \\ \mu'_{q_2} = \sigma_n^2 \varepsilon \rho(DNR) / \omega (1 - \delta) \end{cases} \quad (3.24)$$

where the other parameters in eq. (3.23) and eq. (3.24) are :

$$\begin{aligned} \delta &= \frac{\sum_{n=1}^N |\eta_n| \eta_n}{\sum_{n=1}^N \eta_n^2}, \quad \varepsilon^2 = \sum_{n=1}^N \eta_n^2, \quad \omega = \frac{\sum_{n=1}^N |\eta_n|}{\sqrt{\sum_{n=1}^N \eta_n^2}}, \quad \rho(DNR) \\ &= 1 + \frac{DNR}{1 + DNR} \end{aligned} \quad (3.25)$$

As the test statistic is given by the difference $q_0 = q_1 - q_2$, its PDF is given by the correlation between the two gamma PDFs which approximate respectively q_1 and q_2 . In order

to simplify the expression of the PDF, as well as the resulting P_{fa} , we restrict to integer values of $n_{q_1} = \text{round}(v_{q_1})$. In practice, approximating the values with the closest integer is not expected to introduce any significant approximation error. As clearly apparent from Table 3.2 to Table 3.5 these values are typically large and in this case the Gamma PDF is well known to have a limited sensitivity to the order parameter values.

By integrating the resulting PDF on the interval $[T_{CVD}, \infty)$, Appendix B, we obtain:

$$P_{fa} = e^{-\frac{T_{CVD}/(\sigma_n^2 \varepsilon)}{\frac{\rho(DNR)}{\omega(1+\delta)}}} (1 + \delta)^{v_{q_2}} \sum_{m=0}^{n_{q_1}-1} \frac{1}{m!} \left(\frac{T_{CVD}/(\sigma_n^2 \varepsilon)}{\rho(DNR)/\omega(1+\delta)} \right)^m \sum_{r=0}^{n_{q_1}-1-m} \frac{\Gamma(r + v_{q_2})}{2^{v_{q_2}+r} \Gamma(v_{q_2})} (1 - \delta)^r \quad (3.26)$$

Figure 3.6 and Figure 3.7 compare the expression above of the P_{fa} with the results from Monte Carlo simulation with 10^7 independent trials based on the exact PDF of the decision statistic q_0 , respectively for the deep far field case, $S=0.085$ and getting close to the near field, $S=0.76$ as function of the threshold, $T_{CVD}/\sigma_n^2 \varepsilon$, namely the decision threshold (T_{CVD}) normalized with respect to the standard deviation of the noise at the output of the matched filter ($\sigma_n^2 \varepsilon$). This last assumption can be easily explained by recalling the decision statistic in eq. (3.14) and the definition of ε^2 in eq. (3.25) that, in presence of noise only, yield a noise power at the output of the matched filter equal to $\sigma_n^4 \varepsilon^2$.

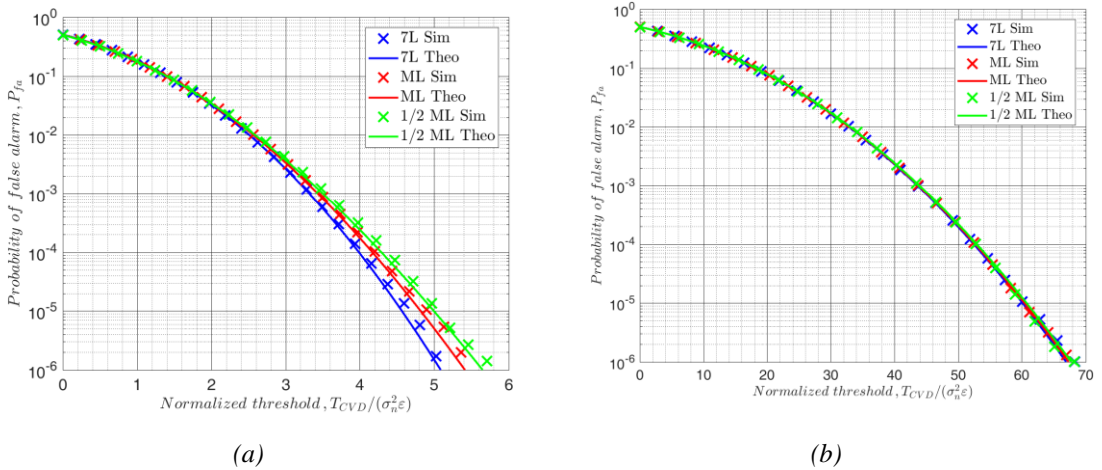


Figure 3.6 Simulated and theoretical P_{fa} as function of $T_{CVD}/(\sigma_n^2 \varepsilon)$ when $S=0.085$ and for (a) $DNR=10$ dB and (b) $DNR=40$ dB.

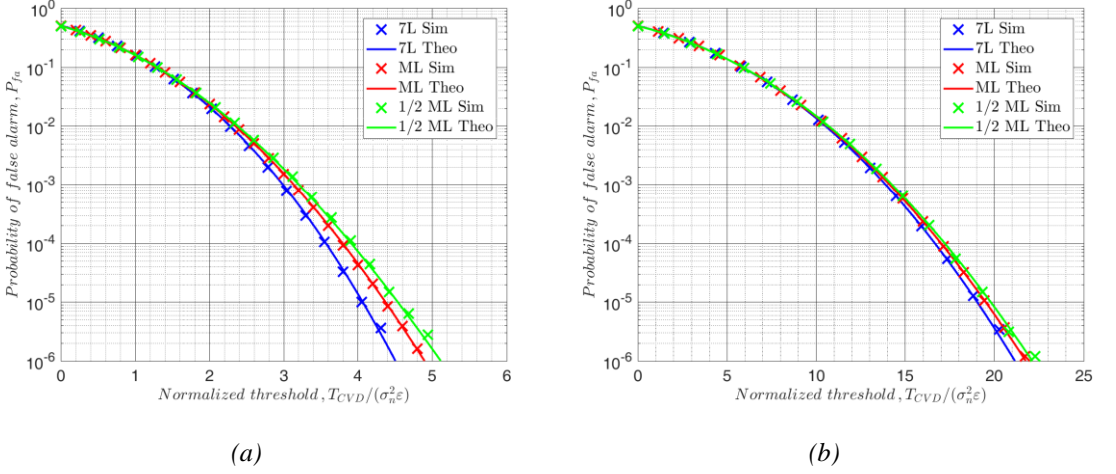


Figure 3.7 Simulated and theoretical P_{fa} as function of $T_{CVD} / (\sigma_n^2 \epsilon)$ when $S=0.76$ and for (a) $DNSR=10$ dB and (b) $DNSR= 40$ dB.

As it can be observed in all the cases there is a close match between the closed form expression in eq. (3.26) and the corresponding simulated results. It is well known that for large shape factor v_{q_m} ($m=1,2$), the Gamma PDF of q_1 and q_2 converges to Gaussian distribution with mean and variance respectively equal to:

$$\begin{cases} \mu_{q_m} = v_{q_m} \mu'_{q_m} = \frac{\sigma_n^2 \epsilon}{2} (1 + DNR) \omega \\ \sigma_{q_m}^2 = v_{q_m} \mu_{q_m}'^2 = \frac{\sigma_n^4 \epsilon^2}{2} (1 + 2DNR)(1 - (-1)^m \delta) \end{cases} \quad (3.27)$$

Therefore, $q_0 = q_1 - q_2$ also converges to a Gaussian random variable with zero mean and variance:

$$\sigma_{q_0}^2 = v_{q_1} \mu_{q_1}'^2 + v_{q_2} \mu_{q_2}'^2 = \sigma_n^4 \epsilon^2 (1 + 2DNR) \quad (3.28)$$

We notice that this certainly applies when DNR goes to infinity, so that both v_{q_1} and v_{q_2} go to infinity. In consequence, for high DNR values, the PDF for q_0 can be approximated with a Gaussian variate:

$$p_{q_0}(q_0) = \frac{1}{\sqrt{2\pi}\sigma_n^2 \epsilon} \frac{1}{\sqrt{1 + 2DNR}} e^{-\frac{q_0^2}{2\sigma_n^4 \epsilon^2 (1 + 2DNR)}} \quad (3.29)$$

and the P_{fa} is expressed as:

$$P_{fa} = \frac{1}{2} \operatorname{erfc} \left(\frac{T_{CVD}/(\sigma_n^2 \varepsilon)}{\sqrt{2(1+2DNR)}} \right) \quad (3.30)$$

The Gaussian approximate expression has been reported in [42], where it is shown that such approximation provides a nice fit to Monte Carlo simulations for DNSR high enough and P_{fa} up to 10^{-3} . Figure 3.8 and Figure 3.9 compare the exact P_{fa} , eq.(3.26) with the approximated P_{fa} , eq.(3.30) for a long (7L) and short (1/ML) time interval cases for both reference scenarios.

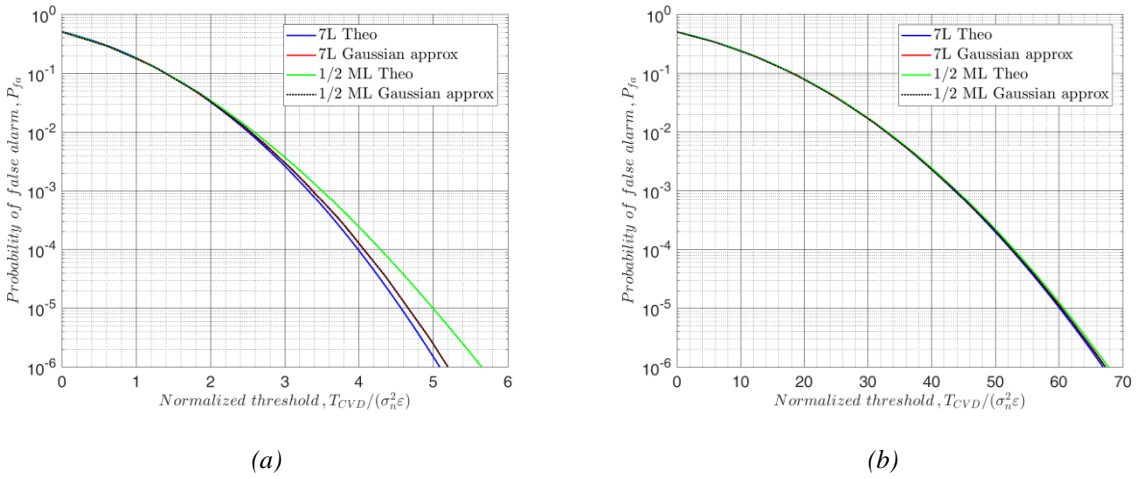


Figure 3.8 Theoretical and approximated P_{fa} as function of $T_{CVD}/(\sigma_n^2 \varepsilon)$ when $S=0.085$ and for (a) $DNSR=10$ dB and (b) $DNSR=40$ dB.

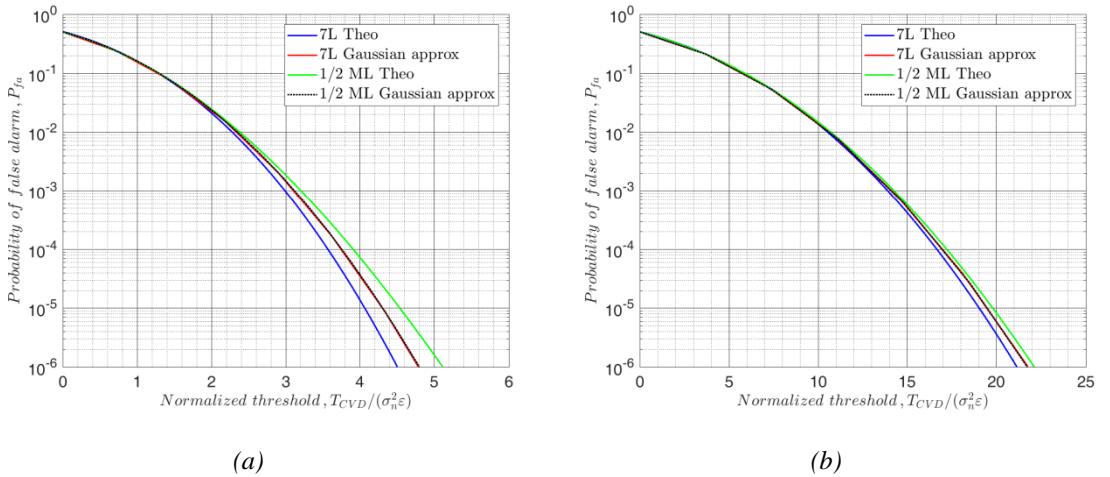


Figure 3.9 Theoretical and approximated P_{fa} as function of $T_{CVD}/(\sigma_n^2 \varepsilon)$ when $S=0.76$ and for (a) $DNSR=10$ dB and (b) $DNSR=40$ dB.

The comparison highlights that the Gaussian approximation can show non-negligible errors in the low P_{fa} region compared to the exact P_{fa} particularly for low values of DNSR.

This can be also verified by comparing the moments of the test statistic to the moments of a zero mean Gaussian random variable with the same variance. Similarly to q_1 and q_2 , q_0 is a quadratic form of Gaussian random variables. Therefore, its generic moment of order s is:

$$\mu_{q_0}(s) = \sum_{i=0}^{s-1} \frac{(s-1)!}{i!} \sigma_n^{2(s-1-i)} (\sigma_n^2 + (s-i)|\alpha|^2) \sum_{n=1}^N \eta_n^{s-i} \mu_{q_0}(i) \quad (3.31)$$

Table 3.6 reports the first ten normalized moment $\mu_{q_0}^N(s) = \mu_{q_0}(s)/\mu_{q_0}^{s/2}(2)$ for DNSR=10 dB and DNSR=40 dB, and the three different integration times for a far field condition of S=0.085. The normalized moments for the zero-mean Gaussian random variable are reported in column 2 for comparison.

Table 3.6 Moments of the CVD statistic q_0 under H_0 hypothesis for S=0.085.

		DNSR=10 dB			DNSR=40 dB		
s	Gaussian	7L	ML	½ ML	7L	ML	½ ML
1	0	4.3x10 ⁻¹⁵	1.9x10 ⁻¹⁵	1.3x10 ⁻¹⁵	3.0x10 ⁻¹⁴	1.3x10 ⁻¹⁴	9.1x10 ⁻¹⁵
2	1	1	1	1	1	1	1
3	0	-0.07	-0.01	0.048	-0.01	-0.00	0.01
4	3	3.07	3.09	3.12	3.01	3.00	3.00
5	0	-0.73	-0.05	0.50	-0.08	-0.01	0.05
6	15	16.23	16.41	16.82	15.01	15.01	15.02
7	0	-8.05	-0.58	5.74	-0.80	-0.06	0.54
8	105	123.66	125.58	132.18	105.18	105.20	105.26
9	0	-104.12	-7.15	77.97	-9.5875	-0.75	6.43
10	945	1251.60	1271.40	1388.90	947.85	947.96	948.91

Table 3.7 reports similar results for a shorter baseline, namely getting close to near field for a far field parameter S=0.76.

Table 3.7 Moments of the CVD statistic q_0 under H_0 hypothesis for $S=0.76$.

s	Gaussian	DNSR=10 dB			DNSR=40 dB		
		7L	ML	½ ML	7L	ML	½ ML
1	0	2.8×10^{-15}	8.1×10^{-17}	2.4×10^{-15}	6.8×10^{-15}	1.9×10^{-16}	5.9×10^{-15}
2	1	1	1	1	1	1	1
3	0	-0.11	-0.02	0.03	-0.04	-0.01	0.01
4	3	3.04	3.05	3.09	3.00	3.00	3.01
5	0	-1.15	-0.22	0.30	-0.37	-0.07	0.09
6	15	15.77	15.75	16.21	15.07	15.07	15.11
7	0	-12.44	-2.34	3.39	-3.86	-0.72	1.00
8	105	117.88	115.81	122.65	106.20	105.98	106.57
9	0	-155.95	-29.67	44.35	-46.52	-8.62	12.11
10	945	1173.40	1113.00	1224.40	965.93	959.79	968.79

By comparing the moments of q_0 to the moments of a Gaussian random variable, the following comments are in order: (i) a disagreement on the high order moments (and particularly on the odd-order) is observed that is consistent with the behavior of the curves in the low P_{fa} region observed in the Figure 3.8 and Figure 3.9 (ii) the disagreement increases as the DNSR decreases as also observed moving from Figure 3.8 (b) and Figure 3.9 (b) to Figure 3.8 (a) and Figure 3.9 (a) respectively.

Furthermore from Figure 3.8 and Figure 3.9 it is also noted that the Gaussian approximation is independent of the integration time providing a fixed threshold dependent only on the DNSR value.

Above results nicely validate the proposed closed form expression, eq.(3.26), that is extremely important for the practical application of the CVD scheme, since it allows us to set the detection threshold required to guarantee a specified false alarm rate, once the noise level and the DNR values are known.

3.4.2 Probability of detection

Likewise, the PDF under hypothesis H_1 need to be defined in order to establish a closed-form expression for the P_d and as the exact fitting of the PDF tails is not strictly required as for the P_{fa} an analysis of the moments of the decision statistic will not be reported and the validation of

the analytical expression will be verified directly by comparison with results obtained from Monte Carlo simulation based on the exact PDF.

Under hypothesis H_1 the PDF of the test statistic q_0 follows very closely the Gaussian PDF, [42]:

$$p_{q_0}(q_0) = \frac{1}{\sqrt{2\pi}\sigma_{q_0}} e^{-\frac{(q_0 - \mu_{q_0})^2}{2\sigma_{q_0}^2}} \quad (3.32)$$

being mean value and variance respectively given by:

$$\mu_{q_0} = \mu_{q_0}(1) = |\beta|^2 \sum_{k=1}^N \eta_k |s_{t0k}|^2 + 2|\alpha||\beta|\varepsilon^2 \quad (3.33)$$

$$\begin{aligned} \sigma_{q_0}^2 &= \mu_{q_0}(2) - \mu_{q_0}^2(1) \\ &= \sigma_n^2 \left[(\sigma_n^2 + 2|\alpha|^2)s^2 + 2|\beta|^2 \sum_{k=1}^N \eta_k^2 |s_{t0k}|^2 \right. \\ &\quad \left. + 4|\alpha||\beta| \sum_{k=1}^N \eta_k^2 h_k^2 \right] \end{aligned} \quad (3.34)$$

as directly obtained from eq. (3.19).

Figure 3.10 compare the test statistic histogram under hypothesis H_1 obtained from Monte Carlo simulation with 10^6 independent trials based on the exact PDF, normalized with respect to its standard deviation, σ_{q_0} and the PDF defined in the eq. (3.32) for two different values of DNR (see (3.6)) and observation times (long, 7L and short, 1/2ML) when the target is in the far field area, $S=0.085$. Figure 3.11 reports similar results for a shorter baseline, namely getting close to near field for a far field parameter $S=0.76$. For all cases is noted a good agreement between the simulated results and the PDF.

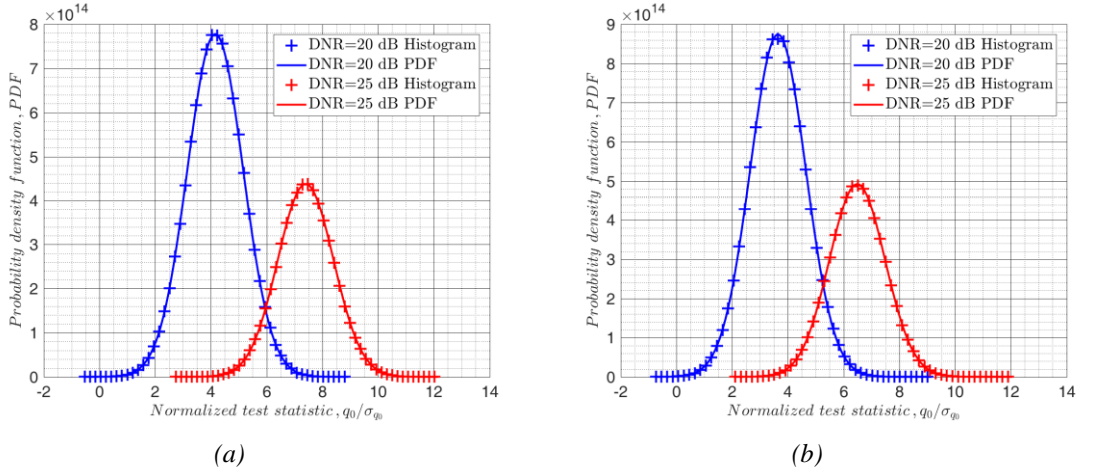


Figure 3.10 Histogram and PDF of the normalized test statistic, q_0 / σ_{q_0} when $S=0.085$ and (a) for a long observation time, $7L$ and (b) short observation time, $1/2ML$.

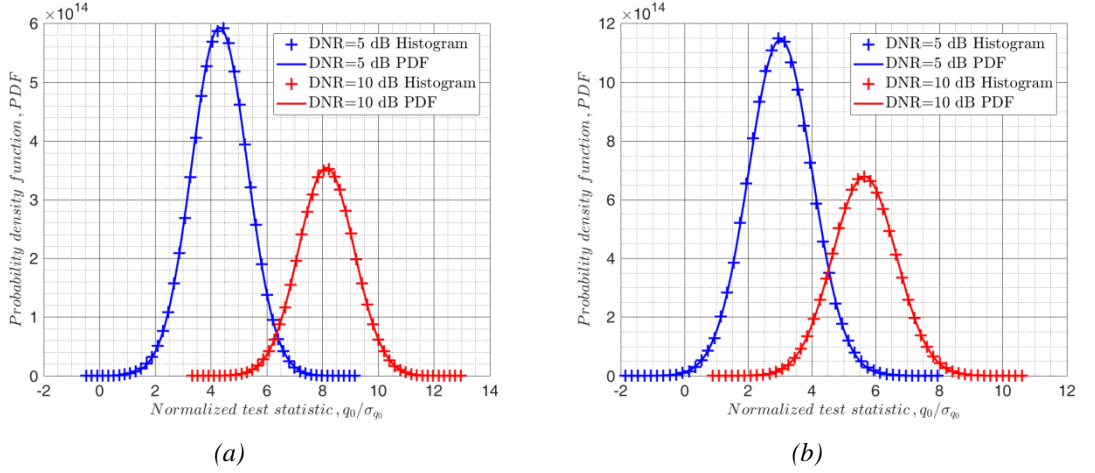


Figure 3.11 Histogram and PDF of the normalized test statistic, q_0 / σ_{q_0} when $S=0.76$ and (a) for a long observation time, $7L$ and (b) short observation time, $1/2ML$.

Therefore, after some simple manipulations, an approximate expression of the CVD detection probability can be obtained as:

$$P_d = \frac{1}{2} \operatorname{erfc} \left\{ \frac{\frac{T_{CVD}}{\sigma_n^2 \varepsilon \sqrt{2(1+2DNR)}} - \frac{DNR}{\sqrt{2(1+2DNR)}} \varepsilon \left(|\gamma|^2 \frac{\sum_{k=1}^N \eta_k^2 |s_{t0k}|^2}{\varepsilon^2} + 2|\gamma| \right)}{\sqrt{1 + \frac{2DNR}{(1+2DNR)} \left(|\gamma|^2 \frac{\sum_{k=1}^N \eta_k^2 |s_{t0k}|^2}{\varepsilon^2} \right) + 2|\gamma| \frac{\sum_{k=1}^N \eta_k^2 h_k}{\varepsilon^2}}} \right\} \quad (3.35)$$

where $\gamma = \beta/\alpha = jl_v l_h / \lambda L$ depends on the target size for an assigned system geometry (λ, L) and the other parameters in eq. (3.35) have been defined in the Section 3.4.1. From the eq. (3.35) it can be easily verified that in absence of the target signal (i.e $\gamma = 0$) the approximated P_{fa} in eq. (3.30) is obtained. The closed form expression for the detection probability in eq. (3.35) as function of the DNR (see (3.6)) is compared to the results of a Monte Carlo simulation with 10^6 independent trials based on the exact PDF of the decision statistic q_0 under hypothesis H_1 in the Figure 3.12 , respectively for the case of deep far field and for the transition between far and near field for three different integration times having set a $P_{fa}=10^{-5}$.

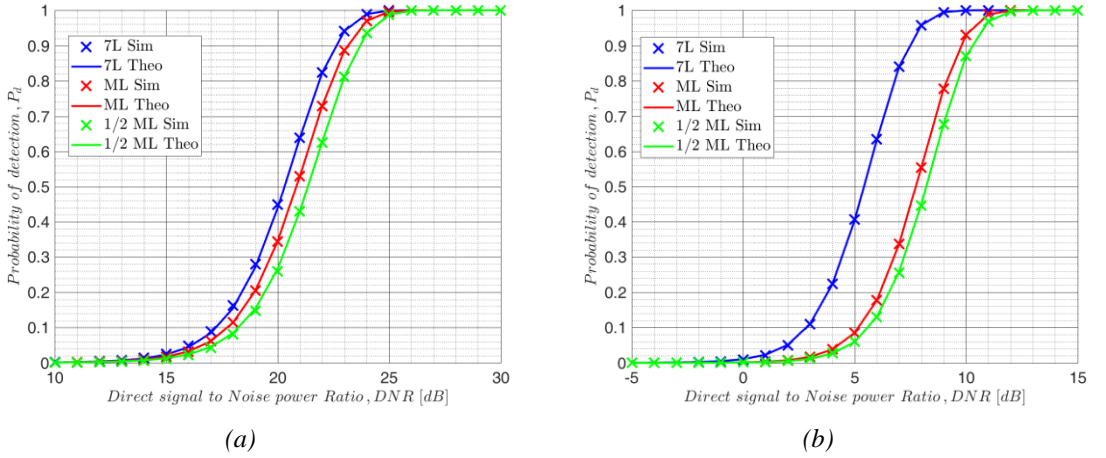


Figure 3.12 Simulated and theoretical P_d of the CVD detector for a $P_{fa}=10^{-5}$ when (a) $S=0.085$ and (b) $S=0.76$.

As apparent, for all considered cases, the theoretical expression provides a complete agreement with the simulated results hence eq. (3.35) can be used to exactly predict the CVD detection performance. Moreover, the denominator term in eq.(3.35) does not change with the DNR being almost constant and equal to one in all considered conditions as shown in the Figure 3.13.

Accordingly, the expression of the P_d can be simplified as follows:

$$P_d^{Approx-1} \cong \frac{1}{2} \operatorname{erfc} \left\{ \frac{T_{CVD}}{\sigma_n^2 \varepsilon \sqrt{2(1+2DNR)}} - \frac{DNR}{\sqrt{2(1+2DNR)}} \varepsilon \left(|\gamma|^2 \frac{\sum_{k=1}^N \eta_k |s_{t0k}|^2}{\varepsilon^2} + 2|\gamma| \right) \right\} \quad (3.36)$$

Equation (3.36) can be further simplified by dropping the term depending on $|\gamma|^2$, by approximating $1 + 2DNR \approx 2DNR$ and by substituting eq. (3.30) we obtain:

$$P_d^{Approx-2} \cong \frac{1}{2} \text{erfc}[\text{erfc}^{-1}(2P_{fa}) - \sqrt{DNR}\epsilon|\gamma|] \quad (3.37)$$

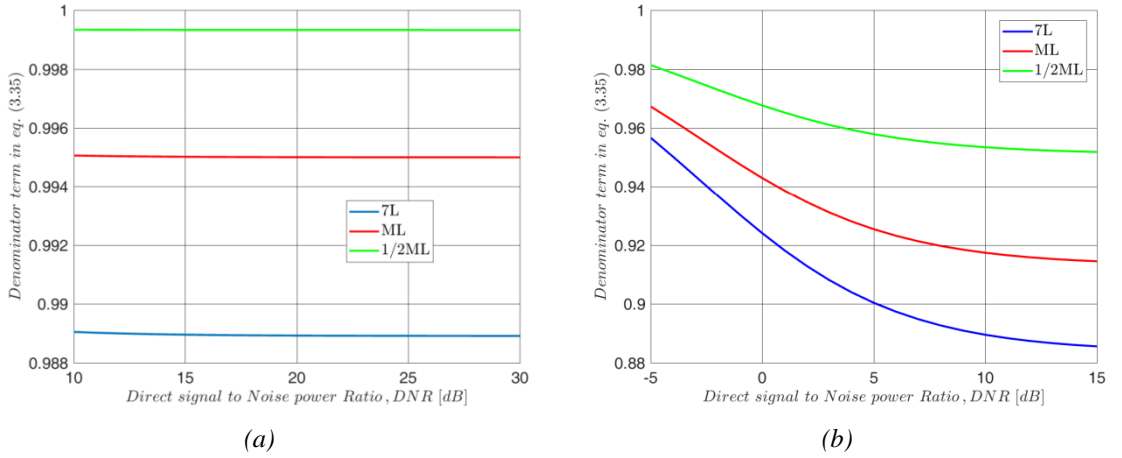


Figure 3.13 The term at the denominator of the analytical expression in eq. (3.35) when (a) $S=0.085$ and (b) $S=0.76$.

Figure 3.14 compares the complete closed form expression in eq. (3.35) to the two approximations in eqs. (3.36) and (3.37) and under the same conditions considered in Figure 3.12.

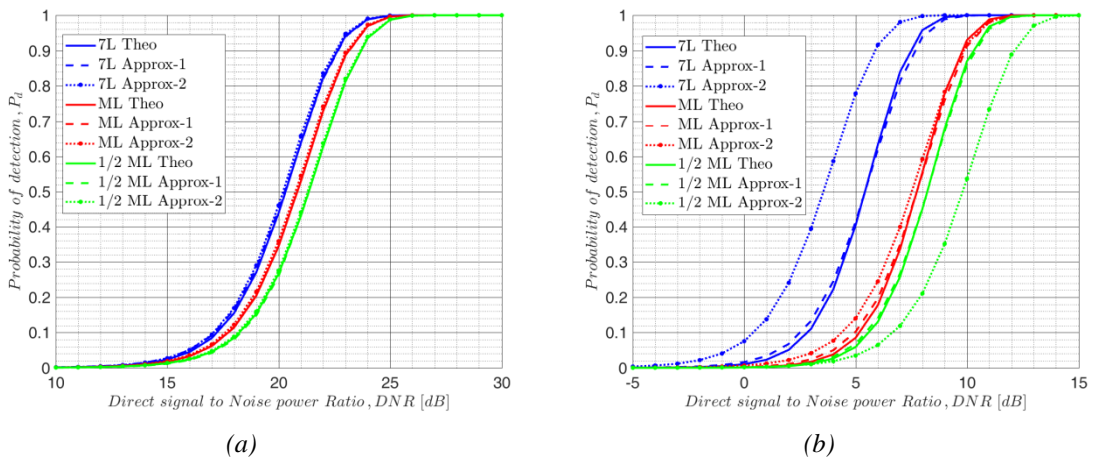


Figure 3.14 Theoretical and approximated P_d of the CVD detector for a $P_{fa}=10^{-5}$ when (a) $S=0.085$ and (b) $S=0.76$.

It is quite apparent that the proposed approximated expression in eq. (3.36) still provides an accurate fit to the complete closed form whereas the approximated expression in the eq. (3.37) shows differences in the order of 2 dB in the worst case for the target getting close to the near field, $S=0.76$ ((b)).

Nevertheless the simplified expression in eq. (3.37) can very usefully support preliminary system design and performance prediction of the FSR system.

3.5 CFAR CVD and performance analysis

The theoretical expression of the probability of false alarm derived in 3.4.1 allows us to select an appropriate threshold for the CVD detector so that a desired P_{fa} value is achieved. However, it is apparent from eq.(3.26) that this fixed threshold depends on both the values of noise variance σ_n^2 and DNR. In some cases these parameters are easy to estimate and vary slowly in time, however the CVD still requires to adapt the fixed threshold accordingly. In some other conditions, the variations are faster and more difficult to track. In any case, it is quite useful to have a detector that does not require to change the threshold as the system conditions change. Therefore, we look for a modified version of the CVD scheme that maintains a constant false alarm rate (CFAR) independent on the values of σ_n^2 and DNR. To obtain the desired CFAR characteristic, we aim at normalizing the CVD test statistic by an appropriate function of the received data that contains a similar dependency of the CVD on noise variance and DNR.

We approach this problem in the following sections under two different assumptions, respectively availability of secondary data (Section 3.5.1) and absence of secondary data (Section 3.5.2). Likewise for the CVD detector firstly the decision statistic is derived and after a closed-form expression of the performance in terms of P_{fa} and P_d is obtained and validated through Monte Carlo simulations. Finally in Section 3.5.3 the performance of the two CFAR CVDs are compared to that provided by the fixed threshold CVD derived in the previous section.

3.5.1 CFAR CVD with secondary data

We first assume that a set of K target-free secondary data are available, namely K independent acquisitions of the same number of samples N under the same system conditions (i.e. sharing the same noise variance and DNR) as the primary data. For example, these sets of data can be relative to the K previous temporal frames preceding the frame under test, where no targets have been detected.

Using these secondary data, \mathbf{z}_k , for $k=1, \dots, K$ that are $N \times 1$ column vectors containing only the direct signal, $s_d(t)$, and the noise component, $n(t)$, defined in the Section 3.2, the normalized CVD test statistic considered is:

$$\psi_0 = \frac{\mathbf{h}^T \mathbf{P}^\perp \mathbf{z}}{\sqrt{\frac{1}{K} \sum_{k=1}^K (\mathbf{h}^T \mathbf{P}^\perp \mathbf{z}_k)^2}} \underset{H_0}{\overset{H_1}{\geq}} T'_{CVD} \quad (3.38)$$

where T'_{CVD} is the threshold selected such that the P_{fa} equals a predetermined value. In the Figure 3.15 the CFAR CVD with secondary data block diagram is sketched.

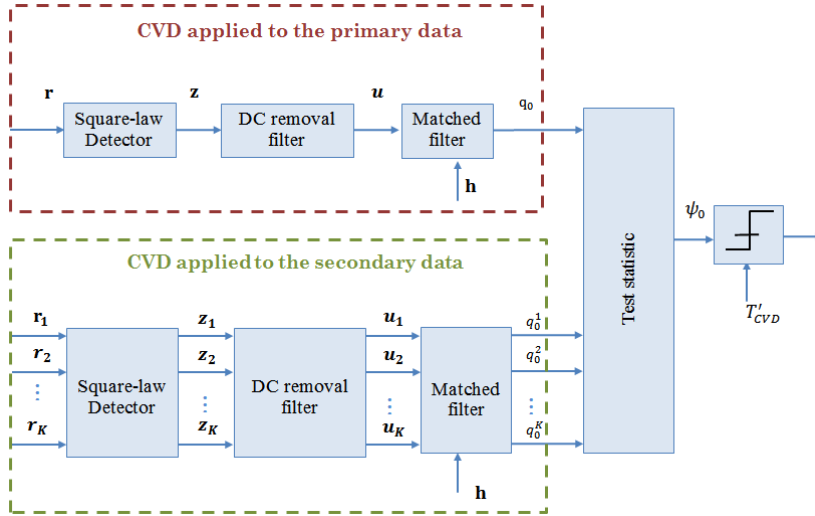


Figure 3.15 *CFAR CVD with secondary data block diagram.*

As apparent, the quantity $\frac{1}{K} \sum_{k=1}^K (\mathbf{h}^T \mathbf{P}^\perp \mathbf{z}_k)$ is a zero mean value random variable under hypothesis H_0 , so that it cannot be used to normalize the decision statistic $q_0 = \mathbf{h}^T \mathbf{P}^\perp \mathbf{z}$ defined in eq.(3.14). However, the quantity $\frac{1}{K} \sum_{k=1}^K (\mathbf{h}^T \mathbf{P}^\perp \mathbf{z}_k)^2$ has a non-zero mean value and is

expected to share the same dependency on noise variance and DNR as q_0 as it actually can be seen as an estimator of the variance of q_0 . Thus, the normalization is expected to provide a test statistic that has a negligible variation with those parameters.

Now the test statistic in eq. (3.38) is examined under each hypothesis. Under hypothesis H_0 , using results in Section 3.4 and assuming that the Gaussian approximation is valid for the PDF of both q_0 and $\mathbf{h}^T \mathbf{P}^\perp \mathbf{z}_k$ ($k=1, \dots, K$), we notice that ψ_0 has a Student's T distribution with K degrees of freedom (dof), [48]:

$$p_{\psi_0}(\psi_0/H_0) = \frac{\left(1 + \psi_0^2/K\right)^{-\frac{(K+1)}{2}}}{\sqrt{KB} \left(\frac{1}{2}, \frac{K}{2}\right)} \quad (3.39)$$

where $B(a, b)$ is beta function, [50].

Figure 3.16 shows the test statistic, ψ_0 histogram under hypothesis H_0 for different values of DNR (see eq. (3.5)) obtained from Monte Carlo simulations with 10^7 independent trials based on the exact PDF for both reference scenarios considering an integration time equal to the main lobe. Also shown is the T-student PDF defined in the eq. (3.39) that provides a good fit to the test statistic histogram. For both reference scenario $K=16$ secondary data is considered.

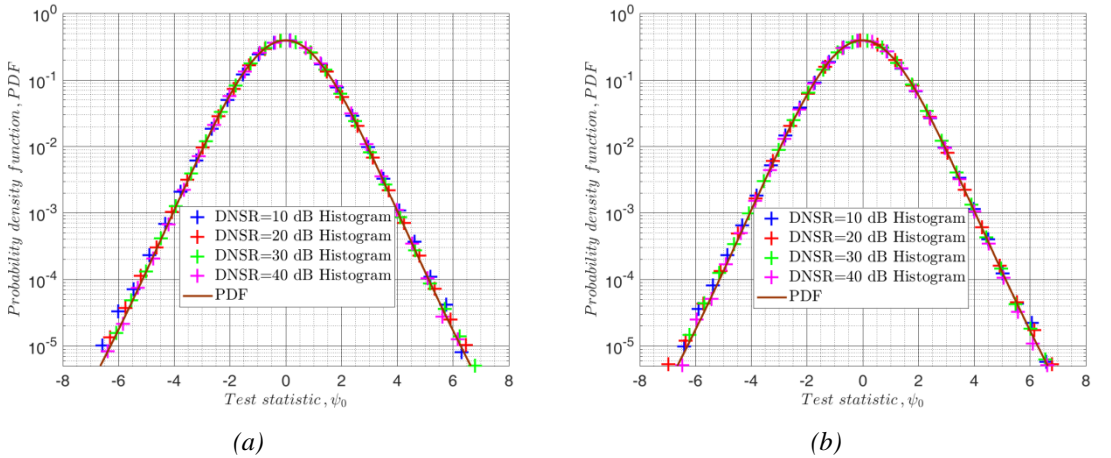


Figure 3.16 Histogram and PDF for different value of the DNR of the test statistic, ψ_0 for an observation time equal to the ML and (a) for $S=0.085$ and (b) for $S=0.76$.

Therefore, the false alarm probability is obtained by integrating eq. (3.39) over the interval $[T'_{CVD}, \infty)$ yielding,[48]:

$$P_{fa} = \frac{1}{2} - \frac{1}{2} I_{\frac{T'_{CVD}}{K+T'_{CVD}}} \left(\frac{1}{2}, \frac{K}{2} \right) \quad (3.40)$$

where $I_x(a, b)$ is the regularized incomplete beta function of order x , [50].

From eq. (3.40) it is clear that no prior knowledge of any unknown parameters is required to set the decision threshold needed in order to achieve a given P_{fa} level.

Figure 3.17 shows the P_{fa} of the CFAR CVD with $K=16$ secondary data versus the threshold T'_{CVD} , for different values of DNSR, as obtained from eq. (3.40) and from Monte Carlo simulations considering an observation time equal to the main lobe. We note a close match between the simulated results and the approximated closed form expression of the P_{fa} .

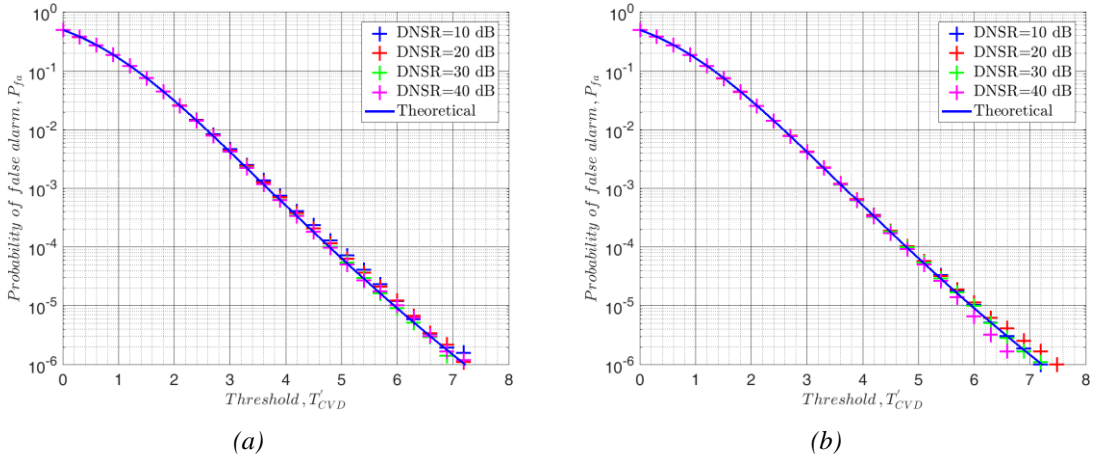


Figure 3.17 Simulated and theoretical P_{fa} of the CFAR CVD detector with secondary data for an observation time equal to ML and for (a) $S=0.085$ and (b) $S=0.76$.

For both scenarios we observe that the CFAR property is ensured as the same value of P_{fa} (i.e. the same test statistic histogram, Figure 3.16) is obtained independently from the specific DNSR. The same results are obtained for long and short observation times (namely, $7L$ and $1/2ML$) even here not reported.

Under hypothesis H_1 , we notice that the numerator $\mathbf{h}^T \mathbf{P}^\perp \mathbf{z}$ and the variable $\mathbf{h}^T \mathbf{P}^\perp \mathbf{z}_k$, $k=1, \dots, K$, at the denominator of eq. (3.38) have a different variance as the secondary data are

assumed to be target free. Let define the quantity R_0 as square root of the ratio between the variance of the numerator (i.e the variance of q_0 under H_1 as from eq.(3.34)) and the variance of the variable $\mathbf{h}^T \mathbf{P}^\perp \mathbf{z}_k$ (i.e. the variance of q_0 under H_0 as from eq.(3.28)):

$$R_0 = \sqrt{\frac{\sigma_{q_0}^2|_{H_1}}{\sigma_{q_0}^2|_{H_0}}} = \sqrt{1 + \frac{2DNR}{(1 + 2DNR)} \left(|\gamma|^2 \frac{\sum_{k=1}^N \eta_k^2 |s_{t0k}|^2}{\varepsilon^2} \right) + 2|\gamma| \frac{\sum_{k=1}^N \eta_k^2 h_k}{\varepsilon^2}} \quad (3.41)$$

By scaling ψ_0 by the ratio R_0 and using the same approximate Gaussian assumption adopted under hypothesis H_0 to derive the PDF in eq. (3.39), the normalized statistic, $\hat{\psi}_0 = \psi_0/R_0$ is nicely approximated by a non-central Student's T distribution, [48], with K degrees of freedom:

$$p_{\hat{\psi}_0} \left(\frac{\hat{\psi}_0}{H_1} \right) = \frac{e^{-\tau_{CVD}^2/2}}{\sqrt{\pi K} \Gamma\left(\frac{K}{2}\right)} \sum_{r=0}^{\infty} \frac{(\hat{\psi}_0 \tau_{CVD})^r}{r! K^{r/2}} \left(1 + \frac{\hat{\psi}_0^2}{K} \right)^{-\frac{K+r+1}{2}} 2^{r/2} \Gamma\left(\frac{K+r+1}{2}\right) \quad (3.42)$$

where $\tau_{CFAR-CVD}$ is non centrality parameter of $\hat{\psi}_0$ that depends on the mean value and variance of the decision statistic q_0 (i.e the numerator of $\hat{\psi}_0$) under hypothesis H_1 defined respectively in eq. (3.33) and eq. (3.34):

$$\tau_{CVD} = \frac{\mu_{q_0}|_{H_1}}{\sqrt{\sigma_{q_0}^2|_{H_0}}} = \frac{DNR \varepsilon}{\sqrt{1 + 2DNR}} \frac{1}{R_0} \left(|\gamma|^2 \frac{\sum_{k=1}^N \eta_k |s_{t0k}|^2}{\varepsilon^2} + 2|\gamma| \right) \quad (3.43)$$

Figure 3.18 compare the test statistic histogram under hypothesis H_1 obtained from Monte Carlo simulation with 10^6 independent trials, and the PDF defined in the eq. (3.32) for two different values of DNR (see (3.6)) and observation times (long, 7L and short, 1/2ML) when the target is in the far field area, $S=0.085$.

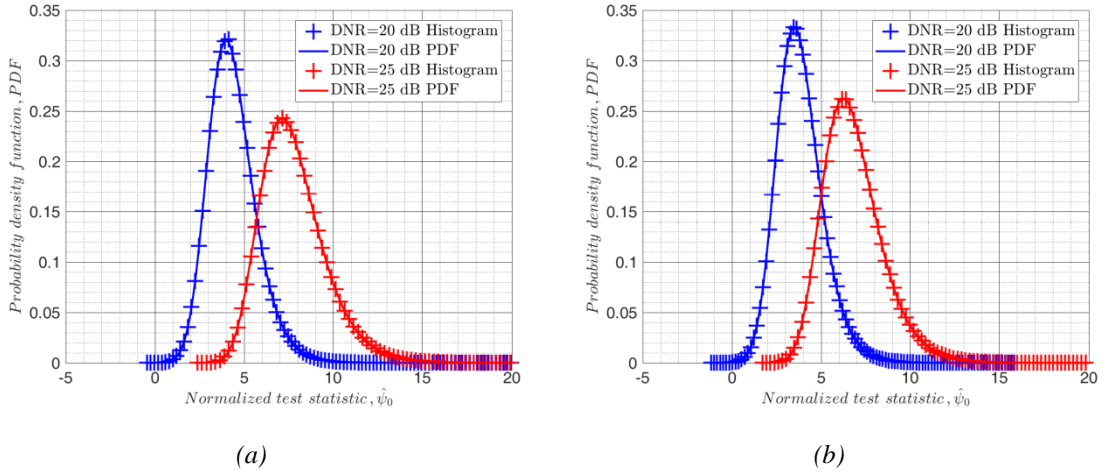


Figure 3.18 Histogram and PDF of the normalized test statistic $\hat{\psi}_0$ when $S=0.085$ and (a) for a long observation time, $7L$ and (b) short observation time, $1/2ML$.

Figure 3.19 reports similar results for a shorter baseline, namely getting close to near field for a far field parameter $S=0.76$. For all cases is noted a good agreement between the simulated results and the PDF.

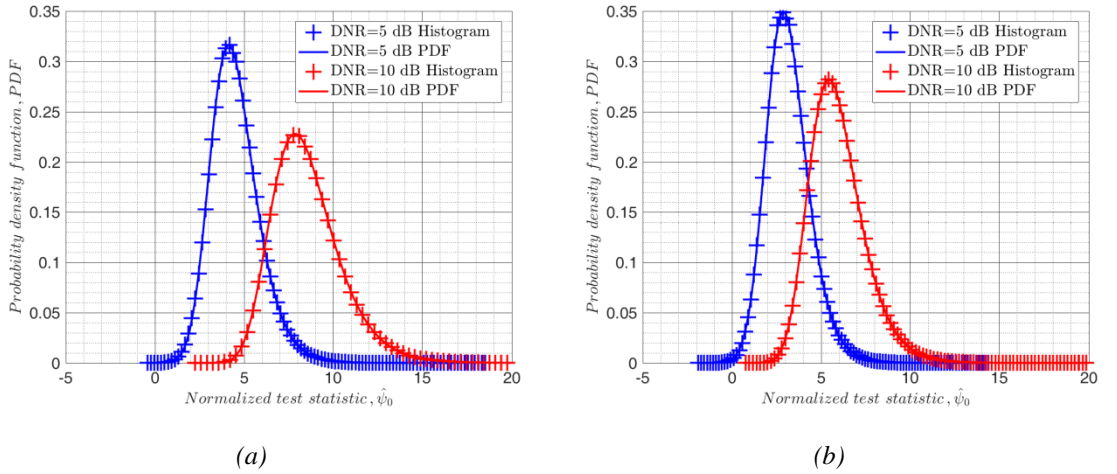


Figure 3.19 Histogram and PDF of the normalized test statistic $\hat{\psi}_0$ when $S=0.76$ and (a) for a long observation time, $7L$ and (b) short observation time, $1/2ML$.

For sake of simplicity by defining the cumulative distribution function, [48], as $nct_cdf(t, n, b) = Prob\{t' < t\}$ where t' is a random variable following the generic noncentral -Student's T distribution with n degrees of freedom and noncentrality parameter b , the detection probability of $\hat{\psi}_0$ is written as:

$$P_d = 1 - nct_cdf\left(\frac{T_{CVD}^l}{R_0}, K, \tau_{CVD}\right) \quad (3.44)$$

The closed form expression in eq. (3.44) for the detection probability is reported in Figure 3.20 as a function of the DNR and compared to the results of Monte Carlo simulations having set a $P_{fa}=10^{-5}$ and again $K=16$. As apparent, the theoretical expression provides a good agreement with the simulated results. Hence eq.(3.44) can be used to predict the detection performance of the CFAR CVD with secondary data.

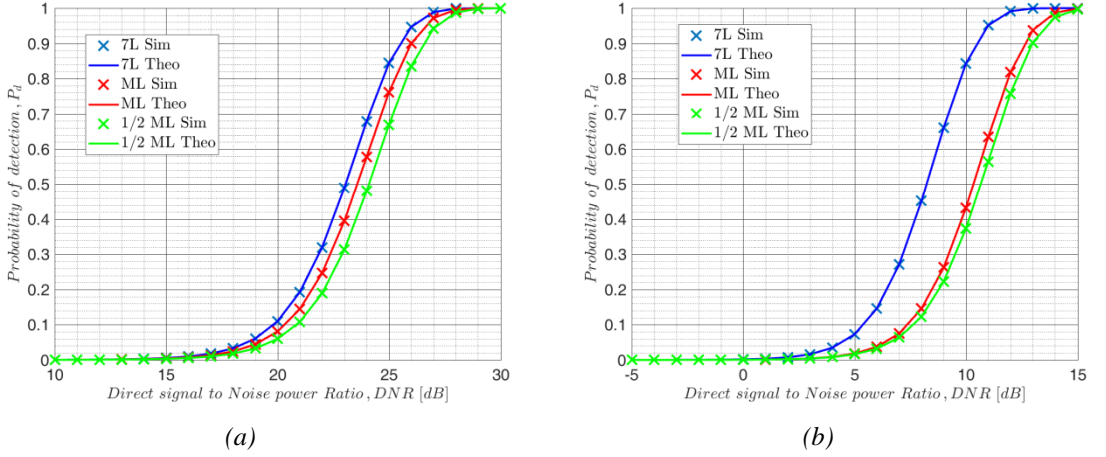


Figure 3.20 Simulated and theoretical P_d of CFAR CVD detector with $K=16$ for a $P_{fa}=10^{-5}$ when (a) $S=0.085$ and (b) $S=0.76$.

3.5.2 CFAR CVD without secondary data

In this section a fully adaptive detector based on the CVD is developed in the absence of secondary data and analytically characterized. By assuming that no secondary data are available, the normalization of the CVD test statistic, q_0 must be obtained from the primary data set. To this purpose, we need to establish a suitable estimator of the variance of the decision statistic q_0 based on primary data only. Since primary data may contain the target signal, the adopted strategy has to include the removal of the corresponding contribution. This is obtained by considering the signal at the output of the DC removal stage, $\mathbf{u} = \mathbf{P}^\perp \mathbf{z}$ and projecting it into the subspace orthogonal to $\boldsymbol{\eta} = \mathbf{P}^\perp \mathbf{h}$ defined in Section 3.4.1. Once this second projection has been accomplished, the variance can be estimated and its square root used to normalize the test statistic, q_0 .

Thus the decision rule can be written as:

$$\psi_1 = \frac{\mathbf{h}^T \mathbf{P}^\perp \mathbf{z} / \sqrt{\mathbf{h}^T \mathbf{P}^\perp \mathbf{h}}}{\sqrt{\mathbf{z}^T \left(\mathbf{P}^\perp - \frac{\mathbf{P}^\perp \mathbf{h} \mathbf{h}^T \mathbf{P}^\perp}{\mathbf{h}^T \mathbf{P}^\perp \mathbf{h}} \right) \mathbf{z} / N - 2}} \underset{H_0}{\overset{H_1}{\geq}} T''_{CVD} \quad (3.45)$$

In the Figure 3.21 the CFAR CVD without secondary data block diagram is sketched. As previously, the performance of the test statistic, ψ_1 in terms of P_{fa} and P_d is derived and its CFAR behavior demonstrated.

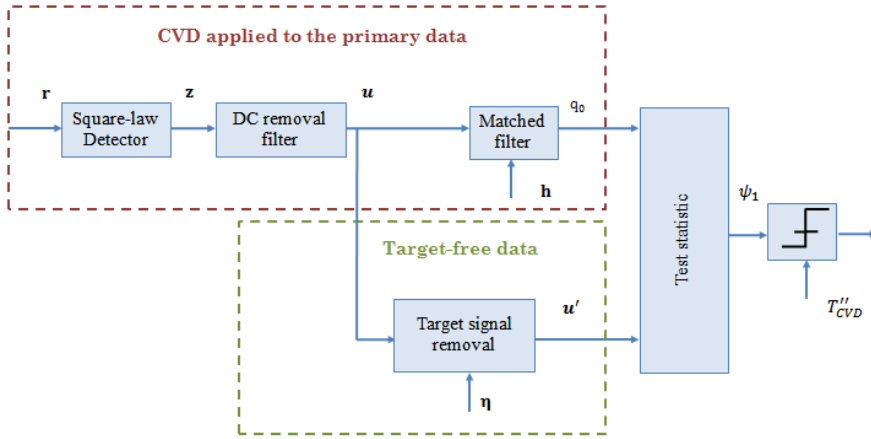


Figure 3.21 CFAR CVD without secondary data block diagram.

Under hypothesis H_0 , we assume that the Gaussian approximation is valid for the PDF of q_0 and a Chi-square distribution with $N-2$ degrees of freedom is a good approximation for the PDF of $\mathbf{z}^T \left(\mathbf{P}^\perp - \frac{\mathbf{P}^\perp \mathbf{h} \mathbf{h}^T \mathbf{P}^\perp}{\mathbf{h}^T \mathbf{P}^\perp \mathbf{h}} \right) \mathbf{z}$ (i.e. can be seen as the sum of squares of $N-2$ independent Gaussian variate) being \mathbf{z} a $N \times 1$ column vector. Under these assumptions, ψ_1 has a Student's T distribution with $N-2$ degrees of freedom, [48]:

$$p_{\psi_1}(\psi_1/H_0) = \frac{\left(1 + \frac{\psi_1^2}{(N-2)}\right)^{-\frac{(N-2+1)}{2}}}{\sqrt{N-2} B\left(\frac{1}{2}, \frac{N-2}{2}\right)} \quad (3.46)$$

Figure 3.22 compare the test statistic, ψ_1 histogram under hypothesis H_0 for different values of DNSR obtained from Monte Carlo simulations with 10^7 independent trials based on the exact PDF with the T-student PDF defined in the eq. (3.46) for both reference scenarios considering an observation time equal to the main lobe. It is noted that the PDF provides a

good fit to the test statistic histogram for both reference scenarios. The same agreement is obtained for a long and short integration time even here not reported.

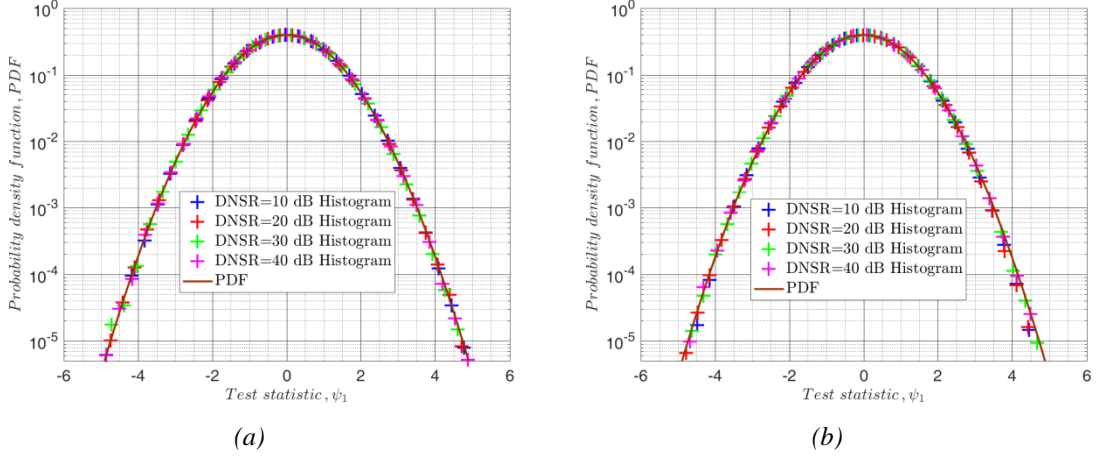


Figure 3.22 Histogram and PDF for different value of the DNSR of the test statistic, ψ_1 for an observation time equal to the ML and (a) for $S=0.085$ and (b) for $S=0.76$.

Hence, the P_{fa} obtained by integrating eq. (3.46) over the interval $[T_{CVD}'' \infty)$ is written as:

$$P_{fa} = \frac{1}{2} - \frac{1}{2} I_{\frac{T_{CVD}''^2}{N-2+T_{CVD}''^2}} \left(\frac{1}{2}, \frac{N-2}{2} \right) \quad (3.47)$$

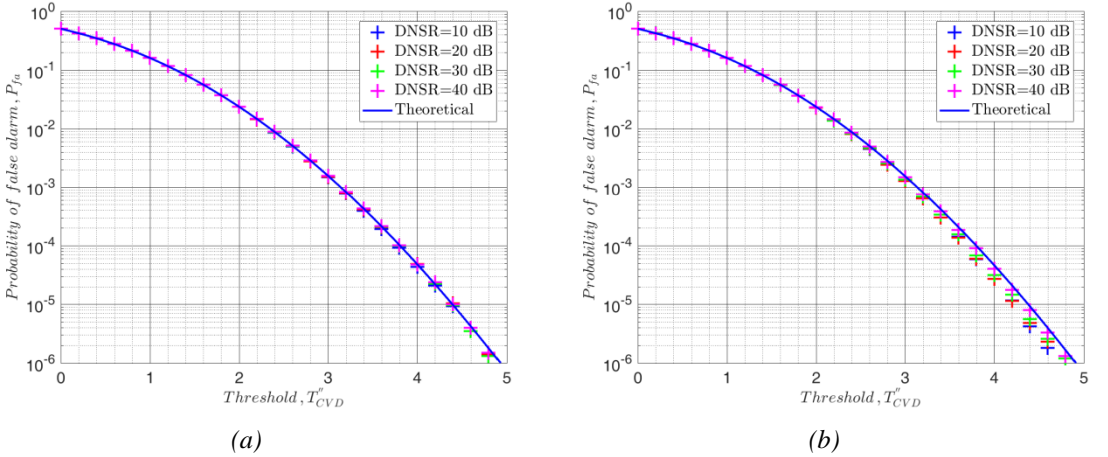


Figure 3.23 Simulated and theoretical P_{fa} of the CFAR CVD detector without secondary data for an observation time equal to ML and for (a) $S=0.085$ and (b) $S=0.76$.

For the same cases considered in Figure 3.17, Figure 3.23 compares the analytical expression of the P_{fa} in eq. (3.47), and the simulated P_{fa} of the CFAR CVD without secondary

data for different values of the DNSR. The reported results show that, despite the absence of secondary data, the proposed detector ensures the CFAR property and also we note a good agreement between simulation results and the approximated closed form of the P_{fa} .

Under hypothesis H_1 , by proceeding in similar way to Section 3.5.1, the numerator and the denominator of the test statistic, ψ_1 in eq. (3.45) have different variance. Let us define R_1 as the square root of the ratio between the variance of the numerator (i.e. obtained normalizing the variance of q_0 under H_1 in eq., (3.34) by $\mathbf{h}^T \mathbf{P}^\perp \mathbf{h}$) and the variance of the generic Gaussian variable that defines the Chi-square variate with $N-2$ dof at the denominator. In accordance with the property of the Chi-square distribution, [48], this variance can be obtained as the mean value of the Chi-square distributed variable divided by the number of dof, namely $E \left\{ \mathbf{z}^T \left(\mathbf{P}^\perp - \frac{\mathbf{P}^\perp \mathbf{h} \mathbf{h}^T \mathbf{P}^\perp}{\mathbf{h}^T \mathbf{P}^\perp \mathbf{h}} \right) \mathbf{z} \right\} / N - 2$ where $E\{\cdot\}$ is the expectation operator. Thus R_1 is written as:

$$R_1 = \sqrt{\frac{\sigma_{q_0}^2|_{H_1} / \mathbf{h}^T \mathbf{P}^\perp \mathbf{h}}{E \left\{ \mathbf{z}^T \left(\mathbf{P}^\perp - \frac{\mathbf{P}^\perp \mathbf{h} \mathbf{h}^T \mathbf{P}^\perp}{\mathbf{h}^T \mathbf{P}^\perp \mathbf{h}} \right) \mathbf{z} \right\} / N - 2}} \quad (3.48)$$

After some simple manipulation it yields:

$$R_1 = \sqrt{\frac{1 + \frac{2DNR}{(N-2)(1+2DNR)} \left(|\gamma|^2 \frac{\sum_{k=1}^N \eta_k^2 |s_{t0k}|^2}{\varepsilon^2} \right) + 2|\gamma| \frac{\sum_{k=1}^N \eta_k^2 h_k}{\varepsilon^2}}{1 + \frac{2DNR}{(N-2)(1+2DNR)} \left[|\gamma|^2 \left(\left(1 - \frac{1}{N} \right) \sum_{k=1}^N |s_{t0k}|^2 - \frac{\sum_{k=1}^N \eta_k^2 |s_{t0k}|^2}{\varepsilon^2} \right) + 2|\gamma| \left(\left(1 - \frac{1}{N} \right) \sum_{k=1}^N h_k - \frac{\sum_{k=1}^N \eta_k^2 h_k}{\varepsilon^2} \right) \right]}} \quad (3.49)$$

Finally, the normalized test statistic with respect to the ratio R_1 , $\hat{\psi}_1 = \psi_1 / R_1$ can be approximated by a non-central Student's T-distribution with $N-2$ dof, [48] and the same non-centrality parameter τ_{CVD} defined for CFAR CVD with secondary data in eq. (3.43).

$$p_{\psi_1} \left(\hat{\psi}_1 / H_1 \right) = \frac{e^{-\tau_{CVD}^2/2}}{\sqrt{\pi(N-2)} \Gamma \left(\frac{N-2}{2} \right)} \quad (3.50)$$

$$\sum_{r=0}^{\infty} \frac{(\hat{\psi}_1 \tau_{CVD})^r}{r! (N-2)^{r/2}} \left(1 + \frac{\hat{\psi}_1^2}{N-2} \right)^{-\frac{N-2+r+1}{2}} 2^{r/2} \Gamma \left(\frac{N-2+r+1}{2} \right)$$

Figure 3.24 compare the test statistic histogram under hypothesis H_1 obtained from Monte Carlo simulation and the PDF defined in the eq. (3.50) for two different values of DNR and observation times (long, $7L$ and short, $1/2ML$) when the target is in the far field area, $S=0.085$.

Figure 3.25 reports similar results for a shorter baseline, namely getting close to near field for a far field parameter $S=0.76$. For all cases as for the CFAR CVD with secondary data is noted a good agreement between the simulated results and the PDF.

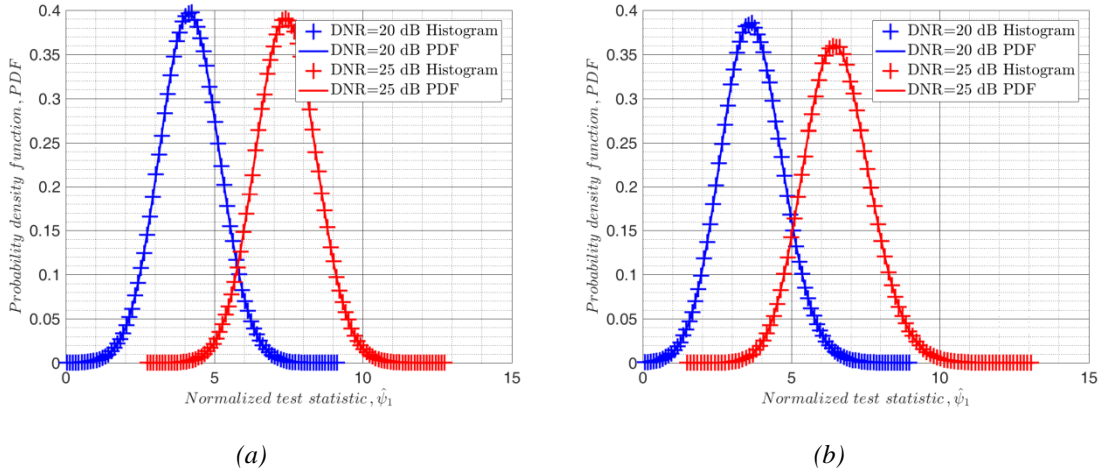


Figure 3.24 Histogram and PDF of the normalized test statistic $\hat{\psi}_1$ when $S=0.085$ and (a) for a long observation time, $7L$ and (b) short observation time, $1/2ML$.

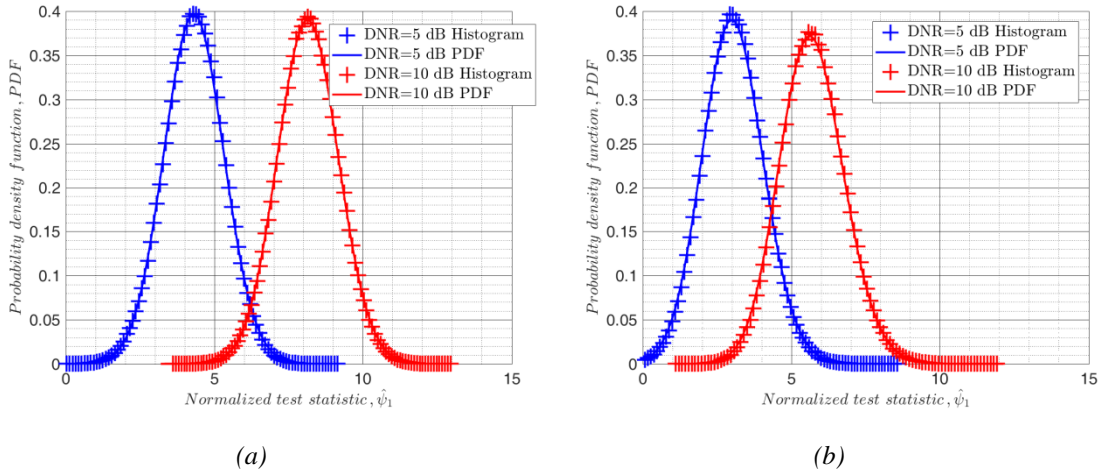


Figure 3.25 Histogram and PDF of the normalized test statistic $\hat{\psi}_1$ when $S=0.76$ and (a) for a long observation time, $7L$ and (b) short observation time, $1/2ML$.

The detection probability in accordance with the cumulative distribution function previously defined in Section 3.5.1 is written as:

$$P_d = 1 - nct_cdf\left(\frac{T''_{CVD}}{R_1}, N - 2, \tau_{CVD}\right) \quad (3.51)$$

Figure 3.26 shows the comparison between the analytical and simulated P_d of the CFAR CVD without secondary data for both reference scenarios and a complete agreement between the analytical and simulated results is noted that validates the proposed theoretical performance investigation.

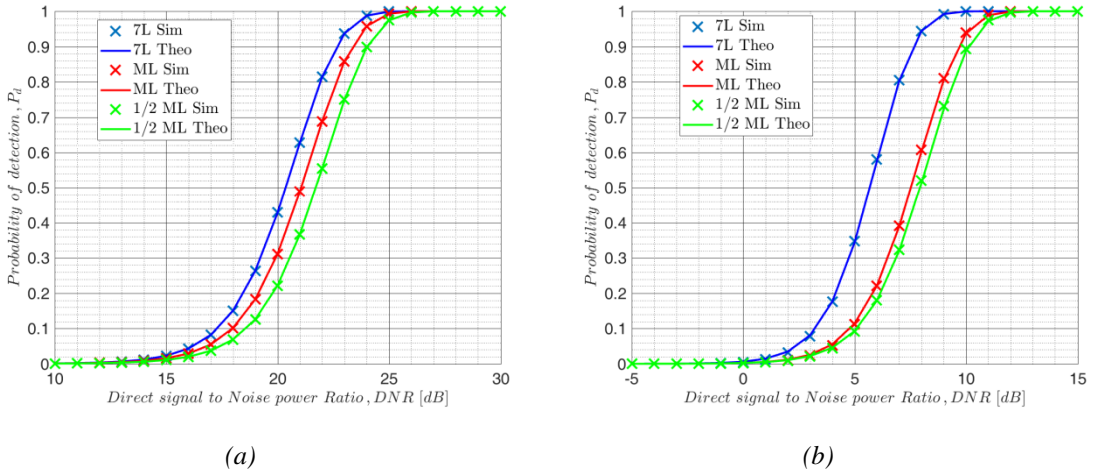


Figure 3.26 Simulated and theoretical P_d of CVD CFAR detector without secondary data for a $P_{fa}=10^{-5}$ when (a) $S=0.085$ and (b) $S=0.76$.

3.5.1 CFAR CVD comparison

By relying the theoretical performance of both CFAR CVD detectors with and without secondary data, the focus of this section is on the comparison of the performance with respect to the fixed threshold CVD in terms of probability of detection.

Figure 3.27 compares the theoretical P_d as a function of the DNR of the three detectors when the target is in the far field area, $S=0.085$ and for three different observation times. Again $K=16$ is assumed for the CFAR CVD with secondary data. Figure 3.28 reports similar results for a target getting close to the near field, $S=0.76$.

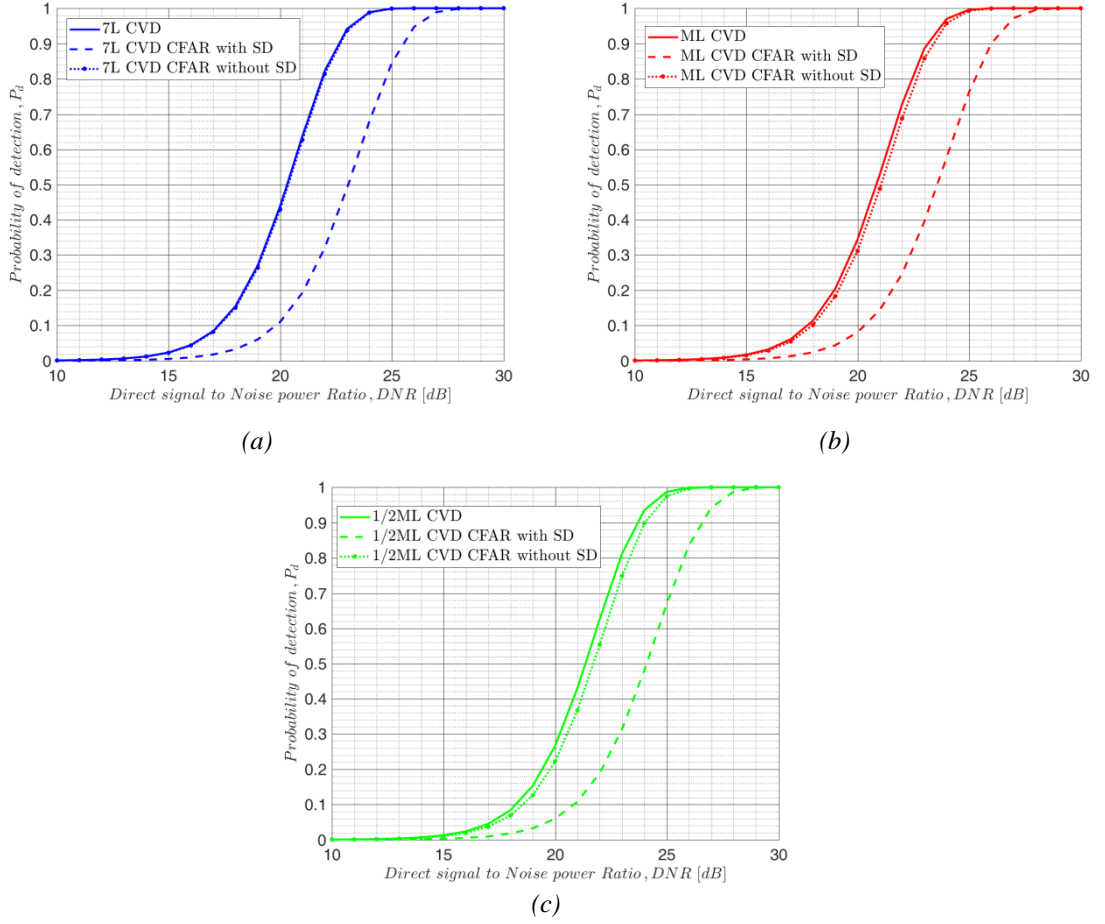
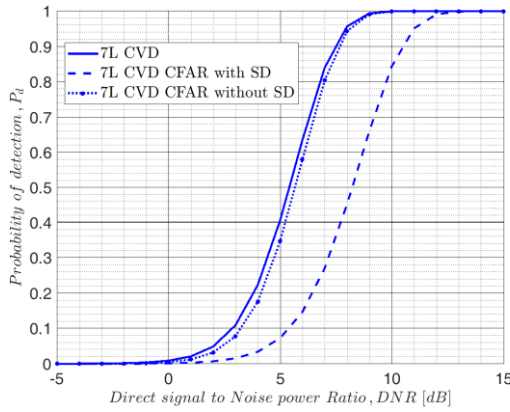


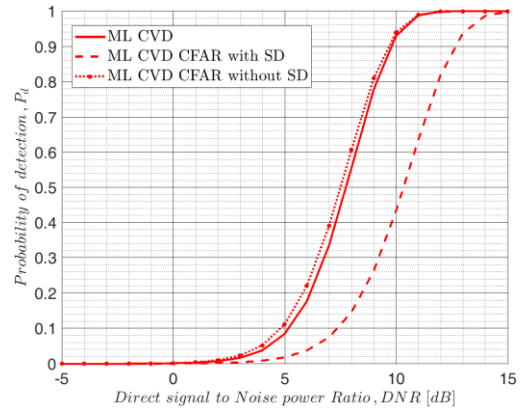
Figure 3.27 Theoretical P_d for a $P_{fa}=10^{-5}$ of the CVD detector compared to the CFAR CVD detector with $K=16$ and CFAR CVD without secondary data when $S=0.085$ and for (a) long observation time, 7L, (b) main lobe, ML and (c) short observation time, 1/2ML.

Some comments are in order. First, for the target in the deep far field (Figure 3.27) we observe that the CFAR CVD without secondary data presents performance close to that of the CVD with fixed threshold. In contrast, the CFAR CVD with $K=16$ experiences losses in the order of 3 dB to achieve the same detection performance. This can be explained by investigating the definition of decision statistic of CFAR CVD detector with and without secondary data in eq.(3.38) and eq. (3.45) respectively. It is apparent that the variance estimator in eq. (3.45) (i.e.: the term at the denominator) uses $N-2$ data ($N-2$ degrees of freedom) for the variance estimation, as two orthogonal projections of the primary data are performed before averaging. For the CFAR CVD with secondary data, even though $K \times N \times 1$ target-free vectors are considered, the variance estimator in eq. (3.38) (i.e. the term at the

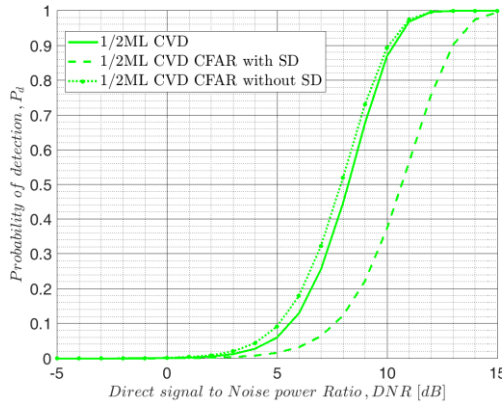
denominator) uses K data (K degrees of freedom) coinciding with the K outputs of the CVD detector applied to each of the K secondary vectors (see Figure 3.15). Since $N-2 \gg K$ a lower fluctuation on the variance estimation is experienced by the CFAR CVD without secondary data and therefore a smaller threshold is needed to guarantee the same P_{fa} , thus improving detection performance. Obviously if $K=N-2$ the P_d of the CFAR CVD detector with secondary data is expected to converge to the P_d of the CFAR CVD without secondary data.



(a)



(b)



(c)

Figure 3.28 Theoretical P_d for a $P_{fa}=10^{-5}$ of the CVD detector compared to the CFAR CVD detector with $K=16$ and CFAR CVD without secondary data when $S=0.76$ and for (a) long observation time, 7L, (b) main lobe, ML and (c) short observation time, 1/2ML.

The above considerations also apply for the target in the border between the far and near field, namely $S=0.76$ (Figure 3.28) with the difference that the P_d of the CFAR CVD without secondary data slightly outperforms the fixed threshold CVD for integration time smaller than 7L (Figure 3.28(b) and Figure 3.28 (c)). This behavior can be explained by recalling that an

estimator of the noise power is used to normalize the decision statistic of the CFAR CVD detector (i.e. the denominator term in the eq. (3.45)): such power changes when moving from hypothesis H_0 ($2\sigma_n^2|\alpha|^2$) to hypothesis H_1 (mean noise power over the integration interval $2\sigma_n^2\|\alpha + \beta \mathbf{s}_{t0}\|^2/N$) and, due to use of primary data only, this change affects the normalization factor. Additionally the fixed threshold CVD could be written similarly to the CFAR CVD with a normalization factor equal to the square root of the noise variance under hypothesis H_0 . In the border between far and near field, when very short (short than $1/2ML$) or very long integration times are involved, the power under H_1 is higher than or almost equal to that under H_0 . In contrast, for intermediate values of the integration time (i.e. ML and $1/2ML$), the reverse situation can occur. This particular situation implies that the decision threshold optimized to cope with the fluctuations of the estimator when primary data are constituted by direct signal and noise (so that a desired P_{fa} is achieved) will face fluctuations in a region characterized by lower values when primary data include also the target contribution (H_1). This causes the very slight outperformance. Obviously the disturbance variance changes from H_0 to H_1 also in the far field case but the considerable phase variation observed for all the values of the integration time (see Figure 3.4) prevents the occurrence of this unusual behavior. Concluding, we can state that both the CFAR CVD detectors provide performance close to the CVD with all parameters known.

Summary

In this chapter analytical expressions have been provided to fully characterize the detection performance of FSR radar based on the CVD. Both P_{fa} and P_d have been accurately approximated and validated by comparison to Monte Carlo simulations. This allows us to design a FSR that guarantees assigned detection performance. Moreover, two adaptive detection schemes have been proposed assuming: (i) the availability of target free secondary data and (ii) that some form of secondary data has to be extracted from the individual snapshot. Their performance has been fully characterized with both analytical and simulated analysis for both detection and false alarm probability and the desired CFAR propriety was demonstrated. The comparison of the detection performance shows limited losses of the CFAR detectors with respect to the fixed threshold CVD.

Chapter 4

GLRT-based techniques and performance analysis

This chapter introduces innovative detection schemes for FSR based on the GLRT for both cases, where a fixed threshold can be used and where a fully adaptive CFAR scheme is desired. The detection performance of the newly proposed detectors is characterized analytically and compared to the performance of the CVD scheme introduced in the previous chapter. This shows that the new detectors always outperform the standard FSR detector. In most cases the improvement has an upper bound of 3 dB, but there are specific cases where the standard FSR detector shows significant losses, while the new GLRT schemes suffer a much smaller degradation. Finally, simplified equivalent SNR expressions are introduced that relate the GLRT detection performance to the main parameters describing the FSR observation geometry and the target size and motion. These expressions are shown to be useful for the design of effective FSR geometries that guarantee desired detection performance for specific targets.

4.1 Introduction

Optimized detection schemes by exploiting the GLRT approach applied to the I & Q baseband components of the specific FSR signal model are devised. The forward scatter signal model exploited is the same introduced in Section 3.2 referring to a rectangular target large with respect to the wavelength and in the far field area of both transmitter and receiver. The performance of the obtained detectors is carefully investigated by providing a closed form characterization of the probabilities of false alarm and detection. This also provides analytical tools to predict the FSR detection performance of the new GLRT schemes as a function of the system parameters and of the target characteristics. The performance comparison of the newly derived detectors with the CVD and its CFAR version derived in the previous chapter shows that the GLRT schemes always outperform the CVD.

By analyzing the GLRT schemes and their performance, we notice that under some conditions, they may experience performance losses related to a small number of available independent samples. This yields in turn a coarse estimate of the parameters used inside the detector, thus degrading performance in terms of both false alarm and detection probability. Therefore, we derive a second set of GLRT detection schemes that also exploit secondary data that are target-free, but are assumed to share the same direct signal and noise power. We show that they further improve the performance especially in the cases where the CVD has its major losses. The obtained analytical performance expressions depend on equivalent SNR (Signal to Noise Ratio). By resorting to appropriate analytical approximations of the equivalent SNR, we propose simplified expressions that allow to easily relate the SNR to the main parameters encoding observation geometry, as well as target size and motion parameters. These measures are shown to be useful to design desired FSR operation geometries that are able to guarantee the desired detection performance against specified classes of targets.

Therefore we can summarize that in this chapter the issue of moving target detection against Additive White Gaussian Noise under the assumption that the target follows a linear trajectory is addressed through: (i) the development of advanced FSR detector schemes based on GLRT using both fixed threshold and CFAR threshold, (ii) by providing a performance analysis of the new detectors also in comparison with the standard scheme introduced in the Chapter 3 and (iii) by providing simplified equivalent SNR parameters which can be used for the design of effective FSR geometries.

4.2 GLRT-based detectors and performance analysis

In accordance with the Forward scatter received signal model introduced in Section 3.2, coherent detection strategies are derived based on the Maximum Likelihood criterion and under the assumption that the global target signature, $s_{t0}(t)$ define in eq. (3.3) of the rectangular target is known. Specifically, three GLRT-based detectors are derived indicated as:

- GLRT-1 with $\Omega = [\angle\beta]$
- GLRT-2 with $\Omega = [\alpha \ \beta]$ and
- GLRT-3 with $\Omega = [\alpha \ \beta \ \sigma_n^2]$

where the Ω vector collects the unknown parameters and then an analytical characterization of their performance is provided (Section 4.2.2). The consideration of a progressively increasing number of unknowns allows us to assess the impact on the performance of the different unknowns providing in this way a complete analysis. In particular we move from GLRT-1 detector which is an upper bound of any coherent detector in a FSR configuration to GLRT-3 detector which is independent on the noise power and the direct signal ensuring the constant false alarm rate condition.

The FSR geometry taken under investigation is the same of the Figure 3.1 and the detection problem consists of testing the null-hypothesis H_0 , i.e. absence of the target signal (the received signal is the sum of the direct signal and the noise component assumed AWGN with variance σ_n^2) versus the alternative hypothesis, H_1 , i.e. presence of the target signal as defined in the eq. (3.7).

4.2.1 GLRT-detectors

To deal with the unknown parameters we resort to the generalized likelihood ratio approach deriving the test:

$$\frac{\max_{\Omega} P_r(\mathbf{r}/H_1)}{\max_{\Omega} P_r(\mathbf{r}/H_0)} \geq T_{\Lambda} \quad (4.1)$$

where T_{Λ} is the threshold and $P_r(\mathbf{r}/H_0)$ and $P_r(\mathbf{r}/H_1)$ are the PDF of the received signal under hypothesis H_0 and H_1 respectively, (i.e. circular complex Gaussian distribution) defined in the eq. (3.8).

4.2.1.1 GLRT-1: Target signal phase unknown

The GLRT-1 provides an upper bound for the achievable detection performance being all signal parameters completely known, except for the target signal phase. The test statistic derived in Appendix C is:

$$x_1 = \left| \frac{\mathbf{s}_{t0}^H (\mathbf{r} - \alpha \mathbf{s}_{d0})}{\sqrt{\mathbf{s}_{t0}^H \mathbf{s}_{t0} \sigma_n}} \right| \underset{H_0}{\overset{H_1}{\geq}} \frac{(\sigma_n^2 \ln T_A + |\beta|^2 \|\mathbf{s}_{t0}\|^2)}{2|\beta| \sqrt{\|\mathbf{s}_{t0}\|^2} \sigma_n} = T_{GLRT1} \quad (4.2)$$

where $(\cdot)^H$ denotes the Hermitian operator, T_{GLRT1} is the new threshold to be set accordingly to the desired false alarm rate value, P_{fa} and the other signal parameters are defined in Section 3.2. We observe that GLRT-1 detector is equivalent to the cancellation of the direct contribution by simply subtracting it from the received signal followed by a filter matched to the global target signature, $\mathbf{s}_{t0}(t)$. Then the absolute value of the output of this filter is compared to the detection threshold, T_{GLRT1} as shown in Figure 4.1.

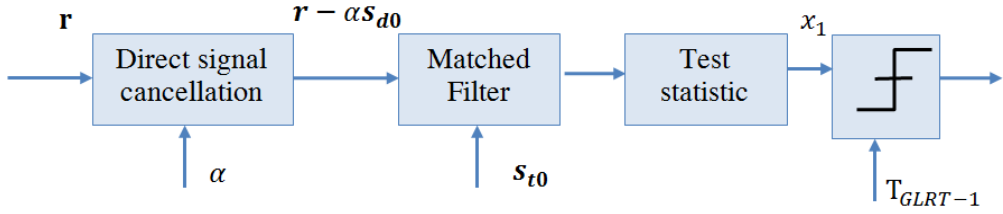


Figure 4.1 *GLRT-1 detector block diagram.*

Based on the signal model of the Section 3.2, $\mathbf{s}_{t0}^H (\mathbf{r} - \alpha \mathbf{s}_{d0}) / \sqrt{\mathbf{s}_{t0}^H \mathbf{s}_{t0} \sigma_n}$ is a circular complex Gaussian variate with zero-mean under hypothesis H_0 and with mean value equal to $\beta \sqrt{\mathbf{s}_{t0}^H \mathbf{s}_{t0}} / \sigma_n$ under the hypothesis H_1 and unit variance under both hypothesis. Therefore, the test statistic x_1 has a Rayleigh distribution under H_0 and a Rice distribution under H_1 :

$$\begin{cases} P_{x_1}(x_1/H_0) = 2x_1 e^{-x_1^2} \\ P_{x_1}(x_1/H_1) = 2x_1 e^{-\left(x_1^2 + \frac{|\beta|^2 \|\mathbf{s}_{t0}\|^2}{\sigma_n^2}\right)} I_0\left(2x_1 \frac{|\beta| \sqrt{\mathbf{s}_{t0}^H \mathbf{s}_{t0}}}{\sigma_n}\right) \end{cases} \quad (4.3)$$

where $I_0(\cdot)$ is the modified Bessel function of the first kind with order zero, [50].

4.2.1.2 *GLRT-2: Direct and target signal complex amplitudes unknown*

In this case it is assumed that only the noise power σ_n^2 is known. The direct signal is unknown and also the β parameter as far as depend on α (see Section 3.2). The test statistic is derived as (see Appendix C):

$$x_2 = \left| \frac{\tilde{\mathbf{s}}_{t0}^H \tilde{\mathbf{r}}}{\sqrt{\tilde{\mathbf{s}}_{t0}^H \tilde{\mathbf{s}}_{t0} \sigma_n}} \right| \begin{matrix} H_1 \\ \geq \sqrt{\ln T_A} = T_{GLRT2} \\ H_0 \end{matrix} \quad (4.4)$$

where $\tilde{\mathbf{r}} = \mathbf{P}_{s_d}^\perp \mathbf{r}$ and $\tilde{\mathbf{s}}_{t0} = \mathbf{P}_{s_d}^\perp \mathbf{s}_{t0}$ denotes the projection of the received signal and of the global target signature respectively onto the subspace orthogonal to the direct signal. $\mathbf{P}_{s_d}^\perp = \mathbf{I} - \frac{\mathbf{s}_{d0} \mathbf{s}_{d0}^H}{\|\mathbf{s}_{d0}\|^2}$ is a $N \times N$ symmetric and idempotent matrix representing the orthogonal projector onto the subspace of the direct signal, [47] and \mathbf{s}_{d0} is a $N \times 1$ column vector with all elements set to unity (see eq. (3.7)). We note that GLRT-2 detector is equivalent to the cancellation of the direct signal by projecting the received signal onto the subspace orthogonal to the direct component. The residual signal $\tilde{\mathbf{r}}$ is then passed through the filter matched to $\tilde{\mathbf{s}}_{t0}$, namely the global target signature projected onto the subspace orthogonal to the direct signal. Then the absolute value of the output is compared to the threshold T_{GLRT2} selected to guarantee the desired P_{fa} as shown in the Figure 4.2.

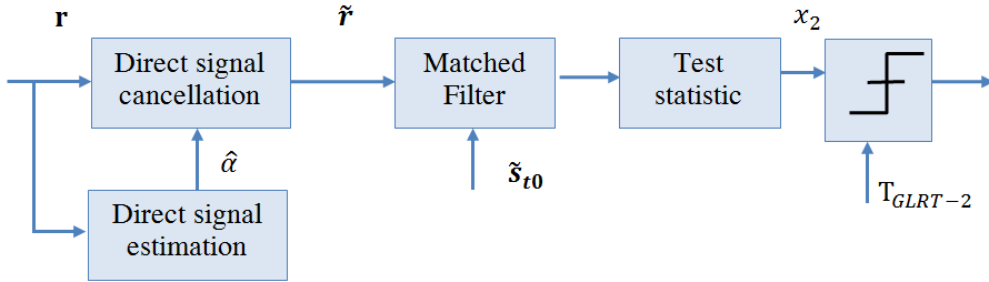


Figure 4.2 GLRT-2 detector block diagram.

Once more exploiting the proprieties of the Gaussian distribution of the received signal in eq. (3.8), $\tilde{\mathbf{s}}_{t0}^H \tilde{\mathbf{r}} / \sqrt{\tilde{\mathbf{s}}_{t0}^H \tilde{\mathbf{s}}_{t0} \sigma_n}$ is still a circular complex Gaussian variate with zero-mean value under hypothesis H_0 and mean value equal to $\beta \sqrt{\tilde{\mathbf{s}}_{t0}^H \tilde{\mathbf{s}}_{t0} / \sigma_n}$ under hypothesis H_1 and unit variance under both hypothesis. As previously, the test statistic x_2 has a Rayleigh distribution under H_0 and a Rice distribution under H_1 :

$$\begin{cases} P_{x_2}(x_2/H_0) = 2x_2 e^{-x_2^2} \\ P_{x_2}(x_2/H_1) = 2x_2 e^{-\left(x_2^2 + \frac{|\beta|^2 \|\tilde{\mathbf{s}}_{t0}\|^2}{\sigma_n^2}\right)} I_0\left(2x_2 \frac{|\beta| \sqrt{\tilde{\mathbf{s}}_{t0}^H \tilde{\mathbf{s}}_{t0}}}{\sigma_n}\right) \end{cases} \quad (4.5)$$

4.2.1.3 GLRT-3: All parameters unknown

The aim now is to define a GLRT detector with the direct signal, the β parameter and the noise power, unknown, [51]. The test statistic of GLRT-3 detector is derived by maximizing the PDF in eq. (3.8) with respect to these parameters and is written as follows (see Appendix C):

$$x_3 = \left[\frac{\|\tilde{\mathbf{r}}\|^2}{\|\mathbf{P}_{\tilde{\mathbf{s}}_{t0}}^\perp \tilde{\mathbf{r}}\|^2} \right]^N \begin{matrix} H_1 \\ \geq T_\Lambda \\ H_0 \end{matrix} \quad (4.6)$$

$$x_3 = (N - 2) \frac{\|\mathbf{P}_{\tilde{\mathbf{s}}_{t0}} \tilde{\mathbf{r}}\|^2}{\|\mathbf{P}_{\tilde{\mathbf{s}}_{t0}}^\perp \tilde{\mathbf{r}}\|^2} \begin{matrix} H_1 \\ \geq (N - 2) (T_\Lambda^{1/N} - 1) \\ H_0 \end{matrix} = T_{GLRT3} \quad (4.7)$$

Two orthogonal projections of the received signal are performed: (i) first onto the subspace orthogonal to the direct signal, $\tilde{\mathbf{r}} = \mathbf{P}_{\mathbf{s}_d}^\perp \mathbf{r}$ and (ii) after onto the subspace orthogonal to $\tilde{\mathbf{s}}_{t0}$, $\mathbf{P}_{\tilde{\mathbf{s}}_{t0}}^\perp \tilde{\mathbf{r}}$ being $\mathbf{P}_{\tilde{\mathbf{s}}_{t0}}^\perp = \mathbf{I} - \frac{\tilde{\mathbf{s}}_{t0} \tilde{\mathbf{s}}_{t0}^H}{\|\tilde{\mathbf{s}}_{t0}\|^2}$ $N \times N$ symmetric and idempotent matrix, [47]. Meanwhile, $\mathbf{P}_{\tilde{\mathbf{s}}_{t0}} = \frac{\tilde{\mathbf{s}}_{t0} \tilde{\mathbf{s}}_{t0}^H}{\|\tilde{\mathbf{s}}_{t0}\|^2}$ define the projector onto the subspace of the $\tilde{\mathbf{s}}_{t0}$ which in turn is orthogonal to the subspace of the direct signal. T_{GLRT3} is the new decision threshold selected such that the P_{fa} equals an assigned value.

In Figure 4.3 is sketched the block diagram of the GLRT-3 detector in accordance with the test statistic defined in eq. (4.6).

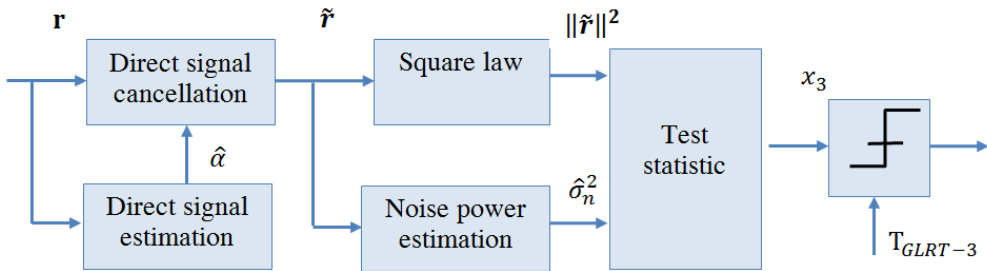


Figure 4.3 GLRT-3 detector block diagram.

As proven in Appendix C it is possible to rewrite the test statistic, x_3 as:

$$x_3 = \frac{x_2^2/2}{\frac{\sum_{k=1}^{N-2} |\tilde{n}_k|^2}{2(N-2)\sigma_n^2}} \underset{H_0}{\overset{H_1}{\geq}} T_{GLRT3} \quad (4.8)$$

This mean that the GLRT-3 detector is obtained by normalizing the squared of the GLRT-2 test statistic defined in eq. (4.4) with a suitable noise variance estimator based on the received signal orthogonally projected in order to remove the contribution of the direct and of the target signal.

Therefore exploiting the definition of a non-central F-distribution, [51] the test statistic x_3 under hypothesis H_0 has a central F-distribution with 2 and $2(N-2)$ degree of freedom and under hypothesis H_1 has a non-central F-distribution with the same dof as in the null-hypothesis and non-central parameter $\tau_{GLRT-3} = \frac{2|\beta|^2 s_{t0}^H \tilde{s}_{t0}}{\sigma_n^2}$ where in eq. (4.9), $B(x,y)$ denotes the beta function, [50].

$$\begin{cases} P_{x_3}(x_3/H_0) = \frac{1}{B(N-2,1)} \frac{x_3(N-2)^{N-2}}{(N-2+x_3)^{N-1}} \\ P_{x_3}(x_3/H_1) = \sum_{k=0}^{\infty} \frac{e^{-\frac{\tau_{GLRT-3}^2}{2}} \left(\frac{\tau_{GLRT-3}^2}{2}\right)^k x_3^k (N-2)^{N-2}}{k! B(N-2, k+1) (N-2+x_3)^{N-1+k}} \end{cases} \quad (4.9)$$

4.2.2 Performance analysis

This section focuses on the analytical characterization of the performance of the GLRT-based detectors in terms of probability of false alarm and probability of detection. Specifically the analytical expressions of the P_{fa} as function of the decision threshold and of the P_d as function of the target signal-to-noise power ratio (SNR) are derived using the PDFs introduced in Section 4.2.1. In Chapter 3 the correctness of the theoretical expression of the CVD and CFAR-CVD detectors needed to be validated as all our analytical formulations are obtained by approximating the exact PDFs of the test statistics, under both P_{fa} and P_d conditions. The approximations of the PDFs were carefully selected in order to allow us to obtain analytical expressions for the detection performance (P_{fa} and P_d). For this reason also a comparison of the

histograms of the test statistics obtained through Monte Carlo simulations based on the exact PDF with the derived approximated PDF expressions was shown. Meanwhile for the GLRT-based detectors the analytical formulations of the P_{fa} and of the P_d derived from the exact expressions of the PDF are verified by comparing them to simulated results without investigating the agreement between the analytical expressions of the PDFs and the simulated PDFs.

The test statistic of GLRT-1 and GLRT-2 detectors under hypothesis H_0 have a Rayleigh distribution (see eq. (4.3) and eq. (4.5)) and as a consequence the P_{fa} is written as:

$$P_{fa}|_{GLRT_i} = e^{-T_{GLRT_i}} \quad (4.10)$$

where $i=1,2$.

Under hypothesis H_1 the test statistics have a Rice distribution (see eq. (4.3) and eq. (4.5)), therefore the P_d is expressed by the Marcum function, $Q_M(\cdot)$:

$$P_d|_{GLRT_i} = Q_M\left(\sqrt{2SNR_{GLRT_i}}, \sqrt{2 \ln P_{fa}|_{GLRT_i}}^{-1}\right) \quad (4.11)$$

where SNR_{GLRT_i} is the target signal-to-noise power ratio of GLRT-i respectively defined as:

$$SNR_{GLRT1} = \frac{|\beta|^2 \mathbf{s}_{t0}^H \mathbf{s}_{t0}}{\sigma_n^2} \quad (4.12)$$

$$SNR_{GLRT2} = \frac{|\beta|^2 \tilde{\mathbf{s}}_{t0}^H \tilde{\mathbf{s}}_{t0}}{\sigma_n^2} \quad (4.13)$$

Recall that $\beta \mathbf{s}_{t0}$ represents the signal scattered by the target and $\beta \tilde{\mathbf{s}}_{t0}$ represents the received target signal projected onto the subspace orthogonal to the direct component.

For the GLRT-3 detector the P_{fa} and the P_d are obtained from the cumulative F-distribution and the cumulative non-central F-distribution respectively,[52]:

$$P_{fa}|_{GLRT_3} = \left[\frac{1}{1 + T_{GLRT3}/(N-2)} \right]^{N-2} \quad (4.14)$$

$$P_d|_{GLRT_3} = 1 - \sum_{j=0}^{\infty} \frac{\left(\frac{\tau_{GLRT-3}^2}{2}\right)^j e^{-\frac{\tau_{GLRT-3}^2}{2}}}{j!} \frac{B(1 - P_{fa|GLRT_3}^{1/N-2}, 1 + j, N - 2)}{B(1 + j, N - 2)} \quad (4.15)$$

where $B(x, a, b)$ is the incomplete beta function, [50]. From (4.14) it is clear that no prior knowledge of any unknown parameters is required to set the decision threshold needed in order to achieve a given P_{fa} level thus assuring the achievement of the CFAR property. It is also noted that the non-central parameter τ_{GLRT-3} depends on the SNR_{GLRT2} , $\tau_{GLRT-3} = 2SNR_{GLRT2}$.

The theoretical performances of the three GLRT-based detectors are compared in the following to results from Monte-Carlo simulations. The simulated results are obtained by generating 10^7 (10^5) independent realizations of the received signal under hypothesis H_0 (under hypothesis H_1) in agreement with the model described in Section 3.2 and by processing such samples according to the detection techniques reported above. The same reference scenarios of the Section 3.3 are taken as references in this analysis, namely: when the target is in the deep far field area, $S=0.085$ and when the target is approaching the transition between the near and the far field, $S=0.76$ (see Table 3.1 for the System and target parameters). For both scenarios we assume the target crosses the baseline perpendicularly in the middle.

Figure 4.4 compares the theoretical expressions of the Pfa of the GLRT-1 and GLRT-2 detectors defined in the eq. (4.10) as function of the threshold, T_{GLRTi} for $i=1,2$ with the simulated results for a long and a short observation time when the target in the deep far field area, $S=0.085$. Meanwhile Figure 4.5 reports similar results for a target getting close to the near field, $S=0.76$.

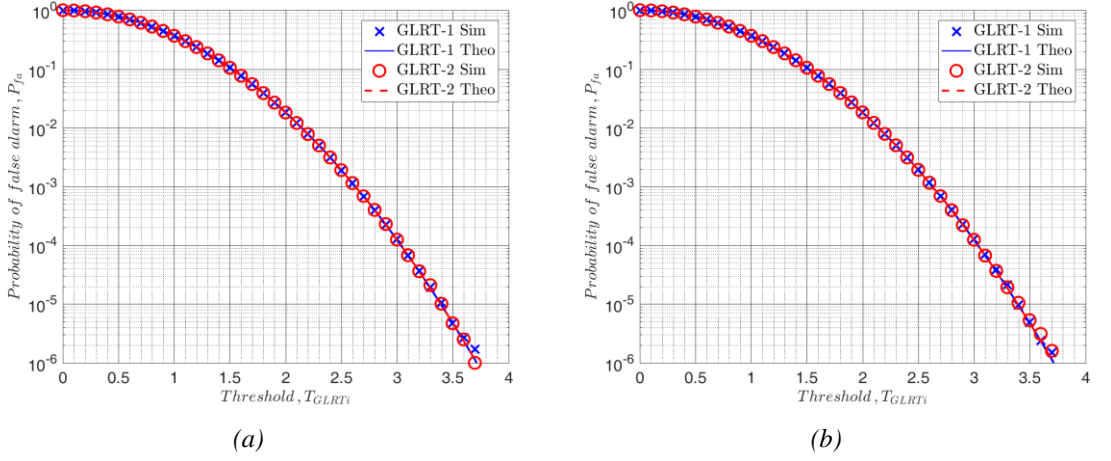


Figure 4.4 Simulated and theoretical P_{fa} of GLRT-1 and GLRT-2 detectors as function of T_{GLRTi} for $i=1,2$ when $S=0.085$ and for (a) long observation time, $7L$ and (b) for a short observation time, $1/2ML$.

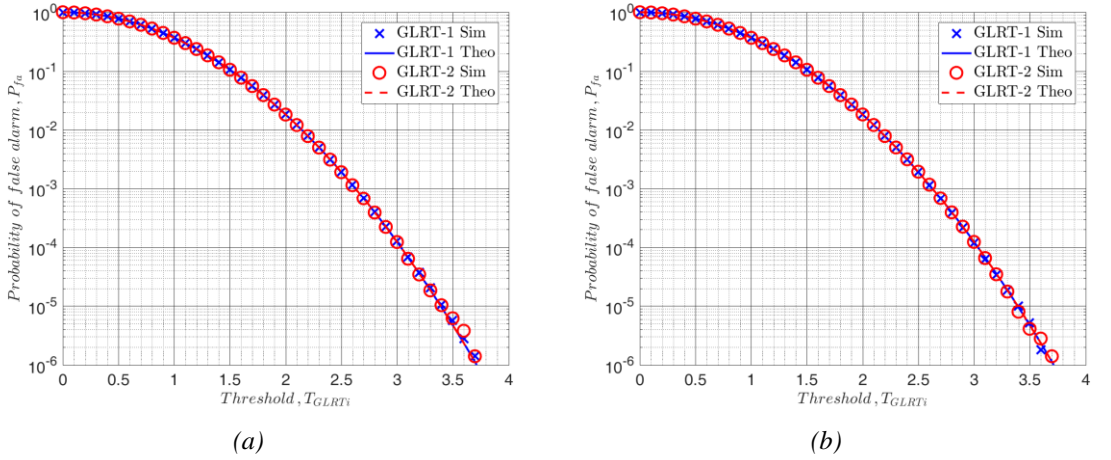


Figure 4.5 Simulated and theoretical P_{fa} of GLRT-1 and GLRT-2 detectors as function of T_{GLRTi} for $i=1,2$ when $S=0.76$ and for (a) long observation time, $7L$ and (b) for a short observation time, $1/2ML$.

It is apparent that for both scenarios the simulated results are in agreement with the theoretical expressions of the P_{fa} .

Figure 4.6 compare the theoretical expression of the P_{fa} of the CFAR coherent detector (GLRT-3) with the simulated results for short and long observation time for both reference scenarios (i.e. $S=0.085$, sub-figure (a) and $S=0.76$ sub-figure (b)).

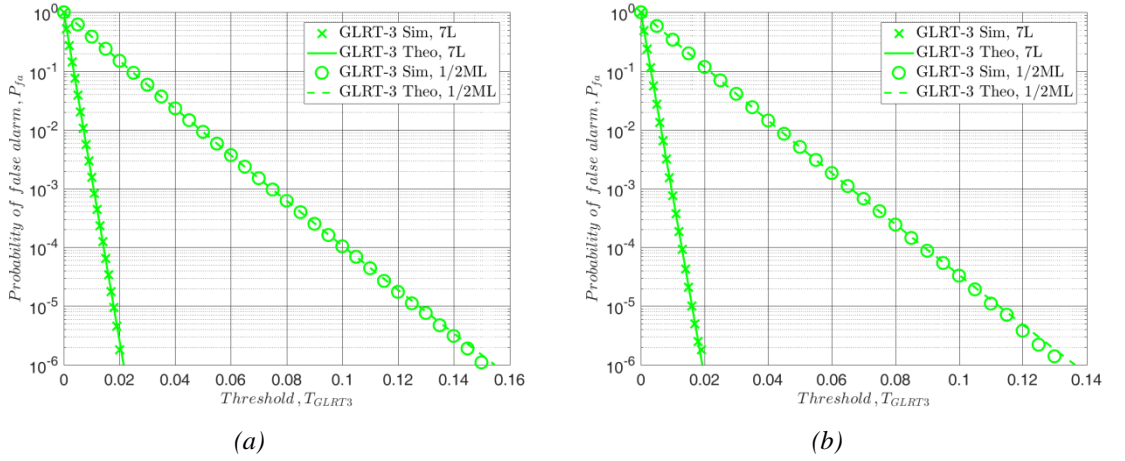


Figure 4.6 Simulated and theoretical P_{fa} of GLRT-3 detector as function of T_{GLRT3} (a) for $S=0.085$, 7L and (b) for $S=0.76$.

Once more a perfect agreement is achieved. Furthermore, as expected for a long integration time a lower fluctuation of on the variance estimation is experienced by the CFAR detector and therefore a smaller threshold is needed to guarantee the same P_{fa} .

As the detection performance of the coherent detection techniques does not depend on the receiver bandwidth, B the probability of detection is evaluated as a function of the DNSR (Direct signal to Noise Spectral Density ratio) defined in eq. (3.5). The results of the P_d in the following are achieved having set a $P_{fa} = 10^{-5}$. In general the comparison of the performance of different detectors is carried out assessing the losses which are defined as the incremental $DNSR$ necessary to achieve the same performance, in our case $P_{fa} = 10^{-5}$ and $P_d = 0.9$.

Figure 4.7 shows the theoretical and simulated results of the P_d of the three GLRT detectors when the target is in the deep far field, $S=0.085$ for three observation times as defined in Table 3.1, i.e. long observation time (7L, blue curve in Figure 3.4), only the main lobe (ML, red curve in Figure 3.4) and a small observation time (1/2ML, green curve in Figure 3.4). It is apparent that the simulated results are in perfect agreement with the results from the theoretical analysis.

Likewise, Figure 4.8 compares the closed form expression of the P_d of the three GLRT detectors as function of the DNSR to the results of Monte Carlo simulations when the target is approaching the near field, $S=0.76$: again an excellent agreement is observed.

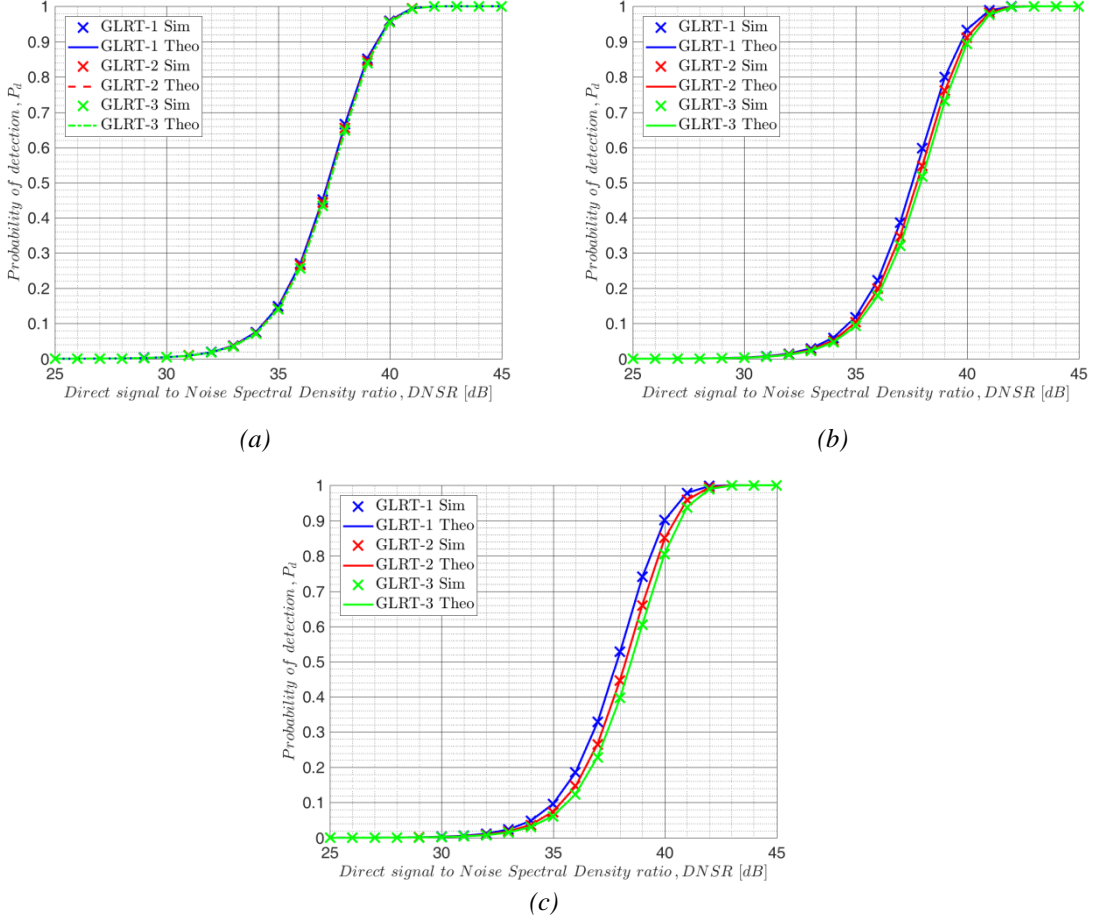


Figure 4.7 Theoretical and simulated P_d for a $P_{fa}=10^{-5}$ when $S=0.085$ (a) for a long observation time, $7L$, (b) only main lobe, ML and (c) for a short observation, $1/2 ML$.

It is noted that when the target is in the far field area (Figure 4.7) the performance of GLRT-2 with direct signal unknown and of GLRT-3 with a CFAR behavior are close to the optimal detector GLRT-1 even for small observation time (i.e. $1/2ML$, Figure 4.7 (c)). This is because the target is in the deep far field area; namely the target is well separated from the direct component assumed constant even for short observation time due to fast variation of its Doppler signature, as it is shown in Figure 3.4 (b).

Also, from Figure 4.8 we note that the GLRT-2 and GLRT-3 detectors present performance close to that of the optimal detector (GLRT-1) when a long integration time (i.e. $7L$) is processed and losses in the order of 3dB for an integration time equal to the main lobe. In contrast, differently from the deep far field condition, they need a considerably higher DNSR

(i.e. 7 dB) to obtain the same performance of the GLRT-1 when short integration time (i.e. $1/2ML$) is involved.

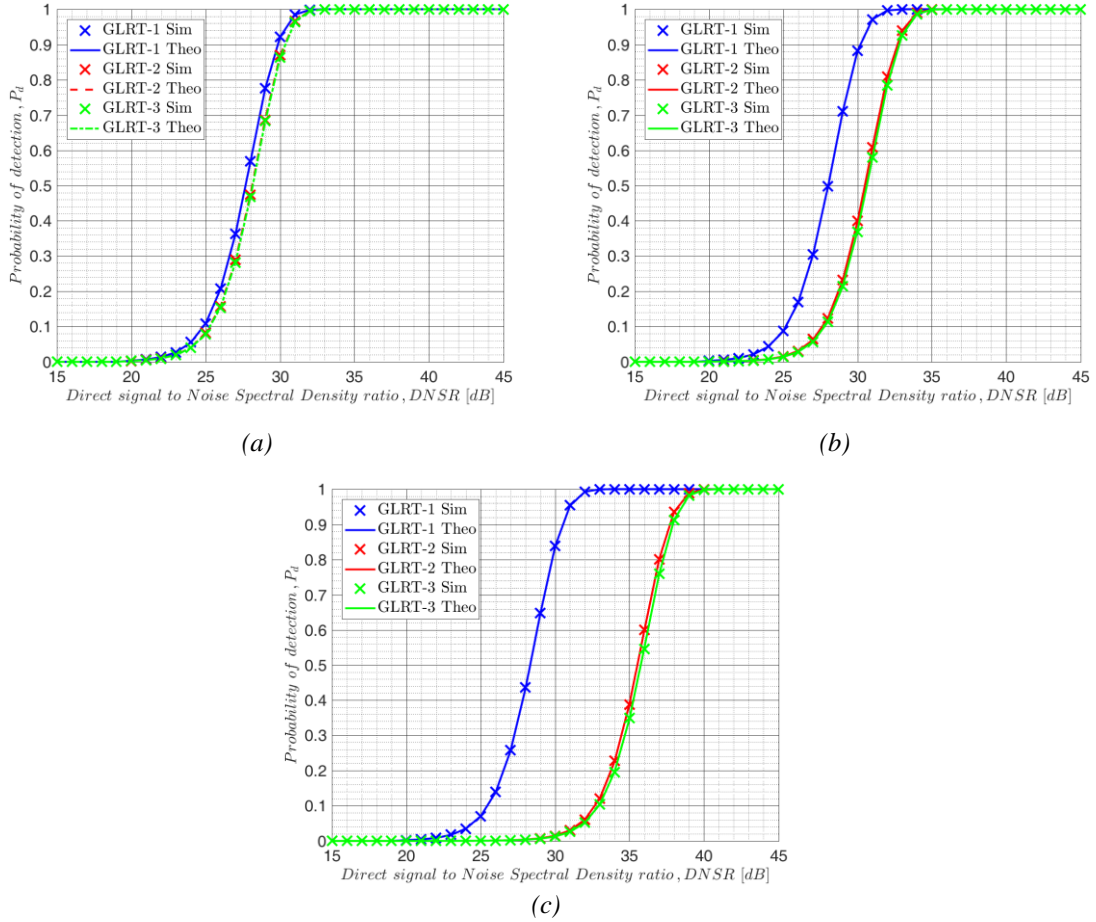


Figure 4.8 Theoretical and simulated P_d for a $P_{fa}=10^{-5}$ when $S=0.76$ (a) for a long observation time, $7L$, (b) only main lobe, ML and (c) for a short observation, $1/2 ML$

This can be easily explained by observing that the target signature shows less Doppler variation when the target is closer to the near field region (see Figure 3.5). While the optimum detector GLRT-1 perfectly removes the direct signal without affecting the target contribution, GLRT-2 and GLRT-3 detectors for small integration time intervals may delete the target signal as it is approximately constant and therefore similar to the direct signal. The results also demonstrate that the GLRT-3 detector that ensures the CFAR condition presents performance close to the GLRT-2 detector.

4.3 Performance comparison with CVD and CFAR CVD

In the previous Chapter we have provided analytical closed-form expressions for the detection performance of the CVD and CFAR CVD scheme. Despite this is widely used, [10],[8] and is considered to provide generally good detection performance, it is interesting to assess how far their performance are from the coherent strategies based on the GLRT approach previously developed.

The theoretical P_d of the CVD defined in the eq. (3.35) is compared to the P_d achieved by means of the coherent detector GLRT-2 (see eq. (4.11)) in Figure 4.9 for the same reference scenarios, i.e. for a target in the deep far field area, $S=0.085$, and for a target getting close to the near field, $S=0.76$. Both detectors GLRT-2 and CVD estimate the unknown direct signal in the acquisition window and remove its contribution through an orthogonal projector; the GLRT-2 through the projection of the received signal meanwhile the CVD through the projection of the signal at the output of the square law detector.

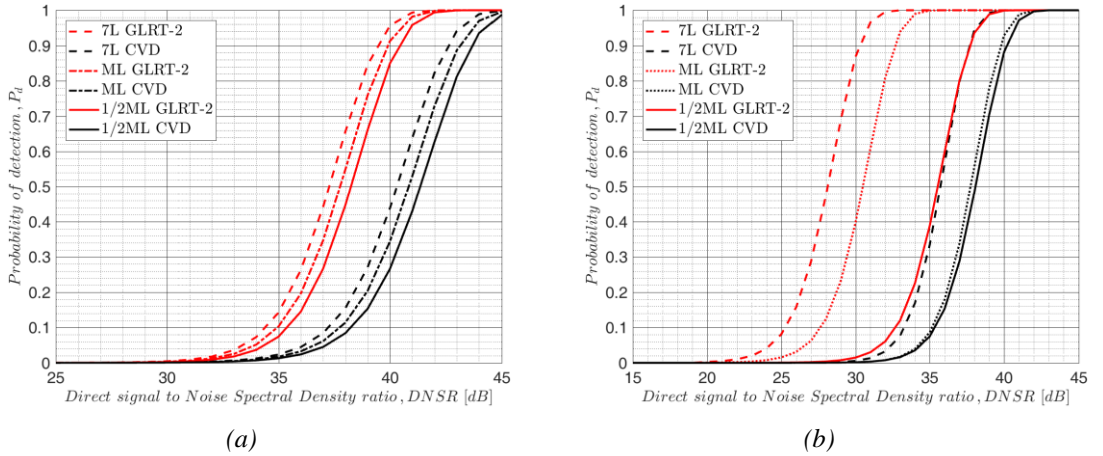


Figure 4.9 Theoretical P_d of the GLRT-2 detector and CVD detector for different observation times and for a $P_{fa}=10^{-5}$ (a) when the target is in the deep far field area, $S=0.085$ and (b) when the target is getting close to the near field, $S=0.76$.

It can be observed that for a target in the deep far field area (Figure 4.9 (a)) the CVD presents limited losses (i.e. around 3dB) with respect to the GLRT-2 even for a small integration time, $1/2ML$ (continuous black and red curves). This is because, as already explained above, the signature of a target in the deep far field shows a fast variation of its Doppler signature (Figure 3.4 (b)) so that it is easy to separate it from the direct component, even by the CVD that only operates on the signal squared modulus. This corresponds to the use of a DC removal filter having a notch considerably narrower of the target Doppler bandwidth, thus successfully allowing the discrimination between the direct and the target signal.

In contrast, when the target is getting close to the near field (Figure 4.9 (b)), the CVD presents higher losses (in the order of 7 dB) with respect to the GLRT-2 detector for processing intervals greater than the main lobe.

Moving to small observation intervals, the CVD approaches the GLRT-2 detector with limited losses (i.e. around 3 dB). This is because for long observation times the GLRT-2 can still separate the target component from the direct component even though less Doppler variation is appreciated with respect to the deep far field scenario (see Figure 3.5 (b)) whereas the squared modulus used by the CVD might strongly affect the target signature making the separation between the two components unfeasible.

Meanwhile the GLRT-3 and CFAR CVD without secondary data detectors estimate and remove the unknown direct signal and the unknown noise power. As previously, the GLRT-3 detector removes the direct signal through the projection of the received signal and the CFAR CVD without secondary data through the projection of the signal at the output of the square law detector. Both detectors establish suitable noise variance estimators through two orthogonal projection in order to remove also the target signal contribution: the GLRT-3 detector through the projection of $\tilde{\mathbf{r}}$ into the subspace orthogonal of the target signal and the CFAR CVD without secondary data through the projection of the signal at the output of the DC removal filter into the subspace orthogonal to $\boldsymbol{\eta} = \mathbf{P}^\perp \mathbf{h}$ (i.e. the impulse response of the matched filter orthogonal projected onto the subspace of the DC component) as defined in Section 3.4.1.

Figure 4.10 compares the theoretical P_d of the CFAR CVD without secondary data defined in Section 3.5.2 and the GLRT-3 detector for the same reference scenarios and the above considerations still apply.

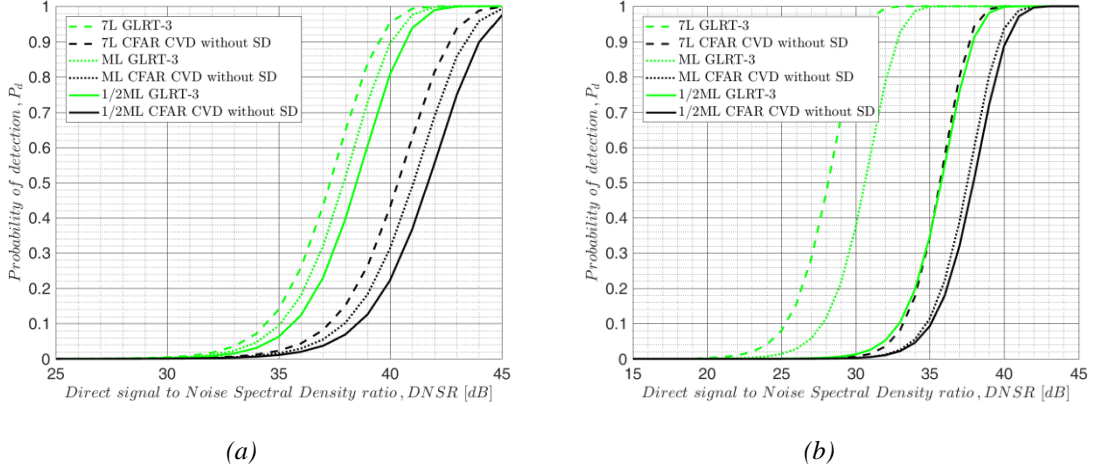


Figure 4.10 Theoretical P_d of the GLRT-3 detector and CFAR CVD without secondary data detector for different observation times and for a $P_{fa}=10^{-5}$ (a) when the target is in the deep far field area, $S=0.085b$ and (b) when the target is getting close to the near field, $S=0.76$.

4.4 GLRT-based detectors with secondary data and performance analysis

As considerable losses are experienced from the sub-optimum GLRT detectors (i.e. GLRT-2 and GLRT-3) for short observation time, 1/2ML and when the target approaches the transition between far and near field, we extend them considering the possibility to have a set of secondary data assumed to be target free. The new detectors with secondary data are derived in Section 4.4.1 and the corresponding detection performance analyzed in Section 4.4.2.

4.4.1 GLRT-detectors with secondary data

The secondary data are assumed to contain direct signal and noise component, independent of and identically distributed as the primary data under H_0 :

$$\mathbf{r}' = \alpha \mathbf{s}'_{d0} + \mathbf{n}' \quad (4.16)$$

where \mathbf{r}' and \mathbf{n}' are $M \times 1$ column vectors collecting the samples respectively of the secondary data and of the noise contribution in the secondary data meanwhile \mathbf{s}'_{d0} is $M \times 1$ column vector

with all elements set to unity. Under this assumption the PDF of the secondary data is the same of the primary data under the null-hypothesis, circular complex Gaussian distribution with mean vector equal to $\alpha \mathbf{s}'_{d0}$ and variance σ_n^2 .

The joint PDF of all the input data under the hypothesis H_0 and H_1 are given by the product as follows:

$$P_r(\mathbf{r}/H_0) P_{r'}(\mathbf{r}'/H_0) = \frac{1}{\pi^{N+M} \sigma_n^{2(N+M)}} e^{-\frac{1}{\sigma_n^2} [\|\mathbf{r} - \alpha \mathbf{s}_{d0}\|^2 + \|\mathbf{r}' - \alpha \mathbf{s}'_{d0}\|^2]} \quad (4.17)$$

$$P_r(\mathbf{r}/H_1) P_{r'}(\mathbf{r}'/H_0) = \frac{1}{\pi^{N+M} \sigma_n^{2(N+M)}} e^{-\frac{1}{\sigma_n^2} [\|\mathbf{r} - \alpha \mathbf{s}_{d0} - \beta \mathbf{s}_{t0}\|^2 + \|\mathbf{r}' - \alpha \mathbf{s}'_{d0}\|^2]} \quad (4.18)$$

As previously, the GRLT in agreement with the eq. (4.17) and eq. (4.18) now is written as:

$$\frac{\max_{\Omega} \{P_r(\mathbf{r}/H_1) P_{r'}(\mathbf{r}'/H_0)\}}{\max_{\Omega} \{P_r(\mathbf{r}/H_0) P_{r'}(\mathbf{r}'/H_0)\}} \underset{H_0}{\geq} T'_\Lambda \quad (4.19)$$

where, as before, $\Omega = [\alpha \beta]$ for GLRT-2 detector and $\Omega = [\alpha \beta \sigma_n^2]$ for GLRT-3 detector, meanwhile T'_Λ is the threshold.

4.4.1.1 GLRT-2 with secondary data

The derivation of the test statistic obtained by substituting the Maximum Likelihood Estimation (MLE) of the unknown parameters under the two hypotheses in eq.(4.17) and eq. (4.18) is reported in the Appendix D and is defined as:

$$x'_2 = \left| \frac{\mathbf{s}_{t0}^H \left[\mathbf{r} - \frac{\mathbf{s}_{d0} (\mathbf{s}_{d0}^H \mathbf{r} + \mathbf{s}_{d0}'^H \mathbf{r}')}{\|\mathbf{s}_{d0}\|^2 + \|\mathbf{s}_{d0}'\|^2} \right]}{\sigma_n \sqrt{\left(\|\mathbf{s}_{t0}\|^2 - \frac{|\mathbf{s}_{d0}^H \mathbf{s}_{t0}|^2}{\|\mathbf{s}_{d0}\|^2 + \|\mathbf{s}_{d0}'\|^2} \right)}} \right| \underset{H_0}{\geq} \sqrt{\ln T'_\Lambda} = T'_{GLRT2} \quad (4.20)$$

It is clear from eq.(4.20) that in absence of secondary data the test statistic in eq. (4.4) is obtained.

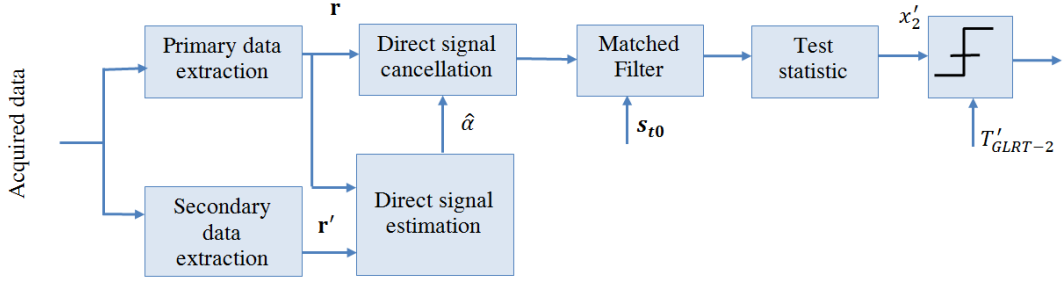


Figure 4.11 *GLRT-2 with secondary data block diagram.*

Aiming at a practical application of the proposed scheme, the secondary data are selected from the previous and successive temporal frames with respect to the frame under test (i.e. representative of the primary data, \mathbf{r}) as shown in the Figure 4.11: in such secondary frames, \mathbf{r}' the target signal component is weak and therefore could be considered negligible. The direct signal is removed from the primary data after its estimation exploiting both the primary and the secondary data followed by a filter matched to the global target signature, $s_{t0}(t)$.

Exploiting the proprieties of the Gaussian distribution it is easy to verify that the term inside the linear envelope detector in eq. (4.20) is a complex Gaussian variate with zero-mean value under hypothesis H_0 and mean value equal to $\frac{\beta}{\sigma_n} \sqrt{\left(\|\mathbf{s}_{t0}\|^2 - |\mathbf{s}_{d0}^H \mathbf{s}_{t0}|^2 / (\|\mathbf{s}_{d0}\|^2 + \|\mathbf{s}'_{d0}\|^2)\right)}$ under hypothesis H_1 and unit variance under both hypothesis. Therefore the test statistic x'_2 has a Rayleigh distribution under hypothesis H_0 and a Rice distribution under hypothesis H_1 :

$$\begin{cases} P_{x'_2}(x'_2/H_0) = 2x'_2 e^{-x'^2_2} \\ P_{x'_2}(x'_2/H_1) = 2x'_2 e^{-\left[x'^2_2 + \frac{|\beta|^2}{\sigma_n^2} \left(\|\mathbf{s}_{t0}\|^2 - \frac{|\mathbf{s}_{d0}^H \mathbf{s}_{t0}|^2}{\|\mathbf{s}_{d0}\|^2 + \|\mathbf{s}'_{d0}\|^2} \right) \right]} I_0 \left(2x'_2 \frac{|\beta|}{\sigma_n} \sqrt{\|\mathbf{s}_{t0}\|^2 - \frac{|\mathbf{s}_{d0}^H \mathbf{s}_{t0}|^2}{\|\mathbf{s}_{d0}\|^2 + \|\mathbf{s}'_{d0}\|^2}} \right) \end{cases} \quad (4.21)$$

4.4.1.2 *GLRT-3 with secondary data*

As above, the GLRT-3 with secondary data is derived by maximizing the likelihood function in eq. (4.19) with respect to the unknown parameters and by exploiting the definition of the non-central F distribution, [51] (see Appendix D):

$$x'_3 = \frac{x_2'^2/2}{w/(2(N+M-2))} \underset{H_0}{\overset{H_1}{\geq}} (N+M-2) \left(1 - \frac{1}{T_A'^{1/(N+M)}} \right) = T_{GLRT3}' \quad (4.22)$$

where x'_2 is defined in eq. (4.22) and w is defined in eq. (D.7) of the Appendix D.

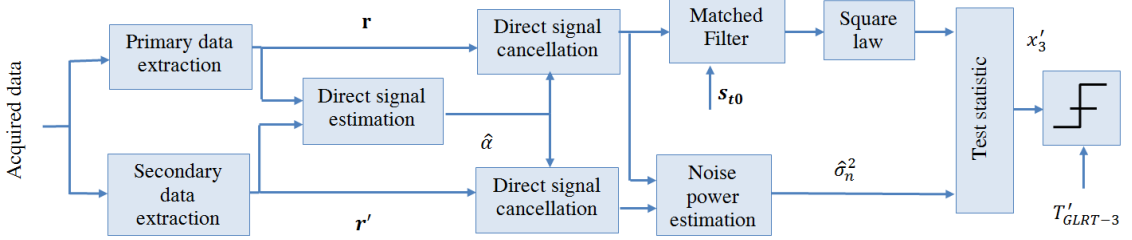


Figure 4.12 GLRT-3 with secondary data block diagram.

As previously for the GLRT-2 detector, the secondary data, \mathbf{r}' are selected from the previous and successive temporal frames with respect to the frame under test, representative of the primary data, \mathbf{r} and both are exploited for the estimation and the cancellation of the direct signal and after for the estimation of the noise variance, as shown in Figure 4.12. The test statistic, x'_3 under the null-hypothesis has central F-distribution with 2 and $2(N+M-2)$ dof and under the alternative hypothesis a non-central F-distribution with the same dof and with a non-

central parameter equal to $\tau'_{GLRT-3} = \frac{2|\beta|^2}{\sigma_n^2} \left(\|\mathbf{s}_{t0}\|^2 - \frac{|\mathbf{s}_{d0}^H \mathbf{s}_{t0}|^2}{\|\mathbf{s}_{d0}\|^2 + \|\mathbf{s}'_{d0}\|^2} \right) :$

$$\left\{ \begin{array}{l} P_{x'_3} \left(x'_3 / H_0 \right) = \frac{1}{B(N+M-2, 1)} \frac{x'_3 (N+M-2)^{N+M-2}}{(N-2+x'_3)^{N+M-1}} \\ P_{x'_3} \left(x'_3 / H_1 \right) = \sum_{k=0}^{\infty} \frac{e^{-\frac{\tau'_{GLRT-3}}{2}} \left(\tau_{GLRT-3}^2 / 2 \right)^k}{k! B(N+M-2, k+1) (N+M-2+x'_3)^{N+M-1+k}} \end{array} \right. \quad (4.23)$$

4.4.2 Performance analysis

Firstly, the analytical characterization of the performance of the GLRT-based detectors with secondary data is provided and then its correctness is verified through comparison with Monte

Carlo simulation. The achievable performance in terms of P_d is also compared with their corresponding GLRT-based detectors without secondary data. In accordance with the PDFs of x'_2 in eq. (4.21) the P_{fa} and the P_d are:

$$P_{fa}|_{GLRT-SD_2} = e^{-T'_{GLRT2}} \quad (4.24)$$

$$P_d|_{GLRT-SD_3} = Q_M \left(\sqrt{\frac{2|\beta|^2}{\sigma_n^2} \left(\|s_{t0}\|^2 - \frac{|s_{d0}^H s_{t0}|^2}{\|s_{d0}\|^2 + \|s'_{d0}\|^2} \right)} \right), \sqrt{2 \ln \left(\frac{1}{P_{fa}|_{GLRT-SD_2}} \right)} \quad (4.25)$$

where T'_{GLRT2} is defined in the previous section.

For the GLRT-3 detector with secondary data the P_{fa} and the P_d are obtained from the cumulative F-distribution and the cumulative non-central F-distribution respectively, [52] as previously:

$$P_{fa}|_{GLRT-SD_3} = \left[\frac{1}{1 + T'_{GLRT3}/(N + M - 2)} \right]^{N+M-2} \quad (4.26)$$

$$P_d|_{GLRT-SD_3} = 1 - \sum_{j=0}^{\infty} \frac{\left(\frac{\tau'_{GLRT-3}}{2} \right)^j e^{-\frac{\tau'_{GLRT-3}}{2}}}{j!} \frac{B(1 - P_{fa}|_{GLRT-SD_3}, 1 + j, N + M - 2)}{B(1 + j, N + M - 2)} \quad (4.27)$$

where τ'_{GLRT-3} is the non-central parameter defined in the previous section. Again from eq. (4.26) it is clear that no priori knowledge of any unknown parameters is required to set the decision threshold needed in order to guarantee a given P_{fa} level, thus ensuring the CFAR condition.

For the case when the target approaches the transition between far and near field, $S=0.76$ and for short observation time, $1/2ML$ Figure 4.13 shows the simulated and the theoretical P_{fa} of the GLRT-2 detector with secondary data as function of the decision threshold, T'_{GLRT2} considering $M=N$ (sub-figure (a)) and $M=4N$ (sub-figure (b)). We note a perfect agreement between the simulated and the theoretical expressions of the P_{fa} .

Meanwhile the Figure 4.14 compare the simulated and the theoretical Pfa of the GLRT-3 detector with the secondary data for the same reference scenario of the Figure 4.13. Once more we note that by increasing the number of the secondary data for the estimation of the unknown direct signal and noise power a smaller threshold is needed to guarantee the same Pfa.

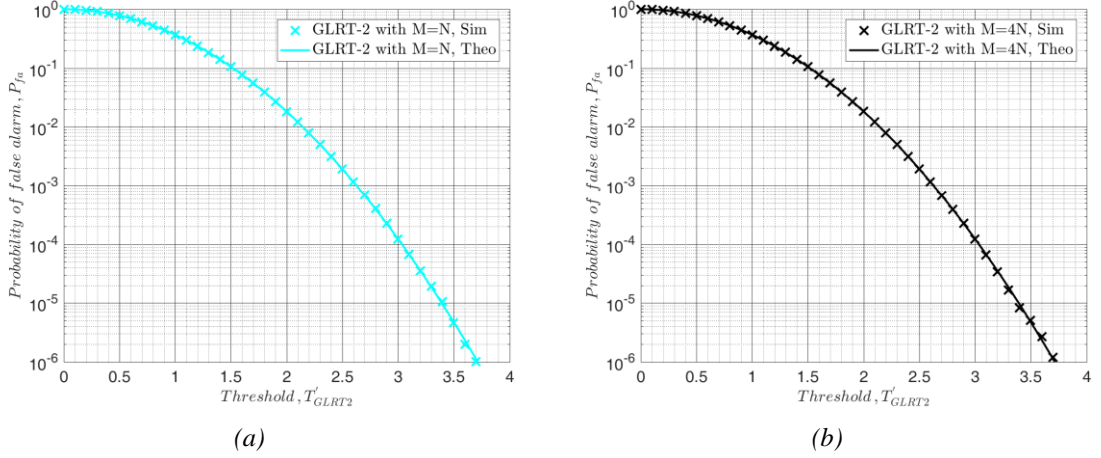


Figure 4.13 Simulated and theoretical P_{fa} of GLRT-2 detector with secondary data as function of T'_{GLRT2} for a target getting close to the near field, $S=0.76$ and small observation time, $1/2ML$ having set (a) $M=N$ and (b) $M=4N$.

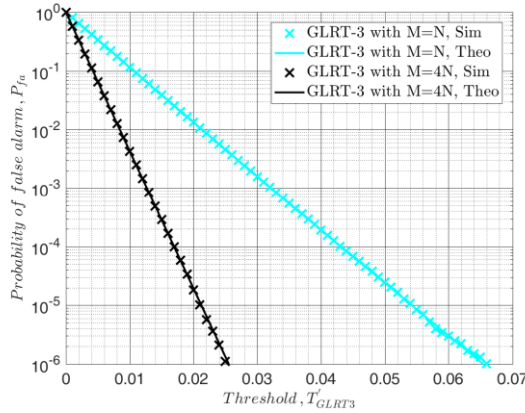


Figure 4.14 Simulated and theoretical P_{fa} of GLRT-3 detector with secondary data for $M=N$ and $M=4N$ as function of T'_{GLRT3} for a target getting close to the near field, $S=0.76$ and small observation time, $1/2ML$.

Figure 4.15 (a) and Figure 4.15 (b) show the theoretical and the simulated P_d of GLRT-2 and GLRT-3 with secondary data respectively, for different M values. In accordance with the

consideration above increasing the size of the secondary data less fluctuation on the estimation of the unknown parameters is expected and consequently a smaller decision threshold is needed and a higher detection probability is obtained. Consistently, from Figure 4.15 we note that the P_d converges to the P_d of the optimum detector, GLRT-1, moving from $M=N/2$ to $M=4N$ where N is the dimension of the primary data. The small differences between the simulated and the theoretical results for $M=N/2$ are due to the presence of the target component in the secondary data differently from the theoretical assumption of target free as mentioned in Section 4.4.1.1 and in Section .

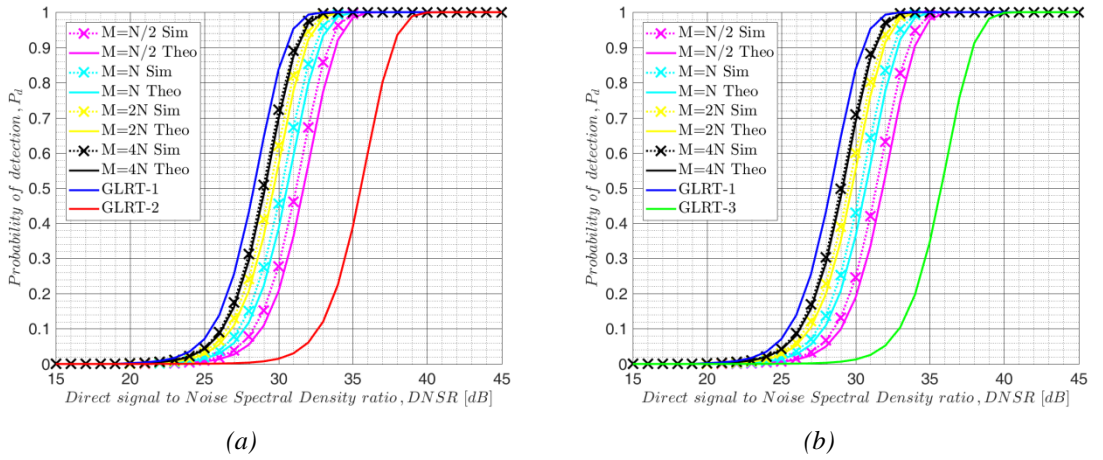


Figure 4.15 Simulated and theoretical P_d when $S=0.76$ and for small observation time, $1/2ML$ (a) of GLRT-2 detector with secondary compared to GLRT-1 and GLRT-2 detector and (b) of GLRT-3 detector with secondary data compared to GLRT-1 and GLRT-3 detector.

4.5 Signal to noise ratio analysis and design criteria for FSR system

The aim of the developed techniques is to increase the output signal-to-noise ratio to improve detection. In particular, the P_d obtained from GLRT-1 detector with all parameters known and from GLRT-2 detector with direct component unknown is function only of the SNR if P_{fa} is fixed (see with SNR specified in eq. (4.12) and eq. (4.13)).

Therefore, this section focuses on the derivation of a closed form expression of SNR_{GLRT1} representing the optimal SNR achievable by means of a coherent technique and of SNR_{GLRT2}

achievable from a non-optimum coherent technique (Section 4.5.1). Moreover exploiting the theoretical SNR aspects of radar system design are addressed in Section 4.5.2.

4.5.1 Theoretical closed form expression of SNR

To simplify the analysis, the global target signature defined in Section 3.2 is approximated using Taylor series expansion. More precisely, the phase signature in eq. (3.2) is obtained by considering a Taylor expansion at second-order around the crossing-time instant:

$$\phi(t) = \frac{\pi}{\lambda} v_x^2 \left[\frac{1}{(L - y_0)} + \frac{1}{y_0} \right] t^2 \quad (4.28)$$

Recall that by referring to the system geometry in Figure 3.1, y_0 is the distance target-RX and $L - y_0$ is the distance target-TX when the target is on the baseline and v_x is the cross-baseline velocity.

It is clear from eq. (4.28) that the Doppler rate is given by:

$$\ddot{\phi} = \frac{1}{2\pi} \frac{d^2\phi(t)}{dt^2} = \frac{v_x^2}{\lambda} \left(\frac{1}{L - y_0} + \frac{1}{y_0} \right) \quad (4.29)$$

and is function of the cross-baseline velocity, v_x and of the baseline crossing point, y_0 .

On the other hand for the pattern signature defined in eq. (3.1), is approximated using a Taylor expansion of order zero for the scale term and of the first-order for the argument of the *sinc* function:

$$\sigma_{fs}(t) = \frac{L^2}{y_0(L - y_0)} \frac{v_x}{v} \text{sinc} \left[\frac{l_h}{\lambda} \frac{v_x^2}{v} \left(\frac{1}{L - y_0} + \frac{1}{y_0} \right) t \right] \quad (4.30)$$

Lastly the global target signature is expressed as follows:

$$s_{t0}(t) = s_0^0 e^{j\pi\ddot{\phi}t^2} \text{sinc}(\ddot{\phi}\epsilon t) \quad (4.31)$$

where $s_0^0 = \frac{L^2}{y_0(L - y_0)} \frac{v_x}{v}$ and $\epsilon = \frac{l_h}{v}$.

From eq. (4.31) we note that the main lobe width of the target signature that specifies the main contribution of the energy of the received target signal depends on the target electrical size and target motion parameters:

$$\theta = \ddot{\phi}\epsilon \quad (4.32)$$

The optimum SNR in eq. (4.12) obtained integrating coherently the received signal after the cancellation of the direct signal can be written as function of DNSR (see eq. (3.5)) as in eq. (4.33) where T is the integration time.

$$SNR_{GLRT1} = DNSR \frac{|\beta|^2}{|\alpha|^2} \int_{-T/2}^{T/2} |s_{t0}(t)|^2 dt \quad (4.33)$$

Moreover from eq. (4.33) we note that the term that multiplies the DNSR is the target signal-to-direct signal power ratio, SDR_{GLRT1} . The closed form expression of the SNR_{GLRT1} is derived by solving the integral in eq. (4.33) as (see Appendix E):

$$SNR_{GLRT1} = 2DNSR \frac{l_v^2 l_h^2 s_0^2}{\lambda^2 L^2 \pi \ddot{\phi} v} \left[Si(\pi \ddot{\phi} \epsilon T) - \frac{1}{\pi \ddot{\phi} v} \frac{\sin^2(\pi \ddot{\phi} \epsilon T/2)}{T/2} \right] \quad (4.34)$$

where $Si(\cdot)$ and $Ci(\cdot)$ are the Sine and the Cosine integral,[50]. Although we integrate coherently N measurements of the received signal the SNR is not improved by a factor of N due to the pattern signature.

Likewise for the GLRT-2, starting from eq. (4.13) and exploiting the definition of the orthogonal projector onto the subspace of the direct component, $\mathbf{P}_{s_d}^\perp$ in Section 4.2.1.2 we have:

$$SNR_{GLRT2} = DNSR \frac{|\beta|^2}{|\alpha|^2} \left\{ \int_{-T/2}^{T/2} |s_{t0}(t)|^2 dt - \frac{1}{T} \left| \int_{-T/2}^{T/2} s_{t0}(t) dt \right|^2 \right\} \quad (4.35)$$

As previously, the term that multiplies the DNSR in eq. (4.35) is the target signal-to-direct signal power ratio, SDR_{GLRT2} . After some approximations of the pattern signature detailed in Appendix E, the SNR_{GLRT2} is defined as in eq.(4.36), where $m = 1 \dots P - 1$ is the number of the side lobes of the pattern signature and $C(\cdot)$ and $S(\cdot)$ are the Fresnel Cosine and Fresnel Sine function respectively, , being X_i for $i=1,\dots,9$ defined in eq. (E. 7) of Appendix E.

$$\begin{aligned}
 SNR_{GLRT2} = SNR_{GLRT1} & - DNSR \frac{|\beta|^2}{|\alpha|^2} \frac{1}{T} \left| \frac{s_0^0}{\sqrt{2\ddot{\phi}}} e^{-j\pi\ddot{\phi}\left(\frac{\epsilon}{4}\right)^2} \{C(X_1) + C(X_2) + \right. \\
 & j[S(X_1) + S(X_2)]\} + \frac{s_0^0}{j\sqrt{2\ddot{\phi}}} e^{-j\frac{\pi}{4}\ddot{\phi}\epsilon^2} \left\{ \left[\frac{4}{\pi} - \frac{1}{\sqrt{2}} \left(1 + \frac{\pi}{4} \right) \right] \{C(X_3) - C(X_4) - \right. \\
 & 2C(X_5) + j[S(X_3) - S(X_4) - 2S(X_5)]\} + \sum_{m=1}^{P-1} \frac{4}{\pi(1+2m)} \{C(X_6) - C(X_7) - \\
 & \left. \left. C(X_8) + C(X_9) + j[S(X_6) - S(X_7) - S(X_8) + S(X_9)]\} \right\} \right|^2
 \end{aligned} \tag{4.36}$$

4.5.2 Design criteria for FSR system

Taking advantage of the closed form expressions of the signal-to-noise ratio, aspects of system design are discussed. More precisely, it is noted that the SNR defined in eq.(4.34) and in eq. (4.36) depends on the system parameters (baseline and integration time) and on the target parameters (namely size and motion described by velocity, baseline crossing point, y_0 and baseline crossing angle, φ as we assume the target follows a linear trajectory).

To better understand the effect of system and target parameters, a separate analysis is proposed. Particularly in the following the reported results refer to the DNSR needed to ensure an established performance in terms of P_{fa} and P_d . Specifically, in our case a $P_{fa} = 10^{-5}$ and a $P_d = 0.9$ is considered corresponding to a SNR value equal to 12.54 dB, (see eq.(4.11)).

4.5.2.1 SNR against system geometry parameters

Firstly the DNSR as function of the baseline length is investigated. We consider the same carrier frequency and target size of the previous sections (see Target related parameters in Table I): the target moves with $v = 36 \text{ m/s}$ and crosses the baseline perpendicularly in the middle. The integration time is set to $T=2.3 \text{ sec}$. Obtained results are shown in Figure 4.16 with upper axis representing the far field condition parameter.

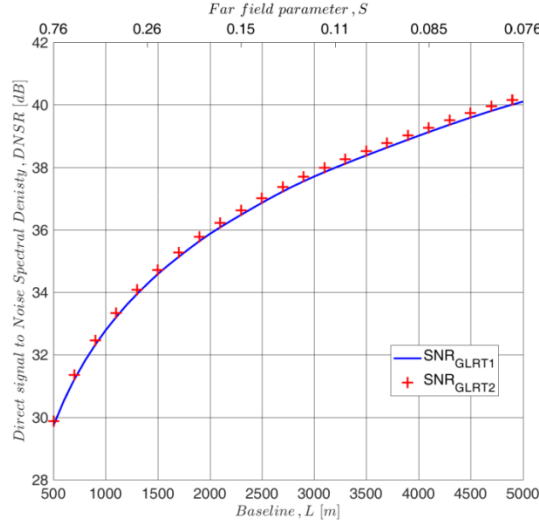


Figure 4.16 DNSR necessary to ensure a $P_{fa}=10^{-5}$ and a $P_d=0.9$ as function of the baseline.

It is clear that for a long baseline the received target signal is weaker and a greater DNSR is necessary to achieve the same performance. In fact in our case study for a baseline equal to $L = 5 \text{ km}$, 10 dB more are needed than for a baseline of $L = 0.5 \text{ km}$ in order to obtain the same performance. In addition in agreement with results in Section 4.2.2 were the performance in terms of P_d of the different GLRT detectors were compared, for the long integration time involved both detectors GLRT-1 and GLRT-2 provide the same performance.

Performance as a function of the integration (observation) time is investigated in Figure 4.17 showing the output SNR for different DNSR values for the case of $L=5 \text{ km}$ considering the same rectangular target with the same motion parameters defined in Table I. The interval of T values considered in , $T=[0, 25]$ sec, corresponds to an angular interval $\Delta\Omega = [0^\circ, 20^\circ]$. From the figure we again observe that for a long integration time both detectors give the same performance; in contrast for a short observation time GLRT-1 outperforms GLRT-2.

Moreover it appears that for a fixed DNSR the SNR of both detectors exhibits an asymptotic trend maintaining an almost constant SNR when increasing the observation time (i.e. including more side lobes of the target pattern). This behavior can be easily explained by recalling that the main contribution from the target is specified by the main lobe of the pattern signature.

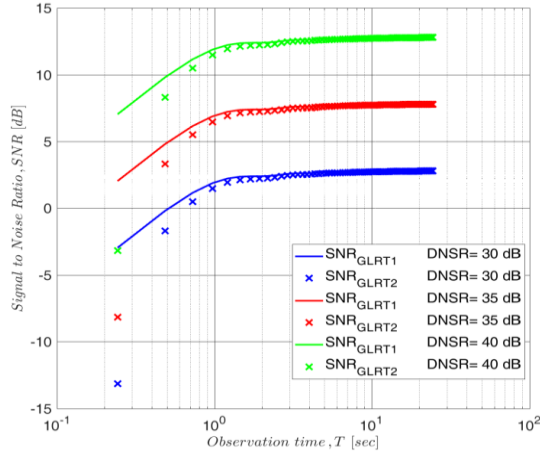


Figure 4.17 SNR achievable from GLRT-1 and GLRT-2 detectors as function of the observation time T for different values of DNSR.

This asymptotic value is derived from the expression of the optimum SNR achievable from coherent detection techniques (i.e. SNR_{GLRT1}) considering an infinite integration time ($T \rightarrow \infty$). From eq. (4.34) recalling that for $T \rightarrow \infty$, we have $Si(\infty) = \pi/2$ and $sinc^2(\infty) \rightarrow 0$, the asymptotic expression of the SNR is obtained as follows:

$$SNR_{\infty}^{opt} = \lim_{T \rightarrow \infty} SNR_{GLRT1} = DNSR \frac{l_v^2 l_h}{\lambda v} \left(\frac{1}{L - y_0} + \frac{1}{y_0} \right) \quad (4.37)$$

The SNR_{∞}^{opt} in eq. (4.37) highlights the dependency of the SNR on the carrier frequency, on the baseline length and on the DNSR. It also shows the higher sensitivity to the vertical dimension of the target with respect to the horizontal one, as shown in [8]. In addition we note the dependence on the velocity of the target and on the baseline crossing point, y_0 but not on the baseline crossing angle, φ . These aspects will be analyzed in detail in the following.

4.5.2.2 SNR against target related parameters

The impact of the target related parameters is now investigated, starting from the motion parameters.

Figure 4.18 shows the DNSR as function of the baseline crossing point , y_0 for the same case study of the Figure 4.17 (the target crosses the baseline perpendicularly) assuming a long integration time set to $T = 15$ sec. The interval of values of the baseline crossing point is selected to guarantee the fulfillment of the far field condition for both transmitter and receiver.

As apparent a greater DNSR is necessary to obtain the same performance when the target crosses the baseline in the middle. The asymptotic expression of the SNR in eq. (4.37) leads at the same result since it is quite clear that the $\text{SNR}_{\infty}^{\text{opt}}$ reaches the minimum when $y_0 = L/2$ ($R_T = R_R = L/2$).

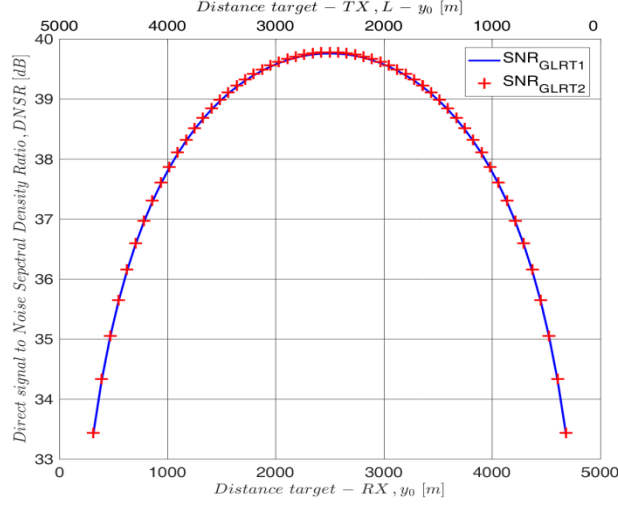


Figure 4.18 DNSR necessary to ensure a $P_{fa}=10^{-5}$ and a $P_d=0.9$ as function of the baseline crossing point.

The impact on the performance of the baseline crossing angle is investigated in Figure 4.19 showing the DNSR of GLRT-1 and GLRT-2 detector needed to obtain a $\text{SNR} = 12.54 \text{ dB}$ as function of φ for a long, $T = 15 \text{ sec}$ (Figure 4.19 (a)), and a short, $T = 1 \text{ sec}$ (Figure 4.19 (b)), integration time for the same case study of Figure 4.17.

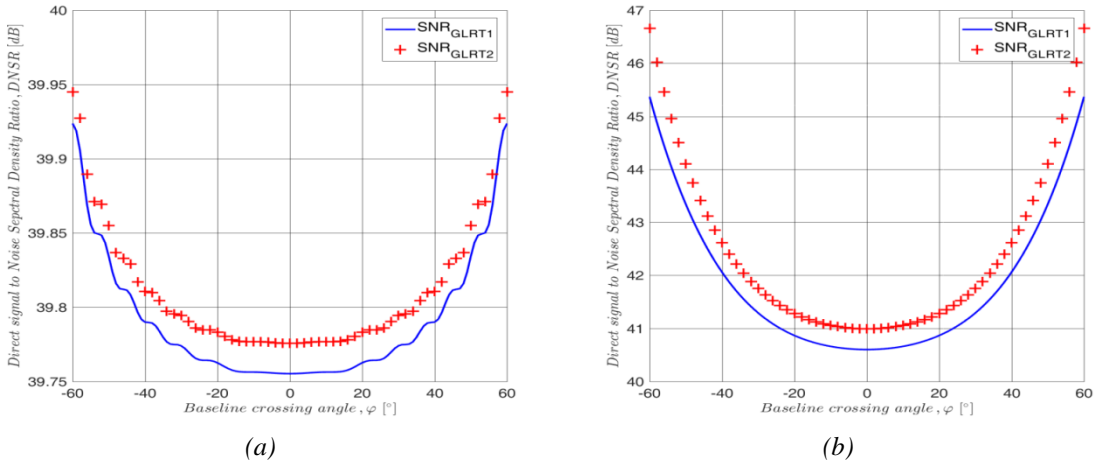


Figure 4.19 DNSR necessary to ensure a $P_{fa}=10^{-5}$ and a $P_d=0.9$ as function of the baseline crossing angle (a) for a long integration time, $T=15 \text{ sec}$ and (b) for short integration time, $T=1 \text{ sec}$.

In contrast, for short integration time, Figure 4.19 (b), a greater DNSR is necessary in the case of non-perpendicular crossing baseline for both detectors. For example when $\varphi = 60^\circ$ (-60°) around 5 dB more are necessary with respect to $\varphi = 0^\circ$ to maintain the same performance.

This different behavior can be explained on the basis of the following observations:

- the effective aperture of the target is the projection of the horizontal dimension along the axis normal to the baseline, $l_h \cos \varphi$, thus resulting in a main lobe lower by a factor equal to $\cos \varphi$ and wider by a factor $1/\cos \varphi$.
- the effective cross-baseline velocity of the target, $v_x = v \cos \varphi$, results in a target with a lower v_x component when $\varphi \neq 0^\circ$ thus further widening the mainlobe as a function of time by a factor $1/\cos \varphi$.

Both effects are clearly visible in Figure 4.20 showing the amplitude pattern for the cases $\varphi = 0^\circ$ and $\varphi \neq 0^\circ$.

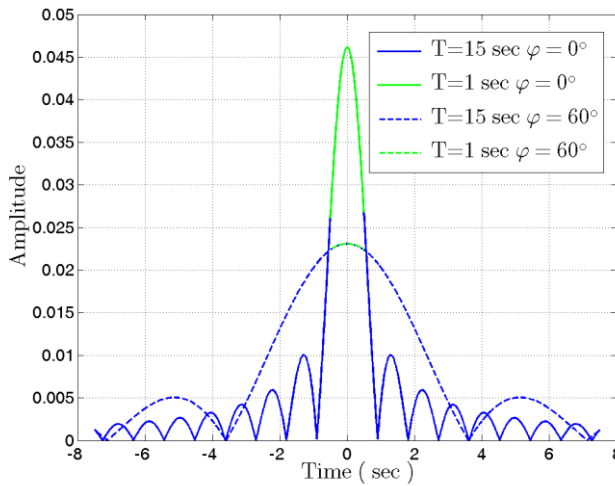


Figure 4.20 Pattern signature for baseline crossing angle $\varphi=0^\circ$ and $\varphi=60^\circ$ of a target size 2.5×1.5 m crossing the baseline at midpoint for different integration times.

When a long integration time is exploited (blue curve in Figure 4.20) the loss on the peak value is compensated by the widening of the main lobe independently from the φ value thus providing the same performance (Figure 4.19 (a)). In contrast this compensation effect does not occur for a short integration time (green curve in Figure 4.20) thus resulting in a lower DNSR is needed for $\varphi = 0^\circ$ with respect to $\varphi \neq 0^\circ$ to achieve the same performance.

Concerning target velocity, it is apparent from the SNR in eq. (4.37) that better performance is obtained for a slowly mover as shown in the Figure 4.21 (a) again for the same case study of Figure 4.17 with $T = 15$ s.

An assessment with respect to the target dimensions is reported in Figure 4.21 (b) showing the DNSR of both detectors as function of the horizontal dimension, l_h (vertical dimension, l_v) for a fixed vertical dimension, $l_v = 2$ m (horizontal dimension, $l_h = 2$ m) being the other parameters as in Figure 4.17.

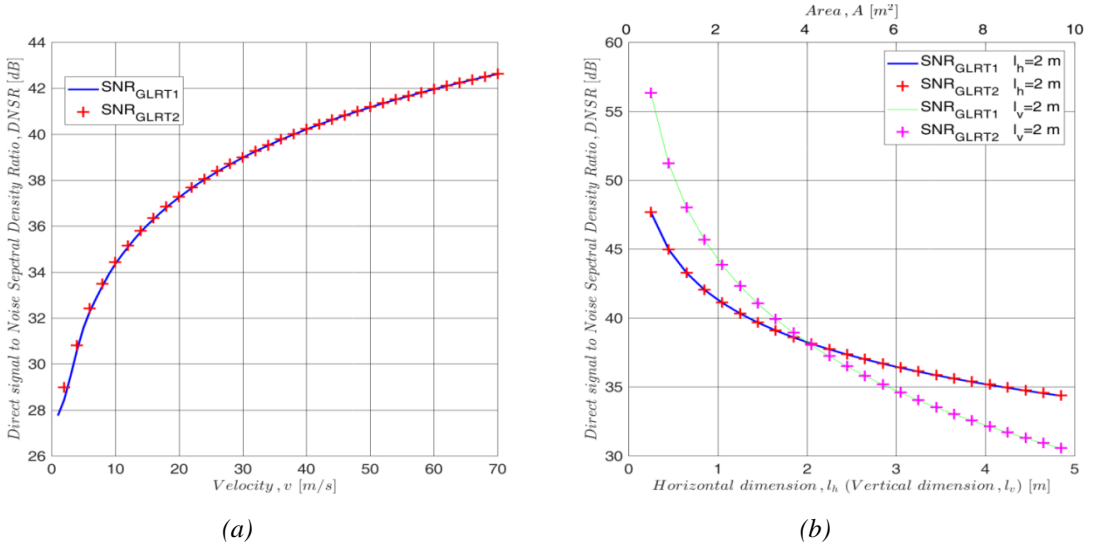


Figure 4.21 DNSR necessary to ensure a $P_{fa}=10^{-5}$ and a $P_d=0.9$ (a) as function of the velocity for a perpendicular and midpoint crossing baseline and (b) as function of the target dimension.

It is apparent that for the same target area, $A = l_v l_h$, for $l_h = 2$ m (see blue curve in Figure 4.21 (b)) and $l_v > l_h$ a greater DNSR is needed to achieve the same performance with respect to the case of $l_v = 2$ m (see green curve in Figure 4.21 (b)) and $l_h > l_v$. Likewise it is noted that for $l_h = 2$ m and $l_v < l_h$ a lower DNSR is needed with respect to $l_v = 2$ m and $l_h < l_v$. Hence, the results demonstrates the higher sensitivity to the vertical dimension of the target with respect to its horizontal dimension, in agreement with the asymptotic expression SNR_{∞}^{opt} in eq. (4.37).

In addition, denoting with $\kappa \in (0:1)$ the baseline crossing parameter, hence $y_0 = \kappa L$ and $L - y_0 = (1 - \kappa)L$, and with $v = l_v/l_h$ the shape parameter of a rectangular target, eq. (4.37) can be rewritten as:

$$SNR_{\infty}^{opt} = DNSR \frac{A^{3/2} v^{1/2}}{\lambda v} \left(\frac{1}{\kappa(1-\kappa)L} \right) \quad (4.38)$$

From the above, target area compared to the baseline length expressed in km is defined as a function of the velocity compared to the carrier frequency expressed in GHz and of the baseline crossing point parameter and shape parameter as follows:

$$\frac{\sqrt{A}|_m}{L|_{km}} = \sqrt[3]{\frac{SNR_{\infty}^{opt}}{a^2/N_0} \frac{c}{\sqrt{v}} \kappa(1-\kappa)} \sqrt[3]{\frac{v|_{m/s}}{f|_{GHz}}} \quad (4.39)$$

Figure 4.22 (a) and Figure 4.22 (b) show the minimum $\sqrt{A}|_m/L|_{km}$ required to achieve $SNR_{\infty}^{opt} = 12.54 \text{ dB}$ as function of $v|_{m/s}/f|_{GHz}$ for different shape factors v when $\kappa = 0.5$ and for different baseline crossing point parameters κ considering a target with $v = 1/2$, respectively. In both analyses different values of a^2/N_0 have been considered.

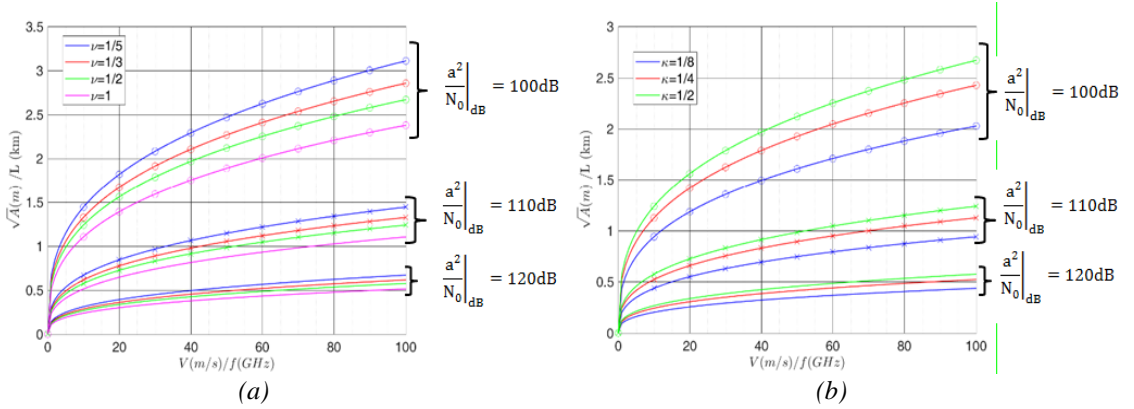


Figure 4.22 $\frac{\sqrt{A}|_m}{L|_{km}}$ as function of $\frac{v|_{m/s}}{f|_{GHz}}$ (a) for a target crossing the baseline in the middle for different value of shape parameter v and (b) for a target with a shape parameter $v = 1/2$ and different baseline crossing points, κ .

The following observations apply: (i) for a fixed baseline and target area if the target moves with a low speed a lower carrier frequency (i.e. a greater wavelength) must be considered in order to achieve the same performance and (ii) for a specific carrier frequency and target velocity if the target has larger dimensions we need a long baseline to guarantee the same performance.

This implies that if we aim at detecting large targets moving with low speed (i.e. ship), for a fixed baseline a smaller carrier frequency must be chosen in order to obtain a desirable P_{fa} and P_d . Conversely if we are interested in the detection of small/medium targets moving with high speed (i.e. stealth aircraft) for a fixed baseline a greater carrier frequency has to be preferred. Similarly above results could be used to design the baseline length once the carrier frequency has been fixed. In addition, with reference to the shape factor and to the baseline crossing point apply the same considerations previously mentioned, namely better performance are obtained for greater shape parameter and when the target does not cross the baseline in the middle.

Summary

In this chapter we have derived new, fully adaptive GLRT schemes to perform CFAR target detection with FSR by starting from the I & Q baseband components. The new schemes are shown to provide detection performance improved with respect to the CVD and CFAR CVD presented in Chapter 3 by an amount ranging from a minimum of 3 dB when the target is in the deep far field area up to 10 dB when the target is getting close to the near field. Moreover, a new set of GLRT schemes obtained by exploiting a set of secondary data assumed target free shows a non-negligible further improvement over the previous adaptive GLRT schemes (namely GLRT-2 and GLRT-3), when the operation conditions get close to the near field transition point.

The analytical performance obtained for the GLRT schemes, also allowed to derive equivalent SNR expressions, appropriately simplified by approximations, that relate the detection performance to the main FSR parameters describing geometry, target size and target motion. This allowed us to investigate the effect of the individual parameters on the global detection performance.

Chapter 5

Motion parameters estimation and performance analysis

This chapter focuses on the use of a Forward Scatter Radar System for the estimation of the kinematic parameters of targets following a linear trajectory: particularly both single baseline (one transmitter and one receiver) and dual baseline (one transmitter and two separate receivers) systems are considered. First, based on the Crystal Video scheme introduced in Chapter 3 a two-dimensional filter bank approach is proposed with the generic impulse response depending on the unknown target electrical size and target trajectory thus allowing the estimate of the following target signal parameters: Doppler rate, baseline crossing time and main lobe width of the pattern signature. Then taking advantage of the estimated signal parameters and exploiting some a priori knowledge, the cross-baseline velocity is estimated in the single baseline configuration. Meanwhile the dual baseline configuration ensures the possibility to estimate two parameters without a priori knowledge: the cross-baseline velocity and the baseline crossing point. The performance of the proposed technique is investigated from a theoretical point of view in terms of accuracy. The achievable accuracy is also compared to the Cramer Rao Lower Bound (CRLB) that establishes the minimum achievable variance of any unbiased estimator. Finally simplified closed-form expressions of the CRLB, relating the accuracy to the main parameters describing the FSR geometry and the target, are derived.

5.1 Introduction

The target signature extracted by the Crystal Video based scheme (see Chapter 3) it is useful not only to perform target detection but also for motion parameters estimation by investigating the Doppler signature carrying out the kinematic information. The forward scatter signal model considered is the same introduced in Section 3.2, referring to a rectangular target

with size large with respect to the wavelength and moving in the far field area of both transmitter and receiver.

In particular following, the line in [10] and [8] introduced in Section 2.6, we derive a two-dimensional bank of filters matched to the Doppler rate and to the main lobe width of the pattern signature. To support practical applications, a two-step processing is proposed: in the first step a rough estimate of the Doppler rate is obtained by applying the Radon transform to the spectrogram of the acquired signal while in the second step the bank is exploited to refine the Doppler rate estimation provided by the previous step and also to provide an estimation of the baseline crossing instant and main lobe width of the target pattern signature. Obviously this greatly reduces the range of Doppler rate values to be investigated by the bank thus reducing the required computational load. To assess the performance on the estimation of the target parameters of the proposed technique the CRLB as a universally accepted tool is derived and used for comparison. The Cramer Rao Bound (CRB) provides the lower limit on the mean square error achievable by an unbiased estimator of the target signal parameters and, therefore, provides a fundamental performance bound on the system's accuracy.

To estimate the kinematic parameters of moving targets we take into account the dependence of these parameters on the target signal parameters estimated by the bank. Especially for a single baseline configuration the extraction of the Doppler rate is exploited. Such information combined with a priori knowledge on the baseline crossing point allows to estimate the cross-baseline velocity. Moreover, we consider the possibility to estimate also the baseline crossing point by means of a dual receive antenna without a priori knowledge on other target parameters. The latter is achieved by separately processing the signals acquired by the two receivers by means of two 2D matched filters and exploiting the extraction of the Doppler rate and of the baseline crossing instants.

The performance of the kinematic parameters estimation for both FSR configurations taken under investigation is theoretically evaluated for different target trajectories and under different signal to noise conditions in terms of expected accuracy through Monte Carlo simulation. The latter is compared with the corresponding CRLB.

Therefore we can summarize that this chapter addresses the issue of the motion parameters estimation of a moving target under the assumption that follows a linear trajectory and its

corresponding signal is embedded in White Gaussian Noise through: (i) the development of a two-dimensional bank of filters based on the Crystal Video scheme for the target signature extraction and (ii) by providing a performance analysis in terms of the accuracy through Monte Carlo simulations and closed-form expressions of the CRLB for both single and dual baseline FSR configuration.

5.2 Signal parameter estimation technique

In Chapter 3 it was shown that the target time domain signature, in our case embedded in the noise component and the direct signal, may be extracted from a square-law detector followed by a DC removal filter (see Figure 3.3). In particular in Section 3.3 we showed that the DC removal filter performed through a orthogonal projection of the square law signal, $z(t)$ (see eq. (3.10)) onto the subspace orthogonal to the DC component perfectly removes the direct component: $\mathbf{u} = \mathbf{P}^\perp \mathbf{z}$. As the noise and the target-scattered signal are much smaller than the direct signal, the squared envelope of these two terms was neglected. Therefore, the surviving signal after the DC removal filter was approximated as the sum of two components: $\mathbf{u} \cong \mathbf{s}_u + \mathbf{s}_n$ representative of the new useful signal, \mathbf{s}_u given by the mixed term between the direct and the scattered target signal (see eq. (3.11)) and of the new noise component, \mathbf{s}_n that is still zero mean white Gaussian noise. Moreover it was shown that the impulse response of the matched filter defined in eq. (3.13) depends on the FS pattern signature and the Doppler signature which in turn depend on the target electrical size and target trajectory that are a priori unknown. This also means that targets with different dimension, different velocity and different baseline crossing angle and crossing point have different signatures.

5.2.1 Two-dimensional filter bank approach

To address this issue a two dimensional bank of matched filters is considered: aiming to simplify the analysis the global target signature, $s_{t0}(t)$ is approximated using Taylor series expansion as derived in Section 4.5.1. In particular it is considered a Taylor series expansion of bistatic distance at second order around crossing-time instant for the approximation of the phase signature as in eq. (4.28) and a Taylor series expansion at zero order for the scale term

of the pattern signature and at first order for the *sinc* function as in eq. (4.30). Some aspects related to the phase error approximation are discussed in the Section 5.3.

Hence, by substituting eq. (4.28) and eq. (4.30) into eq. (3.13) and disregarding possible scale parameters it is clear that the impulse response of the matched filter in the CVD scheme is function of the Doppler rate defined in eq. (4.29) and of the main lobe width defined in eq.(4.32):

$$h(t) = \text{sinc}(\theta t) \sin(\pi \ddot{\phi} t^2) \quad (5.1)$$

Since both Doppler rate and main lobe width are a priori unknown a two-dimensional filter bank is designed:

$$h_{\ddot{\phi},\theta}(t) = \kappa \text{sinc}(\theta t) \sin(\pi \ddot{\phi} t^2) \quad (5.2)$$

being $\kappa = 1/\sqrt{\int_{-T/2}^{T/2} h_{\ddot{\phi},\theta}^2(t)dt}$. The subscripts $\ddot{\phi},\theta$ are used to indicate that the impulse response is function of both Doppler rate and main lobe width.

In order to limit the computational load required by the bank and to support practical applications a two-step processing is proposed (see Figure 5.1): (i) in the first step a preliminary rough estimation of the Doppler rate, $\tilde{\ddot{\phi}}$ is obtained through the Radon transform applied to the spectrogram and (ii) in the second step the bank is exploited to refine the estimation of the Doppler rate and to estimate the main lobe width and the baseline crossing instant.

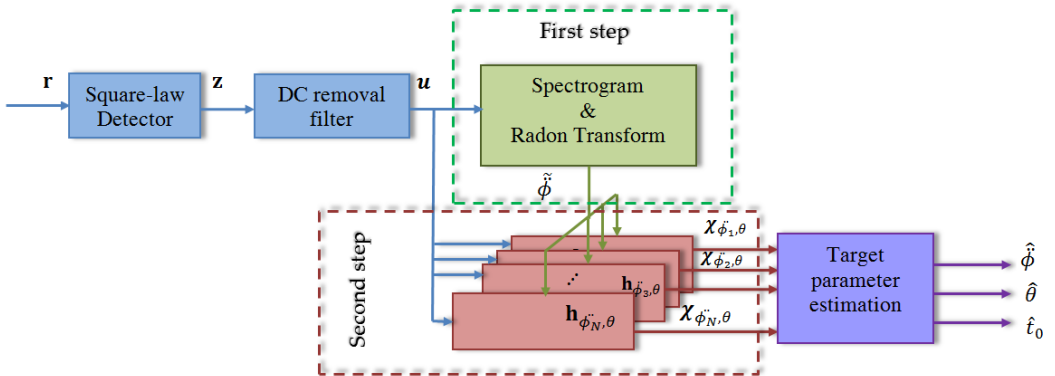


Figure 5.1 Two-dimensional filter bank block diagram.

Firstly, the signal at the output of the DC removal filter is analyzed for the estimation of the Doppler rate through a time-frequency analysis such as the Short Time Fourier Transform (STFT). The STFT approaches the problem of determining when a particular frequency occurs by partitioning the signal into short segments and then applying a weighting function to the signal within each segment, prior to evaluating the Fourier transform, and is given by:

$$S_u(t, f) = \int_{-\infty}^{+\infty} w(\tau - t) u(\tau) e^{-j2\pi f_c \tau} d\tau \quad (5.3)$$

where $w(\tau)$ is the analysis window centered at time t with duration T_w . With the STFT a linear phase term is compensated which should be sufficient for short enough time window. The possibility to estimate the target velocity with the STFT for a target in FSR configuration, assuming a priori information on baseline crossing angle and baseline crossing point, has been shown in [21] and [34].

Since the STFT is a complex-value in general, we used the so called spectrogram that is the squared magnitude of the short-time Fourier transform, $|S_u(t, f)|^2$. The Radon transform (RT), $RT_{S_u}(\theta_r, x_r)$ is then applied to $|S_u(t, f)|^2$ and a preliminary rough estimate of the target Doppler rate $\tilde{\phi}$ is obtained from the absolute maximum observed on the Radon plane:

$$\tilde{\phi} = -\cot(\theta_{rmax}) \frac{\Delta f}{\Delta t} \quad (5.4)$$

where Δf , Δt are the Doppler frequency spacing and time spacing, respectively.

This greatly reduces the range of Doppler rate values to be investigated by the bank in the second step thus limiting the required computational load. The impulse response in eq. (5.2) is firstly defined by considering different values of the Doppler rate in the range: $\ddot{\phi} = [\tilde{\phi} - \Delta\ddot{\phi}_{max1} : \delta\ddot{\phi} : \tilde{\phi} + \Delta\ddot{\phi}_{max2}]$ where $\Delta\ddot{\phi}_{max1}$ and $\Delta\ddot{\phi}_{max2}$ are the maximum offsets from the estimated Doppler rate from RT and $\delta\ddot{\phi}$ is the Doppler rate step. As a rule of thumb the Doppler rate step may be chosen assuming $\pi/4$ as the maximum tolerable phase error.

Then some a priori information on the expected ranges of the target velocity, v' and target size, (l'_h, l'_v) taken under investigation (i.e. large target moving with low speed, as ship or small/medium targets moving with high speed, as stealth aircraft or UAVs etc.) is needed to set

the initial value of the main lobe width, $\tilde{\vartheta} = \tilde{\phi} \frac{l'_h}{v'}$ in order to define the range values of the main lobe width to be investigated by the bank.

As previously, let define with $\theta = [\tilde{\vartheta} - \Delta\theta_{max1} : \delta\theta : \tilde{\vartheta} + \Delta\theta_{max2}]$ the range values of the main lobe width where $\Delta\theta_{max1}$ and $\Delta\theta_{max2}$ are the maximum offsets from the initial value, $\tilde{\vartheta}$, and $\delta\theta$ is the main lobe width step. In this work the step size of the main lobe width is set in order to guarantee that the energy loss is not more than 10% .

After the full construction of the impulse response in eq. (5.2) as shown in Figure 5.2 , the cross-correlation of the signal at the output of the DC removal filter with the impulse response of each filter is performed:

$$\chi_{\ddot{\phi},\theta}(t) = \int_{-T/2}^{T/2} u(\tau) h_{\ddot{\phi},\theta}(t - \tau) d\tau \quad (5.5)$$

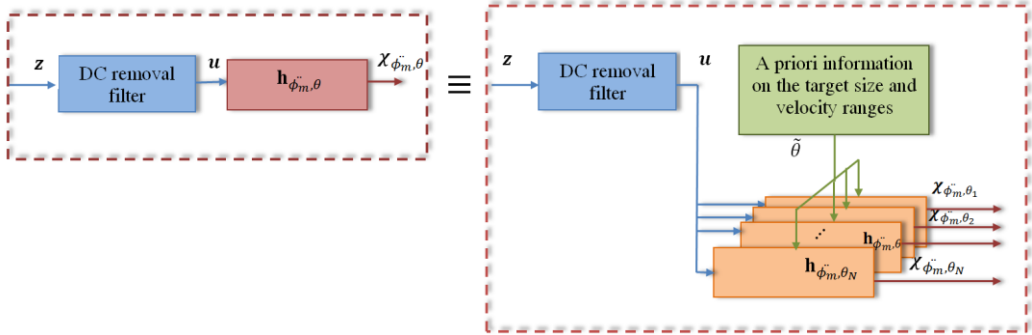


Figure 5.2 Full construction of the impulse response.

We define the cost function $\Delta(\ddot{\phi}, \theta) = \max_t \chi_{\ddot{\phi},\theta}(t)$. Finally the estimated Doppler rate and main lobe width, $(\hat{\ddot{\phi}}, \hat{\theta})$, corresponds to the matched filter providing the highest output and the baseline crossing instant \hat{t}_0 is estimated as the instant in correspondence to the highest peak of the signal at the output of the matched filter with impulse response $h_{\hat{\ddot{\phi}},\hat{\theta}}(t)$:

$$\begin{cases} (\hat{\ddot{\phi}}, \hat{\theta}) = \max_{\ddot{\phi}, \theta} \Delta(\ddot{\phi}, \theta) \\ \hat{t}_0 = \max_t \chi_{\hat{\ddot{\phi}},\hat{\theta}}(t) \end{cases} \quad (5.6)$$

5.2.2 Performance evaluations

In this sub-section the performance of the proposed technique is assessed and discussed for different target trajectories. A reference scenario similar to that introduced in Section 3.3 with the target in the deep far field is here considered for an observation time of $T=3.24$ sec and four different cases characterized by different baseline crossing points e baseline crossing angles. Table 5.1 summarize the main system and target parameters of the reference scenario.

Table 5.1 *System parameters and target related parameters of the reference scenario.*

<i>System parameters</i>	
Carrier frequency	$f_c = 4.612 \text{ GHz}$ ($\lambda = 6.5 \text{ cm}$)
Baseline	$L=4500 \text{ m}$
Observation time	$T=3.24 \text{ sec}$
<i>Target related parameters</i>	
Target size	$l_h = 2.5 \text{ m}$ ($l_h/\lambda \approx 38$) $l_v = 1.5 \text{ m}$ ($l_v/\lambda \approx 23$)
Velocity	$v = 36 \text{ m/s}$

Table 5.2 reports the main parameters of the different case studies showing that the fixed observation time corresponds to different angular intervals from which the target is viewed as depend on the baseline crossing angle, $\Delta\Omega = 2\tan^{-1}(v_x T/L)$. Moreover the fulfillment of the far field condition is guaranteed for all the case studies and is evaluated considering the effective aperture of the rectangular target as $S = 2l_h^2 \cos^2 \varphi / \lambda R$ where $R = \min\{y_0, L - y_0\}$.

Table 5.2 *Case studies parameters.*

Case study	Baseline crossing angle	Baseline crossing point	Far field parameter	Observation angle
(A)	$\varphi = 0^\circ$	$y_0 = L/2$	$S=0.085$	$\Delta\Omega = 2.97^\circ$
(B)	$\varphi = 45^\circ$	$y_0 = L/2$	$S=0.043$	$\Delta\Omega = 2.10^\circ$
(C)	$\varphi = 0^\circ$	$y_0 = L/4$	$S=0.17$	$\Delta\Omega = 2.97^\circ$
(D)	$\varphi = 45^\circ$	$y_0 = L/4$	$S=0.086$	$\Delta\Omega = 2.10^\circ$

Figure 5.3 shows the received signal after the DC removal filter for all the different target trajectories of Table 5.1 in noise free condition. In all cases we assume the target crossing the baseline at time $t_0 = 0$.

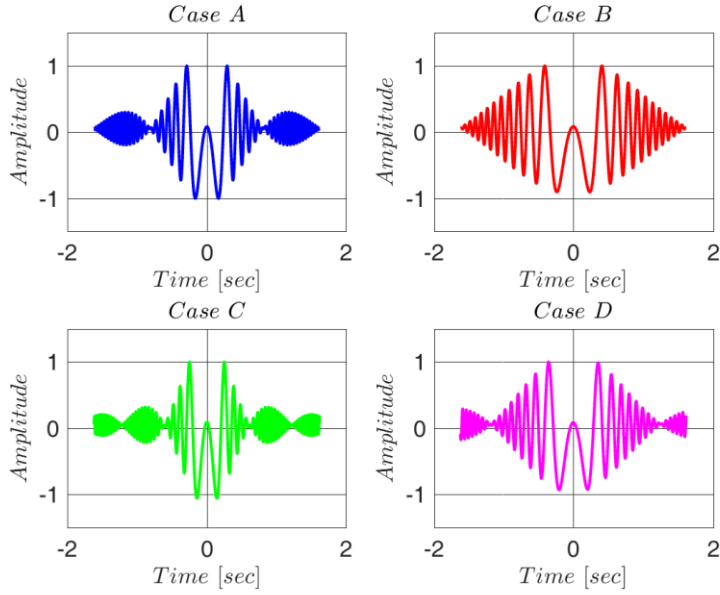


Figure 5.3 Received signal after DC removal for different target trajectories as defined in Table 5.1.

Focusing on the first step of the proposed approach, a Hamming window for the estimation of the STFT equal to $T_w=0.5$ s is considered. Figure 5.4 shows the spectrograms (normalized with respect to their maximum values) of the case study (A) and (B). Meanwhile Figure 5.5 shows their respective Radon transform. Figure 5.6 and Figure 5.7 report similar results, the spectrogram and the Radon transform respectively, for the case study (C) and (D).

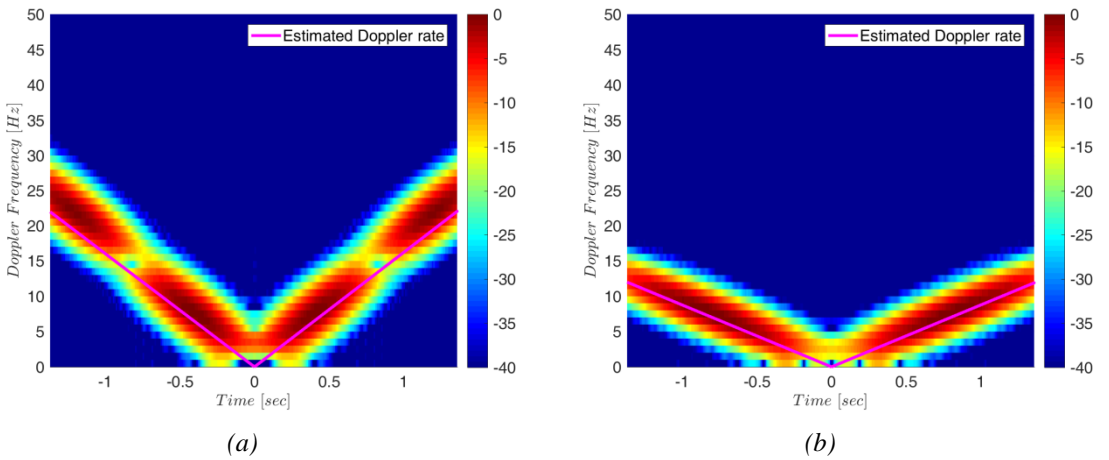


Figure 5.4 Spectrogram normalized with respect to its maximum related to (a) case study (A) and (b) case study (B).

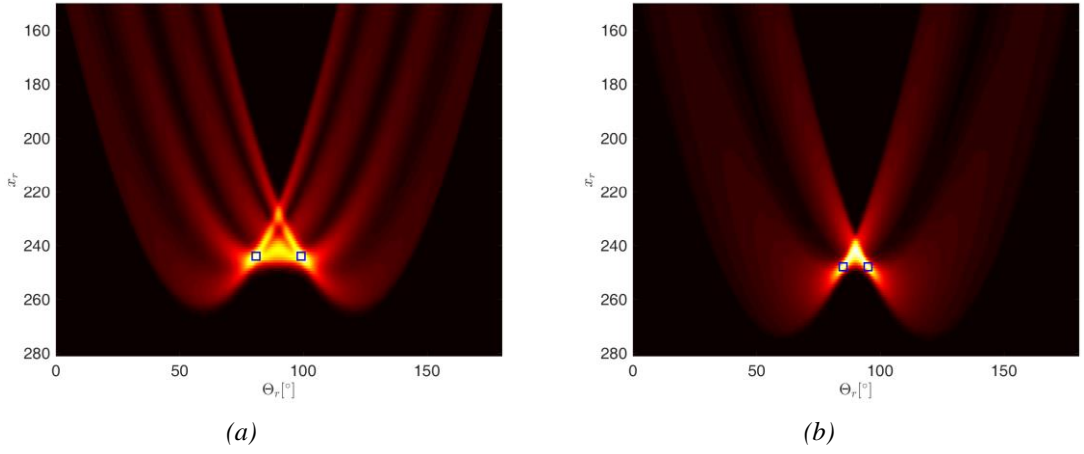


Figure 5.5 Radon transform of the spectrograms related to (a) case study (A) and (b) case study (B).

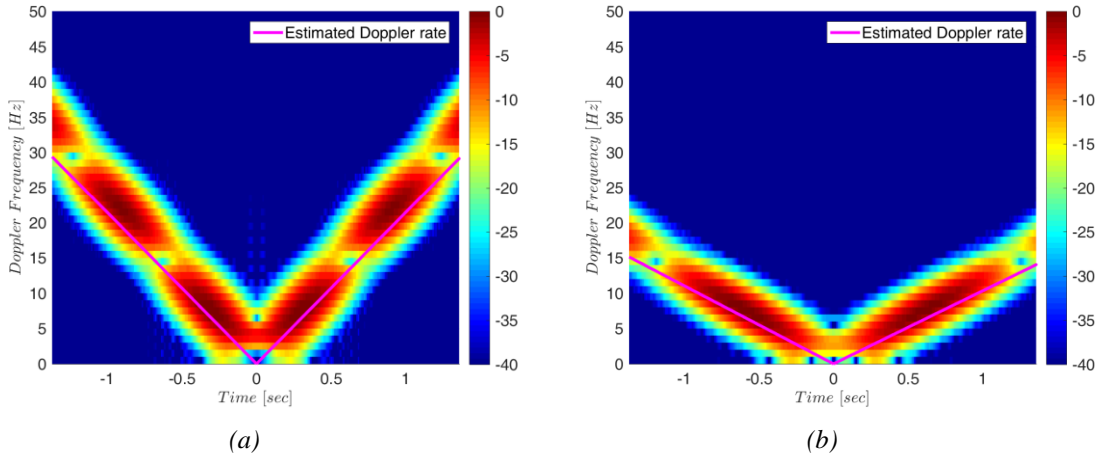


Figure 5.6 Spectrogram normalized with respect to its maximum related to (a) case study (C) and (b) case study (D).

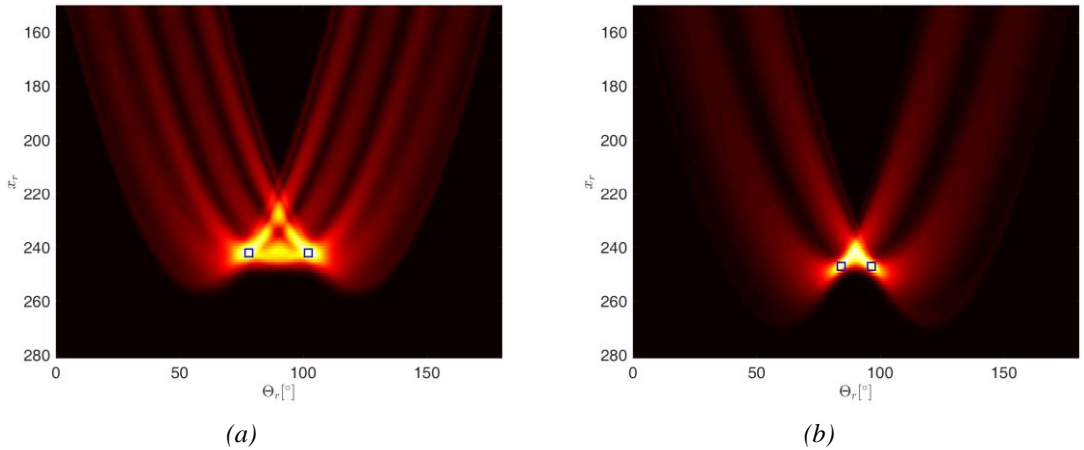


Figure 5.7 Radon transform of the spectrograms related to (a) case study (C) and (b) case study (D).

The two red straight lines superimposed to the spectrograms represent the instantaneous Doppler frequency that vary linearly with time, $f_d(t) = \tilde{\phi}(t - t_0)$ as reconstructed by means of the rough estimate of the chirp rate achieved from the Radon transform: it is noted that in all case studies a good initial Doppler rate estimation is provided. When the target does not cross the baseline perpendicularly or in the middle, the branches of the spectrogram are not symmetrical as it is observed for the case study (D) in Figure 5.6 (b) and two different values of the Doppler rate are estimated from the Radon transform. This is more noticeable if a long observation time is involved, as in Figure 5.8 showing the received signal after DC removal filter of the case study (D) for a long observation time, $T=9$ sec, and its respective spectrogram are reported.

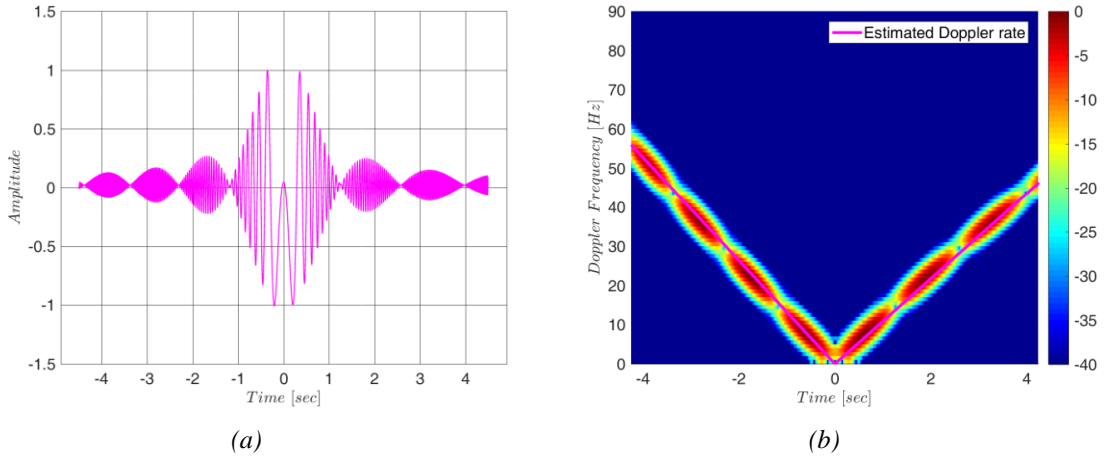


Figure 5.8 (a) Received signal after DC removal filter when the target crosses the baseline with an angle of 45° and at $L/4$ from the RX for a long observation time and (b) its spectrogram normalized with respect to its maximum value.

In this case, the initial value of the Doppler rate, $\tilde{\phi}$ may be set equal to the mean value of the estimated Doppler rates from the two branches of the spectrogram.

By this time, after the preliminary estimation of the Doppler rate, $\tilde{\phi}$, and considering that in this scenario we are interested in the detection of small targets, the impulse response in eq. (5.2) for each case study of Table 5.2 is constructed considering (i) different values of the Doppler rate in the range $\check{\phi} = [\tilde{\phi} - 0.9\tilde{\phi} : \delta\check{\phi} : \tilde{\phi} + \tilde{\phi}]$, and (ii) different values of the main lobe width in the range $\theta = [\tilde{\theta} - 0.9\tilde{\theta} : \delta\theta : \tilde{\theta} + 3\tilde{\theta}]$ where $\tilde{\theta} = \tilde{\phi} \frac{l'_h}{v'}$ with l'_h and v' relative to small

targets as UAVs for example. In accordance with the consideration in the section 5.2.1 the Doppler rate step is chosen in order that the maximum phase error is smaller than $\pi/4$ and the main lobe width step is chosen in order that the energy loss is not more than 10%. Therefore, the Doppler rate step is set $\delta\ddot{\phi} = 1/T^2 = 0.095$ being $T=3.24$ sec and the main lobe width step is set $\delta\theta = 0.1$. Figure 5.9 and Figure 5.10 show the cost function $\Delta(\ddot{\phi}, \theta)$ (normalized with respect to its maximum value) as a function of the normalized Doppler rate error and normalized main lobe width error.

$\ddot{\phi}^0$ and θ^0 are the theoretical value of the Doppler rate and main lobe width respectively (different for the different target trajectories).

In all cases the highest value of $\Delta(\ddot{\phi}, \theta)$ occurs in (0,0): hence we can state that in all the case studies both the Doppler rate and the main lobe width are well estimated.

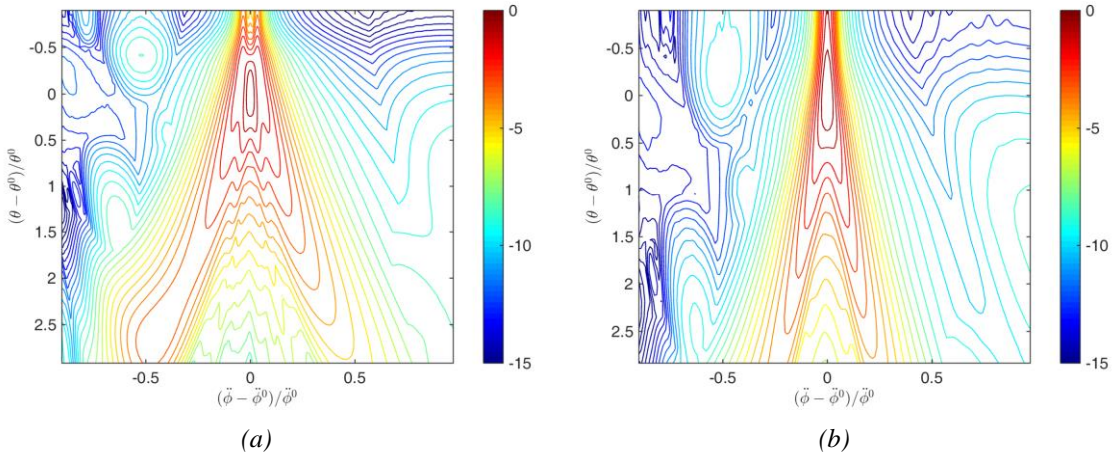


Figure 5.9 Contour plot of $\Delta(\ddot{\phi}, \theta)$ as function of the normalized Doppler rate error and of the normalized main lobe width error (a) for a perpendicular and midpoint crossing baseline, (A) and (b) for a midpoint and non-perpendicular crossing baseline, (B).

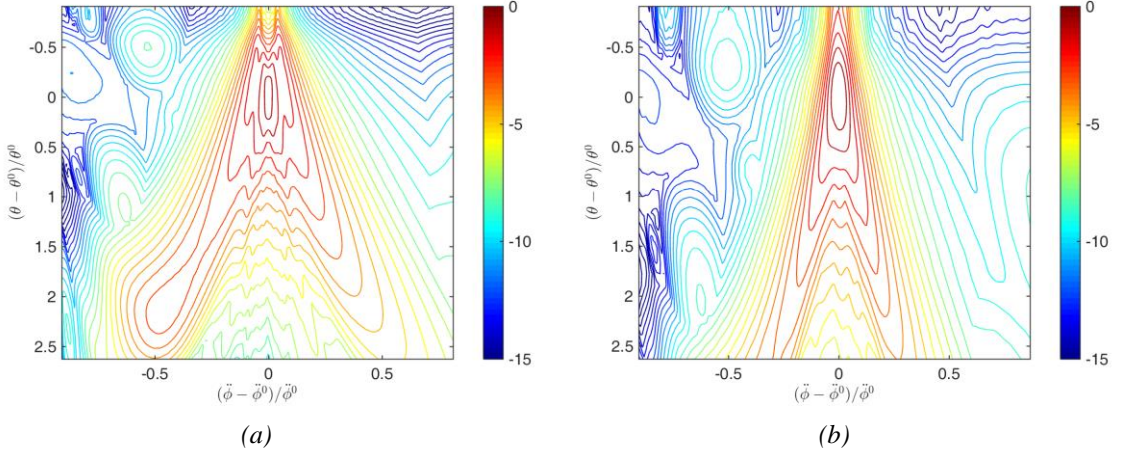


Figure 5.10 Contour plot of $\Delta(\phi, \theta)$ as function of the normalized Doppler rate error and of the normalized main lobe width error (a) for a perpendicular and non-midpoint crossing baseline, (C) and (b) for a non-midpoint and non-perpendicular crossing baseline, (D).

The $\Delta(\phi, \theta)$ cut along Doppler rate axis and along the main lobe width axis are shown in Figure 5.11.

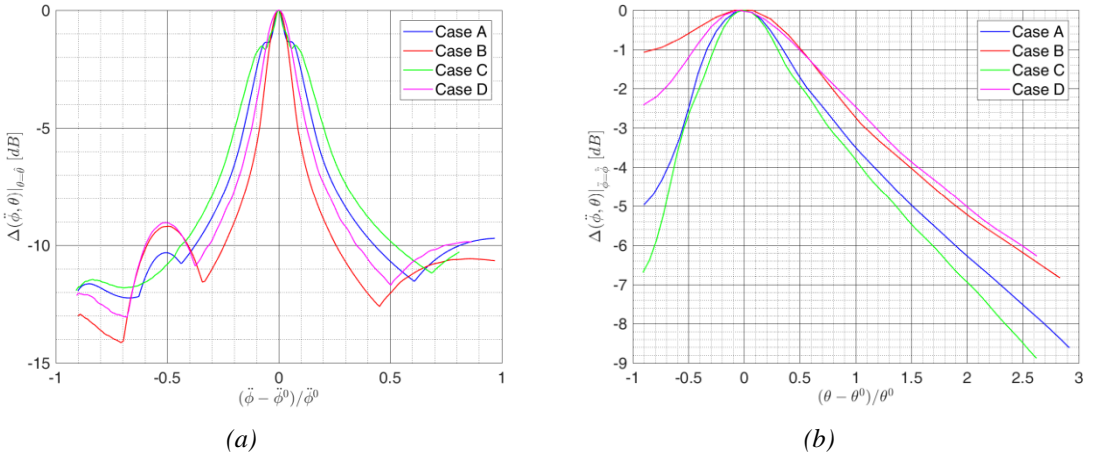


Figure 5.11 (a) $\Delta(\phi, \theta)|_{\theta=\theta^0}$ cut along the Doppler rate axis and (b) $\Delta(\phi, \theta)|_{\phi=\phi^0}$ cut along the main lobe width axis.

As expected a peak in zero that corresponds to the Doppler rate and main lobe width of the target of interest is noted. In addition, we also note that the effect of pattern error is far less than that of Doppler rate error. This is consistent with the considerations in [10] and [8] (see Section 2.6) where it was shown that the cross-correlation of the signal at the output of the DC removal

filter with a set of reference function for the estimation of the target motion parameters depends more on the phase signature presenting fast variation than on the envelope signature that varies more slowly.

All the results reported in this section refers to a noise free condition. In the following the performance of the two-dimensional filter bank approach proposed will be investigated under different noise conditions.

5.3 Accuracy performance analysis

In this section an accuracy analysis related to the estimation of the target parameters of interest is provided. Initially, we want to know the optimum achievable accuracy on the estimation of the target parameters that can be obtained by observing the samples of the signal u_i for $i=1, \dots, N$ at the output of the DC removal filter in CVD scheme for a specific target characterized by a certain signal-to-noise ratio. This leads us to the definition of the signal-to-noise ratio at the output of the Maximum Likelihood detector that coherently combines the N samples of the received signal namely the GLRT-1 detector derived in Section 4.2.1.1 but with the target signal phase known. By deriving the log-likelihood function $\log \{P_r(\mathbf{r}/H_1)/P_r(\mathbf{r}/H_0)\}$ being $P_r(\mathbf{r}/H_1)$ and $P_r(\mathbf{r}/H_0)$ defined in eq. (3.8), we obtain:

$$x_{ML} = \Re \left\{ \frac{e^{-\angle \beta} \mathbf{s}_{t0}^H (\mathbf{r} - \alpha \mathbf{s}_{d0})}{\sqrt{\mathbf{s}_{t0}^H \mathbf{s}_{t0} \sigma_n^2}} \right\} \quad (5.7)$$

It is clear from eq. (5.7) that the $SNR_{ML} \equiv SNR$ is:

$$SNR = 2 \frac{|\beta|^2 \mathbf{s}_{t0}^H \mathbf{s}_{t0}}{\sigma_n^2} \quad (5.8)$$

Moreover, in accordance with the definition of the direct signal to noise ratio, DNR in eq. (3.6), the SNR may be written as:

$$SNR = 2DNR \frac{|\beta|^2}{|\alpha|^2} \mathbf{s}_{t0}^H \mathbf{s}_{t0} \quad (5.9)$$

where all the parameters in eq. (5.9) are defined in Section 3.2.

Finally, the CRLB is derived and the performance of the proposed technique is investigated via Monte Carlo simulations in terms of accuracy and compared with the derived CRLB. The same reference scenario of the Table 5.1 and the same four case studies of the Table 5.2 are analyzed.

5.3.1 Cramer Rao Lower Bound

We derive first the joint probability density function of the signal $u(t)$. In agreement with the signal model at the output of the DC removal filter discussed in Section 3.3 the i -th sample u_i can be approximated as a Gaussian variate with mean value μ_{u_i} and variance $\sigma_{u_i}^2$. The mean value of u_i equal to the useful component, s_{ui} defined in eq. (3.11) after some simple manipulations that exploits the Taylor approximations in eqs. (4.28) and (4.30) may be written as:

$$\mu_{u_i} = -2M_d M_t \text{sinc}[\theta(t_i - t_0)] \sin[\pi\ddot{\phi}(t_i - t_0)^2] \quad (5.10)$$

where M_d is the amplitude of the received direct signal and M_t is the peak amplitude of the received target signal defined both in Section 3.2. By exploiting the eq.(4.30) we have $M_t = \frac{l_v l_h}{\lambda} \frac{L^2}{y_0(L-y_0)} \frac{v_x}{v} M_d$. In accordance with the consideration in Section 3.3 that the random component after DC removal filter is still white Gaussian noise, it is easy to obtain the variance of u_i by substituting the eq. (4.28) and eq. (4.30):

$$\begin{aligned} \sigma_{u_i}^2 = & 2\sigma_n^2 \{ M_d^2 + M_t^2 \text{sinc}^2[\theta(t_i - t_0)] \} \\ & - 4\sigma_n^2 M_d M_t \text{sinc}[\theta(t_i - t_0)] \sin[\pi\ddot{\phi}(t_i - t_0)^2] \end{aligned} \quad (5.11)$$

As the target signal component is weak its square envelope in the eq. (5.11) gives a negligible contribution and the variance $\sigma_{u_i}^2$ may be approximated as:

$$\sigma_{u_i}^2 \cong 2\sigma_n^2 \{ M_d^2 - 2M_d M_t \text{sinc}[\theta(t_i - t_0)] \sin[\pi\ddot{\phi}(t_i - t_0)^2] \} \quad (5.12)$$

The primary signal parameters of interest to be estimated include the Doppler rate, the baseline crossing instant and the main lobe width of the pattern signature ($\boldsymbol{\vartheta}^A \triangleq [\ddot{\phi} \ t_0 \ \theta]$). These parameters will allow us to estimate the target motion parameters which is addressed in Section 5.4.

It is clear from the eq. (5.10) and eq. (5.12) that the mean value and the variance depends also on the amplitude of the direct and target signal and on the noise variance ($\boldsymbol{\vartheta}^B \triangleq [M_d M_t \sigma_n]$). In order to assess the impact of these parameters on the estimation of the primary parameters of interest we define the vector of the unknowns $\boldsymbol{\vartheta} \triangleq [\boldsymbol{\vartheta}^A \boldsymbol{\vartheta}^B] = [\ddot{\phi} t_0 \theta M_d M_t \sigma_n]$.

In agreement with the Gaussian assumption the joint density probability function of \mathbf{u} parametrized by the unknown parameters vector $\boldsymbol{\vartheta}$ is given by:

$$p(\mathbf{u}|\boldsymbol{\vartheta}) = \prod_{i=1}^N \left[\frac{1}{\sqrt{2\pi\sigma_{u_i}^2}} e^{-\frac{(u_i - \mu_{u_i})^2}{2\sigma_{u_i}^2}} \right] \quad (5.13)$$

Taking the logarithm and substituting the expressions of μ_{u_i} and $\sigma_{u_i}^2$ defined in the eq. (5.10) and eq. (5.12) respectively we obtain the log-likelihood function:

$$\begin{aligned} \ln p(\mathbf{u}|\boldsymbol{\vartheta}) = & -N \ln\{\sigma_n\} \\ & -\frac{1}{2} \sum_{n=1}^N \ln\{[M_d^2 - 2M_d M_t \text{sinc}[\theta(t_i - t_0)] \sin[\pi\ddot{\phi}(t_i - t_0)^2]]\} \\ & -\frac{1}{4\sigma_n^2} \sum_{n=1}^N \frac{\{u_i + 2M_d M_t \text{sinc}[\theta(t_i - t_0)] \sin[\pi\ddot{\phi}(t_i - t_0)^2]\}^2}{M_d^2 - 2M_d M_t \text{sinc}[\theta(t_i - t_0)] \sin[\pi\ddot{\phi}(t_i - t_0)^2]} \\ & + C \end{aligned} \quad (5.14)$$

where C is a constant independent from the parameters collected in $\boldsymbol{\vartheta}$.

The CRLB states that given the vector parameter $\boldsymbol{\vartheta}$ its unbiased estimate $\hat{\boldsymbol{\vartheta}}$ satisfies the following inequality:

$$\sigma_{\hat{\vartheta}_r}^2 \geq J_{r,r}^{-1}(\boldsymbol{\vartheta}) \quad (5.15)$$

for $r=1, \dots, 6$ in our case and where $J(\boldsymbol{\vartheta})$ is the Fisher Information Matrix (FIM) (6×6) given as:

$$J(\boldsymbol{\vartheta}) = E \left\{ \frac{\partial}{\partial \boldsymbol{\vartheta}} \ln p(\mathbf{u}|\boldsymbol{\vartheta}) \left[\frac{\partial}{\partial \boldsymbol{\vartheta}} \ln p(\mathbf{u}|\boldsymbol{\vartheta}) \right]^T \right\} \quad (5.16)$$

where $\frac{\partial}{\partial \boldsymbol{\vartheta}}\{\cdot\}$ denotes the partial derivative with respect to $\boldsymbol{\vartheta}$. In order to simplify the analysis the FIM can be written in the compact form by partitioning it as follows:

$$J(\boldsymbol{\vartheta}) = \begin{bmatrix} J^A & J^{AB} \\ J^{AB} & J^B \end{bmatrix} \quad (5.17)$$

where the upper left J^A is a 3x3 matrix that denotes the FIM of the primary parameters of interest $\boldsymbol{\vartheta}^A$, J^B is a 3x3 matrix that denotes the FIM of the parameters of secondary interest $\boldsymbol{\vartheta}^B$ and J^{AB} denotes a 3x3 matrix collecting the off diagonal elements of $J(\boldsymbol{\vartheta})$ that measure how the parameters of secondary interest $\boldsymbol{\vartheta}^B$ influence the estimation of the desired parameters in $\boldsymbol{\vartheta}^A$. According to the partitioned matrix inverse lemma the inverse of the Fisher information matrix, C_{CRLB} of the primary parameters of interest is:

$$C_{CRLB} = \left(J^A - J^{AB} J^B^{-1} J^{AB} \right)^{-1} \quad (5.18)$$

In particular, the variances of the estimation errors of the parameters of interest are the elements on the main diagonal of this matrix. By carrying out the derivatives and the expectations in eq. (5.15) even here not reported for the sake of compactness it can be shown that FIM can be approximated as a block diagonal matrix.

Figure 5.12 (a) and Figure 5.12 (b) report the normalized elements of FIM, $\hat{J}_{r,k}(\boldsymbol{\vartheta}) = J_{r,k}(\boldsymbol{\vartheta}) / \sqrt{J_{r,r}(\boldsymbol{\vartheta}) J_{k,k}(\boldsymbol{\vartheta})}$ for four different values of SNR related to the case study (A) and (B) respectively. Figure 5.13 reports similar results for the case study (C) and (D).

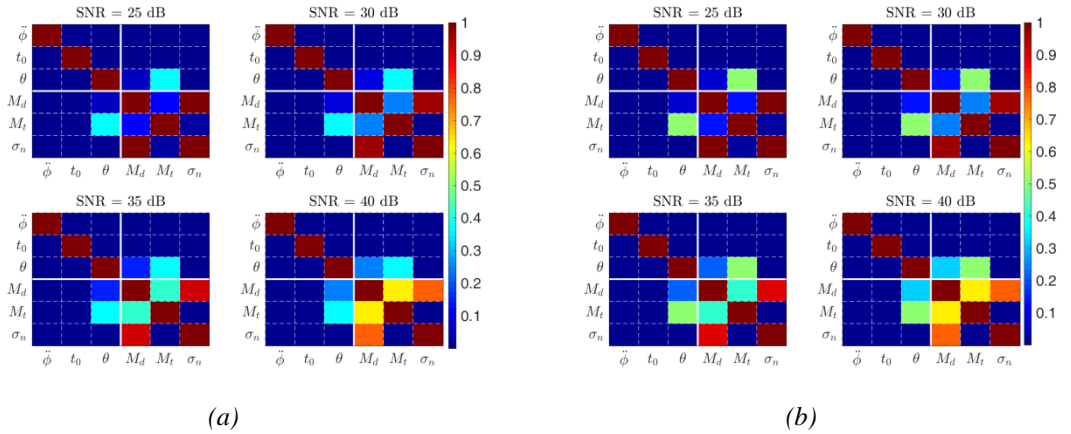


Figure 5.12 Normalized elements of $J(\boldsymbol{\vartheta})$ as function of SNR (a) of the case study (A) and (b) of the case study (B).

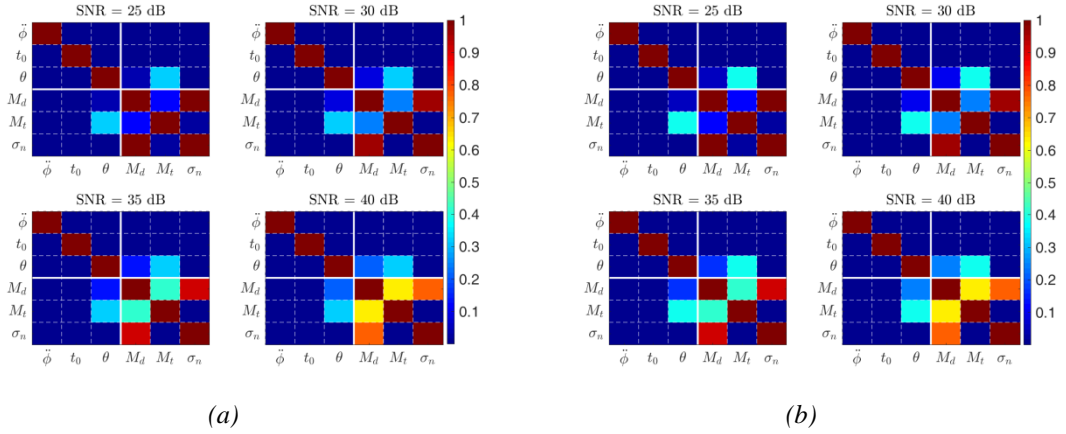


Figure 5.13 Normalized elements of $\mathbf{J}(\boldsymbol{\theta})$ as function of SNR (a) of the case study (C) and (b) of the case study (D).

Some comments are in order:

(i) the elements of \mathbf{J}^{AB} block matrix (see upper right and down left block matrix in Figure 5.12 and Figure 5.13) give a negligible contribution compared to the elements on the main diagonal of \mathbf{J}^A for all the SNR values. $\hat{J}_{3,5} = \hat{J}_{5,3}$ is the element with the highest contribution in all case studies and this is expected as M_t and θ are respectively the peak and the main lobe width of the pattern signature.

(ii) the off diagonal elements of \mathbf{J}^A (upper left block matrix in Figure 5.12 and Figure 5.13) give a negligible contribution compared to the diagonal elements of \mathbf{J}^A for all the SNR value and for all the case studies.

In accordance with (i) we first assume that the estimation of the desired parameters in $\boldsymbol{\vartheta}^A$ is independent from the parameters in $\boldsymbol{\vartheta}^B$. Therefore the FIM in the eq. (5.16) may be simplified as:

$$\mathbf{J}(\boldsymbol{\vartheta}) \cong \begin{bmatrix} \mathbf{J}^A & \mathbf{0}_{3,3} \\ \mathbf{0}_{3,3} & \mathbf{J}^B \end{bmatrix} \quad (5.19)$$

having approximated $\mathbf{J}^{AB} \approx \mathbf{0}_{3,3}$ where $\mathbf{0}_{m,m}$ is a $m \times m$ zero matrix. This simplify the computation of the CRLB of the primary parameters of interest, $\mathbf{C}_{CRLB}^{Approx-1} = \mathbf{J}^A{}^{-1}$. Moreover in accordance with the observation (ii) we assume that the estimates of the Doppler rate,

baseline crossing instant and main lobe width are decoupled. Thus the 3×3 matrix \mathbf{J}^A can be simplified as a diagonal matrix and consequently the $\mathbf{C}_{CRLB}^{Approx-2} = \text{diag} \{J_{1,1}^{A-1}, J_{2,2}^{A-1}, J_{3,3}^{A-1}\}$.

Focusing in the block matrix, \mathbf{J}^A and based on the log-likelihood function in the eq. (5.14) the element $J_{r,r}^A$ after some approximation detailed in the Appendix F may be written as:

$$\tilde{J}_{r,r}^A \cong \mathbf{C}_{\boldsymbol{\theta}_r} \mathbf{A} \mathbf{C}_{\boldsymbol{\theta}_r}^T = \sum_{i=1}^N \sigma_{u_i}^2 \mathbf{C}_{\boldsymbol{\theta}_{ri}}^2 \quad (5.20)$$

where $\mathbf{A} = \text{diag}\{\sigma_{u_1}^2, \sigma_{u_2}^2, \dots, \sigma_{u_N}^2\}$ and $\mathbf{C}_{\boldsymbol{\theta}_r}$ is a $N \times 1$ column vector collecting the approximated coefficient of the partial derivatives with respect to $\boldsymbol{\theta}_r$ defined in the eq. (F. 6) of the Appendix F. Finally, bounds on the error standard deviation of the Doppler rate, baseline crossing instant and main lobe width estimates are obtained from the above approximation, $\mathbf{C}_{CRLB}^{Approx-3} = \text{diag}\{\tilde{J}_{1,1}^{A-1}, \tilde{J}_{2,2}^{A-1}, \tilde{J}_{3,3}^{A-1}\}$, as follows:

$$\begin{cases} CRLB_{\ddot{\phi}} = \frac{1}{\pi\sqrt{2DNR}} \frac{M_d}{M_t} \left\{ \sum_{i=1}^N \text{sinc}^2[\theta(t_i - t_0)] \cos^2[\pi\ddot{\phi}(t_i - t_0)^2] (t_i - t_0)^4 \right\}^{-1/2} \\ CRLB_{t_0} = \frac{1}{2\pi\dot{\phi}\sqrt{2DNR}} \frac{M_d}{M_t} \left\{ \sum_{i=1}^N \text{sinc}^2[\theta(t_i - t_0)] \cos^2[\pi\ddot{\phi}(t_i - t_0)^2] (t_i - t_0)^2 \right\}^{-1/2} \\ CRLB_{\theta} = \frac{\theta}{\sqrt{2DNR}} \frac{M_d}{M_t} \left\{ \sum_{i=1}^N \sin^2[\pi\ddot{\phi}(t_i - t_0)^2] \cos^2[\pi\theta(t_i - t_0)] \right\}^{-1/2} \end{cases} \quad (5.21)$$

Figure 5.14 reports the theoretical and the approximated normalized error standard deviation of the three parameters of interest as function of the SNR when the target crosses the baseline in the middle with an angle $\varphi = 0^\circ$, case (A) (Figure 5.14 (a)) and with an angle $\varphi = 45^\circ$, case (B) (Figure 5.14 (b)). The normalized error standard deviation of the Doppler rate and main lobe width are defined as the ratio of the error standard deviation obtained from the different approximation of the CRLB to their theoretical value, $\ddot{\phi}^0$ and θ^0 respectively. Meanwhile as we assume that the target crosses the baseline at time $t=0$ sec the normalized error standard deviation of the crossing time is defined as the ratio of the error standard deviation obtained from the different approximation of the CRLB to the time step (inverse of the sampling frequency). For example for an SNR=30 dB and when the target crosses the baseline in the middle with an angle $\varphi = 0^\circ$ (see Figure 5.14 (a)) we can obtain an accuracy of the order of the time step for the crossing time having set the sampling frequency equal to 1000 Hz. It is quite apparent that the approximated expressions of the CRLB in eq.(5.21) provides an accurate fit to the theoretical expressions.

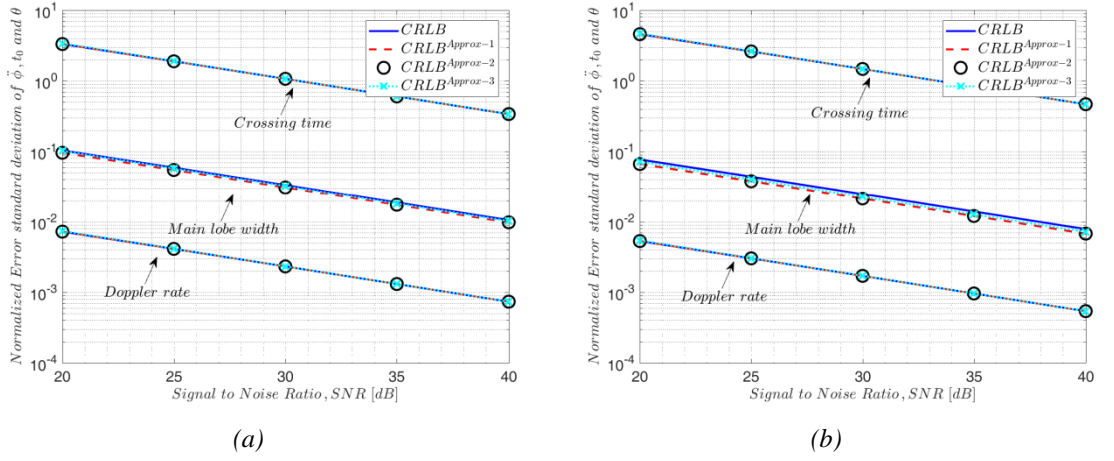


Figure 5.14 Theoretical and approximated accuracy of the Doppler rate, crossing time and main lobe width against SNR (a) for the case study (A) and (b) for the case study (B).

Figure 5.15 reports similar results for a target crossing the baseline at a distance $L/4$ from RX with an angle $\varphi = 0^\circ$, case (C) (Figure 5.15 (a)) and with an angle $\varphi = 45^\circ$, case (D) (Figure 5.15 (b)).

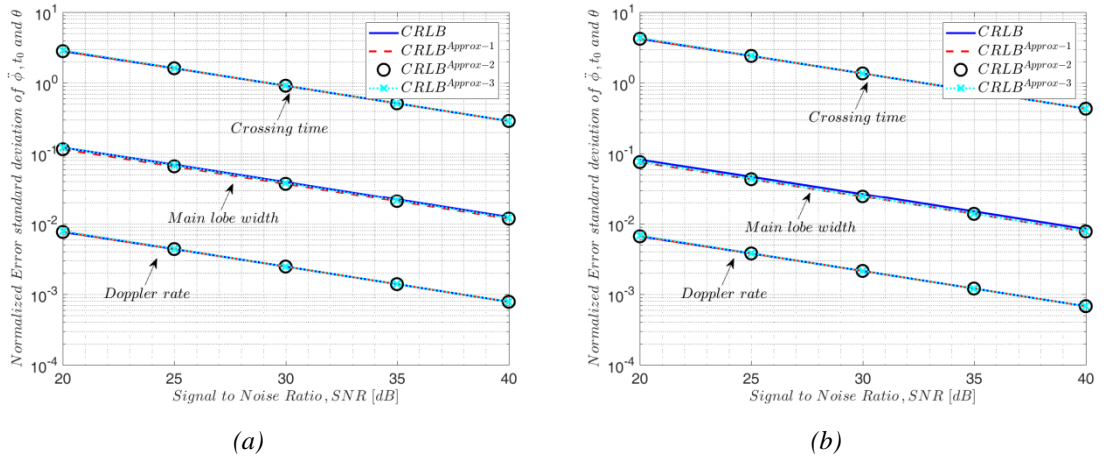


Figure 5.15 Theoretical and approximated accuracy of the Doppler rate, crossing time and main lobe width against SNR for the case study (a) (C) and (b) (D).

As previously, the approximated expressions of the CRLB provides an accurate fit to the theoretical expressions.

It is worth mentioning here that in some cases for non-perpendicular and non-midpoint crossing baseline the approximation of the phase signature in eq. (4.28) provides a non-negligible phase error with respect to the effective phase variation in eq. (3.2) for long

observation time and a Taylor expansion at third order or fourth order will be necessary. We chose $\pi/4$ as the maximum tolerable phase error. For observation time that provides a phase error smaller than $\pi/4$ the CRLB derived is valid. On the other hand observation times smaller than the main lobe width will not allow an accurate estimation of θ .

Figure 5.16 shows the phase error approximation (i.e. $\phi(t)$ in eq. (3.2) - $\phi(t)$ in eq. (4.28)) as function of the observation time for all the case studies. We note that the case study (D) presents a greater phase error approximation with respect to the other case studies.

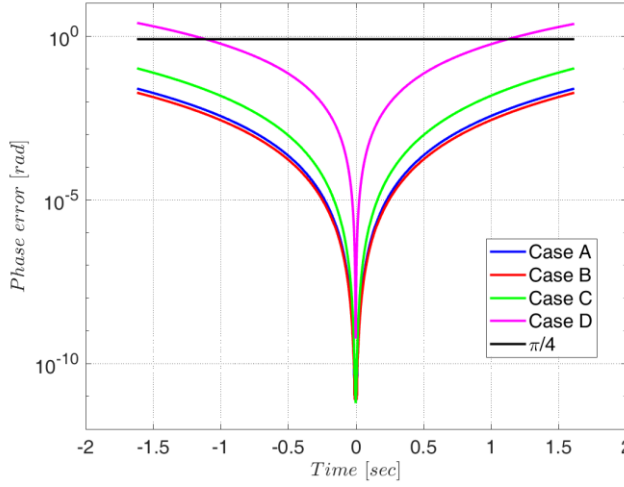


Figure 5.16 Phase error approximation as function of the observation time, T for all the case studies.

5.3.2 Performance comparison

In this section the performance of the 2D filter bank technique is investigated via Monte Carlo simulations in terms of accuracy and compared with the CRLB derived in the previous section.

We assume that the estimated parameters by the bank in eq. (5.6) suffers from errors:

$$\begin{cases} \hat{\phi} = \ddot{\phi}^0 + \delta_{\ddot{\phi}} \\ \hat{t}_0 = t_0^0 + \delta_{t_0} \\ \hat{\theta} = \theta^0 + \delta_{\theta} \end{cases} \quad (5.22)$$

characterized by a mean value $\mu_{\ddot{\phi}}, \mu_{t_0}, \mu_{\theta}$ and variances $\sigma_{\ddot{\phi}}^2, \sigma_{t_0}^2$ and σ_{θ}^2 being $\ddot{\phi}^0, t_0^0$ and θ^0 their theoretical value. The performance of this technique is investigated for the four different target trajectories defined in Table 5.2 and the analysis proved the 2D filter bank approach to be unbiased, $\mu_{\ddot{\phi}} = \mu_{t_0} = \mu_{\theta} \cong 0$. For all the case studies we have considered a 2D filter bank with Doppler rate in the range $\left[\ddot{\phi}^0 - 5CRLB_{\ddot{\phi}} : \ddot{\phi}^0 + 5CRLB_{\ddot{\phi}} \right]$ and main lobe width in the range $\left[\theta^0 - 5CRLB_{\theta} : \theta^0 + 5CRLB_{\theta} \right]$ where $CRLB_{\ddot{\phi}}$ and $CRLB_{\theta}$ are defined in eq. (5.21).

The normalized error standard deviation of the three parameters of interest as function of the SNR obtained from the Monte Carlo simulations with 1000 trials is compared with the approximated CRLB derived in Figure 5.17 (a) and Figure 5.17(b) for the case study (A) and (B) for an observation time equal to $T=3.24$ sec.

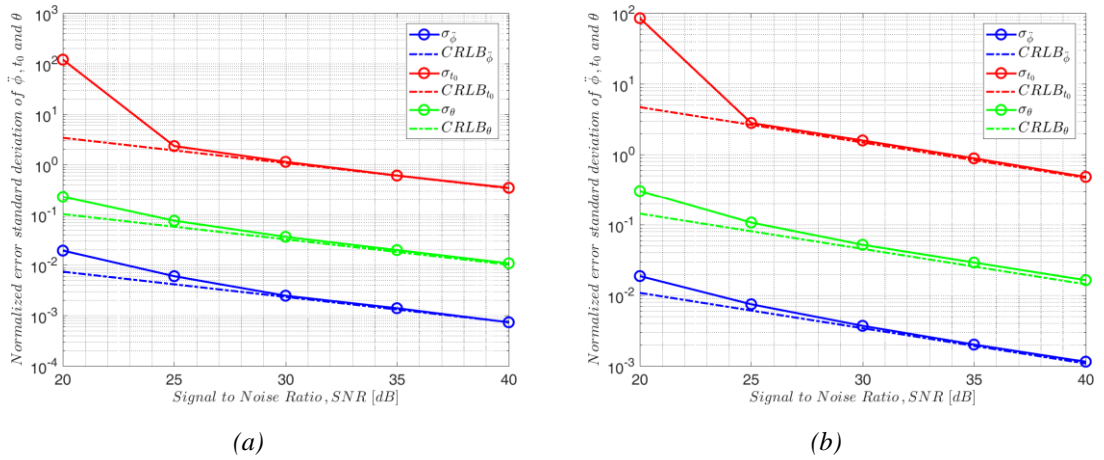


Figure 5.17 Normalized error standard deviation of the Doppler rate, the crossing time and the main lobe width against integrated SNR (a) for the case study (A) and (b) for the case study (B).

As apparent, for each parameter to be estimated, the accuracy achievable by means of the 2D filter bank technique (continuous curve) in the high SNR region approaches the corresponding approximated CRLB (dash-dotted curves). Some losses with respect to the CRLB are experienced for values of SNR below 25 dB for the Doppler rate and the main lobe width estimation. Meanwhile for values of the SNR below 25 dB the 2D filter bank gives poor estimation accuracy of the crossing time instant and greater losses with respect to the corresponding CRLB are experienced. It is worth noting that such threshold value of SNR=25

dB corresponds to a $\text{DNR} \cong 20$ dB that, in agreement with the results of the probability of detection of the CVD shown in Chapter 3 corresponds to a low probability of target detection.

Figure 5.18 (a) and Figure 5.18 (b) reports similar results for the case study (C) and (D) for the same observation time, $T=3.24$ sec. The above considerations also applies for the cases when the target crosses the baseline perpendicularly at $L/4$ from RX, case (C).

Meanwhile for the case study (D) we note that the curves of the accuracy obtained from the 2D filter bank for high SNR value shows the same trend although some extra losses are experienced with respect to the CRLB in particular for the Doppler rate. In agreement with the consideration above in Section 5.3.1, for an observation time $T=3.24$ sec the case study (D) presents a phases error approximation greater than $\pi/4$ (see Figure 5.16).

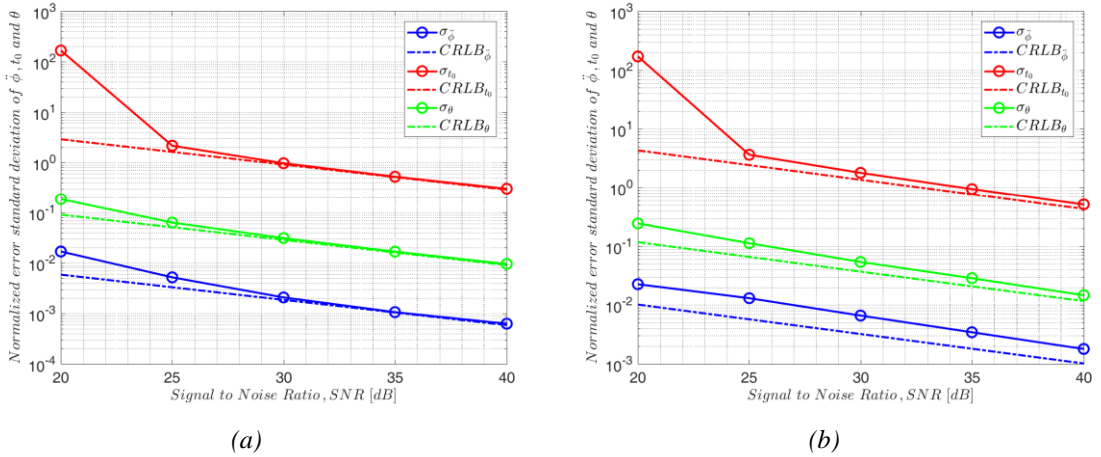


Figure 5.18 Normalized error standard deviation of the Doppler rate, the crossing time and the main lobe width against integrated SNR (a) for the case study (C) and (b) for the case study (D).

For this reason in Figure 5.19 are compared the normalized error standard deviation of the three parameters of interest obtained from the Monte Carlo simulations to approximated CRLB derived for an observation time $T \approx 2.4$ sec, time to span only the main lobe of the pattern signature that gives a phase error smaller than $\pi/4$. Is apparent that the accuracy achievable from the 2D filter bank (continuous curve) in the high SNR region approaches the corresponding approximated CRLB (dash-dotted curves).

Therefore, we can state that in all cases the Doppler rate, the crossing time and the main lobe width are accurately estimated thus proving the effectiveness of the proposed approach.

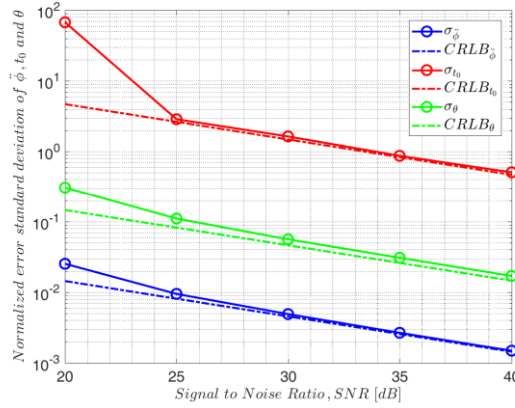


Figure 5.19 Normalized error standard deviation of the Doppler rate, the crossing time and the main lobe width against integrated SNR for the case study (D) and for an observation time equal to the main lobe.

5.4 Target motion estimation and performance analysis

The focus of this section is on the estimation of the motion parameters of moving targets following a linear trajectory firstly by means of a single baseline configuration and after by exploiting a dual receive antenna FSR configuration with small angular separation between the two baselines. From a single baseline configuration the cross-baseline velocity is estimated and its CRLB derived. Meanwhile the dual baseline ensures the possibility to estimate two parameters without a priori knowledge, the cross-baseline velocity and the baseline crossing point and also their CRLB is derived and analyzed.

5.4.1 Single baseline configuration

The coordinate system of the single baseline configuration is shown in Figure 3.1.

Exploiting the extraction of the Doppler rate from the 2D filter bank approach previously introduced and under the assumption that the baseline crossing point is known it is possible to estimate the cross-baseline velocity as follows:

$$\hat{v}_x = \sqrt{\frac{(L-y_0)y_0}{L}} \lambda \sqrt{\hat{\phi}} \quad (5.23)$$

Now the CRLB of \hat{v}_x is derived by considering firstly a Taylor expansion at first order around the estimated Doppler rate, $\hat{\ddot{\phi}}$ that provides a linearized equation:

$$\hat{v}_x = v_x^0 + \left. \frac{\partial \hat{v}_x}{\partial \hat{\ddot{\phi}}} \right|_{\ddot{\phi}^0} \delta \ddot{\phi} \quad (5.24)$$

being $v_x^0 = \sqrt{\frac{(L-y_0)y_0}{L}} \lambda \sqrt{\ddot{\phi}^0}$ the theoretical value of the cross-baseline velocity. Recall that the Doppler rate estimation, $\hat{\ddot{\phi}} = \ddot{\phi}^0 + \delta \ddot{\phi}$, suffers from errors characterized by a mean null value, $\mu_{\ddot{\phi}} \cong 0$ and a variance $\sigma_{\ddot{\phi}}^2$. By carrying out the derivate with respect to the Doppler rate the eq. (5.24) become:

$$\hat{v}_x = v_x^0 + \sqrt{\frac{(L-y_0)y_0}{L}} \lambda \frac{1}{2\sqrt{\ddot{\phi}^0}} \delta \ddot{\phi} \quad (5.25)$$

This mean the cross-baseline velocity estimation suffers from errors ($\hat{v}_x = v_x^0 + \delta v_x$) characterized by a zero mean value, $\mu_{v_x} = 0$ and variance defined as follows:

$$\sigma_{v_x}^2 = \frac{(L-y_0)y_0}{L} \frac{\lambda}{4\ddot{\phi}^0} \sigma_{\ddot{\phi}}^2 \quad (5.26)$$

The expression in eq. (5.26) is valid independently from the technique used for the estimation of the Doppler rate.

Finally, substituting the approximated CRLB of the Doppler defined in eq. (5.21), the CRLB for the estimation of the cross-baseline velocity is:

$$CRLB_{v_x} = \sqrt{\frac{(L-y_0)y_0}{L}} \lambda \frac{1}{\sqrt{\ddot{\phi}^0}} \frac{1}{2\pi\sqrt{2DNR}} \frac{M_d}{M_t} \quad (5.27)$$

$$\left\{ \sum_{i=1}^N \text{sinc}^2[\theta^0(t_i - t_0)] \cos^2[\pi \ddot{\phi}^0(t_i - t_0)^2] (t_i - t_0)^4 \right\}^{-1/2}$$

Figure 5.20 compare the normalized error standard deviation of v_x achieved through Monte Carlo simulations that exploits the Doppler rate extraction from the 2D filter bank with the CRLB previously derived (eq. (5.27)) for the case study (A) with T=3.24 sec.

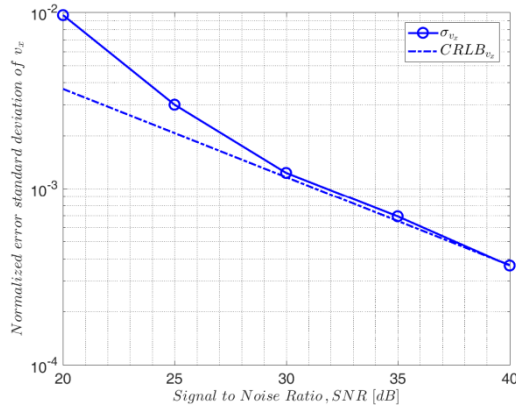


Figure 5.20 *Normalized error standard deviation of the cross-baseline velocity against integrated SNR of the case study (A).*

It is noted that the accuracy achievable from the 2D filter bank technique (continuous curve) in the high SNR region (SNR greater than 30 dB) approaches the corresponding approximated CRLB (dash-dotted curves). As expected some losses are experienced for SNR lower than 30 dB.

Despite this losses the overall performance can still be considered suitable for a practical application since an accuracy in the order of 1% is obtained for a SNR=20 dB thus proving the effectiveness of the proposed approach.

5.4.2 *Dual baseline configuration*

The coordinate system of the dual baseline configuration with the x and y axis specifying the ground plane and the target moving perpendicularly to this ground plane is shown in Figure 5.21. The first receiver, RX_1 , is placed at the origin of the coordinate system (x, y) and the second receiver, RX_2 is placed along the x-axis at a distance d from RX_1 meanwhile the transmitter, TX, is placed at $(0, L_1)$ along the y-axis. L_1 and L_2 indicate the first baseline (TX- RX_1) and the second baseline (TX- RX_2) respectively. We assume that the angular separation between the two baselines is small and therefore the target crosses the two baselines maintaining the same velocity.

It is worth mentioning here that the target direction specified by the angle φ with respect to the x-axis (see Section 3.2) implies that the target crosses the two baselines with different

angles . Moreover we assume that the target crosses the first baseline, L_1 at $t_{01}=0$ sec and the second baseline, L_2 at time $t_{02}=(L_1 - y_{01})d/(v_x L_1 + v_y d)$ being y_{01} the baseline crossing point related to the first baseline.

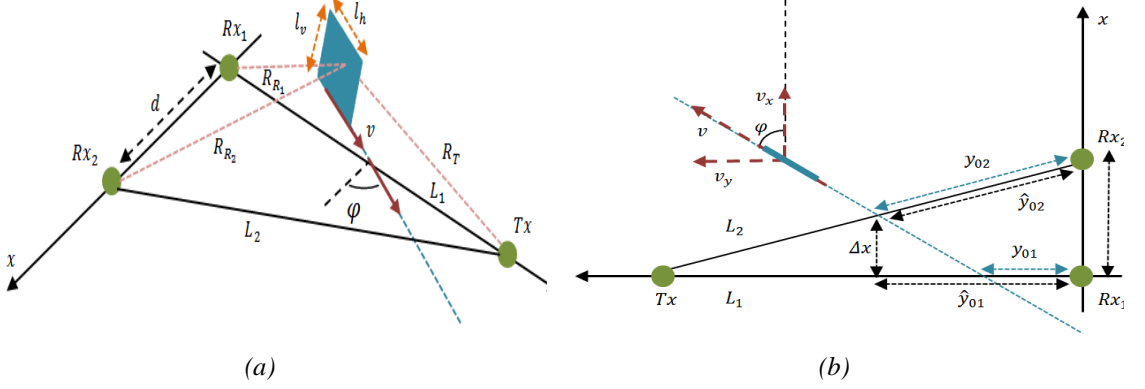


Figure 5.21 (a) Dual-baseline FSR system geometry and (b) top view of the dual-baseline FSR configuration.

Following the same approach in [53] v_x and y_{0i} for $i=1,2$ are here estimated by applying separately to the signals acquired by the two receivers, $r_1(t)$ and $r_2(t)$ the 2D filter bank technique being $\hat{\boldsymbol{\theta}}_1^A = [\hat{\phi}_1, \hat{t}_{01}, \hat{\theta}_1]$ and $\hat{\boldsymbol{\theta}}_2^A = [\hat{\phi}_2, \hat{t}_{02}, \hat{\theta}_2]$ the estimated target parameters related to the Rx_1 and Rx_2 respectively.

In agreement with the assumption of the linear trajectory, the distance covered by the target in the x -between the two baselines in the elapsed time $\Delta t = t_{02} - t_{01}$, along the x -axis, is $\Delta x = v_x \Delta t$.

In addition, drawing on this geometry (see Figure 5.21 (b)), the relation between the estimated time difference of arrival, $\widehat{\Delta t} = \hat{t}_{02} - \hat{t}_{01}$, and the estimated \hat{v}_x and \hat{y}_0 can be written as:

$$\widehat{\Delta t} = \frac{L_i - \hat{y}_{0i}}{L_i} \frac{d}{\hat{v}_x} \quad (5.28)$$

When the target crosses the baseline perpendicularly ($\varphi = 0^\circ$) the effective y_{01} is estimated. While for non-perpendicular baseline crossing angle, the estimated \hat{y}_{01} (see Figure 5.21 (b)) is not equal to the effective y_{01} and the estimation error will depend on the baseline and on the baseline crossing angle.

By exploiting the Doppler rate and the crossing times extraction from the 2D filter bank the estimated cross baseline velocity and baseline crossing point are retrieved as follows:

$$\begin{cases} \hat{v}_x = \frac{1}{\left(1 + \frac{1}{L_i \lambda \hat{\phi}_i} \frac{d^2}{\widehat{\Delta t}^2}\right)} \frac{d}{\widehat{\Delta t}} \\ \hat{y}_{0i} = \frac{1}{\left(\frac{1}{L_i} + \lambda \hat{\phi}_i \frac{\widehat{\Delta t}^2}{d^2}\right)} \end{cases} \quad (5.29)$$

which is a nonlinear system of equations. By substituting in eq. (5.29) the baseline length, L_i and the corresponding estimated Doppler rate, $\hat{\phi}_i$ for $i=1,2$ we should obtain the same value of the cross-baseline velocity, $\hat{v}_{x1} = \hat{v}_{x2} = \hat{v}_x$. For a long baseline the distance covered by the target between the two baselines can be assumed equal to the spacing between the two antennas, d and the cross baseline velocity may be approximated as $\hat{v}_x \approx d / \widehat{\Delta t}$.

The CRLB of \hat{v}_x and \hat{y}_{0i} is derived by considering firstly a Taylor expansion at first order around the estimated Doppler rate, $\hat{\phi}_i$ and estimated time delay, $\widehat{\Delta t}$ that provides an equivalent linearized system:

$$\begin{cases} \hat{v}_x = v_x^0 + \left. \frac{\partial \hat{v}_x}{\partial \hat{\phi}_i} \right|_{(\hat{\phi}_i^0, \Delta t^0)} \delta \ddot{\phi}_i + \left. \frac{\partial \hat{v}_x}{\partial \widehat{\Delta t}} \right|_{(\hat{\phi}_i^0, \Delta t^0)} \delta \Delta t \\ \hat{y}_{0i} = y_{0i}^0 + \left. \frac{\partial \hat{y}_{0i}}{\partial \hat{\phi}_i} \right|_{(\hat{\phi}_i^0, \Delta t^0)} \delta \ddot{\phi}_i + \left. \frac{\partial \hat{y}_{0i}}{\partial \widehat{\Delta t}} \right|_{(\hat{\phi}_i^0, \Delta t^0)} \delta \Delta t \end{cases} \quad (5.30)$$

being $v_x^0 = \frac{1}{\left(1 + \frac{1}{L_i \lambda \ddot{\phi}_i^0} \frac{d^2}{\Delta t^{0^2}}\right)} \frac{d}{\Delta t^0}$, $y_{0i}^0 = \frac{1}{\left(\frac{1}{L_i} + \lambda \ddot{\phi}_i^0 \frac{\Delta t^{0^2}}{d^2}\right)}$ the theoretical value of v_x and y_{0i} respectively.

Recall that the Doppler rate and the crossing time estimation, $\hat{\phi} = \ddot{\phi}^0 + \delta \ddot{\phi}$, $\hat{t}_0 = t_0^0 + \delta t_0$ suffers from errors characterized by a mean null value, $\mu_{\ddot{\phi}} = \mu_{t_0} \cong 0$ and variance $\sigma_{\ddot{\phi}}^2$ and $\sigma_{t_0}^2$ respectively. Therefore the time delay estimation, $\widehat{\Delta t} = \hat{t}_{02} - \hat{t}_{01} = \Delta t^0 + \delta \Delta t$ suffers from errors characterized by a mean null value and variance $\sigma_{\Delta t}^2 = 2\sigma_{t_0}^2$.

By carrying out the derivatives and after some simple manipulations the eq. (5.30) become:

$$\begin{cases} \hat{v}_x = v_x^0 + \frac{d^3 L_i \lambda \Delta t^0}{(L_i \lambda \ddot{\phi}_i^0 \Delta t^{0^2} + d^2)^2} \delta \ddot{\phi}_i + \frac{L_i \lambda \ddot{\phi}_i^0 d^3 - d L_i^2 \lambda^2 \ddot{\phi}_i^{0^2} \Delta t^{0^2}}{(L_i \lambda \ddot{\phi}_i^0 \Delta t^{0^2} + d^2)^2} \delta \Delta t \\ \hat{y}_{0i} = y_{0i}^0 - \frac{L_i^2 d^2 \lambda \Delta t^{0^2}}{(\lambda L_i \ddot{\phi}_i^0 \Delta t^{0^2} + d^2)^2} \delta \ddot{\phi}_i - \frac{2 L_i^2 d^2 \lambda \ddot{\phi}_i^0 \Delta t^0}{(\lambda L_i \ddot{\phi}_i^0 \Delta t^{0^2} + d^2)^2} \delta \Delta t \end{cases} \quad (5.31)$$

This means the cross-baseline velocity and the baseline crossing point estimation suffers from errors ($\hat{v}_x = v_x^0 + \delta v_x$, $\hat{y}_{0i} = y_{0i}^0 + \delta y_{0i}$) characterized by a zero mean value, $\mu_{v_x} = \mu_{y_{0i}} = 0$ and variances defined as follows:

$$\begin{cases} \sigma_{v_x}^2 = \frac{L_i^2 d^6 \lambda^2 \Delta t^{0^2}}{(L_i \lambda \ddot{\phi}_i^0 \Delta t^{0^2} + d^2)^4} \sigma_{\ddot{\phi}}^2 + \frac{2 [L_i d^3 \lambda \ddot{\phi}_i^0 - L_i^2 d \lambda^2 \ddot{\phi}_i^{0^2} \Delta t^{0^2}]^2}{(L_i \lambda \ddot{\phi}_i^0 \Delta t^{0^2} + d^2)^4} \sigma_{\Delta t}^2 \\ \sigma_{y_{0i}}^2 = \frac{L_i^4 d^4 \lambda^2 \Delta t^{0^4}}{(L_i \lambda \ddot{\phi}_i^0 \Delta t^{0^2} + d^2)^4} \sigma_{\ddot{\phi}}^2 + \frac{8 L_i^4 d^4 \lambda^2 \ddot{\phi}_i^{0^2} \Delta t^{0^2}}{(L_i \lambda \ddot{\phi}_i^0 \Delta t^{0^2} + d^2)^4} \sigma_{\Delta t}^2 \end{cases} \quad (5.32)$$

The expression in eq. (5.32) is valid for a dual baseline configuration with small angular separation between the two baselines independently from the technique used for the estimation of the Doppler rate and of the time difference of arrival. Finally, substituting the approximated CRLB of the Doppler and crossing time instant defined in eq. (5.21) the CRLB for the estimation of the cross-baseline velocity and of the baseline crossing point are:

$$\begin{cases} CRLB_{v_x} = \frac{1}{\pi \sqrt{2DNR}} \frac{M_d}{M_t} \frac{L_i d^3 \lambda}{(L_i \lambda \ddot{\phi}_i^0 \Delta t^{0^2} + d^2)^2} \\ CRLB_{y_0} = \frac{1}{\pi \sqrt{2DNR}} \frac{M_d}{M_t} \frac{L_i^2 d^2 \lambda \Delta t^{0^2}}{(L_i \lambda \ddot{\phi}_i^0 \Delta t^{0^2} + d^2)^2} \end{cases} \quad (5.33)$$

Figure 5.22 compare the normalized error standard deviation of v_x and y_{01} achieved through Monte Carlo simulation to the CRLB previously derived (eq. (5.33)) for the case study (A) with $T=3.24$ sec. It is noted that the accuracy achievable by means of the 2D filter bank technique (continuous curve) in the high SNR region (SNR greater than 30 dB) approaches the

corresponding approximated CRLB (dash-dotted curves) for both cross-baseline velocity and baseline crossing point. As previously some losses are experienced for SNR lower than 30 dB.

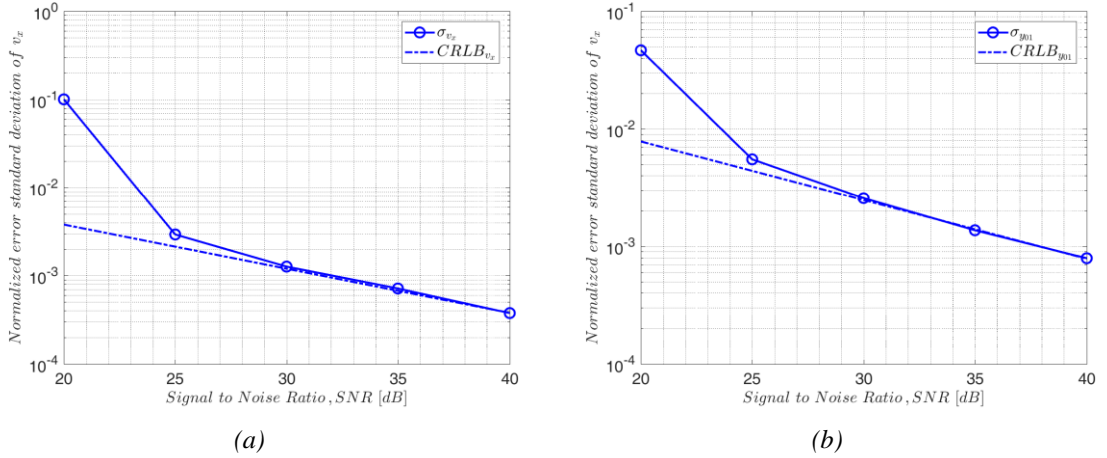


Figure 5.22 Normalized error standard deviation (a) of the cross-baseline velocity and (b) of the baseline crossing point against integrated SNR of the case study (A).

Considering a multi-node FSR configuration the kinematic information extraction may be improved and all the target motion parameters may be estimated, [14] nevertheless using a dual baseline configuration we observe that without a priori knowledge it is possible to unambiguously estimate two parameters with high accuracy even in low SNR condition.

Summary

In this chapter we dealt with the problem of the target motion parameter estimation by exploiting both a single baseline and dual baseline configuration with a small angular separation between the two baselines. We proposed a two-dimensional filter bank based on the Crystal Video scheme for the estimation of the target signal parameters such as the Doppler rate, the crossing time and the main lobe width in order to retrieve than the kinematic information. Firstly simplified closed-form expressions of the CRLB were derived for the estimation of the target signal parameters, that can be attained by observing the signal at the output of the DC removal filter in the Crystal Video scheme. Then the performance of the 2D filter bank was investigated and the analysis proved that unbiased estimates of the target parameters can be obtained approaching the derived CRLB in the high SNR region. Taking

advantage of the estimated target signal parameters: in a single baseline configuration the cross-baseline velocity component was estimated by assuming a priori knowledge of the baseline crossing point while in a dual baseline configuration also the baseline crossing point is estimated without requiring any a priori knowledge. The analysis proved that unbiased estimates of the target motion parameters can be obtained with high accuracy even for low SNR conditions.

Chapter 6

Experimental data in Passive FSR configuration

This chapter presents results related to an experimental campaign exploiting FM transmission as signals of opportunity in a FSR configuration. The aim of the acquisition campaign is to detect aircrafts landing at 16L runway of “Leonardo Da Vinci” airport of Rome, Italy. The recorded signal data is used: (i) to assess the theoretical performance of the CVD derived in Chapter 3 in real environment and (ii) to assess the effectiveness of the two dimensional filter bank approach for the estimation of the target motion parameters through both single baseline and dual baseline configuration.

6.1 Introduction

*P*assive radar exploit existing transmitters as illuminators of opportunity to perform target detection and localization, while avoiding RF emissions with the following advantages:

- low cost,
- covert operation,
- low vulnerability,
- reduced impact on the environment.

These emitters could be other radars, television signals, radio signals, cell phone signals; in general waveforms that are not tailored for radar applications. Due to their wide coverage, the generally high level of transmitted power, and the limited cost of the receivers, the commercial FM broadcast signals with a nominal frequency bandwidth of 200 kHz in the very high frequency (VHF) band, [88–108] MHz, are the most common signals used today for passive radars,[57],[60]. Specifically, with reference to air traffic control (ATC) applications, many experimental campaigns have demonstrated the effectiveness of FM-based PCL in detecting, localizing, and tracking aerial targets,[55]-[59].

It is important to mention here that performance in this extreme configuration of bistatic radar, FSR, does not depend on the particular PCL signal modulation scheme and, therefore will not influence FSR signal processing complexity, implying that any available transmitter of opportunity could be used, [39]. Moreover in the same paper, [39], the PCL operating in VHF/UHF bands was recommended for the detection of airborne targets in a Forward Scatter configuration, while for the surface targets practically all PCL sources could be used.

Based on the above considerations an experimental campaign exploiting FM transmissions as waveforms of opportunity was carried out in December 2016 at Fregene, about 25 km West of Rome (Italy). The aim of the acquisition campaign was to detect aircrafts landing at “Leonardo Da Vinci” airport of Rome (Italy) that follow the 16L runway. The recorded signals are used to assess the theoretical performance of the CVD detector derived in Chapter 3 in a real environment and to assess the effectiveness of the technique proposed in Chapter 5 (two-dimensional filter bank) for the motion parameters estimation exploiting both a single baseline and a dual baseline configuration.

6.2 Acquisition campaign set-up

As previously mentioned, the experiment took place near the “Leonardo Da Vinci” airport (Rome, Italy) with the aim to detect planes landing at the 16L runway. This runway was chosen because, differently from 16R, does not intersect the departing runway and is most commonly used. Among the different available transmitters in the surroundings of the airport, the one located at Monte Gennaro is selected as emitter of opportunity. By means of an accurate study of the International Approach Chart (IAC) provided by the local standard arrival procedure (see Figure 6.1), the aircraft path, altitude and also the velocity range that the pilots have to abide by during the landing procedure are known.

► Experimental data in Passive FSR configuration

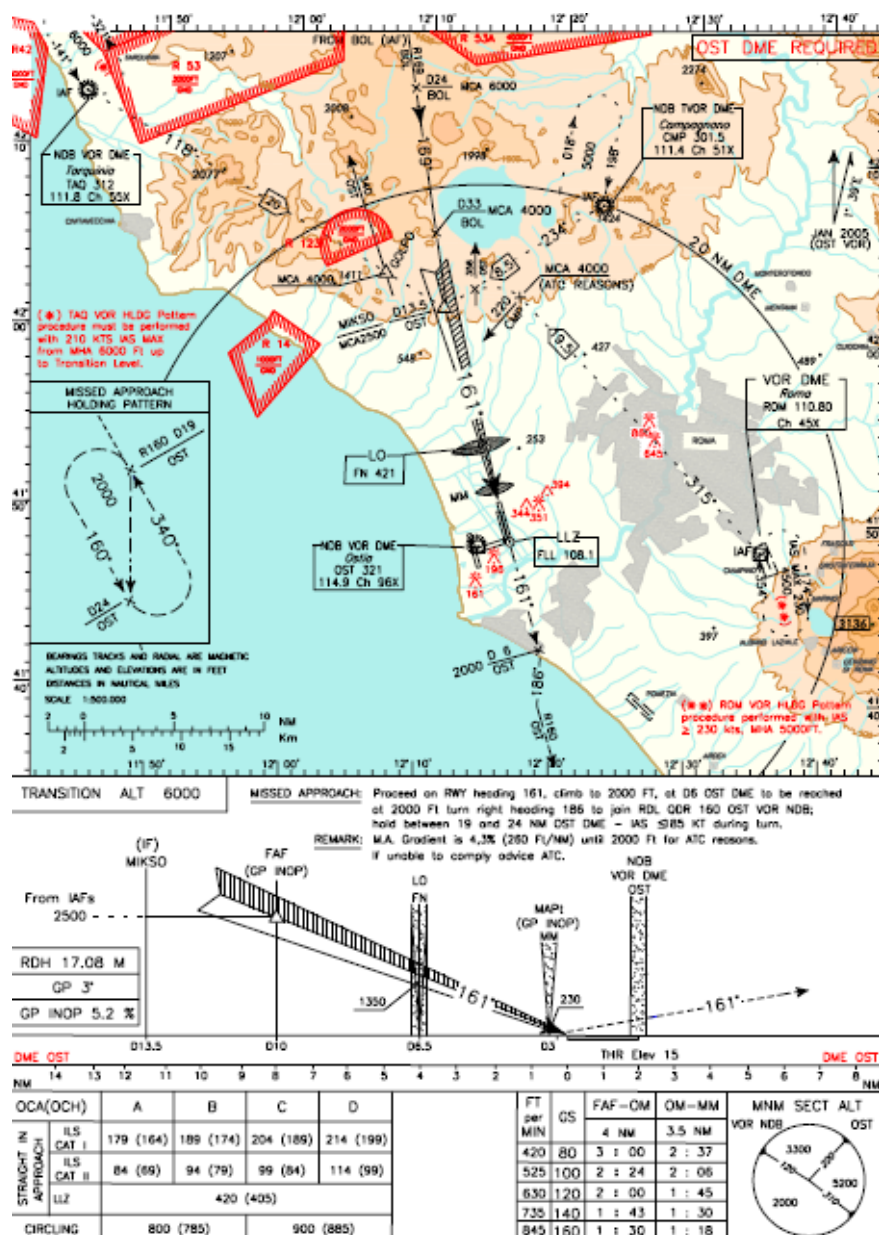


Figure 6.1 16L-Instrumental approach chart.

This information, combined with the knowledge of transmitter position, allowed to determinate suitable positions of the receiving antennas in order to achieve the Forward Scatter geometry. Among the positions provided, the seaside resort “La Riviera” at 56 km (baseline) far from the transmitter was chosen as suitable location for the carrying out of the experimental campaign (see Figure 6.2).



Figure 6.2 *Experimental topology of the FSR system used for data collection: the blue and the red markers indicate the TX and RXs position respectively, the yellow lines are the baseline and the red line indicates the trajectory of the aircraft during the landing.*

Two directive FM antennas with beamwidth around 90° , at a distance $d=11.95$ m from each other were steered toward the transmitter of Monte Gennaro. The antennas height is around 5 m, so a full visibility of the runway followed by the airplanes was achieved, as near the airport tall buildings are not allowed.

Moreover it is possible to retrieve some information related to the baseline crossing angle φ and the baseline crossing point y_0 since the trajectory of the target during the approach to the 16L runway is known, as previously mentioned (see Figure 6.1). At a first approximation, after projecting the positions of Tx, Rx and aircraft (when approaching the 16L runway) onto a 2D coordinate system by dropping the altitude information, the baseline crossing angle is equal to $\varphi \approx 10^\circ$ and the baseline crossing angle is $y_0 \approx 4.95$ km. As the distance d between the two antennas is small with respect to the baseline, the same y_0 is retrieved for both antennas. The non-cooperative targets have been monitored through a commercial ADS-B receiver which provides useful information to be used as ground-truth for the velocity estimation.

The multi-channel receiver used has been developed at the Department of Information Engineering, Electronics and Telecommunications, Sapienza University of Rome (see Figure 6.3), and is based on a direct Radio Frequency (RF) sampling approach. In the analogue

► Experimental data in Passive FSR configuration

section, the received signal from each receiving channel is passed firstly through a band-pass filter to reject out-of-band interferences. Proper variable attenuators and amplifiers are used to match the A/D converter dynamic range. The amplifiers have a fixed gain of 20 dB, for this reason the use of variable attenuators is necessary, to avoid exceeding the maximum dynamic range of the A/D ($1.125 V_{pp}$).

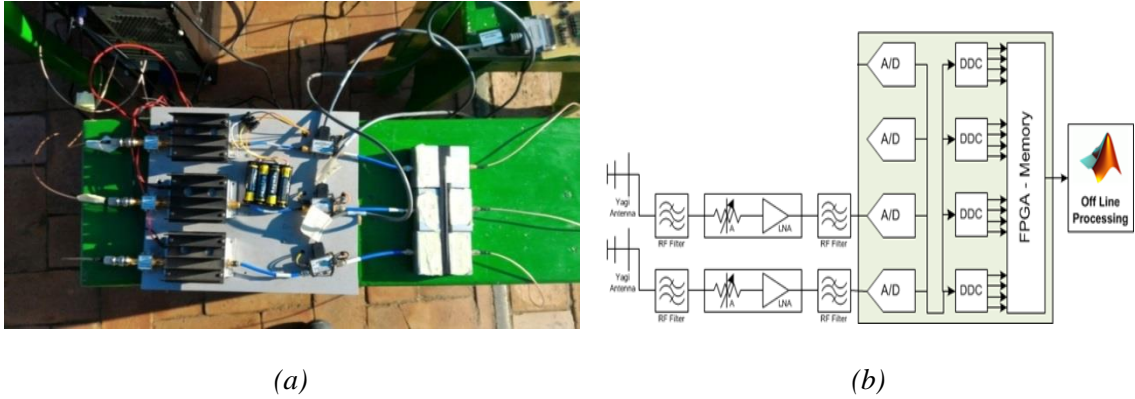


Figure 6.3 (a)Multi channel receiver and (b)block diagram of the multi-channel receiver

The A/D converter dynamic range is adapted to receive all the power in the FM spectrum. The main features of the A/D converter shown in Figure 6.4 are summarized in the Table 6.1.



Figure 6.4 ICS-155 (GE Intelligence Platforms).

Table 6.1 *Main feature of ICS-155.*

ICS-155
<ul style="list-style-type: none"> • 4 Analog Channels (4 ADCs) • ADC resolution: 16 bits • Full scale input: $1.125 V_{pp}$ (about 5dBm) • Input Signal Bandwidth: $2 \div 300\text{MHz}$ • Sampling Rate: $1 \div 180\text{MHz}$ for 4 channels, simultaneous • Simultaneous down-conversion of up to 16 signal bands: on board decimation, software selectable • Output data can be in either real or complex format

After digital down-conversion of the acquired signals, single FM channels of interest are extracted, in particular in our case FM channel 107.4 MHz ($\lambda=2.85$ m) is considered.

6.3 CVD detection performance

The theoretical performance of the CVD detector in terms of both probability of false alarm and probability of detection, derived respectively in Section 3.4.1 and Section 3.4.2, are assessed by applying the processing scheme of the CVD detector to the recorded data acquired during the experimental campaign described above. The required impulse response of the matched filter is obtained from the recorded signal after DC removal stage by selecting a time window centred on the time instant when the target crosses the baseline.

Figure 6.5 shows the signal $u(t)$ obtained from the received signal, after passing through the square law-detector and the DC removal filter. Due to the high signal level, the noise is negligible and $u(t)$, which has unit $[V^2]$, represents the so-called target Doppler signature. It is worth mentioning here that the received signal with a sampling frequency of 200KHz, after the square-law detector is downsampled to the frequency of 390.25 Hz, suitable for non-ambiguous observation of the target Doppler signature.

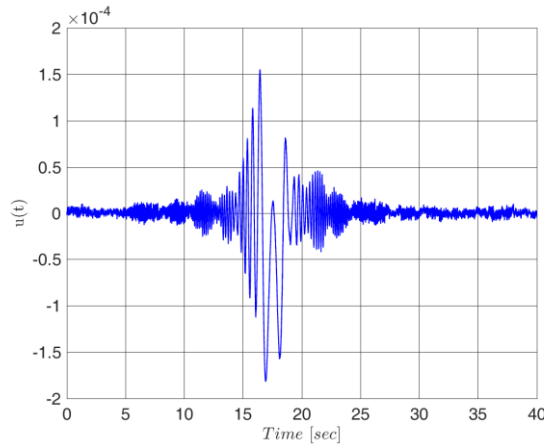



Figure 6.5 Received signal time signature after DC removal filter of an Airbus A320 (Test-1).

Figure 6.6 shows the signature of an Airbus A320 with the target parameters reported in Table 6.2: from the figure it is observed the noticeable amplitude modulation due to the target crossing.

Table 6.2 Main characteristic of the target-Test 1

Target type	Target size [length × height]	Target photo
Airbus A320	37.57m × 11.76 m	

To validate the proposed theoretical performance analysis, firstly the P_{fa} is obtained through Monte Carlo simulations by processing a frame of the received signal in absence of the target contribution signal (i.e. representative of the direct signal only) added with AWGN in order to achieve a given DNSR value (defined in eq.). Figure 6.6 (a) compares the P_{fa} obtained from the real data through Monte Carlo simulation with 10^7 independent trials as function of the normalized threshold for three different value of the DNSR with the theoretical close-form expression defined in eq. :from the figure a very good agreement is noted.

The P_d is obtained following a similar procedure by processing a frame of the received signal including also the target contribution added again with AWGN in order to obtain the desired DNSR. Figure 6.6 (b) compares the P_d obtained from real data through Monte Carlo simulation with 10^5 independent trials as function of the normalized threshold with the theoretical close-form expression defined in eq.: once more a good agreement is observed. Moreover as

expected, for the same normalized threshold, a better probability of detection is achieved for higher DNSR. For example in Figure 6.6 (b) for a normalized threshold equal to zero a $P_d=0.45$ is obtained for a DNSR=10 dB (see blue curve) while the P_d approaches 1 for a DNSR=40 dB (see green curve).

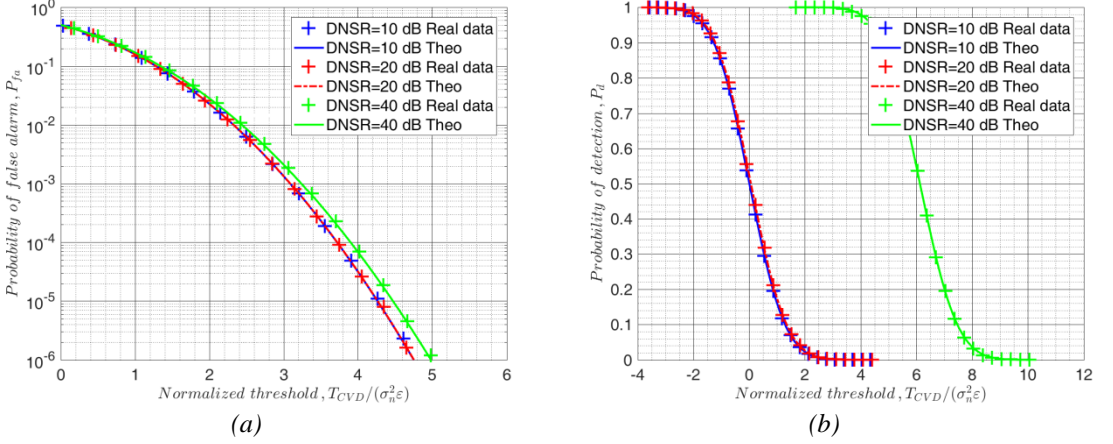


Figure 6.6 (a) Theoretical P_{fa} and P_{fa} in presence of real data as function of $T/(\sigma_n^2 \epsilon)$ for different value of DNSR and (b) theoretical P_d and P_d in presence of real data as function of $T/(\sigma_n^2 \epsilon)$ for three different value of DNSR.

It is to be remarked that FM signals of opportunity are very different from the constant–amplitude, single tone waveform used in this thesis (see FSR signal model in Section 3.2). Other than the intrinsic continuous frequency variation of a FM modulated waveform, this includes both the amplitude modulation due to multipath and transmit filtering, as well as potential temporary changes of the carrier frequency. By extracting the target signature from the data, we have intrinsically compensated their effect only on the final filter, which is clearly matched to the received target signal. However, their effect on the direct signal has not been removed. Despite the non-ideal direct signal characteristics, the presented performance comparison shows that the CVD remains effective in the removal of the direct signal, and our theoretical performance prediction still matches the detection results.

The complete agreement between experimental and theoretical results show that the presented theoretical performance of the CVD appears to be robust to the specific waveform characteristics. This means that the presented detection performance still apply, provided that

the target signature used in the matched filter includes the changes applied by the channel on the received target signature, despite all the other non-idealities.

6.4 Motion parameters estimation

The effectiveness of the two-dimensional filter bank approach for the estimation of the target motion parameters proposed in Chapter 5 was assessed by exploiting the acquired FM signals from single baseline and dual baseline configuration, addressed respectively in Section 6.4.1 and Section 6.4.2.

6.4.1 Single baseline configuration

Following the processing scheme introduced in Section 5.2.1, the signal received from the RX_1 after the square law detector is decimated by a factor 8^3 , so that the acquired signal is down-sampled to 390.625 Hz. In Figure 6.7 is reported the time domain signature of the received signal after the square law detector of an Airbus A319 with the target parameters reported in Table 6.3.

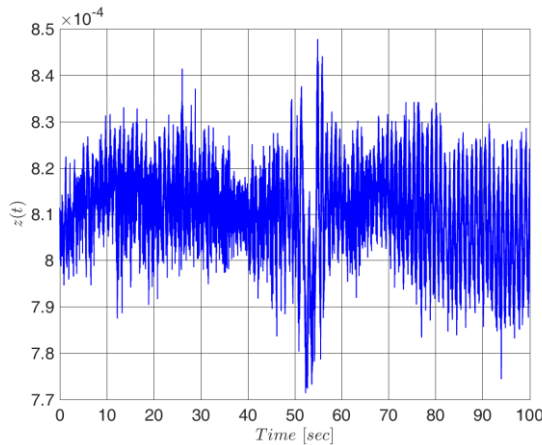



Figure 6.7 Received signal after square law detector and decimation of an Airbus A319 (Test-2).

As it can be observed, the amplitude modulation due to the target movement is clearly noticeable.

Table 6.3 *Main characteristic of the target-Test 2*

Target type	Target size [length × height]	Target photo
Airbus A319	33.84m × 11.76 m	

Firstly, the signal at the output of the DC removal filter is analyzed for the estimation of the Doppler rate through the STFT and the Radon transform. Figure 6.8 (a) shows the spectrogram (normalized with respect to its maximum value) of the signal in Figure 6.7. The Hamming window for the estimation of the STFT is set equal to 2.56 sec. It is clear the correspondence between the spectrogram and the corresponding time Doppler signature in terms of crossing instant located at 52 sec.

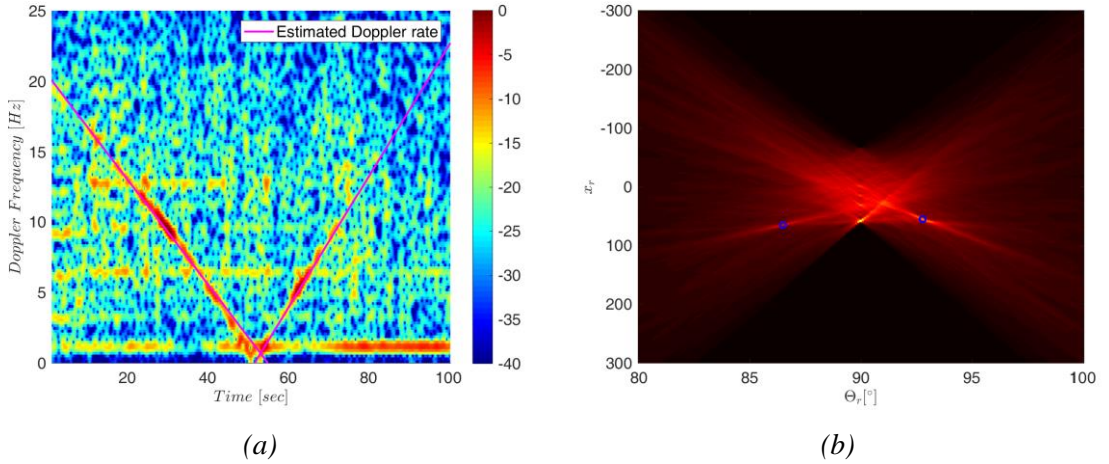


Figure 6.8 (a) *Spectrogram of the signal received from RX1 and (b) its corresponding Radon transform (Test-2).*

As the target in this case does not cross the baseline in the middle and perpendicularly, the two branches of the spectrogram are not completely symmetrical. The Radon transform is performed to the spectrogram (see Figure 6.8 (b)) and two different Doppler rates are well estimated with value equal to $\tilde{\phi} = 0.4666$ and $\tilde{\phi} = -0.3731$. The strong peak in the Radon plane for $\Theta_r = 90^\circ$ is because a part of continuous component after DC removal filter still remains.

Then, the 2D filter bank is performed with the impulse response (eq. (5.2)) constructed for an integration time $T=8$ sec and considering: (i) different values of the Doppler rate in the range $\ddot{\phi} = [\ddot{\phi}_a - 3\ddot{\phi}_a : \delta\ddot{\phi} : \ddot{\phi}_a + 3\ddot{\phi}_a]$ and (ii) different values of the main lobe width in the range $\theta = [\tilde{\theta} - 0.9\tilde{\theta} : \delta\theta : \tilde{\theta} + 4\tilde{\theta}]$. In accordance with the considerations in Section 5.2.1 and Section 5.2.2, $\ddot{\phi}_a$ is set equal to the mean value of the Doppler rates extracted from the Radon transform and $\tilde{\theta} = \ddot{\phi}_a \frac{l'_h}{v'}$, where $\frac{l'_h}{v'} = 0.5$ as we are interested in the detection of aircrafts with l'_h in the range 25-35 m and that are close to the landing, so with v' in the range 65-75 m/s . The Doppler rate step is set $\delta\ddot{\phi} = 1/T^2 = 0.0156$ and the main lobe width step is set $\delta\theta = 0.05$.

Figure 6.9 shows the contour plots related to $\Delta(\ddot{\phi}, \theta)$ (normalized with respect to its maximum value) as a function of the Doppler rate and of the main lobe width: it is clear the presence of a peak in correspondence of $(\hat{\ddot{\phi}} = 0.4883, \hat{\theta} = 0.2210)$, as it is also shown in Figure 6.10.

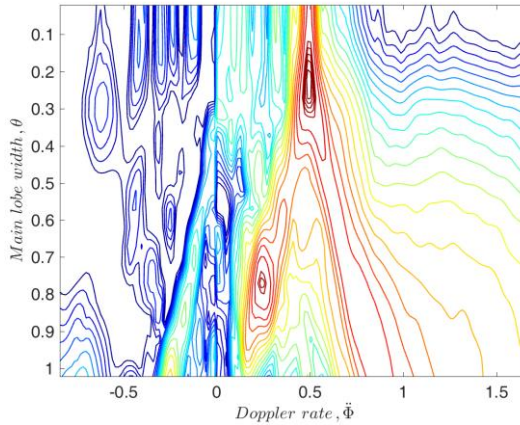


Figure 6.9 Contour plot of $\Delta(\ddot{\phi}, \theta)$ as function of the Doppler rate and of the main lobe width.

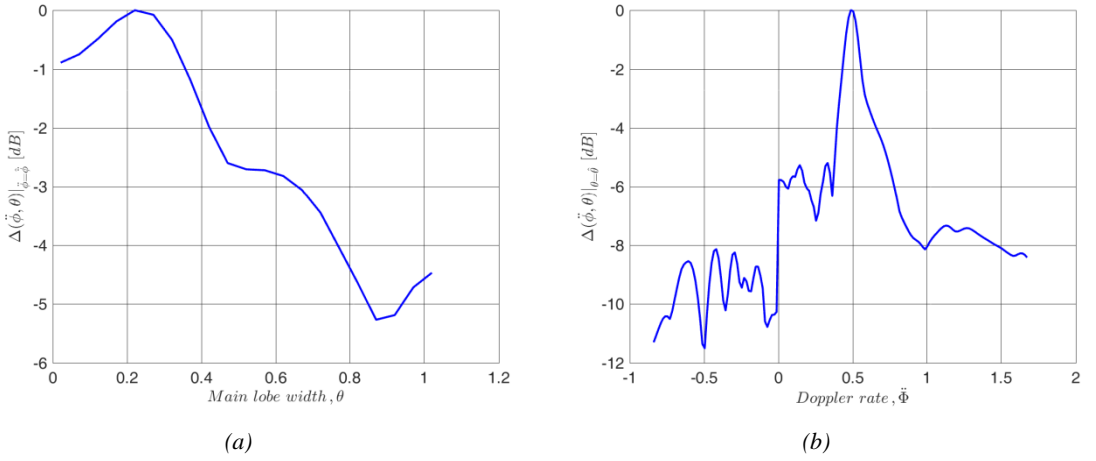


Figure 6.10 (a) $\Delta(\hat{\phi}, \theta)$ cut along Doppler rate axis and (b) $\Delta(\hat{\phi}, \theta)$ cut along the main lobe width axis.

Figure 6.11 compares a part of the measured signal where the target signature is present, having the same duration of the impulse responses of the bank of filters ($T=8$ sec), with the impulse response from the matched filter, $h_{\hat{\phi}, \hat{\theta}}(t)$: visual waveform analysis confirms the agreement between experimental data and the impulse response with the same number of phase cycles due to the Doppler component.

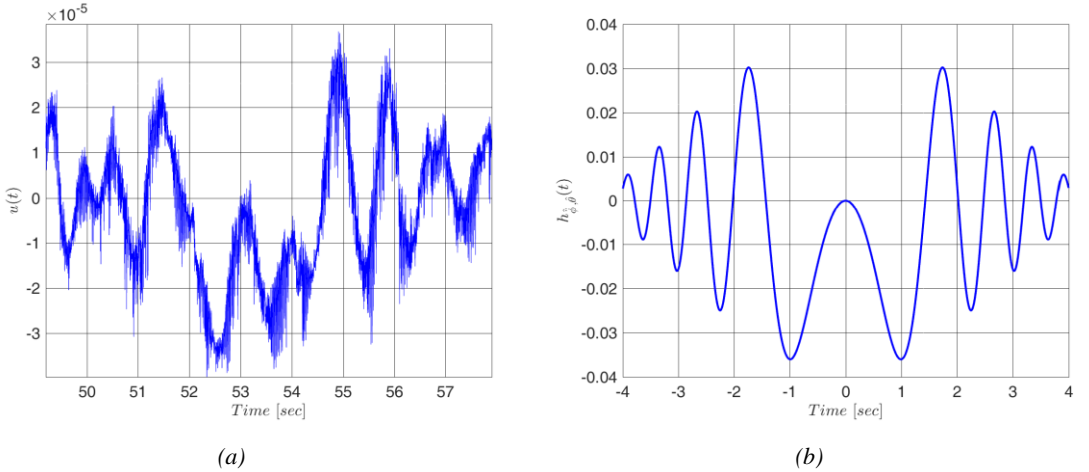


Figure 6.11 Comparison of (a) the measured signal with (b) the impulse response of the matched filter, $h_{\hat{\phi}, \hat{\theta}}(t)$.

In accordance with the geometry introduced in Section 6.2, as the baseline crossing point is known it is possible to estimate the cross baseline velocity in agreement with eq.(5.23), $\hat{v}_x = 79.58$ m/s . The velocity provided by the ADS-B is equal to $v = 72.07$ m/s and, as the


baseline crossing angle is 10° (i.e. the velocity cross-baseline is $v_x = v \cos \varphi = 71.07$ m/s) a good estimation of v_x from 2D filter bank is achieved with 10.4% relative error. This shows the practical effectiveness of the 2D filter bank technique and validates the proposed approach.

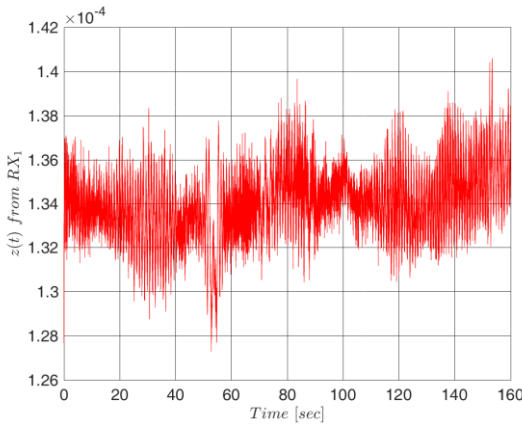
6.4.2 Dual baseline configuration

Taking advantage of the dual baseline configuration, the cross-baseline velocity and the baseline crossing point are estimated by performing the 2D filter bank to each signal received from the two separated antennas.

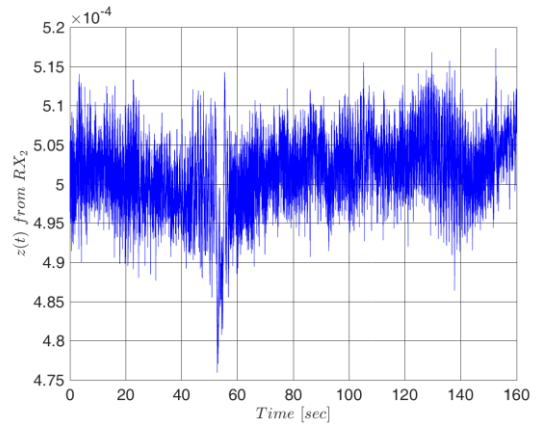
Figure 6.12 reports the signal received at both antennas, related to a Boeing 737-800 with the target parameters reported in Table 6.4: the amplitude modulation due to the target movement is clearly visible.

Table 6.4 *Main characteristic of the target-Test 3.*

Target type	Target size [length \times height]	Target photo
Boeing 737-800	33.40m \times 11.13 m	



(a)



(b)

Figure 6.12 *Received signal after square law detector and decimation of a Boeing 737-800 (Test-3):*

(a) RX_1 and (b) RX_2 .

It is worth mentioning that the gain of the two receiving chains is different, based on the disturbance received from each antenna. For this reason there is a difference in the signal level $z(t)$ received from RX_1 and RX_2 . The signal at the output of the DC removal filter is analyzed through STFT using a Hamming window with dimension equal to $T_w=2.56$ sec for the estimation of the Doppler rate, $\dot{\phi}$. Figure 6.13(a) and Figure 6.13(b) show the spectrogram of the signal received from the first antenna, RX_1 , and the second antenna, RX_2 , respectively, normalized with respect to their maximum values.

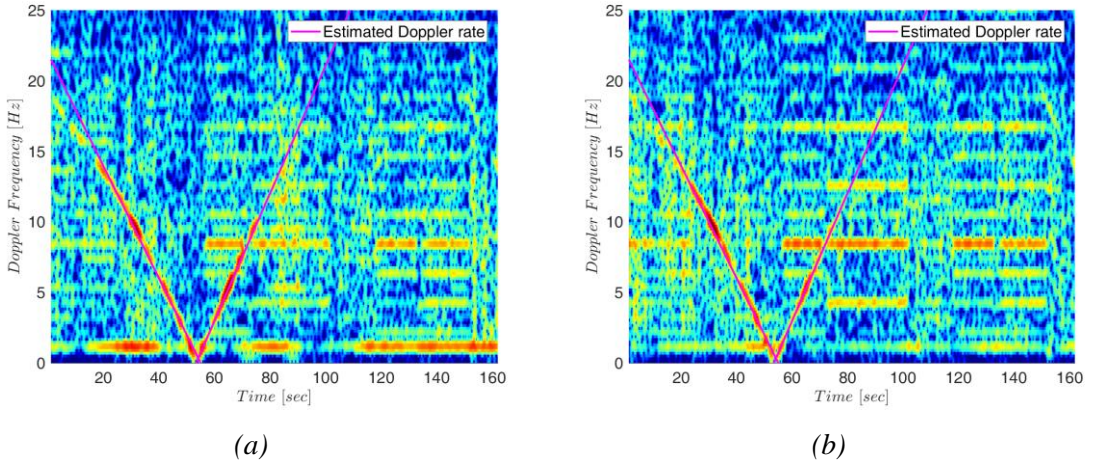


Figure 6.13 (a) Spectrogram of the signal received from RX_1 and (b) spectrogram of the signal received from RX_2 .

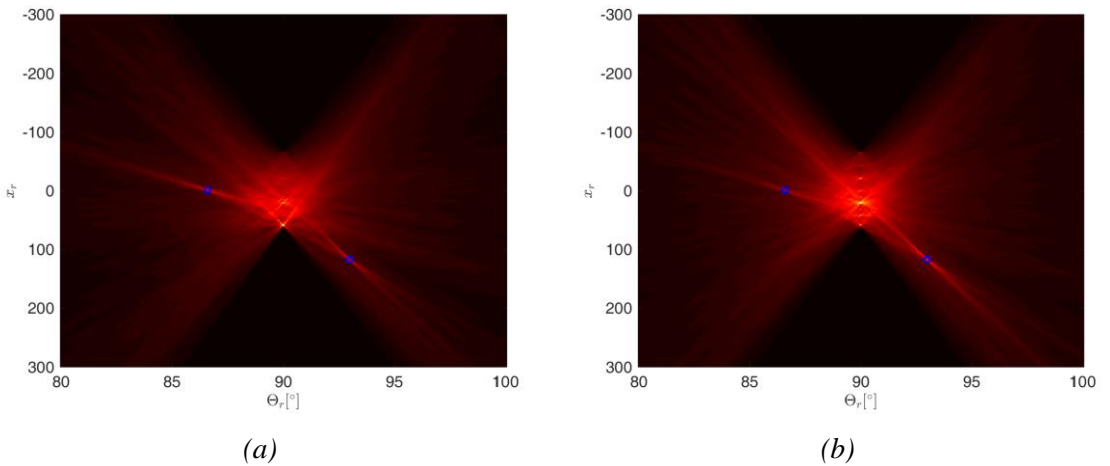


Figure 6.14 Radon transform of the spectrogram related to (a) the signal received from RX_1 and (b) to the signal received from RX_2 .

► Experimental data in Passive FSR configuration

As for the Test-2 in Section 6.4.1, the target does not cross the baseline in the middle and perpendicularly so the two branches of the spectrograms are not completely symmetrical and two different Doppler rates are extracted from the Radon transform (see Figure 6.14): $\tilde{\phi} = 0.4533$ and $\tilde{\phi} = -0.33998$. The same Doppler rate values are obtained from both antennas, RX_1 and RX_2 .

As for the single baseline configuration, the 2D filter bank then is performed to each signal received from the two separated antennas with the impulse response (eq. (5.2)) constructed for an integration time of $T=8$ sec and considering: (i) different values of the Doppler rate in the range $\ddot{\phi} = [\tilde{\phi}_a - 3\tilde{\phi}_a : \delta\ddot{\phi} : \tilde{\phi}_a + 3\tilde{\phi}_a]$ and (ii) different values of the main lobe width in the range $\theta = [\tilde{\theta} - 0.9\tilde{\theta} : \delta\theta : \tilde{\theta} + 4\tilde{\theta}]$. Once more, $\tilde{\phi}_a$ is set equal to the mean value of the Doppler rates extracted from the Radon transform, $\tilde{\theta} = \tilde{\phi}_a \frac{l'_h}{v'}$, where $\frac{l'_h}{v'} = 0.5$, the Doppler rate step is set $\delta\ddot{\phi} = 1/T^2 = 0.0156$ and the main lobe width step is $\delta\theta = 0.05$.

Figure 6.15 (a) and Figure 6.15 (b) show the contour plots of the cost function $\Delta(\ddot{\phi}, \theta)$ (normalized with respect to their maximum values) as a function of the Doppler rate and of the main lobe width related to the first receiver and the second receiver, respectively.

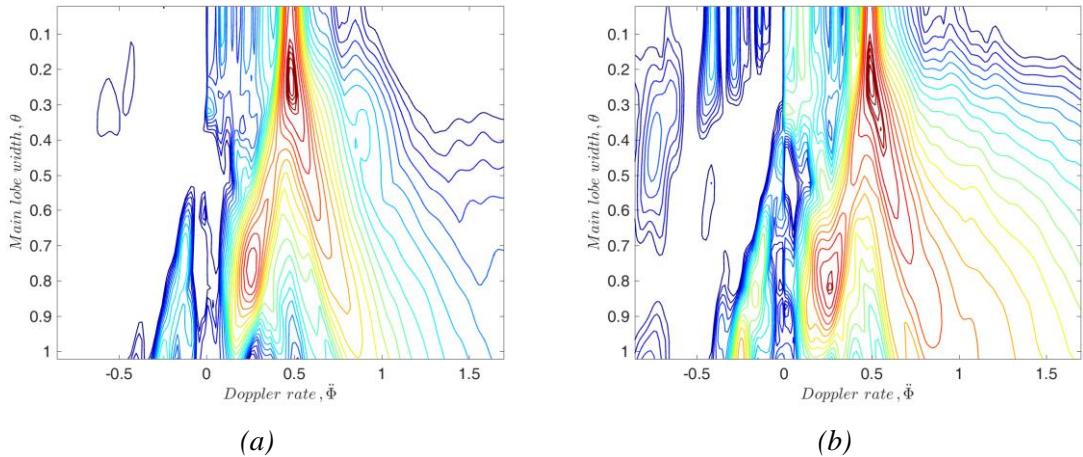


Figure 6.15 Contour plot of $\Delta(\ddot{\phi}, \theta)$ as function of the Doppler rate and of the main lobe width related to (a) RX_1 and (b) RX_2 .

In both cases it is clear the presence of a peak in correspondence of $(\hat{\phi} = 0.4907, \hat{\theta} = 0.2213)$ as it is also shown in Figure 6.16 that reports the cut of the cost function along the

Doppler rate and main lobe width. The same Doppler rate values are obtained from both antennas, RX₁ and RX₂.

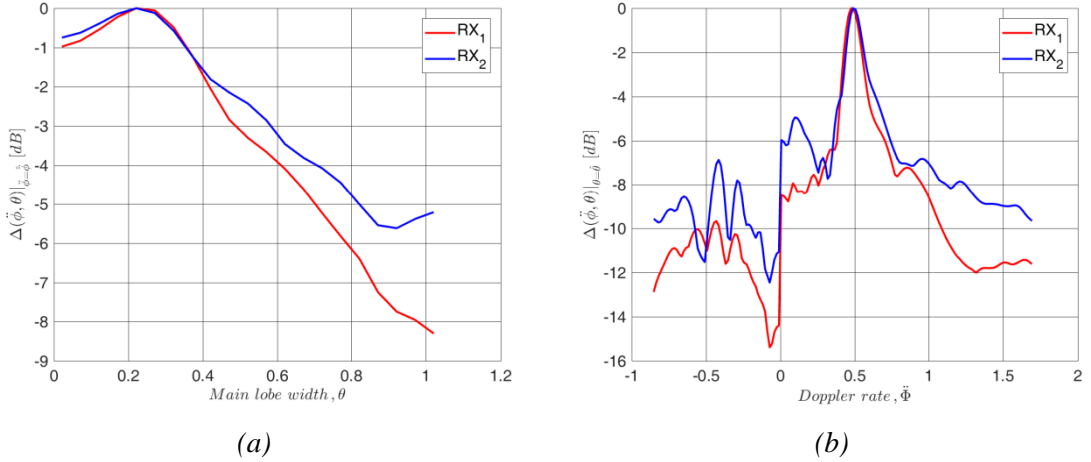


Figure 6.16 (a) $\Delta(\tilde{\phi}, \theta)$ cut along Doppler rate axis and (b) $\Delta(\tilde{\phi}, \theta)$ cut along the main lobe width axis.

Figure 6.17 compares a part of the received signal from RX₁ where the target signature is present, having the same duration of the impulse responses of the bank of filters ($T=8$ sec), with the impulse response from the matched filter, $h_{\tilde{\phi}, \hat{\theta}}(t)$, which provides the highest peak in the cost function, $\max_{\tilde{\phi}, \theta} \Delta(\tilde{\phi}, \theta)$.

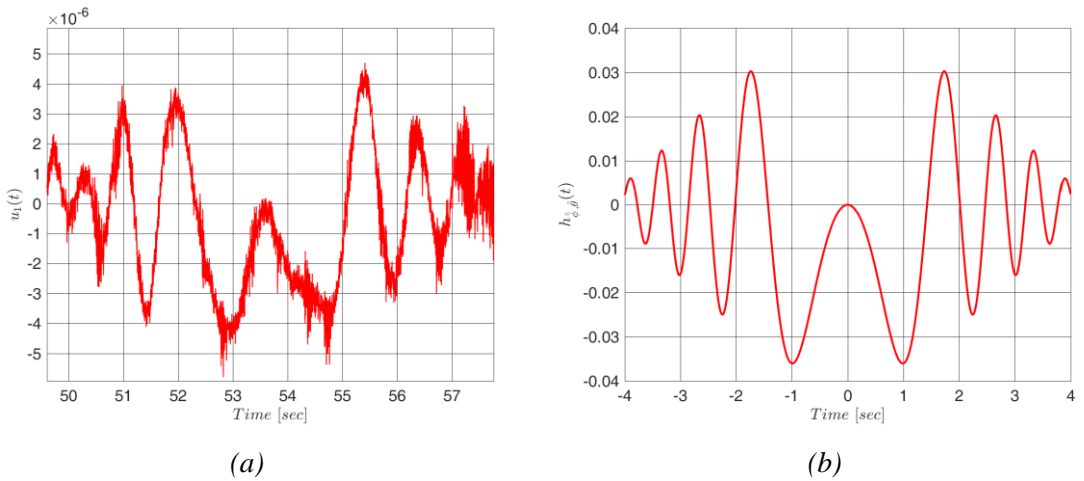


Figure 6.17 Comparison of (a) the received signal from RX₁ with the (b) impulse response of the matched filter, $h_{\tilde{\phi}, \hat{\theta}}(t)$.

Visual waveform analysis confirm the agreement between experimental data and the impulse response with the same number of the phase cycles due to the Doppler component.

Figure 6.18 reports similar results for the signal received from RX₂ and the above consideration still apply.

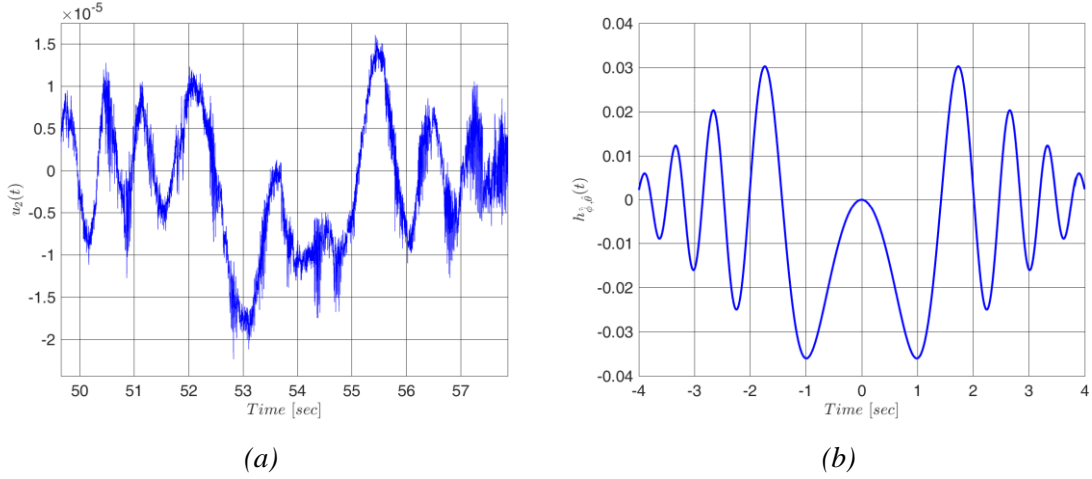


Figure 6.18 Comparison of (a) the received signal from RX₂ with the (b) impulse response of the matched filter, $h_{\hat{\phi}, \hat{\theta}}(t)$.

After the estimation of the Doppler rate and main lobe width, the baseline crossing instant \hat{t}_0 is estimated (see eq. (5.6)) as the time coordinate of the peak amplitude of the signal at the output of the matched filter with impulse response $h_{\hat{\phi}, \hat{\theta}}(t)$. Figure 6.19 reports a part of the signal at the output of the matched filter with impulse response $h_{\hat{\phi}, \hat{\theta}}(t)$ and it is clear that the peak is located in correspondence of a different time coordinate. A time delay equal to $\Delta t = 0.1254$ sec is estimated.

Exploiting the relation in eq.(5.29), the cross-baseline velocity and the baseline crossing point are estimated, respectively as $\hat{v}_x = 85.03$ m/s and $\hat{y}_0 = 5.9$ km. The cross baseline velocity obtained by considering the velocity provided by the ADS-B and the baseline crossing angle is $v_x = 78.61$ m/s. Finally, we can conclude that a good estimation of v_x and y_0 is achieved with 8.17% and 19.19 % relative error, respectively. This shows the practical effectiveness of the technique and validates the proposed approach.

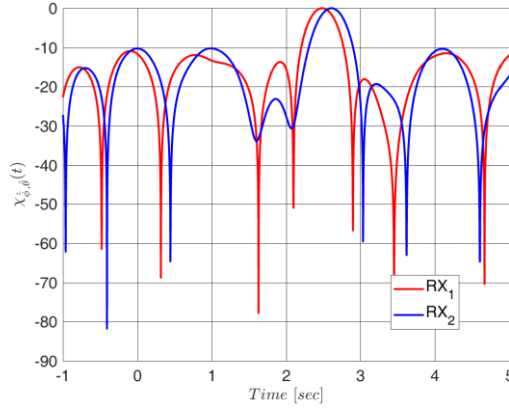


Figure 6.19 Part of the signal at the output of the matched filter with impulse $h_{\phi^{-};\theta^{-}}(t)$ related to the first and second receivers.

Summary

This chapter has presented an overview of a Passive-based FSR experimental campaign carried out on December 2016, where FM waveforms have been exploited as signals of opportunity in a dual baseline configuration. Several tests performed during the acquisition campaign have been reported and discussed to assess the validation of the theoretical performance analysis of the Crystal Video Detector in a real environment, and to assess the effectiveness of the developed technique for the target motion parameters estimation described in the previous chapters.

Acknowledgments

I want to thank Mr. Andrea Salce, owner of the seaside resort “La Riviera”, for his kind hospitality and support that allowed us to carry out the acquisition campaign.

Conclusions and Future work

To close this thesis a set of definite conclusions are drawn from the novel research described in the previous chapters. The section closes with the identifications of a series of areas for further investigations.

The principal contribution of this research presented in Chapter 3 to Chapter 5 was described in Section 1.3 and in the summaries at the end of each chapter. From these contribution it is possible to draw several conclusions for the two broad areas taken under investigation: *target detection* and *motion parameters estimation*.

With regard to the first area the issue of moving *target detection* that follows a linear trajectory in a single node FSR configuration against Additive White Gaussian Noise was addressed: (i) by a theoretical point of view through the derivation of closed form expressions of the detection performance and (ii) by developing new detection schemes. Aiming to give a thorough analysis two different geometrical scenarios was considered, particularly: (a) when the target is in the deep far field area and (b) when the target is approaching the near field condition for different integration times. The obtained results led to the following concluding remarks:

- *CVD*, a widely used scheme based on the square law detector, followed by mean level cancellation and matched filter: In order to theoretically set the detection threshold required to obtain an assigned probability of false alarm, a moment-based approximation of the density probability function of the decision statistic as a combination of two gamma PDFs was derived. The results demonstrated that the P_{fa} always provide an accurate fit with the Monte Carlo simulations based on the exact PDF for both reference scenarios. For high value of the DNSR and for a P_{fa} up to 10^{-3} , a simplified asymptotic expression of the P_{fa} , based on the Gaussian approximation of the PDF, may be used to set the threshold in order to guarantee a desired P_{fa} . This was followed by a closed form expression of the P_d that in all cases provides an accurate fit to the Monte Carlo simulations. Also approximated simplified expression of the P_d were derived that showed small differences with respect to the closed form expression. Even though the approximated expression of the P_d can be used

as a tool for analytical FSR performance prediction. The theoretical performance were shown to be robust to the specific characteristics of the waveform. This was shown by the complete agreement between experimental data and theoretical P_{fa} and P_d . The experimental data were acquired by a passive FSR systems that exploits FM signals as waveform of opportunity. Therefore, the presented detection performance still apply, provided that the target signature used in the matched filter includes the changes applied by the channel on the received target signature, despite all non-idealities.

- *CFAR-CVD detectors derived with the aim to remove the need to operate with a fixed detection threshold:* Modified version of the CVD scheme that maintains a constant false alarm rate (CFAR) independent on the values of σ_n^2 and DNR were derived under two different assumption: availability of secondary data and absence of secondary data. Their performance were fully characterized with both analytical and simulated analysis for both detection and false alarm probability. The obtained results demonstrated the desired CFAR propriety. The comparison of their detection performance showed limited losses of the CFAR detectors with respect to the fixed threshold CVD. For the CFAR-CVD with secondary data, deliberately was used a small set of secondary data to show how this scheme was dependent on the number of samples averaged. For this reason the CFAR-CVD with secondary data experienced losses in the order of 3 dB to achieve the same detection performance of the CVD with fixed threshold and CFAR-CVD without secondary data.
- *GLRT-based schemes that exploits the I&Q baseband components:* Optimized detection schemes in order to operate effectively under all conditions were derived and analytically characterized. The results showed the new schemes provided detection performance improved with respect to the CVD by an amount ranging from a minimum of 3 dB up to 10 dB. The 3dB improvement when the target is in the deep far field area was always present and was due to the use of the individual I&Q components instead of the detected power. Meanwhile the larger improvement was noticed when the target moves towards the limits of the far field conditions. In fact, getting close to the near-field transition point, the number of phase cycles present in the target signature largely reduces and the crystal video operation get towards its limits of validity. By comparing the fully adaptive versions of the GLRT (namely GLRT-2 that knows only the noise power and GLRT-3 that ensures the

CFAR condition) to the more ideal version (GLRT-1) that assumes the knowledge of the direct signal amplitude and phase, it was noted that the limited loss present under far field conditions was replaced by a major loss, when getting toward the transition between far field and near field.

- *GLRT-based schemes with secondary data derived with the aim to improve the detection performance of the GLRT when operating in a condition that is not too far from the near-field:* The new set of GLRT schemes , that include the use of target-free secondary data, together with the primary data, showed a non-negligible further improvement over the previous GLRT schemes, when the operation conditions get close to the near field transition point.
- *Design criteria for FSR systems:* The analytical performance obtained for the GLRT schemes, also allowed to derive equivalent SNR expressions, that relate the detection performance to the main FSR parameters describing geometry, target size and target motion. This allowed to investigate the effect of the individual parameters on the global detection performance. The main results can be summarized as follows: (i) the SNR was shown to exhibits an asymptotic trend when increasing the observation time; this is because the main contribution from the target is specified by the main lobe of the pattern signature, (ii) a greater DNSR was necessary to obtain the same performance when the target crosses the baseline in the middle for the same target size that moves with the same velocity and crosses the baseline with the same angle, (iii) for a long integration time the performance did not depend on the baseline crossing angle, (iv) better performance were obtained for slow moving target and (v) the performance presented a higher sensitivity to the vertical dimension of the target with respect to its horizontal dimension.

With regard to the second area the issue of *motion parameters estimation* of moving target that follows a linear trajectory embedded in the direct signal and AWGN was addressed (i) by developing a two dimension filter bank based on the Crystal Video scheme to extract the target signal parameters and (ii) by investigating the accuracy of the proposed approach from a theoretical point of view through the derivation of closed form expressions of the Cramer Rao Lower Bound. Aiming to give a thorough analysis two different FSR configuration were considered: (a) single baseline configuration and (b) dual baseline configuration with small

angular separation between the two baselines. The obtained results led to the following concluding remarks:

- *Two dimensional filter bank, a technique useful for the estimation of the main unknown target parameters* : The two-dimensional filter bank derived with the generic impulse response depending on the unknown target electrical size and target trajectory allowed the estimate the following target signal parameters: Doppler rate, baseline crossing time and main lobe width of the pattern signature. In particular, the impulse response was defined by considering different values of the Doppler rate and of the main lobe width of the pattern signature. In order to support practical applications to limit the computational load required by the bank a two-step processing and some design criteria related to the Doppler rate and main lobe width steps were proposed. The obtained results showed that for different target trajectories the Doppler rate and the main lobe width were well estimated. Then, closed form expressions of the CRLB that represents the optimum achievable accuracy on the estimation of the target signal parameters that can be obtained by observing the samples of the signal at the output of the DC removal filter in CVD scheme for a specific target characterized by a certain signal-to-noise ratio were derived. The obtained results showed that the target signal parameters of interest were independent from the other parameters: amplitude of the direct and target signal and noise variance. Also was proved that the estimates of the Doppler rate, baseline crossing instant and main lobe width are decoupled. The performance of the 2D filter bank was investigated and the analysis showed that for different target trajectories unbiased estimates of the target parameters were obtained that approaches the derived CRLB in the high SNR region.
- *Motion parameters estimation in a single baseline and dual baseline FSR configuration*: Exploiting the extraction of the Doppler rate from the 2D filter bank and under the assumption that the baseline crossing point is known it was possible to estimate the cross-baseline velocity from a single baseline configuration. Meanwhile from a dual baseline configuration with one transmitter and two separated receives by exploiting the Doppler rate and the crossing times extraction from the 2D filter bank the cross baseline velocity and baseline crossing point were retrieved without a priori knowledge on the other target motion parameters. The analysis demonstrated that the accuracy achievable from the 2D filter bank technique in the high SNR region approached the corresponding approximated

CRLB. The overall performance of the proposed approach was shown to be suitable for a practical application as accuracy in the order of 1% is obtained for a SNR=20 dB. The effectiveness was proved also through experimental data acquired by a passive FSR systems that exploits FM signals as waveform of opportunity.

The investigation reported in this thesis suggest further work that could be performed in the same field.

One of the main research interest in the field of *target detection* in FSR configuration regards the analysis of the detection performance of the considered detectors, based on the CVD and on the GLRT approach, when different waveforms from the constant-amplitude single tone waveform here considered, may be used. In the Chapter 6 the processing of live data acquired from a passive FSR prototype by exploiting FM signals as waveforms of opportunity showed the robustness to the specific waveform characteristics of the theoretical performance of the CVD. It is to be remarked that FM signals of opportunity are very different from the constant-amplitude single tone waveform, used in this work for the derivation of the theoretical performance. Other than the intrinsic continuous frequency variation of a FM modulated waveform, this includes both the amplitude modulation due to multipath and transmit filtering, as well as potential temporary changes of the carrier frequency. By extracting the target signature from the data, we have intrinsically compensated their effect only on the final filter, which is clearly matched to the received target signal. However, their effect on the direct signal has not been removed. Despite the non-ideal direct signal characteristics, the presented performance comparison shows that the CVD remains effective in the removal of the direct signal, and our theoretical performance prediction still matches the detection results. It is worth mentioning that when using a theoretical target signature to create the matched filter, all non-idealities mentioned above provide a mismatch between the received target signature and the one used in the filter. This mismatch of the filter, which was intrinsically avoided in this work, is expected to provide a global performance degradation for the CVD. Therefore the analysis of the detection performance and of the robustness not only of the CVD scheme but also of the GLRT-based detectors under the above-mentioned conditions will be of great interest.

The purpose of this work was to assess the detection performance achievable from the CVD and the GLRT-based detectors when the filter matched to the actual target parameters was used: in this respect knowledge of the two signatures, Doppler and pattern signature,

was assumed. In practical cases, as shown in Chapter 5 where a target with unknown size and velocity is searched for, a bank of matched filters may be used. Therefore the performance analyzed here represents the performance provided by the branch of the bank matched to the specific condition. The design of such bank of filters, in particular for the GLRT-based detectors, here not addressed and the analysis of the overall performance will allow to move to a more realistic environment.

With regard to the *motion parameters estimations* would be of large interest to investigate the estimation of all kinematic parameters for a target that follows a linear trajectory from a single baseline configuration by exploiting a Taylor expansion of the phase variation at third or fourth order. To estimate all the kinematic parameters of moving targets we can take into account the dependence of these parameters on the extracted third and fourth order parameters other than the Doppler rate.

In addition, in this work it has been discussed the importance of a dual baseline configuration that ensures the possibility to estimate two parameters without requiring a priori knowledge on the other target kinematic parameters. In this work the dual baseline configuration exploited was assumed to have a small angular separation between the two baselines, therefore the target crosses the two baselines maintaining the same velocity. Therefore would be interesting to analyze the possibility to estimate the motion parameters from a dual baseline configuration with large angular separation (one transmitter and two separated receivers or two separated transmitters and only one receiver) where the assumption that the target crosses the two baselines with the same velocity will not be valid.

Moreover, future radar systems are likely to be distributed an multistatic offering greater flexibility and greater robustness. Hence, would be of great interest to estimate all the kinematic parameters and analyze the performance in terms of the accuracy from a multi-node FSR configuration by applying the 2D filter bank of developed in Section 5.2.1 to the signals received from each receiver.

The research activities proposed, as an extension of the work done for this thesis project represents a challenging opportunity for future investigations.

Appendix: Analytical derivation

Appendix A Moments of the CVD

As shown in [48] the s -th cumulant of the generic quadratic form $\mathbf{x}^T \mathbf{A} \mathbf{x}$, where the $(N \times 1)$ real random vector \mathbf{x} has mean vector $\boldsymbol{\xi}$ and covariance matrix $\boldsymbol{\Sigma}$, is given by:

$$k(s) = 2^{s-1} s! [tr(\mathbf{A} \boldsymbol{\Sigma})^s / s + \boldsymbol{\xi}^T (\mathbf{A} \boldsymbol{\Sigma})^{s-1} \mathbf{A} \boldsymbol{\xi}] \quad (\text{A. 1})$$

where $tr(\mathbf{Q})$ is the trace of matrix \mathbf{Q} . To represent the quadratic form q_m defined in eq. (3.17) for $m=0,1,2$ of the complex Gaussian random vector \mathbf{r} ($N \times 1$), we can still benefit of eq. (A. 1) using $2N$ real components (real and imaginary parts), $q_m = \sum_{n=1}^N \theta_n(q_m) (r_{nR}^2 + r_{nI}^2)$. Therefore, in our case of interest:

- \mathbf{A} is a diagonal matrix with size $2N$, with the first N diagonal elements equal to $\theta_n(q_m)$ defined in eq.(3.18), $n=1, \dots, N$ followed by other N diagonal elements again equal to $\theta_n(q_m)$, $n=1, \dots, N$.

- $\boldsymbol{\Sigma} = \sigma_n^{2/2} \mathbf{I}_{2N}$, being \mathbf{I}_{2N} the identity matrix of size $2N$.

- vector $\boldsymbol{\xi}$, is a $(2N \times 1)$ vector with the first N elements equal to the real part of the mean value of vector \mathbf{r} and the following N elements equal to the imaginary part of the mean value of vector \mathbf{r} .

Thus, the s -th cumulant is $k_{q_m}(s)$, of q_m for $m=0,1,2$, and is given by:

$$k_{q_m}(s) = (s-1)! \sigma_n^{2(s-1)} \left(\sigma_n^2 \sum_{k=1}^N \theta_k^s(q_m) + s \sum_{k=1}^N \theta_k^s(q_m) |\chi_k|^2 \right) \quad (\text{A. 2})$$

being $\chi_k = \alpha + \beta s_{tok}$ in the presence of the target signal. Therefore, under hypothesis H_1 it yields:

$$k_{q_m}(s) = (s-1)! \sigma_n^{2(s-1)} \left[(\sigma_n^2 + s|\alpha|^2) \sum_{k=1}^N \theta_k^s(q_m) + s|\beta|^2 \sum_{k=1}^N \theta_k^s(q_m) |\chi_k|^2 + 2s|\alpha||\beta| \sum_{k=1}^N \theta_k^s(q_m) h_k \right] \quad (\text{A. 3})$$

and, under hypothesis H_0 , simplifies to:

$$k_{q_m}(s) = (s-1)! \sigma_n^{2(s-1)} (\sigma_n^2 + s|\alpha|^2) \sum_{k=1}^N \theta_k^s(q_m) \quad (\text{A. 4})$$

By recalling that the moments can be obtained from the cumulants using the well-known recursive relationship:

$$\mu_{q_m}(s) = \sum_{i=0}^{s-1} \frac{(s-1)!}{(s-1-i)! i!} k_{q_m}(s-i) \mu_{q_m}(i) \quad (\text{A. 5})$$

which under hypothesis H_1 yields:

$$\mu_{q_m}(s) = \sum_{i=0}^{s-1} \frac{(s-1)!}{i!} \sigma_n^{2(s-1)} \mu_{q_m}(i) [(\sigma_n^2 + (s-1)|\alpha|^2) \sum_{k=1}^N \theta_k^{s-i}(q_m) + (s-i)|\beta|^2 \sum_{k=1}^N \theta_k^{s-i}(q_m) |s_{t0k}|^2 + 2(s-i)|\alpha||\beta| \sum_{k=1}^N \theta_k^{s-i}(q_m) h_k] \quad (\text{A. 6})$$

Under hypothesis H_0 , the generic moment of q_m for $m=0,1,2$ is given by the simplified recursive expression:

$$\mu_{q_m}(s) = \sum_{i=0}^{s-1} \frac{(s-1)!}{i!} \sigma_n^{2(s-1)} \mu_{q_m}(i) (\sigma_n^2 + (s-1)|\alpha|^2) \sum_{k=1}^N \theta_k^{s-i}(q_m) \quad (\text{A. 7})$$

Appendix B Evaluation of the P_{fa} of the CVD

As the test statistic is given by the difference $q_0 = q_1 - q_2$, its PDF is given by the correlation between the gamma PDFs of q_1 and q_2 defined in eq. (3.21):

$$p_{q_0}(q_0) = \begin{cases} \int_{-q_0}^{\infty} \frac{(q_0+y)^{\nu_{q_1}-1}}{\mu'_{q_1}{}^{\nu_{q_1}} \Gamma(\nu_{q_1})} e^{-\frac{q_0+y}{\mu'_{q_1}}} \frac{y^{\nu_{q_2}-1}}{\mu'_{q_2}{}^{\nu_{q_2}} \Gamma(\nu_{q_2})} e^{-\frac{y}{\mu'_{q_2}}} dy, & q_0 < 0 \\ \int_0^{\infty} \frac{(q_0+y)^{\nu_{q_1}-1}}{\mu'_{q_1}{}^{\nu_{q_1}} \Gamma(\nu_{q_1})} e^{-\frac{q_0+y}{\mu'_{q_1}}} \frac{y^{\nu_{q_2}-1}}{\mu'_{q_2}{}^{\nu_{q_2}} \Gamma(\nu_{q_2})} e^{-\frac{y}{\mu'_{q_2}}} dy, & q_0 \geq 0 \end{cases} \quad (\text{B. 1})$$

► Appendix: Analytical derivation

Since q_0 has a zero mean under hypothesis H_0 , to provide P_{fa} values smaller than 0.5, the detection threshold T_{CVD} must have a positive value. Therefore, we are only interested in the PDF of q_0 for positive values. In order to simplify the expression of the PDF, as well as the resulting P_{fa} , we restrict to integer values of $n_{q_1} = \text{round}(v_{q_1})$. By evaluating the integration, we obtain:

$$p_{q_0}(q_0) = \left(\frac{\mu'_{q_1}}{\mu'_{q_1} + \mu'_{q_2}} \right)^{v_{q_2}} \sum_{p=0}^{n_{q_1}-1} \frac{\Gamma(n_{q_1} - 1 + v_{q_2} - p)}{\Gamma(v_{q_2})(n_{q_1} - 1 - p)!} \left(\frac{\mu'_{q_2}}{\mu'_{q_1} + \mu'_{q_2}} \right)^{n_{q_1}-1-p} \frac{1}{p!} \frac{1}{\mu'_{q_1}} \left(\frac{q}{\mu'_{q_1}} \right)^p e^{-\frac{q}{\mu'_{q_1}}} \quad (\text{B. 2})$$

To obtain a closed form expression for the P_{fa} , the PDF above is integrated from the threshold T_{CVD} to infinity:

$$P_{fa} = \int_{T_{CVD}}^{\infty} p_{q_0}(q_0) dq_0 = e^{-\frac{T_{CVD}}{\mu'_{q_1}}} \left(\frac{\mu'_{q_1}}{\mu'_{q_1} + \mu'_{q_2}} \right)^{v_{q_2}} \sum_{m=0}^{n_{q_1}-1} \frac{1}{m!} \left(\frac{T_{CVD}}{\mu'_{q_1}} \right)^m \sum_{r=0}^{n_{q_1}-1-m} \frac{\Gamma(r + v_{q_2})}{\Gamma(v_{q_2})r!} \left(\frac{\mu'_{q_2}}{\mu'_{q_1} + \mu'_{q_2}} \right)^r \quad (\text{B. 3})$$

By recalling the expressions in eq.(3.24) and observing that:

$$\begin{cases} \frac{\mu'_{q_1}}{\mu'_{q_1} + \mu'_{q_2}} = \frac{1 + \delta}{2} \\ \frac{\mu'_{q_2}}{\mu'_{q_1} + \mu'_{q_2}} = \frac{1 - \delta}{2} \end{cases} \quad (\text{B. 4})$$

it yields:

$$P_{fa} = e^{-\frac{T_{CVD}/(\sigma_n^2 \varepsilon)}{\frac{\rho(DNR)}{\omega(1+\delta)}}} (1 + \delta)^{v_{q_2}} \sum_{m=0}^{n_{q_1}-1} \frac{1}{m!} \left(\frac{T_{CVD}/(\sigma_n^2 \varepsilon)}{\rho(DNR)/\omega(1+\delta)} \right)^m \sum_{r=0}^{n_{q_1}-1-m} \frac{\Gamma(r + v_{q_2})}{2^{v_{q_2}+r} \Gamma(v_{q_2})} (1 - \delta)^r \quad (\text{B. 5})$$

Appendix C Derivation of GLRT-based detectors

In this appendix the derivation of the decision statistic of the GLRT-based detectors is reported. The MLE of the unknown parameters which maximize the joint PDF (see eq. (3.8)) is obtained by nulling the derivatives of the logarithm of the joint PDF under hypothesis H_0 and under hypothesis H_1 :

$$\ln \{P_r(\mathbf{r}/H_0)\} = -N \ln \pi - N \ln \sigma_n^2 - \frac{1}{\sigma_n^2} \|\mathbf{r} - \alpha \mathbf{s}_{d0}\|^2 \quad (\text{C. 1})$$

$$\ln \{P_r(\mathbf{r}/H_1)\} = -N \ln \pi - N \ln \sigma_n^2 - \frac{1}{\sigma_n^2} \|\mathbf{r} - \alpha \mathbf{s}_{d0} - \beta \mathbf{s}_{t0}\|^2 \quad (\text{C. 2})$$

For the GLRT-1 the MLE of the phase of β parameter is obtained as:

$$\max_{\angle \beta} \{ \ln P_r(\mathbf{r}/H_1) \} = -\frac{1}{\sigma_n^2} \min_{\angle \beta} \{ \|\beta \mathbf{s}_{t0}\|^2 - 2 \text{Re}[(\mathbf{r} - \alpha \mathbf{s}_{d0})^H \beta \mathbf{s}_{t0}] \} \quad (\text{C. 3})$$

which yields:

$$\widehat{\angle \beta} = -\angle \{ (\mathbf{r} - \alpha \mathbf{s}_{d0})^H \mathbf{s}_{t0} \} \quad (\text{C. 4})$$

By substituting eq. (C. 4) into eq. (4.1) and after some simple algebraic transformations the test statistic of the GLRT-1 detector in eq. (4.2) is obtained.

Concerning the GLRT-2 detector, the MLE of the complex amplitudes of the direct and target signal is obtained by nulling the derivative of eq. (C. 1) and eq. (C. 2) with respect to α and β yielding:

$$\hat{\alpha}|_{H_0} = \frac{\mathbf{s}_{d0}^H \mathbf{r}}{\|\mathbf{s}_{d0}\|^2}, \hat{\alpha}|_{H_1} = \frac{\mathbf{s}_{d0}^H (\mathbf{r} - \beta \mathbf{s}_{t0})}{\|\mathbf{s}_{d0}\|^2} \quad (\text{C. 5})$$

$$\hat{\beta} = \frac{\tilde{\mathbf{s}}_{t0}^H \tilde{\mathbf{r}}}{\|\tilde{\mathbf{s}}_{t0}\|^2} \quad (\text{C. 6})$$

where $\tilde{\mathbf{r}} = \mathbf{P}_{s_d}^\perp \mathbf{r}$, $\tilde{\mathbf{s}}_{t0} = \mathbf{P}_{s_d}^\perp \mathbf{s}_{t0}$ and $\mathbf{P}_{s_d}^\perp$ are defined in the Section 4.2.1.2 Substituting jointly the eq. (C. 5) under both hypothesis and eq. (C. 6) under hypothesis H_1 into eq. (3.8) and after some simple manipulations the test statistic in eq. (4.4) is obtained.

The test statistic of the GLRT-3 detector with all parameters unknown is obtained from results concerning GLRT-2 by nulling also the derivative of eq. (C. 1) and eq. (C. 2) with respect to σ_n^2 which yields:

$$\hat{\sigma}_n^2|_{H_0} = \frac{\|\tilde{\mathbf{r}}\|^2}{N}, \hat{\sigma}_n^2|_{H_0} = \frac{\|\tilde{\mathbf{r}} - \mathbf{P}_{\tilde{\mathbf{s}}_{t0}}\tilde{\mathbf{r}}\|^2}{N} \quad (\text{C. 7})$$

where $\mathbf{P}_{\tilde{\mathbf{s}}_{t0}}$ is defined in Section 4.2.1.3

Substituting jointly in eq. (3.8) the MLE of α and σ_n^2 under both hypothesis defined in eq. (C. 5) and eq. (C. 7) respectively and the MLE of β defined in eq. (C. 6) under hypothesis H_1 we have:

$$\left[\frac{\|\mathbf{P}_{\tilde{\mathbf{s}}_{t0}}\tilde{\mathbf{r}}\|^2 + \|\mathbf{P}_{\tilde{\mathbf{s}}_{t0}}^\perp\tilde{\mathbf{r}}\|^2}{\|\mathbf{P}_{\tilde{\mathbf{s}}_{t0}}^\perp\tilde{\mathbf{r}}\|^2} \right]^N \underset{H_0}{\overset{H_1}{\geq}} T_\Lambda \quad (\text{C. 8})$$

where $\mathbf{P}_{\tilde{\mathbf{s}}_{t0}}^\perp$ is defined in Section 4.2.1.3. After simple manipulations the test statistic in eq. (4.7) is obtained. The PDF of x_3 in eq. (4.7) can be derived by observing that the received signal model in defined in eq. (3.7) and the properties of the orthogonal projectors imply that $\mathbf{P}_{\tilde{\mathbf{s}}_{t0}}^\perp\tilde{\mathbf{r}} = \mathbf{P}_{\tilde{\mathbf{s}}_{t0}}^\perp\mathbf{n}$ belong to a subspace of dimension N-2. Thus, using also the definition of $\mathbf{P}_{\tilde{\mathbf{s}}_{t0}}$ the test in eq. (C. 8) can be written as:

$$\frac{\|\mathbf{P}_{\tilde{\mathbf{s}}_{t0}}\tilde{\mathbf{r}}\|^2}{\|\mathbf{P}_{\tilde{\mathbf{s}}_{t0}}^\perp\tilde{\mathbf{r}}\|^2} = \frac{|\tilde{\mathbf{s}}_{t0}^H\tilde{\mathbf{r}}|^2 / \|\tilde{\mathbf{s}}_{t0}\|^2}{\sum_{k=1}^{N-2} |\tilde{n}_k|^2} \underset{H_0}{\overset{H_1}{\geq}} T_\Lambda^{1/N} - 1 \quad (\text{C. 9})$$

$$x_3 = \frac{x_2^2}{\sum_{k=1}^{N-2} \frac{|\tilde{n}_k|^2}{\sigma_n^2}} \underset{H_0}{\overset{H_1}{\geq}} T_\Lambda^{1/N} - 1 \quad (\text{C. 10})$$

where x_2 is defined in eq. (4.4) and \tilde{n}_k with $k=1, \dots, N-2$ are i.i.d complex zero mean Gaussian random variables with variance σ_n^2 . The numerator of the test statistic in eq. (C. 10) under the null-hypothesis is a Chi square distribution with 2 degree of freedom and with the variance of the constituent Gaussian variates equal to $1/2$ and under the alternative hypothesis is a non-central Chi square distribution with the same dof and the same variances of the constituent Gaussian variate and non-central parameter equal to $\frac{2|\beta|^2\tilde{\mathbf{s}}_{t0}^H\tilde{\mathbf{s}}_{t0}}{\sigma_n^2}$. Meanwhile the

denominator under both hypotheses is a Chi square distribution with $2(N-2)$ dof and variances of the constituent Gaussian variate equal to $\frac{1}{2}$, [51]. Therefore, the F-distribution is obtained for the test statistic of the GLRT-3 detector under H_0 and the non-central F-distribution under H_1 , [51].

Appendix D Derivation of GLRT-based detectors with secondary data

Likewise, for the GLRT detectors with secondary data the MLE of the unknown parameters is obtained by nulling the derivatives of the logarithm of the joint PDF under hypothesis H_0 and under hypothesis H_1 :

$$\ln \{P_r(\mathbf{r}/H_0)P_{r'}(\mathbf{r}'/H_0)\} = -(N+M)\ln\pi - (N+M)\ln\sigma_n^2 - \frac{1}{\sigma_n^2} [\|\mathbf{r} - \alpha\mathbf{s}_{d0}\|^2 + \sum_{m=1}^M \|\mathbf{r}'_m - \alpha\mathbf{s}'_{d0}\|^2] \quad (\text{D. 1})$$

$$\ln \{P_r(\mathbf{r}/H_1)P_{r'}(\mathbf{r}'/H_0)\} = -(N+M)\ln\pi - (N+M)\ln\sigma_n^2 - \frac{1}{\sigma_n^2} [\|\mathbf{r} - \beta\mathbf{s}_{t0} - \alpha\mathbf{s}_{d0}\|^2 + \sum_{m=1}^M \|\mathbf{r}'_m - \alpha\mathbf{s}'_{d0}\|^2] \quad (\text{D. 2})$$

Concerning the GLRT-2, the MLE of the direct and target signal complex amplitudes derived by nulling the corresponding derivatives of eq. (D. 1) and eq. (D. 2) are:

$$\hat{\alpha}|_{H_0} = \frac{\mathbf{s}_{d0}^H \mathbf{r} + \mathbf{s}_{d0}'^H \mathbf{r}'}{\|\mathbf{s}_{d0}\|^2 + \|\mathbf{s}_{d0}'\|^2}, \hat{\alpha}|_{H_1} = \frac{\mathbf{s}_{d0}^H (\mathbf{r} - \beta\mathbf{s}_{t0}) + \mathbf{s}_{d0}'^H \mathbf{r}'}{\|\mathbf{s}_{d0}\|^2 + \|\mathbf{s}_{d0}'\|^2} \quad (\text{D. 3})$$

$$\hat{\beta} = \frac{\mathbf{s}_{t0}^H \left(\mathbf{r} - \frac{\mathbf{s}_{d0}\mathbf{s}_{d0}^H \mathbf{r} + \mathbf{s}_{d0}\mathbf{s}_{d0}'^H \mathbf{r}'}{\|\mathbf{s}_{d0}\|^2 + \|\mathbf{s}_{d0}'\|^2} \right)}{\left(\|\mathbf{s}_{t0}\|^2 - \frac{|\mathbf{s}_{d0}^H \mathbf{s}_{t0}|^2}{\|\mathbf{s}_{d0}\|^2 + \|\mathbf{s}_{d0}'\|^2} \right)} \quad (\text{D. 4})$$

Substituting jointly $\hat{\alpha}|_{H_0}$ and $\hat{\alpha}|_{H_1}$ and $\hat{\beta}$ into eq. (4.19) and after some simple manipulations the test statistic in eq. (4.20) is obtained.

Whereas for the GLRT-3 firstly the MLE of σ_n^2 is derived:

$$\hat{\sigma}_n^2|_{H_1} = \frac{\|\mathbf{r}\|^2 + \|\mathbf{r}'\|^2 - \frac{|\mathbf{s}_{d0}^H \mathbf{r} + \mathbf{s}_{d0}'^H \mathbf{r}'|^2}{\|\mathbf{s}_{d0}\|^2 + \|\mathbf{s}_{d0}'\|^2}}{(N + M)} \quad (\text{D. 5})$$

$$\hat{\sigma}_n^2|_{H_1} = \frac{\|\mathbf{r} - \beta \mathbf{s}_{t0}\|^2 + \|\mathbf{r}'\|^2 - \frac{|\mathbf{s}_{d0}^H (\mathbf{r} - \beta \mathbf{s}_{t0}) + \mathbf{s}_{d0}'^H \mathbf{r}'|^2}{\|\mathbf{s}_{d0}\|^2 + \|\mathbf{s}_{d0}'\|^2}}{(N + M)}$$

By substituting jointly the MLE of α and σ_n^2 defined in eq. (D. 3) and (D. 5) respectively under both hypothesis and the MLE of β parameter defined in eq. (D. 4) under hypothesis H_1 into (4.19) the likelihood function may be written as follows:

$$\left[\frac{\|\mathbf{r}\|^2 + \|\mathbf{r}'\|^2 - \frac{|\mathbf{s}_{d0}^H \mathbf{r} + \mathbf{s}_{d0}'^H \mathbf{r}'|^2}{\|\mathbf{s}_{d0}\|^2 + \|\mathbf{s}_{d0}'\|^2}}{w} \right]^{N+M} \begin{matrix} H_1 \\ \geq T'_\lambda \\ H_0 \end{matrix} \quad (\text{D. 6})$$

where the denominator w is :

$$w = \frac{\|\mathbf{r}\|^2 + \|\mathbf{r}'\|^2 - \frac{|\mathbf{s}_{d0}^H \mathbf{r} + \mathbf{s}_{d0}'^H \mathbf{r}'|^2}{\|\mathbf{s}_{d0}\|^2 + \|\mathbf{s}_{d0}'\|^2} - \frac{\left| \mathbf{s}_{t0}^H \left(\mathbf{r} - \frac{\mathbf{s}_{d0} \mathbf{s}_{d0}^H \mathbf{r} + \mathbf{s}_{d0} \mathbf{s}_{d0}'^H \mathbf{r}'}{\|\mathbf{s}_{d0}\|^2 + \|\mathbf{s}_{d0}'\|^2} \right) \right|^2}{\left(\|\mathbf{s}_{t0}\|^2 - \frac{|\mathbf{s}_{d0}^H \mathbf{s}_{t0}|^2}{\|\mathbf{s}_{d0}\|^2 + \|\mathbf{s}_{d0}'\|^2} \right)}}{\sigma_n^2} \quad (\text{D. 7})$$

After some simple manipulations the test statistic of the GLRT-3 with secondary data in eq. (4.22) is obtained.

It is easy to verify that in eq. (4.24) the numerator $x_2'^2$ is a Chi square variate with 2 degree of freedom and with variance of the constituent Gaussian variates equal to 1/2 under the null-hypothesis meanwhile under the hypothesis H_1 has a non-central Chi square distribution with the same dof and the same variances of the constituent Gaussian variates as in the H_0 and non-central parameter equal to $\frac{2|\beta|^2}{\sigma_n^2} \left(\|\mathbf{s}_{t0}\|^2 - \frac{|\mathbf{s}_{d0}^H \mathbf{s}_{t0}|^2}{\|\mathbf{s}_{d0}\|^2 + \|\mathbf{s}_{d0}'\|^2} \right)$. Meanwhile the denominator w in eq. (D. 7) is the sum of non-central Chi-squared variates with dof and non-central parameter being the sum of the corresponding parameters of the individual distributions. Finally, we can state

that w has a Chi square distribution with $2(N+M-2)$ dof and with variances of the constituent Gaussian variate equal to $\frac{1}{2}$. On this basis the non-central F distribution is obtained for x'_3 under H_1 and the F-distribution under H_0 .

Appendix E Evaluation of the SNR of GLRT-1 and GLRT-2 detector

This appendix reports the derivation of the SNR of GLRT-1 and GLRT-2 detectors.

The closed-form expression of SNR_{GLRT1} in eq. (4.34) is obtained by solving the integral in eq. (4.33) as follows:

$$\int_{-T/2}^{T/2} |s_{t0}(t)|^2 dt = s_0^2 \int_{-T/2}^{T/2} \text{sinc}^2(\ddot{\phi}\epsilon t) dt \quad (\text{E. 1})$$

$$\int_{-T/2}^{T/2} |s_{t0}(t)|^2 dt = \left(\frac{s_0^0}{\pi \ddot{\phi} \epsilon} \right)^2 \int_{-T/2}^{T/2} \sin^2(\ddot{\phi}\epsilon t) d\left(\frac{1}{t}\right) \quad (\text{E. 2})$$

Through the integration by parts of eq. (E. 2) we have:

$$\int_{-T/2}^{T/2} |s_{t0}(t)|^2 dt = 2 \frac{s_0^2}{\pi \ddot{\phi} \epsilon} \left[Si(\pi \ddot{\phi} \epsilon T) - \frac{1}{\pi \mu \eta} \frac{\sin^2(\pi \ddot{\phi} \epsilon T/2)}{T/2} \right] \quad (\text{E. 3})$$

Exploiting the definitions of α and β introduced in Section 3.2, it is simple to obtain the closed form expression of the GLRT-1 detector in eq. (4.34).

Concerning GLRT-2, the closed-form expression in eq. (4.36) is obtained by substituting eq. (E. 3) into eq. (4.35) and solving the integral. The last is derived by approximating the $\text{sinc}(\ddot{\phi}\epsilon t)$ in eq. (4.31) as follows:

$$\text{sinc}[\pi x] \cong \begin{cases} \cos\left(\pi \frac{x}{2}\right) + k \sin(\pi x) & 0 \leq x \leq 1 \\ p \sin(\pi x) & m \leq x \leq m+1, m \geq 1 \end{cases} \quad (\text{E. 4})$$

where

$$k = \frac{4}{\pi} - \frac{1}{\sqrt{2}} \left(1 + \frac{\pi}{4}\right)$$

$$p = \frac{4}{\pi(1 + 2m)}$$
(E. 5)

Hence we have:

$$\int_{-T/2}^{T/2} s_0^0 e^{j\pi\mu t^2} \text{sinc}(\dot{\phi}\epsilon t) dt =$$

$$s_0^0 \int_{-T/2}^{T/2} e^{j\pi\phi t^2} \cos\left(\pi \frac{\dot{\phi}\epsilon t}{2}\right) dt + s_0^0 k \int_{-T/2}^{T/2} e^{j\pi\phi t^2} \sin(\pi \dot{\phi}\epsilon t) dt +$$

$$s_0^0 \sum_{m=1}^{P-1} \int_m^{m+1} p e^{j\pi\phi t^2} \sin(\pi \dot{\phi}\epsilon t) dt$$
(E. 6)

where P-1 is the number of integrated side lobes of the pattern signature. The integrals in eq. (E. 6) are obtained by recalling the Euler's identity and the Fresnel Cosine and Fresnel Sine function in [50], which yields to the expression reported in where the arguments of the Fresnel Cosine and Sine functions are:

$$X_1 (X_2) = \sqrt{2\tau} \left(\frac{T}{2} \pm \frac{\epsilon}{4} \right) \quad X_3 (X_4) = \sqrt{2\tau} \left(\frac{T}{2} \pm \frac{\epsilon}{2} \right)$$

$$X_5 = \sqrt{2\tau} \frac{\epsilon}{2}$$

$$X_6 = \sqrt{2\tau} \left(\frac{m+1}{\epsilon\tau} + \frac{\epsilon}{2} \right) \quad X_7 = \sqrt{2\tau} \left(\frac{m}{\epsilon\tau} + \frac{\epsilon}{2} \right)$$

$$X_8 = \sqrt{2\tau} \left(\frac{m+1}{\epsilon\tau} - \frac{\epsilon}{2} \right) \quad X_9 = \sqrt{2\tau} \left(\frac{m}{\epsilon\tau} - \frac{\epsilon}{2} \right)$$
(E. 7)

Appendix F Cramer Rao Lower Bound derivation of the 2D filter bank approach

This appendix reports the derivation of the Cramer Rao Lower Bound of the main target parameters estimated from the 2D filter bankd. In accordance with the definition of the log-likelihood function, $\ln p(\mathbf{u}|\boldsymbol{\theta})$ in eq. (5.14) each diagonal element of FIM define in eq. (5.16) is:

$$\begin{aligned}
 J_{1,1} &= E \left\{ \left[\frac{\partial}{\partial \vec{\phi}} \ln p(\mathbf{u}|\boldsymbol{\vartheta}) \right]^2 \right\}, J_{2,2} = E \left\{ \left[\frac{\partial}{\partial t_0} \ln p(\mathbf{u}|\boldsymbol{\vartheta}) \right]^2 \right\}, \\
 J_{3,3} &= E \left\{ \left[\frac{\partial}{\partial \theta} \ln p(\mathbf{u}|\boldsymbol{\vartheta}) \right]^2 \right\}, J_{4,4} = E \left\{ \left[\frac{\partial}{\partial M_d} \ln p(\mathbf{u}|\boldsymbol{\vartheta}) \right]^2 \right\}, \\
 J_{5,5} &= E \left\{ \left[\frac{\partial}{\partial M_t} \ln p(\mathbf{u}|\boldsymbol{\vartheta}) \right]^2 \right\}, J_{6,6} = E \left\{ \left[\frac{\partial}{\partial \sigma_n} \ln p(\mathbf{u}|\boldsymbol{\vartheta}) \right]^2 \right\}
 \end{aligned} \tag{F. 1}$$

Meanwhile the off-diagonal elements of FIM are:

$$\begin{aligned}
 J_{1,2} &= J_{2,1} = E \left\{ \left[\frac{\partial}{\partial \vec{\phi}} \ln p(\mathbf{u}|\boldsymbol{\vartheta}) \right] \frac{\partial}{\partial t_0} [\ln p(\mathbf{u}|\boldsymbol{\vartheta})] \right\}, \\
 J_{1,3} &= J_{3,1} = E \left\{ \left[\frac{\partial}{\partial \vec{\phi}} \ln p(\mathbf{u}|\boldsymbol{\vartheta}) \right] \frac{\partial}{\partial \theta} [\ln p(\mathbf{u}|\boldsymbol{\vartheta})] \right\}, \\
 J_{1,4} &= J_{4,1} = E \left\{ \left[\frac{\partial}{\partial \vec{\phi}} \ln p(\mathbf{u}|\boldsymbol{\vartheta}) \right] \frac{\partial}{\partial M_d} [\ln p(\mathbf{u}|\boldsymbol{\vartheta})] \right\}, \\
 J_{1,5} &= J_{5,1} = E \left\{ \left[\frac{\partial}{\partial \vec{\phi}} \ln p(\mathbf{u}|\boldsymbol{\vartheta}) \right] \frac{\partial}{\partial M_t} [\ln p(\mathbf{u}|\boldsymbol{\vartheta})] \right\}, \\
 J_{1,6} &= J_{6,1} = E \left\{ \left[\frac{\partial}{\partial \vec{\phi}} \ln p(\mathbf{u}|\boldsymbol{\vartheta}) \right] \frac{\partial}{\partial \sigma_n} [\ln p(\mathbf{u}|\boldsymbol{\vartheta})] \right\}, \\
 J_{2,3} &= J_{3,2} = E \left\{ \left[\frac{\partial}{\partial t_0} \ln p(\mathbf{u}|\boldsymbol{\vartheta}) \right] \frac{\partial}{\partial \theta} [\ln p(\mathbf{u}|\boldsymbol{\vartheta})] \right\}, \\
 J_{2,4} &= J_{4,2} = E \left\{ \left[\frac{\partial}{\partial t_0} \ln p(\mathbf{u}|\boldsymbol{\vartheta}) \right] \frac{\partial}{\partial M_d} [\ln p(\mathbf{u}|\boldsymbol{\vartheta})] \right\}, \\
 J_{2,5} &= J_{5,2} = E \left\{ \left[\frac{\partial}{\partial t_0} \ln p(\mathbf{u}|\boldsymbol{\vartheta}) \right] \frac{\partial}{\partial M_t} [\ln p(\mathbf{u}|\boldsymbol{\vartheta})] \right\}, \\
 J_{2,6} &= J_{6,2} = E \left\{ \left[\frac{\partial}{\partial t_0} \ln p(\mathbf{u}|\boldsymbol{\vartheta}) \right] \frac{\partial}{\partial \sigma_n} [\ln p(\mathbf{u}|\boldsymbol{\vartheta})] \right\}, \\
 J_{3,4} &= J_{4,3} = E \left\{ \left[\frac{\partial}{\partial \theta} \ln p(\mathbf{u}|\boldsymbol{\vartheta}) \right] \frac{\partial}{\partial M_d} [\ln p(\mathbf{u}|\boldsymbol{\vartheta})] \right\}, \\
 J_{3,5} &= J_{5,3} = E \left\{ \left[\frac{\partial}{\partial \theta} \ln p(\mathbf{u}|\boldsymbol{\vartheta}) \right] \frac{\partial}{\partial M_t} [\ln p(\mathbf{u}|\boldsymbol{\vartheta})] \right\}, \\
 J_{3,6} &= J_{6,3} = E \left\{ \left[\frac{\partial}{\partial \theta} \ln p(\mathbf{u}|\boldsymbol{\vartheta}) \right] \frac{\partial}{\partial \sigma_n} [\ln p(\mathbf{u}|\boldsymbol{\vartheta})] \right\}, \\
 J_{4,5} &= J_{5,4} = E \left\{ \left[\frac{\partial}{\partial M_d} \ln p(\mathbf{u}|\boldsymbol{\vartheta}) \right] \frac{\partial}{\partial M_t} [\ln p(\mathbf{u}|\boldsymbol{\vartheta})] \right\}, \\
 J_{4,6} &= J_{6,4} = E \left\{ \left[\frac{\partial}{\partial M_d} \ln p(\mathbf{u}|\boldsymbol{\vartheta}) \right] \frac{\partial}{\partial \sigma_n} [\ln p(\mathbf{u}|\boldsymbol{\vartheta})] \right\}, \\
 J_{5,6} &= J_{6,5} = E \left\{ \left[\frac{\partial}{\partial M_t} \ln p(\mathbf{u}|\boldsymbol{\vartheta}) \right] \frac{\partial}{\partial \sigma_n} [\ln p(\mathbf{u}|\boldsymbol{\vartheta})] \right\}
 \end{aligned} \tag{F. 2}$$

► Appendix: Analytical derivation

The derivative with respect to ϑ_r (for $r=1,...,6$) needed to evaluate the FIM may be written in a compact form as follows:

$$\frac{\partial}{\partial \vartheta_r} [\ln p(\mathbf{u}|\boldsymbol{\vartheta})] = \sum_{i=1}^N u_i^2 \mathcal{C}_{\vartheta_{ri}}^1 + \sum_{i=1}^N u_i \mathcal{C}_{\vartheta_{ri}}^2 + \sum_{i=1}^N \mathcal{C}_{\vartheta_{ri}}^3 \quad (\text{F. 3})$$

where $\mathcal{C}_{\vartheta_{ri}}^1$, $\mathcal{C}_{\vartheta_{ri}}^2$ and $\mathcal{C}_{\vartheta_{ri}}^3$ are the coefficient of the derivatives with respect to ϑ_r for $i=1,...,N$. We showed firstly in Section 5.3.1 that the FIM matrix is a block diagonal matrix and after that the matrix of the parameters of interest, \mathbf{J}^A is a diagonal matrix. Focusing on the latter, by substituting eq. (F. 3) into eq. (F. 2) each diagonal element of \mathbf{J}^A may be written in the compact form as follows:

$$\begin{aligned} J_{r,r}^A = & \sum_{i=1}^N E\{u_i^4\} \mathcal{C}_{\vartheta_{ri}}^1{}^2 + \sum_{i=1}^N \sum_{j=1 \atop (i \neq j)}^N E\{u_i^2\} E\{u_j^2\} \mathcal{C}_{\vartheta_{ri}}^1 \mathcal{C}_{\vartheta_{rj}}^1 + 2 \sum_{i=1}^N E\{u_i^3\} \mathcal{C}_{\vartheta_{ri}}^1 \mathcal{C}_{\vartheta_{ri}}^2 \\ & + 2 \sum_{i=1}^N \sum_{j=1 \atop (i \neq j)}^N E\{u_i^2\} E\{u_j^2\} \mathcal{C}_{\vartheta_{ri}}^1 \mathcal{C}_{\vartheta_{rj}}^2 + 2 \sum_{i=1}^N \mathcal{C}_{\vartheta_{ri}}^3 \sum_{i=1}^N E\{u_i^2\} \mathcal{C}_{\vartheta_{ri}}^1 \\ & + \sum_{i=1}^N E\{u_i^2\} \mathcal{C}_{\vartheta_{ri}}^2{}^2 + \sum_{i=1}^N \sum_{j=1 \atop (i \neq j)}^N E\{u_i\} E\{u_j\} \mathcal{C}_{\vartheta_{ri}}^2 \mathcal{C}_{\vartheta_{rj}}^2 \\ & + 2 \sum_{i=1}^N \mathcal{C}_{\vartheta_{ri}}^3 \sum_{i=1}^N E\{u_i\} \mathcal{C}_{\vartheta_{ri}}^2 + \left[\sum_{i=1}^N \mathcal{C}_{\vartheta_{ri}}^3 \right]^2 \end{aligned} \quad (\text{F. 4})$$

It can be shown that all the terms in eq. (F. 4) that depends on the fourth and third moments, also the cross-terms give a negligible contribution. Furthermore, the term that depend on $\mathcal{C}_{\vartheta_{ri}}^3$ can be neglected. Therefore, the eq. (F. 4) can be approximated as:

$$J_{r,r}^A = \sum_{i=1}^N E\{u_i^2\} \mathcal{C}_{\vartheta_{ri}}^2{}^2 \quad (\text{F. 5})$$

Indicating with $\mathcal{C}_{\vartheta_{ri}} = \mathcal{C}_{\vartheta_{ri}}^2$ the eq. (5.20) is obtained. The $\mathcal{C}_{\vartheta_{ri}}$ are:

$$\begin{aligned}
 \mathcal{C}_{\ddot{\phi}i} &= -\frac{2M_d M_t \text{sinc}[\theta(t_i - t_0)] \cos[\pi \ddot{\phi}(t_i - t_0)^2] (t_i - t_0)^2}{2\sigma_n^2 \{M_d^2 - 2M_d M_t \text{sinc}[\theta(t_i - t_0)] \sin[\pi \ddot{\phi}(t_i - t_0)^2]\}} \\
 \mathcal{C}_{t_0i} &= \frac{M_d^3 M_t 2\pi \ddot{\phi}(t_i - t_0) \text{sinc}[\theta(t_i - t_0)] \cos[\pi \ddot{\phi}(t_i - t_0)^2]}{\sigma_n^2 \{M_d^2 - 2M_d M_t \text{sinc}[\theta(t_i - t_0)] \sin[\pi \ddot{\phi}(t_i - t_0)^2]\}^2} \\
 \mathcal{C}_{\theta i} &= -\frac{M_d^3 M_t \sin[\pi \ddot{\phi}(t_i - t_0)^2] \left[\frac{\cos[\pi \theta(t_i - t_0)]}{\theta} - \frac{\sin[\pi \theta(t_i - t_0)]}{\theta^2 \pi(t_i - t_0)} \right]}{\sigma_n^2 \{M_d^2 - 2M_d M_t \text{sinc}[\theta(t_i - t_0)] \sin[\pi \ddot{\phi}(t_i - t_0)^2]\}^2}
 \end{aligned} \tag{F. 6}$$

After substituting eq. (F. 6) and the approximated variance of each sample, u_i defined in eq. (5.12) into eq. (F. 5) the diagonal elements of \mathbf{J}^A are written as follows:

$$\begin{aligned}
 J_{1,1}^A &= 2 \sum_{i=1}^N \frac{M_d M_t^2 \pi^2 (t_i - t_0)^4 \cos^2(\pi \ddot{\phi}(t_i - t_0)^2) \text{sinc}^2[\theta(t_i - t_0)]}{\sigma_n^2 [M_d - 2M_t \text{sinc}[\theta(t_i - t_0)] \sin(\pi \ddot{\phi}(t_i - t_0)^2)]} \\
 J_{2,2}^A &= 8 \sum_{i=1}^N \frac{M_d^5 M_t^2 \pi^2 \ddot{\phi}^2(t_i - t_0)^2 \cos^2(\pi \ddot{\phi}(t_i - t_0)^2) \text{sinc}^2[\theta(t_i - t_0)]}{\sigma_n^2 [M_d - 2M_t \text{sinc}[\theta(t_i - t_0)] \sin(\pi \ddot{\phi}(t_i - t_0)^2)]^3} \\
 J_{3,3}^A &= 2 \sum_{i=1}^N \frac{M_d^5 M_t^2 \sin^2(\pi \ddot{\phi}(t_i - t_0)^2) \left[\frac{\cos[\pi \theta(t_i - t_0)]}{\theta} - \frac{\sin[\pi \theta(t_i - t_0)]}{\pi \theta^2(t_i - t_0)} \right]^2}{\sigma_n^2 [M_d - 2M_t \text{sinc}[\theta(t_i - t_0)] \sin(\pi \ddot{\phi}(t_i - t_0)^2)]^3}
 \end{aligned} \tag{F. 7}$$

After some approximation the closed form expressions of the CRLB derived in eq. (5.21) are obtained.

List of publications

This research has resulted in the following publications:

Journals

[J1] N. Ustalli, P. Lombardo and D. Pastina, "Detection performance of Forward Scatter Radar using a Crystal Video Detector", IEEE Transactions on Aerospace and Electronic Systems, in print.

[J2] N. Ustalli, P. Lombardo and D. Pastina, "GLRT-detection schemes for Forward Scatter Radar", submitted to IEEE Transactions on Aerospace and Electronic Systems, July 2017.

Conferences

[C1] N. Ustalli, D. Pastina, C. Bongioanni, P. Lombardo, "Motion parameters estimation in dual-baseline Forward Scatter Radar configuration", International Conference in Radar Systems, 2017, Belfast.

[C2] N. Ustalli, F. Di Lello, D. Pastina, C. Bongioanni, S. Rainaldi and P. Lombardo, "Two-dimensional filter bank design for velocity estimation in Forward Scatter Radar configuration," 2017 18th International Radar Symposium (IRS), Prague, 2017, pp. 1-10.

[C3] A. Arcangeli, C. Bongioanni, N. Ustalli, D. Pastina and P. Lombardo, "Passive forward scatter radar based on satellite TV broadcast for air target detection: Preliminary experimental results," 2017 IEEE Radar Conference (RadarConf), Seattle, WA, 2017, pp. 1592-1596.

[C4] N. Ustalli, D. Pastina and P. Lombardo, "Theoretical performance prediction for the detection of moving targets with Forward Scatter Radar Systems", 2016 17th International Radar Symposium (IRS), Krakow, 2016, pp. 1-6.

References

- [1] N.J. Willis, Bistatic Radar , 2nd ed. SciTech Publishing Inc., 2005.
- [2] P.Y.Ufimtsev,,: ‘Fundamentals of the physical theory of diffraction’ (John Wiley & Sons, 2007).
- [3] Siegel, K. M.: Bistatic Radars and Forward Scattering, Proc. Nat. Conf. Aeronaut. Electron., pp. 286-290, May 12-14, 1958.
- [4] R. E. Hiatt, K. M. Siegel and H. Weil, "Forward Scattering by Coated Objects Illuminated by Short Wavelength Radar," in *Proceedings of the IRE*, vol. 48, no. 9, pp. 1630-1635, Sept. 1960.
- [5] J. I. Glaser, "Bistatic RCS of Complex Objects near Forward Scatter," in *IEEE Transactions on Aerospace and Electronic Systems*, vol. AES-21, no. 1, pp. 70-78, Jan. 1985.
- [6] M. Cherniakov, R. S. A. R. Abdullah, P. Jancovic, M. Salous and V. Chapursky, "Automatic ground target classification using forward scattering radar," in *IEE Proceedings - Radar, Sonar and Navigation*, vol. 153, no. 5, pp. 427-437, Oct. 2006.
- [7] V. Sizov, M. Cherniakov and M. Antoniou, "Forward scattering radar power budget analysis for ground targets," in *IET Radar, Sonar & Navigation*, vol. 1, no. 6, pp. 437-446, Dec. 2007.
- [8] M. Gashinova, L. Daniel, V. Sizov, E. Hoare and M. Cherniakov, "Phenomenology of Doppler forward scatter radar for surface targets observation," in *Radar, Sonar & Navigation, IET* , vol.7, no.4, pp.422-432, April 2013.
- [9] M. Antoniou; V. Sizov; Cheng Hu; P. Jancovic; R. Abdullah; N. E. A. Rashid; M. Cherniakov, “The concept of a forward scattering micro-sensors radar network for situational awareness”, 2008 International Conference on Radar, 2008, pp. 171 – 176.
- [10] C. Hu, V. Sizov, M. Antoniou, M. Gashinova and M. Cherniakov, "Optimal Signal Processing in Ground-Based Forward Scatter Micro Radars," in *IEEE Transactions on Aerospace and Electronic Systems*, vol. 48, no. 4, pp. 3006-3026, October 2012.
- [11] Gashinova, M., Sizov, V., Zakaria, N.A., et al.: ‘Signal detection in multi-frequency forward scatter radar’. Seventh European Radar Conf., 2010, Paris, France, pp. 276–279.
- [12] Blyakhman, A., Runova, I.: ‘Forward scattering radiolocation bistatic RCS and target detection’. IEEE Int. Radar Conf., Waltham, MA, April 1999, pp. 203–208.
- [13] A. G. Ryndyk, A. V. Myakinkov, D. M. Smirnova and M. S. Gashinova, "Estimation of coordinates of ground targets in multi-static forward scattering radar," *IET International Conference on Radar Systems (Radar 2012)*, Glasgow, UK, 2012, pp. 1-4.

-
- [14] D. Pastina, M. Contu, P. Lombardo, M. Gashinova, A. De Luca, L. Daniel, M. Cherniakov, "Target motion estimation via multi-node forward scatter radar system," in *IET Radar, Sonar & Navigation*, vol. 10, no. 1, pp. 3-14, 1 2016.
 - [15] A. B. Blyakhman; A. V. Myakinkov; A. G. Ryndyk, "Tracking algorithm for three-dimensional bistatic forward scattering radar with weighting of primary measurements", European Radar Conference, 2005. EURAD 2005. 2005, pp. 153 – 156.
 - [16] A. De Luca, L. Daniel, M. Gashinova and M. Cherniakov, "Target parameter estimation in moving transmitter moving receiver forward scatter radar," 2017 18th International Radar Symposium (IRS), Prague, 2017, pp. 1-7.
 - [17] M. Cherniakov; M. Salous; V. Kostylev; R. Abdullah, "Analysis of forward scattering radar for ground target detection", European Radar Conference, 2005. EURAD 2005, 2005, pp. 145 – 148.
 - [18] R. S. A. Raja Abdullah, Cherniakov, M., Jancovic, P., Solous M., "Progress on Using Principle Component Analysis in FSR for Vehicle Classification," in 2nd International Workshop in Intelligent Transportation, WIT2005, Germany, 2005, pp.7-12.
 - [19] N. E. A. Rashid; M. Antoniou; P. Jancovic; V. Sizov; R. Abdullah; M. Cherniakov, "Automatic target classification in a low frequency FSR network", 2008 European Radar Conference, 2008, pp. 68 – 71.
 - [20] R. S. A. Raja Abdullah, M. I. Saripan and M. Cherniakov, "Neural network based for automatic vehicle classification in forward scattering radar," 2007 IET International Conference on Radar Systems, Edinburgh, UK, 2007, pp. 1-5.
 - [21] M. Contu, A. De Luca, S. Hristov, L. Daniel, A. Stove, M. Gashinova, M. Cherniakov , D. Pastina, P. Lombardo, A. Baruzzi, D. Cristallini "Passive Multi-frequency Forward-Scatter Radar Measurements of Airborne Targets using Broadcasting Signals", IEEE Transactions on Aerospace and Electronic Systems, in print.
 - [22] M. I. Skolnik, "Introduction to radar systems", McGraw- Hill 1962.
 - [23] A.H.Taylor, L.C. Young and L.A.Hyland, "System for the detecting objects by radio", U.S. patent No 1,981,884; Novembre 27, 1934.
 - [24] IEEE Standard Radar Definitions, IEEE Std 686-1997, September 16, New York, 1997.
 - [25] H. D. Griffiths, "From a different perspective: principles, practice and potential of bistatic radar," 2003 Proceedings of the International Conference on Radar (IEEE Cat. No.03EX695), 2003, pp. 1-7.
 - [26] M. C. Jackson, "The geometry of bistatic radar systems," in Communications, Radar and Signal Processing, IEE Proceedings F, vol. 133, no. 7, pp. 604-612, December 1986.

-
- [27] M. Cherniakov, M. Gashinova, Cheng Hu, M. Antoniou, V. Sizov and L. Y. Daniel, "Ultra wideband forward scattering radar: Concept and prospective," 2007 IET International Conference on Radar Systems, Edinburgh, UK, 2007, pp. 1-5.
 - [28] L.A. Gebhard, "Evolution of Naval Radio-electronics and Contributions of the Naval Research Laboratory", 1979, p.186.
 - [29] P. Y. Ufimtsev, "Comments on diffraction principles and limitations of RCS reduction techniques," in Proceedings of the IEEE, vol. 84, no. 12, pp. 1830-1851, Dec. 1996.
 - [30] J. Glaser, "Forward Scatter Radar for Future Systems", WSTIAC Quarterly, Vol. 10, N. 3, pp. 3-8, 2011.
 - [31] I. Suberviola, I. Mayordomo and J. Mendizabal, "Experimental Results of Air Target Detection With a GPS Forward-Scattering Radar," in *IEEE Geoscience and Remote Sensing Letters*, vol. 9, no. 1, pp. 47-51, Jan. 2012.
 - [32] P. Krysik, K. Kulpa and P. Samczyński, "GSM based passive receiver using forward scatter radar geometry," 2013 14th International Radar Symposium (IRS), Dresden, 2013, pp. 637-642.
 - [33] T. Martelli, F. Colone and P. Lombardo, "First experimental results for a WiFi-based passive forward scatter radar," 2016 IEEE Radar Conference (RadarConf), Philadelphia, PA, 2016, pp. 1-6.
 - [34] A. De Luca, M. Contu, S. Hristov, L. Daniel, M. Gashinova and M. Cherniakov, "FSR velocity estimation using spectrogram," 2016 17th International Radar Symposium (IRS), Krakow, 2016, pp. 1-5.
 - [35] M. Gashinova, M. Cherniakov, N. A. Zakaria and V. Sizov, "Empirical model of vegetation clutter in forward scatter radar micro-sensors," 2010 IEEE Radar Conference, Washington, DC, 2010, pp. 899-904.
 - [36] V. Sizov, M. Gashinova, N. Zakaria and M. Cherniakov, "VHF communication channel characterisations over complex wooded propagation paths with applications to ground wireless sensor networks," in *IET Microwaves, Antennas & Propagation*, vol. 7, no. 3, pp. 166-174, February 19 2013.
 - [37] K. Kabakchiev, L. Daniel, M. Gashinova, E. Hoare, M. Cherniakov and V. Sizov, "Radar parameters influence on the clutter in maritime forward scatter radar," 2014 11th European Radar Conference, Rome, 2014, pp. 113-116.
 - [38] Eigel Jr, R., Collins, P., Terzuoli Jr, A., Nesti, G., and Fortuny, J. Bistatic scattering characterization of complex objects. *IEEE Transactions on Geoscience and Remote Sensing* (2000).
 - [39] Gashinova, M., Daniel, L., Hoare, E., Sizov, V., Kabakchiev, K., Cherniakov, M.: "Signal characterisation and processing in the forward scatter mode of bistatic passive coherent location systems", *EURASIP J. Adv. Signal Process.*, 2013, 2013, (1), pp. 1–13.

-
- [40] W.E.Ayer, ‘Characteristics of Crystal-Video Receivers employing RF preamplification’. Technical Report No.150-3, Standord Electronics Laboratories, Standford Univerisity, Standford, California, Sep.20, 1956.
 - [41] J. Edwards, “Sensitivity of crystal video receivers”, IEE Proceedings F: Communications, Radar and Signal Processing, 1985, Vol. 132, N. 4, pp. 233 – 244.
 - [42] N.Ustalli, D.Pastina and P.Lombardo, “ Theoretical performance prediction for the detection of moving targets with Forward Scatter Radar Systems”, 2016 17th International Radar Symposium (IRS), Krakow, 2016, pp.1-6.
 - [43] N. Ustalli, P. Lombardo and D. Pastina, “Detection performance of Forward Scatter Radar using a Crystal Video Detector”, IEEE Transactions on Aerospace and Eelectronic Systems, in print.
 - [44] F. Kretschmer, F. C. Lin, B. Lewis, “A Comparison of Noncoherent and Coherent MTI Improvement Factors”, IEEE Transactions on Aerospace and Eelectronic Systems, Vol 19, N. 3, May1983, pp. 398-404.
 - [45] E.J. Barlow, “Doppler radar”, Proceeding of the IRE, Vol. 37, N. 4, April 1949, pp. 340-355, in D. Barton Radars, Vol 7: CW and Doppler Radar, ,Artech House 1978.
 - [46] Stutzman and G. Thiele, Antenna Theory and Design 3nd ed, Wiley (pg.43)
 - [47] S.M. Kay, Fundamentals of Statistical Signal Processing: Estimation Theory, Prentice Hall, 1983.
 - [48] Ha, Hyung-Tae, and Serge B. Provost. "An accurate approximation to the distribution of a linear combination of non-central chi-square random variables." REVSTAT–Statistical Journal 11.3 (2013): 231-254.
 - [49] C. Walck. “Handbook on Statistical Distributions for Experimentalists”; International Report SUF-PFY/96-01; University of Stockholm: Stockholm, Sweden, 2007.
 - [50] M.Abramovitz and I. A. Stegun, Handbook of Mathematical Functions, U.S. Government Printing Office, Washington, D.C.:National Bureau of Standards, 1964.
 - [51] T.W. Anderson, An Introduction to Multivariate Statistical Analysis, 3rd ed. New York, NY, USA: Wiley-Intersci., 2003.
 - [52] Robertson, G. H. "Computation of the noncentral F distribution (CFAR) detection." Aerospace and Electronic Systems, IEEE Transactions on 5 (1976): 568-571.
 - [53] N.Ustalli, D.Pastina, C.Bongioanni, P. Lombardo, “ Motion parameters estimation in dual-baseline Forward Scatter Radar configuration”, 2017 Iet conference
 - [54] A. De Luca, L. Daniel, M. Gashinova and M. Cherniakov, "Target parameter estimation in moving transmitter moving receiver forward scatter radar," 2017 18th International Radar Symposium (IRS), Prague, 2017, pp. 1-7.

-
- [55] F. Colone, C. Bongioanni and P. Lombardo, "Multifrequency integration in FM radio-based passive bistatic radar. Part I: Target detection," in *IEEE Aerospace and Electronic Systems Magazine*, vol. 28, no. 4, pp. 28-39, April 2013.
 - [56] F. Colone, C. Bongioanni and P. Lombardo, "Multifrequency integration in FM radio-based passive bistatic radar. Part II: Direction of arrival estimation," in *IEEE Aerospace and Electronic Systems Magazine*, vol. 28, no. 4, pp. 40-47, April 2013.
 - [57] P. E. Howland, D. Maksimiuk, and G. Reitsma "FM radio based bistatic radar", *IEE Proc. Radar Sonar Navig.*, vol. 152, no. 3, pp. 107–115, Jun. 2005.
 - [58] A. Di Lallo, A. Farina, R. Fulcoli, P. Genovesi, R. Lalli, and R. Mancinelli "Design, development and test on real data of an FM based prototypical passive radar" In *Proc. 2008 IEEE Radar Conf.*, May 2008, pp. 1–6.
 - [59] M. Malanowski, K. Kulpa, J. Kulpa, P. Samczynski, and J. Misiurewicz "Analysis of detection range of FM-based passive radar" *IEE Proc. Radar Sonar Navig.*, vol. 8, no. 2, pp. 153–159, Feb. 2014.
 - [60] Griffiths, H. D., and Baker C. J. Passive coherent location radar systems. Part 1: performance prediction. *IEE Proceedings on Radar, Sonar and Navigation*, Vol. 152, 3 (Jun. 2005), 153–159.